8-2019

Angles-Only EKF Navigation for Hyperbolic Flybys

Iggy Matheson
Utah State University

ANGLES-ONLY EKF NAVIGATION FOR HYPERBOLIC FLYBYS

by

Iggy Matheson

A thesis submitted in partial fulfillment
of the requirements for the degree

of

MASTER OF SCIENCE

in

Aerospace Engineering

Approved:

David K. Geller, Ph.D. Major Professor	Geordie Richards, Ph.D. Committee Member
Stephen A. Whitmore, Ph.D. Committee Member	Richard S. Inouye, Ph.D. Vice Provost for Graduate Studies

UTAH STATE UNIVERSITY
Logan, Utah

2019

ABSTRACT

Angles-Only EKF Navigation for Hyperbolic Flybys

by

Iggy Matheson, Master of Science

Utah State University, 2019

Major Professor: David K. Geller, Ph.D.
Department: Mechanical and Aerospace Engineering

Recent concepts for interstellar travel, notably the Breakthrough Starshot initiative, attempt to define a minimum feasible probe to return *in situ* data about a nearby star within the career lifetime of a single researcher with minimal investment in ground-based or space-based infrastructure. These concepts generally propose launching gram-scale probes, consisting of little more than an optical camera and a microprocessor, to speeds on the order of $0.1c$ on an enormous laser. For lack of onboard computational resources, an extremely simple navigation technique is required to autonomously estimate position and velocity; most authors suggest some form of Kalman filter. This study shows that a simple extended Kalman filter processing angles-only measurements is capable of consistently estimating position and velocity for a Starshot-style probe when provided with highly accurate initial estimates and small initial uncertainty at speeds characteristic of current space probes ($2 \cdot 10^{-5}\ c$), as well as the gravity of the target star, but does not investigate filter performance at proposed Starshot speeds.

(175 pages)

PUBLIC ABSTRACT

Angles-Only EKF Navigation for Hyperbolic Flybys

Iggy Matheson

Space travelers in science fiction can drop out of hyperspace and make a pinpoint landing on any strange new world without stopping to get their bearings, but real-life space navigation is an art characterized by limited information and complex mathematics that yield no easy answers. This study investigates, for the first time ever, what position and velocity estimation errors can be expected by a starship arriving at a distant star - specifically, a miniature probe like those proposed by the Breakthrough Starshot initiative arriving at Proxima Centauri. Such a probe consists of nothing but a small optical camera and a small microprocessor, and must therefore rely on relatively simple methods to determine its position and velocity, such as observing the angles between its destination and certain guide stars and processing them in an algorithm known as an extended Kalman filter. However, this algorithm is designed for scenarios in which the position and velocity are already known to high accuracy. This study shows that the extended Kalman filter can reliably estimate the position and velocity of the Starshot probe at speeds characteristic of current space probes, but does not attempt to model the filter's performance at speeds characteristic of Starshot-style proposals. The gravity of the target star is also estimated using the same methods.

ACKNOWLEDGEMENTS

The last three years have been an extraordinary opportunity for personal and professional growth, thanks to the location of Utah State University in beautiful Cache Valley and the freedom that a fellowship provides to pursue research questions of uniquely personal interest. Without the support of Dr. David Long, Dr. Bradley Adams, and Dr. David Allred at Brigham Young University from 2013-2016, along with the friendship of Patrick Walton, the circumstances that enabled this study would not have been possible. Here at Utah State University, thanks are due to Dr. David Geller for graciously serving as the faculty advisor during 2016-2019 for several more students than he had previously expected, including myself. I also thank Dr. Geller for his patience with my consistently slow progress towards the degree, and Dr. Randy Christensen for teaching a course on optimal estimation that provided the stimulus to finally prepare a thesis proposal. I also thank Dr. Geller, Dr. Christensen, and Dr. Todd Moon, among others, for opening doors to future opportunities through their generous responses to my many requests for letters of reference.

This material is based upon work supported by the National Science Foundation Graduate Research Fellowship Program under the fellowship ID number 2016234284. This fellowship was administered by Utah State University as part of NSF Grants 1147384 and 1745048. Any opinions, findings, and conclusions or recommendations expressed in this material are mine alone, and do not necessarily reflect the views of the National Science Foundation.

CONTENTS

LIST OF TABLES

LIST OF FIGURES

NOTATION

Matrices

$\mathbf{0}$	Zero matrix
$\mathbf{A}$	Component matrix of state dynamics matrix
$\mathbf{B}$	State control matrix
$\mathbf{B}$	Component matrix of state dynamics matrix
$\mathbf{C}$	Component matrix of state dynamics matrix
$\mathbf{G}$	State noise matrix
$\mathbf{F}$	State dynamics matrix
$\mathbf{H}$	Measurement geometry matrix
$\mathbf{I}$	Identity matrix
$\mathbf{L}$	Lower triangular Cholesky factorization of covariance matrix
$\mathcal{O}$	Linear time-invariant observability matrix
$\mathbf{P}$	State covariance matrix
$\mathbf{Q}$	Process noise strength matrix
$\mathbf{R}$	Measurement noise covariance matrix
$\mathbf{W}$	Linear time-varying observability Gramian

Prefixes

δ	Small error or deviation from nominal, depending on context

Scalars and Abbreviations

α	Used with confidence levels and intervals
Δt	Duration of short time interval
δ	Declination, in celestial coordinates
θ	Angle measurement or generic angle
μ	Inverse-square gravity term of star
ν	Measurement noise

ν	True anomaly
σ	Standard deviation
ϕ	Clock angle for orbit orientation
χ^2	Chi-squared distribution
Ω	Right ascension of the ascending node
a	Semi-major axis
b	Semi-minor axis
c	Speed of light
e	Eccentricity
f	A small number between 0 and 1
$h(\cdot)$	Nonlinear scalar-valued measurement equation
h	Specific angular momentum
r	Magnitude of position vector
t	Time
v	Magnitude of velocity vector
x	First rectangular component of position
y	Second rectangular component of position
z	Third rectangular component of position
AU	Astronomical unit
CL	Confidence level
EKF	Extended Kalman Filter
ICRF	International Celestial Reference Frame
MU	Scaled mass unit
RSS	Root sum square
TU	Scaled time unit
VU	Scaled velocity unit
F	Hyperbolic eccentric anomaly
M	Hyperbolic mean anomaly

$\mathcal{N}$	Gaussian distribution
N	Number of time steps or Monte Carlo runs
Q	Scalar magnitude of all entries in process noise matrix
R	Variance of scalar measurement

Subscripts

$(\cdot)_\infty$	Evaluated at infinity
$(\cdot)_\theta$	Associated with an angle measurement
$(\cdot)_\mu$	Associated with mass of target star
$(\cdot)_0$	Associated with initial conditions
$(\cdot)_1$	Associated with guide star 1
$(\cdot)_2$	Associated with guide star 2
$(\cdot)_3$	Associated with guide star 3
$(\cdot)_{M\times N}$	Matrix of dimensions $M \times N$
$(\cdot)_B$	Associated with principal vector of B-plane
$(\cdot)_f$	Associated with final time
$(\cdot)_i$	Associated with ith Monte Carlo run
$(\cdot)_k$	Evaluated at time $t = t_k$
$(\cdot)_{MC}$	Associated with a Monte Carlo simulation
$(\cdot)_{\text{nom}}$	Associated with nominal trajectory
$\dot{()}_P$	Associated with space probe
$(\cdot)_p$	Associated with periapse
$(\cdot)_{\text{pos}}$	Associated with position
$(\cdot)_S$	Associated with destination star
$(\cdot)_S$	Associated with arrival asymptote in perifocal frame
$(\cdot)_{\text{Sun}}$	Associated with the Sun
$(\cdot)_t$	Associated with tangential direction
$[\cdot]_{\mathbf{a}=\mathbf{b}}$	Evaluated with substitutions such that $\mathbf{a} = \mathbf{b}$
$(\cdot)_{\text{vel}}$	Associated with velocity

$(\cdot)_x$	Associated with first rectangular component of position
$(\cdot)_y$	Associated with second rectangular component of position
$(\cdot)_z$	Associated with third rectangular component of position

Superscripts

$\hat{(\cdot)}$	Associated with filter model
$\dot{(\cdot)}$	First time derivative
$(\cdot)^T$	Matrix transpose
$(\cdot)^-$	Before measurement update
$(\cdot)^-$	Lower endpoint of confidence interval
$(\cdot)^+$	After measurement update
$(\cdot)^+$	Upper endpoint of confidence interval
$(\cdot)^\circ$	Degree of arc
$(\cdot)'$	Minute of arc
$(\cdot)'$	New expression of $(\cdot)$ in different coordinates

Vectors

$\delta\mathbf{x}$	State error vector
ν	Measurement noise vector
$\mathbf{f}(\cdot)$	Nonlinear vector-valued state equation
$\mathbf{h}(\cdot)$	Nonlinear vector-valued measurement equation
$\mathbf{k}$	Generic three-dimensional unit vector
$\mathbf{n}$	Initial state perturbation vector
$\mathbf{r}$	Position vector
$\mathbf{u}$	Control vector
$\mathbf{v}$	Velocity vector
$\mathbf{v}$	Generic three-dimensional vector
$\mathbf{w}$	Process noise vector
$\mathbf{x}$	State vector
$\mathbf{z}$	Measurement vector

B	Principal vector in B-plane
P	First coordinate axis in perifocal frame
Q	Second coordinate axis in perifocal frame
R	Third coordinate axis in perifocal frame
S	Arrival asymptote in perifocal frame

CHAPTER 1

INTRODUCTION

Navigation, or onboard determination of position and velocity relative to some reference frame, has not yet been studied in the context of approach to another star despite its critical importance to the success of any interstellar mission concept. To address that gap, this thesis investigates how accurately a small interstellar probe can estimate its own position and velocity, plus the gravity of the destination star, using only observations of the time-varying angles between the destination star and guide stars, as well as the time-varying angular diameter of the destination star. Although the frequently investigated topics of propulsion, power, communications, structures, and materials may define a spacecraft theoretically capable of crossing the interstellar void, without accurate onboard navigation algorithms a notional interstellar probe may deviate too far from its planned course to return useful scientific data, or the data returned from its nominal course may be difficult to analyze.

Recent concepts call for launching "starchips" - essentially a single optical camera and a small transmitter on a silicon wafer - to Alpha Centauri on photon sails that are discarded after a short boost from an Earth-based laser. Since these probes have no room for sophisticated navigational equipment and may suffer enormous position dispersions by the end of the boost phase [1], they are more vulnerable to navigation errors than traditional self-propelled starship concepts. However, their simplicity makes them useful model systems for studying navigation errors achievable in interstellar flight using current camera technology and simple estimation algorithms. Surprisingly, navigation errors and dispersions are not addressed in any published literature about these concepts.

1.1 Research Objective

For this study, a probe is assumed to approach Proxima Centauri on an uncontrolled

hyperbolic path, subject to small zero-mean Gaussian disturbance forces. Its objective is to accurately determine, as a "minimal scientific return," its own relative position and velocity in an inertial reference frame centered at Proxima Centauri, as well as the gravity of the star. To achieve this, it processes angles-only measurements of Proxima Centauri and guide stars in an extended Kalman filter. An observability analysis is also conducted using linear system theory. For this first study, a point-mass gravity law is assumed and all perturbations, including relativistic effects, the proper motion of stars, light-time corrections, and clock errors, are neglected. The probe's navigation objectives are considered to be achieved if the estimated position, velocity, and gravity errors contained within the filter covariance matrix are consistent with the true position, velocity, and gravity errors observed in Monte Carlo simulation. Through simulating a variety of initial conditions and uncertainties, it is shown that the probe's navigation objectives can be achieved when the initial errors and uncertainties are small, but not when the initial position uncertainty is large. Other options for achieving those objectives are then suggested, including different observations, more advanced estimation techniques, or more detailed environment models.

1.2 Thesis Overview

This chapter introduces the question driving the current research. Chapter 2 presents a review of relevant literature in starchip concepts, interstellar navigation, target stars and planets, estimation and observability theory, and gravity estimation. Chapter 3 describes the mathematical procedures used to carry out the study, including the initial conditions and parameters. Chapter 4 presents numerical results. Finally, Chapter 5 states conclusions and describes possible directions for future work.

CHAPTER 2

LITERATURE SURVEY

This chapter places the proposed research in context by briefly describing the navigational aspects of notable historical and ongoing design studies for interstellar probes. Next, current knowledge of the Proxima Centauri system is briefly summarized. Finally, related literature on navigation algorithms, gravity estimation techniques, and observability measures is summarized as background for the procedures described in this report.

2.1 Introduction to Interstellar Studies

The meaning of *interstellar studies* is not as widely standardized as, say, that of *aerospace engineering*, so for this paper it refers broadly to any research related to interstellar travel. Travel between stars is many orders of magnitude more technically challenging than travel between planets, but research into concepts well beyond currently practical limits can sometimes yield useful insight into present-day problems.

A wide variety of propulsion techniques have been proposed for interstellar travel. These can generally be classified as matter rockets powered by hydrogen fusion, photon rockets powered by hydrogen fusion or matter-antimatter reaction, photon sails, or magnetic sails [2]. Whatever the propulsion technique, starship concepts tend to share four characteristics: enormous characteristic length (on the order of kilometers), enormous mass (thousands to millions of tons), enormous power requirements (gigawatts to petawatts), and materials requirements orders of magnitude beyond the state of the art. The details of these concepts are irrelevant to this research, so only those studies that explicitly consider navigation or that closely resemble the "starchip" concept will be individually described.

2.1.1 Project Daedalus

Between 1973 and 1978, the British Interplanetary Society conducted a study intended

to produce as detailed an engineering design for an uncrewed interstellar probe as was then feasible. The resulting starship was a two-stage fusion-powered rocket with an initial mass of 54,000 metric tons, a cruise speed of $0.12c$, and a destination of Barnard's Star, which lies 5.9 light years from Earth [2]. In order to achieve a 1 AU error in flyby distance at the target star, the ship's velocity vector was required to point within 2.6 µrad of the destination. Accounting for stellar aberration, Doppler shifts, parallax, and various assumptions about planetary size, distance, and albedo, an optical telescope with a 5m-diameter mirror was deemed necessary to detect terrestrial planets at a distance of 1.5 AU from the star [3, 4]. Although no attempt was made to model the onboard position determination capabilities of the spacecraft, these results suggest that a key performance metric for interstellar approach navigation is the angle between the estimated velocity vector and the true velocity vector; also that angles-only optical navigation with a camera lens on the order of 5 cm in diameter is unlikely to succeed.

2.1.2 Project Icarus

Project Icarus is an attempt by the British Interplanetary Society and a nonprofit called Icarus Interstellar to revisit the goals of Project Daedalus with 21$^{\text{st}}$-century physics and engineering knowledge. The project is far from complete, but two baseline starship designs have been identified. The so-called "Ghost Ship" is a single-stage fusion-powered rocket with an initial mass of 153,800 metric tons, a cruise speed of $0.06c$, and a destination of Proxima Centauri, which lies 4.2 light years from Earth [5]. The "Firefly" differs in the details of its power and propulsion, and has a mass of 23,200 metric tons and a cruise speed of $0.047c$ [6]. Preliminary articles addressing the navigation problem discuss complications encountered in travel at relativistic speeds over interstellar distances, including interference from large, bright exhaust plumes; changes in observed star positions due to parallax, proper motion, and relativistic aberration; changes in observed star magnitudes and colors due to relativistic Doppler effects and changing distances; and the possibility of using pulsars instead of normal stars as position references [7, 8]. These discussions are valuable, but the most recent publications do not yet provide any details about the implementation or

performance of any proposed Icarus navigation system.

2.1.3 Miniature Photon Sail Concepts

Because they require no onboard propellant, photon sails are a popular approach to interstellar propulsion. To deliver a substantial scientific payload to another star, however, they exchange the engineering challenge of assembling and managing extremely large masses of propellant for the challenge of constructing and maintaining an extremely large, extremely thin surface - often on the order of kilometers wide and microns thick. In the past 5 years, the "starchip" concept has become a popular alternative to the large scientific probe riding a single photon sail. A very small probe massing on the order of 1 to 100 grams can be placed on a photon sail on the order of 1 to 10 meters wide and accelerated to relativistic speeds with a laser much smaller than that required to power a larger probe, though the laser is still enormous [9]. Theoretically, this allows a large swarm of such sailcraft ("starchips") to be dispatched toward a nearby star and return encounter data about the target in decades, not centuries. Because each starchip has minimal onboard control capability, a swarm of starchips must be launched to ensure that at least one passes the target star at the desired distance [9]. It has been suggested that nearby probes could communicate with each other to augment their communication, navigation, and scientific capacity using a distributed architecture, but this idea has not been explored in detail and is outside the scope of this work [10, 11].

Notable mission concepts in this class include Project Dragonfly, Andromeda, and Breakthrough Starshot. Some details of these concepts follow.

2.1.4 Project Dragonfly

Project Dragonfly developed from a 2014 student competition sponsored by the Initiative for Interstellar Studies and the International Space University. It proposes [12] to propel a 4000-kg spacecraft to Alpha Centauri at a cruise speed of $0.05c$ using a 100 GW laser based in a heliocentric orbit. Such a large probe is not a "starchip," but it is still much smaller than many other mission concepts. By carefully optimizing the properties

of the sail and laser, the concept achieves a "modest" laser aperture diameter of 183.1 km and a "modest" sail diameter of 4.6 km. The authors suggest a pulsar navigation system for position determination during interstellar cruise, but make no attempt to model its performance.

2.1.5 The Andromeda Study

The "starchip" concept produced by the Initiative for Interstellar Studies itself [13] uses a relatively modest 15 GW laser 95 m in diameter to propel a 23g probe to Alpha Centauri at $0.1c$. The size of the sail is not discussed, but the probe itself is described as a 5×10 cm plate carrying a camera, a small radioisotope battery, and a flight computer. It is to use sets of three orthogonal gyroscopes, accelerometers, and magnetometers for inertial navigation, along with a star tracker and a sun sensor for celestial navigation during cruise and the flyby encounter. A Kalman filter is suggested for measurement processing. Again, no attempt is made to model the performance of the navigation algorithm.

2.1.6 Breakthrough Starshot

The most well-publicized starchip (and the source of the term) is that of Breakthrough Starshot, an initiative established in 2016 by a group of private investors with the stated goal of launching a probe to Alpha Centauri by 2036. A 2018 paper [14] describes the current concept as a 3.6g scientific payload carried at $0.2c$ by a 4.1 m sail; the sail is powered by a 200 GW laser with an aperture diameter of 2.7 km. No onboard navigation system is described, much less modeled.

2.2 Proxima Centauri

The details of the destination star system modeled in this work do not matter, since the research question is more concerned with observability at a high level than with the numerical performance of the EKF. However, since each starchip concept takes Alpha Centauri or Proxima Centauri as its destination, it is not amiss to describe the system here. The star is located 4.2 light years from Earth at a right ascension of 14 hr 29 min and a

declination of -62° 40' on the celestial sphere. Its diameter and mass are estimated at about 14% and 12% that of the Sun, respectively. Anglada-Escude reported a planet, Proxima Centauri b, in August 2016. Its mass is estimated at 1.27 times that of Earth, with a 1σ confidence interval of 1.10-1.46 Earth masses. The semi-major axis of the Proxima b's orbit is estimated at 0.0485 AU (1σ 0.0434-0.0526). The orbital eccentricity is estimated at less than 0.35 [15]. The orientation of the orbit in space and the position of the planet at epoch have been described, but they will not be used in this study, so they are omitted here.

2.3 Navigation Algorithms

In the context of aerospace guidance, navigation, and control, the term "navigation" refers specifically to estimation of the time-varying position and velocity of a spacecraft using measurements taken along its trajectory. More broadly, it encompasses the estimation of any parameters necessary for the vehicle to successfully complete its mission. These can include attitude and attitude rate; biases, scale factors, alignment errors, and noise strengths in instrumentation; and elements of the gravity model or other environment models. Navigation algorithms return estimates for the desired quantities over an interval of time and confidence intervals to approximate the uncertainty in the estimates over that interval. The results are then used to plan future mission events. Related algorithms are often applied to retroactively improve past position and velocity estimates for improved analysis of science data; depending on the application and the algorithm, this is known as *orbit determination* or *smoothing* [16]. Most interplanetary spacecraft rely on Earth-based Doppler ranging and navigation estimates computed on the ground, only switching to autonomous onboard algorithms for maneuver sequences that occur too rapidly for ground-based control, such as landing on Mars or choosing where to impact a comet. For examples, see [17–22]. Because light-time delays make Earth-dependent navigation less accurate and less reliable at more distant targets, much theoretical literature on space navigation concerns autonomous techniques, defined as those which achieve a complete navigation solution without depending on instrumentation other than that carried onboard the spacecraft or its companions in a constellation.

2.3.1 Kalman Filtering

Almost all space navigation theory has roots in the Kalman filter, an algorithm most famously described by Rudolf Kalman in 1960. For linear systems, the state estimates produced by the Kalman filter are proven to be the maximum-likelihood and minimum-variance estimates [23].

The Kalman filter describes the true value of the state to be estimated as a Gaussian random variable with mean $\mathbf{x}$ and covariance $\mathbf{P}$ and the estimated value of the state as a Gaussian random variable with mean $\hat{\mathbf{x}}$ and covariance $\hat{\mathbf{P}}$. The true state evolves in time according to a linear differential equation

$$\dot{\mathbf{x}} = \mathbf{F}\mathbf{x} + \mathbf{B}\mathbf{u} + \mathbf{G}\mathbf{w} \tag{2.1}$$

where $\mathbf{F}$ is a (possibly time-varying) matrix describing the state dynamics, $\mathbf{B}$ is a (possibly time-varying) matrix describing the interaction of applied control with the state, $\mathbf{u}$ is a vector representing applied control effort, $\mathbf{G}$ is a (possibly time-varying) matrix describing the interaction of Gaussian white noise with the state, and $\mathbf{w}$ is a zero-mean Gaussian white noise vector with strength $\mathbf{Q}$. Continuous-time Gaussian white noise as described in this model is a mathematical fiction, related to the covariance of Gaussian white noise in a discrete-time system model as

$$\mathrm{cov}(\mathbf{w}_{\mathrm{discrete}}) = \frac{\mathbf{Q}}{\Delta t} \tag{2.2}$$

where Δt is the relevant discrete time interval. The covariance of the truth state evolves in time as

$$\dot{\mathbf{P}} = \mathbf{F}\mathbf{P} + \mathbf{P}\mathbf{F}^T + \mathbf{G}\mathbf{Q}\mathbf{G}^T \tag{2.3}$$

The estimated state evolves as

$$\dot{\hat{\mathbf{x}}} = \hat{\mathbf{F}}\hat{\mathbf{x}} + \hat{\mathbf{B}}\hat{\mathbf{u}} \tag{2.4}$$

and its covariance evolves as

$$\dot{\hat{\mathbf{P}}} = \hat{\mathbf{F}}\hat{\mathbf{P}} + \hat{\mathbf{P}}\hat{\mathbf{F}}^T + \hat{\mathbf{G}}\hat{\mathbf{Q}}\hat{\mathbf{G}}^T \tag{2.5}$$

where each element is marked with a circumflex to emphasize the fact that the dynamics, control, noise interaction, and noise strength matrices used in the filter model may not exactly match those of the real-world system and the control vector may not be known exactly.

The state estimates can be improved by incorporating measurement data. The measurement is modeled as a linear function of the estimated state,

$$\hat{\mathbf{z}} = \hat{\mathbf{H}}\hat{\mathbf{x}} \tag{2.6}$$

The true measurement is assumed to be a linear function of the true state plus zero-mean Gaussian white measurement noise with assumed covariance $\hat{\mathbf{R}}$, such that

$$\mathbf{z} = \mathbf{H}\mathbf{x} + \mathbf{v} \tag{2.7}$$

At some instant t_k, a measurement $\mathbf{z}_k$ is taken and compared with an expected value $\hat{\mathbf{z}}_k^-$ based on the filter measurement model. A gain

$$\hat{\mathbf{K}}_k = \hat{\mathbf{P}}_k^- \hat{\mathbf{H}}_k^T \left[\hat{\mathbf{H}}_k \hat{\mathbf{P}}_k^- \hat{\mathbf{H}}_k^T + \hat{\mathbf{R}}_k\right]^{-1} \tag{2.8}$$

is computed to weight the difference between the true measurement and the expected measurement, and the estimated state is updated as

$$\hat{\mathbf{x}}_k^+ = \hat{\mathbf{x}}_k^- + \hat{\mathbf{K}}_k(\mathbf{z}_k - \hat{\mathbf{z}}_k^-) \tag{2.9}$$

The estimated covariance is also updated as

$$\hat{\mathbf{P}}_k^+ = (\mathbf{I} - \hat{\mathbf{K}}_k\hat{\mathbf{H}}_k)\hat{\mathbf{P}}_k^-(\mathbf{I} - \hat{\mathbf{K}}_k\hat{\mathbf{H}}_k)^T + \hat{\mathbf{K}}_k\hat{\mathbf{R}}_k\hat{\mathbf{K}}_k^T \tag{2.10}$$

The new estimated state can be used to compute another estimated measurement $\hat{\mathbf{z}}_k^+$ for the same time instant; if the Kalman filter is correctly implemented the revised measurement residuals $\mathbf{z}_k - \hat{\mathbf{z}}_k^+$ should behave like zero-mean Gaussian white noise with covariance

$$\hat{\mathbf{V}}_k = \hat{\mathbf{H}}_k \hat{\mathbf{P}}_k^- \hat{\mathbf{H}}_k^T + \hat{\mathbf{R}}_k \tag{2.11}$$

The Kalman filter as described above is only strictly valid for systems with linear dynamics, controls, noise, and measurements, but it is commonly extended to near-linear systems $\dot{\mathbf{x}} = \mathbf{f}(\mathbf{x}, \mathbf{u}, \mathbf{w})$, $\dot{\hat{\mathbf{x}}} = \hat{\mathbf{f}}(\hat{\mathbf{x}}, \hat{\mathbf{u}}, \hat{\mathbf{w}})$, $\mathbf{z} = \mathbf{h}(\mathbf{x}, \mathbf{v})$, $\hat{\mathbf{z}} = \hat{\mathbf{h}}(\hat{\mathbf{x}}, \hat{\mathbf{v}})$ by considering only the error between the true state and the filter state [24]. If the error $\delta\hat{\mathbf{x}} = \mathbf{x} - \hat{\mathbf{x}}$ is sufficiently small, it may be treated as a zero-mean Gaussian random variable. The true state and filter state may then be propagated according to their respective nonlinear differential equations of motion, and the covariance of the state error propagated over short intervals as

$$\dot{\hat{\mathbf{P}}}_k = \hat{\mathbf{F}}_k \hat{\mathbf{P}}_k + \hat{\mathbf{P}}_k \hat{\mathbf{F}}_k^T + \hat{\mathbf{G}}_k \hat{\mathbf{Q}} \hat{\mathbf{G}}_k^T \tag{2.12}$$

where the matrices are defined as

$$\hat{\mathbf{F}}_k = \left[\frac{\partial \hat{\mathbf{f}}}{\partial \hat{\mathbf{x}}}\right]_{\hat{\mathbf{x}}=\hat{\mathbf{x}}(t_k)}, \quad \hat{\mathbf{G}}_k = \left[\frac{\partial \hat{\mathbf{f}}}{\partial \hat{\mathbf{w}}}\right]_{\hat{\mathbf{x}}=\hat{\mathbf{x}}(t_k)}, \quad E[\hat{\mathbf{w}}(t_k)\hat{\mathbf{w}}^T(t_k)] = \hat{\mathbf{Q}}_k \delta(\tau) \tag{2.13}$$

where $\delta(\tau)$ is the Dirac delta function,

$$\delta(\tau) = +\infty \ \text{ if } \tau = 0, \quad \text{else } \delta(\tau) = 0 \ \text{ such that } \int_{-\infty}^{+\infty} \delta(\tau)\, d\tau = 1 \tag{2.14}$$

The filter state and the covariance of the state error are updated as usual, with

$$\hat{\mathbf{H}}_k = \left[\frac{\partial \hat{\mathbf{h}}}{\partial \hat{\mathbf{x}}}\right]_{\hat{\mathbf{x}}=\hat{\mathbf{x}}(t_k)}, \quad \hat{\mathbf{R}}_k = \left[\frac{\partial \hat{\mathbf{h}}}{\partial \hat{\mathbf{v}}}\right]_{\hat{\mathbf{x}}=\hat{\mathbf{x}}(t_k)} \tag{2.15}$$

If the discretization time is sufficiently short, the estimated covariance $\hat{\mathbf{P}}_k$ of the state difference at any time t_k should match the covariance $\mathbf{P}_k$ of the state errors $\mathbf{x}_k - \hat{\mathbf{x}}_k$ computed from an ensemble of Monte Carlo simulations.

The above procedure is known as the "extended Kalman filter," or EKF. The EKF often requires tedious ad-hoc tuning of the noise parameters $\hat{\mathbf{P}}$ and $\hat{\mathbf{R}}$, the covariance $\hat{\mathbf{P}}_0$ of the initial state error, and the measurement frequency in order to function properly. The user-chosen values necessary to keep the filter operating in the linear regime do not always coincide with realistic noise values derived from instrument calibration or dynamic model truncation, with an achievable measurement frequency, or with a realistic initial error covariance interpreted as the probable dispersion of possible spacecraft trajectories about the desired trajectory. Despite these drawbacks, its simplicity makes it a frequent first choice for comparison against more advanced nonlinear estimation techniques.

2.3.2 Advanced Filtering Techniques

A wide variety of techniques are employed to estimate states in nonlinear problems without the assumptions of local linearity and Gaussian probability distributions inherent in the EKF [25].

The class of algorithms known as "particle filters" simultaneously propagate a group of trajectories ("particles") chosen to fill most of the probability distribution of the estimated state and report a state estimate as a weighted average of the particle states. After each state update, the particles are re-sampled from the new probability distribution.

Multiple model estimation techniques, which can be applied to the Kalman filter or to other classes of filters, propagate one or more trajectories from each of several models with slightly different parameters and report a state estimate as a weighted average of the different model states. After each state update, the model parameters are updated as well. Eventually a "best estimate" of noise parameters is achieved without the need for manual tuning as in the EKF.

Other techniques maintain the assumptions of the EKF and reformulate the problem for greater numerical stability or accuracy. "Consider filters" augment the covariance ma-

trix to account for uncertainty in filter parameters that are not estimated in the filter state, like the mass of the central body. "Information filters" propagate the inverse of the covariance matrix to account for the fact that there may be no initial estimates for some states without driving the filter out of the linear regime. "Factorized filters" use the Cholesky decomposition or U-D-U factorization of the covariance matrix to approximately double the numerical precision available for poorly conditioned problems. These filtering techniques are obvious candidates for future work, but their use is beyond the scope of this research.

2.3.3 Angles-Only Navigation

Although measurements of many types can be employed in space navigation, the most conceptually simple position fix is obtained by using some device aboard the spacecraft to measure the angles between a near body (typically the central attractor, like Earth or the Sun) and three reference directions in space (typically bright, distance stars with negligible parallax and proper motion). This defines a line of position in space, and the location of the spacecraft along that line is fixed by measuring the angular diameter of the near body, thus obtaining its range if the physical diameter is known. Angle-based optical navigation has been used in conjunction with other navigation techniques since the 1960s, on virtually every deep space mission from Apollo to New Horizons [20, 26]. It is usually implemented with a star camera, and the details depend strongly on the specific instrumentation. Since the only instrument common to all starchip concepts is the optical camera, for the purposes of this study it is fair to assume angles-only navigation as a worst case and focus on the state errors $\mathbf{x} - \hat{\mathbf{x}}$ achievable with high-level measurement noise, without developing a more detailed camera model. The details of angles-only navigation as implemented in this project are explained in Chapter 3.

2.3.4 Initial Orbit Determination

The extended Kalman filter, and other linear filters derived from it, depend on local linearity. The state dynamics matrix $\mathbf{F}$ and measurement geometry matrix $\mathbf{H}$ are formed by a first-order linear approximation of the state dynamics $\mathbf{f}$ and measurement model $\mathbf{h}$

around the state estimate $\hat{\mathbf{x}}$. If $\mathbf{f}$ and $\mathbf{h}$ are highly nonlinear around $\hat{\mathbf{x}}$, the covariance $\hat{\mathbf{P}}$ of the state estimate errors as calculated by the linearized dynamics of the Kalman filter is unlikely to match the true covariance of the state estimate errors as computed from an ensemble of Monte Carlo simulations, leading at best to an accurate but unreliable state estimate and at worst to a state estimate radically different from the true state.

Due to the extended Kalman filter's sensitivity to local linearity, it is desirable to initialize the filter with a relatively accurate initial estimate of the probe's position and velocity. The process of deriving an initial estimate of a space object's position and velocity from a small number of measurements is known as *initial orbit determination*, and a variety of algorithms exist to convert angles-only observations of a space object to orbit estimates. Among the most prominent are those named after Gauss, Laplace, and Gooding. Each of these methods assumes the existence of three points: the center of the coordinate system, the position vector $\mathbf{r}_{\text{obj}}$ of the object whose position is to be determined, and the position vector $\mathbf{r}_{\text{obs}}$ of an observation site whose location is known exactly [27]. When $\mathbf{r}_{\text{obj}} = \mathbf{r}_{\text{obs}}$ or when $\mathbf{r}_{\text{obs}} = \mathbf{0}$, the Gauss, Laplace, and Gooding methods are singular. The starchip's angles-only observation strategy may be seen as a variation of the case when $\mathbf{r}_{\text{obs}} = \mathbf{0}$, rendering the Gauss, Laplace, and Gooding methods of initial orbit determination useless. Therefore, no initial orbit determination techniques are implemented in this study, and the Kalman filter is always initialized with an identical nominal state estimate.

2.4 Gravity Estimation

It is desirable if the probe estimates the gravity of the destination star, in addition to its own position and velocity. Precise range and range-rate measurements of interplanetary spacecraft relative to the Earth have been used to refine gravity field estimates for several planets in the Solar System, but methods of estimating gravity fields autonomously are much less well-developed. Psiaki developed a method in which relative position measurements between two satellites make the absolute position and velocity of both satellites, as well as gravity terms of the central attractor up to arbitrary degree and order, simultaneously observable without ground-based range measurements [28]. Fujimoto and Stacey developed

a method to observe the gravity field of an asteroid using angles-only observations of a swarm of miniature beacons released on known initial trajectories from a carrier satellite on a known orbit [29]. Smith et al. proposed using range measurements between three spacecraft orbiting separate planets to precisely determine the heliocentric positions and velocities of those planets and higher-order terms of the solar gravity field [30]. As early as 1969, Grosch and Paetznick proposed using angles-only sightings of a small beacon ejected from a primary satellite to estimate the gravity fields of Mars and Venus [31].

None of these techniques are open to a starchip. It is too far from Earth for reliable ground-based range or range-rate estimates, too small to carry a deployable beacon for cooperative angle or range measurements, and probably too far from other starchips to cooperate with them for such measurements. It is therefore expected that the gravity of the destination star will not be observable using angles-only measurements, and this is verified by simulation. Future work might attempt to estimate this gravity using exotic techniques like the relativistic interferometric measurement of acceleration described by Christian and Loeb [32].

2.5 Linear Observability

In linear system theory, observability is a binary quantity: either the desired set of states can be estimated with the available measurements, or it cannot. This is decided by the rank of the "observability matrix." For a time-invariant system of order n, the matrix

$$\mathcal{O} = [\mathbf{H}^T \quad (\mathbf{HF})^T \quad (\mathbf{HF}^2)^T \quad ... \quad (\mathbf{HF}^{n-1})^T]^T \tag{2.16}$$

must be full rank [24]. For a time-invariant discretized system of order n with state transition matrix $\mathbf{\Phi}$, the observability matrix is

$$\mathcal{O}_d = [\mathbf{H}^T \quad (\mathbf{H\Phi})^T \quad (\mathbf{H\Phi}^2)^T \quad ... \quad (\mathbf{H\Phi}^{n-1})^T] \tag{2.17}$$

A time-varying discretized system of order n is said to be observable if the *observability Gramian* is nonsingular:

$$\mathbf{W}_{d0} = \sum_{i=0}^{N} \mathbf{\Phi}^T(i,0)\mathbf{H}_i^T\mathbf{H}_i\mathbf{\Phi}(i,0) \tag{2.18}$$

where $\mathbf{\Phi}(i,0)$ is the state transition matrix between $t = 0$ and $t = t_i$, evolving such that

$$\mathbf{\Phi}(0,0) = \mathbf{I} \tag{2.19}$$

and

$$\mathbf{\Phi}(i_3,i_1) = \mathbf{\Phi}(i_3,i_2)\mathbf{\Phi}(i_2,i_1) \tag{2.20}$$

In other words [24],

$$\dot{\mathbf{\Phi}}(t,t_0) = \mathbf{F}(t)\mathbf{\Phi}(t,t_0) \tag{2.21}$$

This matrix is known as the *observability Gramian*. Using 16-digit machine arithmetic, the practical test is that the condition number of $\mathcal{O}$ or $\mathbf{W}$ must be smaller than about 10^{16} [33]. This leads to a numerical (but still qualitative) means of gauging the observability of a system, or how much the initial uncertainty in state estimates may be expected to decrease as a result of extended observations: perfectly observable systems have observability matrices $\mathcal{O}$ or observability Gramians $\mathbf{W}$ with condition numbers of unity. Condition numbers on the order of $10^3 - 10^6$ are generally satisfactory, and condition numbers above 10^{11} or 10^{12} are unwanted and indicate marginal observability. (See [33] for a rule of thumb on how the utility of a matrix in computations relates to its condition number.) Although the Gramian condition strictly applies only to linear time-varying systems, it is often applied to linearized systems such as those in an EKF, as a sufficient but not necessary condition for observability.

2.6 Summary of Literature Review

This chapter has summarized notable concepts for interstellar probes, current knowledge of Proxima Centauri, introductory estimation and observability theory, and the state

of the art in gravity estimation. This study is shown to contribute the following to the fields of interstellar studies and angles-only navigation:

- First numerical simulation of interstellar flyby navigation.
- High-level demonstration of starchip's ability or inability to estimate gravity of destination star using most likely measurement type.

CHAPTER 3

PROCEDURES

This project examines the "minimal scientific return" for an interstellar probe using the simplest possible implementation of an extended Kalman filter. The modeled system includes the destination star and the probe. The star is fixed at the origin of an inertial reference frame expressed in Cartesian coordinates. The equations of motion for the probe relative to the star only include the point-mass gravity of the star. An extended Kalman filter processes measurements of the angles between the destination star and each of three guide stars, as well as the angular diameter of the destination star. The observability of the system is assessed using the standard observability Gramian.

3.1 Design Model

As described above, the design model consists of the destination star and the probe, which moves under point-mass gravity in an inertial reference frame centered at the destination star. The probe travels an uncontrolled hyperbolic trajectory. The "minimal scientific return" for the probe consists of the estimated position and velocity of the probe relative to the star and the standard gravitational parameter μ of the star. Note that from here forward μ will simply be referred to as the "gravity" of the star, short for "standard gravitational parameter." Likewise, all previous references to the "gravity" of the star have referred to μ, not to the time-varying magnitude or direction of the force that the star's gravity exerts on the probe.

The probe position, probe velocity, and star gravity are ordered in the state vector as

$$\mathbf{x} = \begin{bmatrix} \mathbf{r}_P^T & \mathbf{v}_P^T & \mu_S \end{bmatrix}^T \tag{3.1}$$

For this work, the truth model and the filter design model are exactly the same; that is,

$$\hat{\mathbf{x}} = \begin{bmatrix} \hat{\mathbf{r}}_P^T & \hat{\mathbf{v}}_P^T & \hat{\mu}_S \end{bmatrix}^T \tag{3.2}$$

3.2 Nonlinear State Propagation

The truth state vector is propagated according to the nonlinear differential equation

$$\dot{\mathbf{x}} = \begin{bmatrix} \dot{\mathbf{r}}_P \\ \dot{\mathbf{v}}_P \\ \dot{\mu}_S \end{bmatrix} = \begin{bmatrix} \mathbf{v}_P \\ -\mu_S \frac{\mathbf{r}_P}{r_P^3} \\ 0 \end{bmatrix} + \begin{bmatrix} \mathbf{0}_{3\times 3} \\ \mathbf{I}_{3\times 3} \\ 0 \end{bmatrix} \mathbf{w} = \mathbf{f}(\mathbf{x}) + \mathbf{G}\mathbf{w} \tag{3.3}$$

where

$$E[\mathbf{w}(t)\mathbf{w}(t')^T] = \mathbf{Q}\delta(t - t') \tag{3.4}$$

is a vector of zero-mean Gaussian white noise of strength Q and $\delta(t - t')$ is the Dirac delta function centered at t'. Because the gravity of the star is essentially constant over the duration of the probe's approach, the noise is only mapped to the acceleration of the probe. For simplicity in this first study, the disturbance accelerations experienced by the probe are assumed to be uncorrelated in each Cartesian dimension and of equal strength in each dimension, such that

$$\mathbf{Q} = Q\mathbf{I}_{3\times 3} \tag{3.5}$$

The filter state design model is propagated as

$$\dot{\hat{\mathbf{x}}} = \mathbf{f}(\hat{\mathbf{x}}) \tag{3.6}$$

It is exactly the same as the truth model except for the lack of disturbance accelerations.

3.3 Linearized Design Model

The linearized design model used for the covariance propagation is

$$\delta\dot{\hat{\mathbf{x}}} = \left[\frac{\partial \mathbf{f}}{\partial \hat{\mathbf{x}}}\right]_{\hat{\mathbf{x}}} = \begin{bmatrix} \mathbf{0}_{3\times3} & \mathbf{I}_{3\times3} & \mathbf{0}_{3\times1} \\ \hat{\mathbf{A}}_{3\times3} & \mathbf{0}_{3\times3} & \mathbf{0}_{3\times1} \\ \mathbf{0}_{1\times3} & \mathbf{0}_{1\times3} & 0 \end{bmatrix}_{\hat{\mathbf{x}}} \begin{bmatrix} \delta\hat{\mathbf{r}}_P \\ \delta\hat{\mathbf{v}}_P \\ \delta\hat{\mu}_S \end{bmatrix} = \hat{\mathbf{F}}\delta\hat{\mathbf{x}} \tag{3.7}$$

where

$$\hat{\mathbf{A}}_{3\times3} = \frac{\hat{\mu}_S}{\hat{r}_P^3}\left(3\frac{\hat{\mathbf{r}}_P\hat{\mathbf{r}}_P^T}{\hat{r}_P^2} - \mathbf{I}_{3\times3}\right) \tag{3.8}$$

3.4 Covariance Propagation

The filter covariance is propagated according to the linear differential equation

$$\dot{\mathbf{P}}(t) = \mathbf{F}(t)\mathbf{P}(t) + \mathbf{P}(t)\mathbf{F}(t)^T + \mathbf{G}\mathbf{Q}\mathbf{G}^T \tag{3.9}$$

3.5 Measurement Model

At any time t, there are four angular measurements available to the probe. These are listed below.

1. $\theta_{S,1}$: The angle between the destination star and guide star no. 1.
2. $\theta_{S,2}$: The angle between the destination star and guide star no. 2.
3. $\theta_{S,3}$: The angle between the destination star and guide star no. 3.
4. $\theta_{S,S}$: The angular diameter of the destination star.

These measurements are modeled as follows:

$$\theta_{S,1} = \text{acos}\big(-\frac{\mathbf{i}_1^T\mathbf{r}_P}{r_P}\big) + v = h_{S,1}(\mathbf{x}) + \nu \tag{3.10}$$

$$\theta_{S,2} = \text{acos}\big(-\frac{\mathbf{i}_2^T\mathbf{r}_P}{r_P}\big) + v = h_{S,2}(\mathbf{x}) + \nu \tag{3.11}$$

$$\theta_{S,3} = \text{acos}\big(-\frac{\mathbf{i}_3^T \mathbf{r}_P}{r_P}\big) + v = h_{S,3}(\mathbf{x}) + \nu \tag{3.12}$$

$$\theta_{S,S} = 2\text{asin}\big(\frac{D_S}{2r_P}\big) = h_{S,S}(\mathbf{x}) + \nu \tag{3.13}$$

where ν is a zero-mean Gaussian random variable with scalar variance R. The measurements estimated by the Kalman filter are modeled as:

$$\hat{\theta}_{S,1} = \text{acos}\big(-\frac{\mathbf{i}_1^T \hat{\mathbf{r}}_P}{\hat{r}_P}\big) = h_{S,1}(\hat{\mathbf{x}}) \tag{3.14}$$

$$\hat{\theta}_{S,2} = \text{acos}\big(-\frac{\mathbf{i}_2^T \hat{\mathbf{r}}_P}{\hat{r}_P}\big) = h_{S,2}(\hat{\mathbf{x}}) \tag{3.15}$$

$$\hat{\theta}_{S,3} = \text{acos}\big(-\frac{\mathbf{i}_3^T \hat{\mathbf{r}}_P}{\hat{r}_P}\big) = h_{S,3}(\hat{\mathbf{x}}) \tag{3.16}$$

$$\hat{\theta}_{S,S} = 2\text{asin}\big(\frac{D_S}{2\hat{r}_P}\big) = h_{S,S}(\hat{\mathbf{x}}) \tag{3.17}$$

Note that this assumes that the probe camera's field of view is wide enough to measure any desired angle. The camera is also assumed to be capable of observing several objects of dramatically different magnitude at the same time and identifying the limbs and centroids of each, in order to find the angle between two objects or the angular diameter of a single object. None of these assumptions are realistic, but all are acceptable simplifications for a first study of interstellar-approach position determination.

3.6 State and Covariance Update

When a measurement is taken, the filter state is updated as

$$\hat{\mathbf{x}}^+ = \hat{\mathbf{x}}^- + \hat{\mathbf{K}}(\tilde{\theta} - \hat{\theta}) \tag{3.18}$$

where the Kalman gain is

$$\hat{\mathbf{K}} = \hat{\mathbf{P}}^{-}\hat{\mathbf{H}}^{T}(\hat{\mathbf{H}}\hat{\mathbf{P}}^{-}\hat{\mathbf{H}}^{T} + R)^{-1} \tag{3.19}$$

and the measurement geometry matrices are given by

$$\hat{\mathbf{H}} = \left[\frac{\partial h(\hat{\mathbf{x}})}{\partial \hat{\mathbf{x}}}\right]^{T}_{\hat{\mathbf{x}}} \tag{3.20}$$

with individual cases found as

1. $\hat{\mathbf{H}}_{S,1} = \begin{bmatrix} \frac{1}{\hat{r}_P \sin(\hat{\theta}_{S,1})}\left(\mathbf{i}_1^T + \frac{\hat{\mathbf{r}}_P^T}{\hat{r}_P}\cos(\hat{\theta}_{S,1})\right) & \mathbf{0}_{1\times 3} & 0 \end{bmatrix}$
2. $\hat{\mathbf{H}}_{S,2} = \begin{bmatrix} \frac{1}{\hat{r}_P \sin(\hat{\theta}_{S,2})}\left(\mathbf{i}_2^T + \frac{\hat{\mathbf{r}}_P^T}{\hat{r}_P}\cos(\hat{\theta}_{S,2})\right) & \mathbf{0}_{1\times 3} & 0 \end{bmatrix}$
3. $\hat{\mathbf{H}}_{S,3} = \begin{bmatrix} \frac{1}{\hat{r}_P \sin(\hat{\theta}_{S,3})}\left(\mathbf{i}_3^T + \frac{\hat{\mathbf{r}}_P^T}{\hat{r}_P}\cos(\hat{\theta}_{S,3})\right) & \mathbf{0}_{1\times 3} & 0 \end{bmatrix}$
4. $\hat{\mathbf{H}}_{S,S} = \begin{bmatrix} -\frac{D_S}{\cos(\frac{1}{2})}\left(\frac{\hat{\mathbf{r}}_P^T}{\hat{r}_P^3}\right) & \mathbf{0}_{1\times 3} & 0 \end{bmatrix}$

The filter covariance is updated as

$$\hat{\mathbf{P}}^{+} = (\mathbf{I}_{7\times 7} - \hat{\mathbf{K}}\hat{\mathbf{H}})\hat{\mathbf{P}}^{-}(\mathbf{I}_{7\times 7} - \hat{\mathbf{K}}\hat{\mathbf{H}})^{T} + \hat{\mathbf{K}}R\hat{\mathbf{K}}^{T} \tag{3.21}$$

and symmetrized to ensure positive definiteness as

$$\hat{\mathbf{P}}^{+} \leftarrow \frac{1}{2}(\hat{\mathbf{P}}^{+} + \hat{\mathbf{P}}^{+^{T}}) \tag{3.22}$$

3.7 State and Covariance Initialization

The filter state is initialized to some nominal value,

$$\hat{\mathbf{x}}(t_0) = \mathbf{x}_{\text{nom}} \tag{3.23}$$

The filter covariance is initialized as

$$\hat{\mathbf{P}}(t_0) = \begin{bmatrix} (f_{\text{pos}} r_P(t_0))^2 \mathbf{I}_{3\times 3} & \mathbf{0}_{3\times 3} & \mathbf{0}_{3\times 1} \\ \mathbf{0}_{3\times 3} & (f_{\text{vel}} v_P(t_0))^2 \mathbf{I}_{3\times 3} & \mathbf{0}_{3\times 1} \\ \mathbf{0}_{1\times 3} & \mathbf{0}_{1\times 3} & (f_\mu \mu_S)^2 \end{bmatrix} \tag{3.24}$$

where f_{pos}, f_{vel}, and f_μ are small positive numbers $f_{\text{pos}},\ f_{\text{vel}},\ f_\mu \ll 1$.

The truth state is initialized to the value of the initial filter state plus a small random perturbation with covariance based on the initial filter covariance, as

$$\mathbf{x}(t_0) = \hat{\mathbf{x}}(t_0) + \hat{\mathbf{L}}\mathbf{n} \tag{3.25}$$

where

$$\hat{\mathbf{L}} = \text{chol}(\hat{\mathbf{P}}_0) \tag{3.26}$$

and $\mathbf{n}$ is randomly selected from a normal distribution as

$$\mathbf{n} \sim \mathcal{N}(\mathbf{0}_{7\times 1}, \mathbf{I}_{7\times 7}) \tag{3.27}$$

Note that this assumes that at the beginning of the approach period, the state error covariance encoded in the Kalman filter is completely consistent with the true state error covariance.

3.8 Monte Carlo Simulation

Monte Carlo simulation can be used to verify the proper performance of the Kalman filter. The entire scenario is run from start to finish multiple times, and the truth state, filter state, filter covariance, and observability Gramian are recorded as time series for each run. At each instant in time and for each component of the state, the mean and standard deviation of the filter error can be computed from the Monte Carlo ensemble. If the confidence interval for the mean error includes zero and about 99.7% of the filter errors fall within this confidence interval as judged by visual inspection of the state estimation

error plots, the filter is considered to work satisfactorily. More sophisticated tests exist to verify filter performance, but they will not be applied here. A total of $N_{MC} = 100$ simulation runs are performed for each set of input parameters.

3.9 Variable Scaling

When expressed in units of kilograms, kilometers, and kilometers per second, astrodynamics problems usually involve numbers of widely varying magnitudes: billions of kilograms, millions of kilometers, and single kilometers per second. This can cause numerical difficulties when expressed in double precision arithmetic. The differences in magnitude between the gravity, length, and velocity scales are often reduced with the following scaling, where μ is the standard gravitational parameter of the central body, and LU is a reference length (here 1 AU). A new time unit is defined as

$$\mathrm{TU} = \sqrt{\frac{\mathrm{LU}^3}{\mu}} \tag{3.28}$$

with a new velocity unit as

$$\mathrm{VU} = \frac{\mathrm{LU}}{\mathrm{TU}} \tag{3.29}$$

and a new gravity unit as

$$\mathrm{GU} = \mu \frac{\mathrm{TU}^2}{\mathrm{LU}^3} \tag{3.30}$$

All time, velocity, gravity, and distance variables are then scaled according to the new units. This reduces the gravity of the star to a value of unity, typically leaves the velocities at values near unity, reduces distances to values commensurate with the initial conditions and the length scale, and typically reduces times to values on the order of unity, for closed trajectories.

3.10 Nominal Trajectory

The Breakthrough Starshot concept calls for a flyby of Alpha Centauri with a closest approach of 1 AU [9]. Without considering the engineering problems that must be solved to make such a nominal flyby distance possible, this study initializes the probe on a nominal hyperbolic flyby of Proxima Centauri with a periapse distance of 1 AU. Proxima Centauri lies approximately 4.2 light years from Earth at a right ascension of 14 hr. 29 min. and a declination of -62°40' on the celestial sphere [15]. The reference frame in this study originates at the center of Proxima Centauri and is aligned with the ICRF. An interstellar probe developed using present-day technology might approach Proxima Centauri at a hyperbolic excess velocity of about $2 \cdot 10^{-5}$ c [34], where c is the speed of light. To initialize a nominal trajectory, it is also necessary to specify an initial distance and an angle ϕ to orient the plane of the hyperbola in space. In all cases, an initial distance of 25 AU is used, as this adequately captures the filter behavior in regions of low and high trajectory curvature. A clock angle of 30° is used arbitrarily chosen for all cases; it should have no effect on filter performance. In order to verify that the higher curvature near periastron does not cause the filter to fail, all scenarios are run for equal durations before and after periastron.

The initial position $\mathbf{r}_0$, velocity $\mathbf{v}_0$, and time until periastron t_0 for the probe are found as follows from the flyby periastron radius r_p, the hyperbolic excess velocity v_∞, the initial distance r_0, the right ascension Ω and declination δ of the target star relative to Earth, the orientation angle ϕ, and the gravity μ of the star. First, the semi-major axis of the hyperbola is found as

$$a = \frac{\mu}{v_\infty^2} \tag{3.31}$$

Next, the eccentricity is

$$e = 1 + \frac{r_p}{a} \tag{3.32}$$

The periastron velocity follows as

$$v_p = \sqrt{2\left(\frac{v_\infty^2}{2} + \frac{\mu}{r_p}\right)} \tag{3.33}$$

and the specific angular momentum as

$$h = r_p \cdot v_p \tag{3.34}$$

The true anomaly is

$$\nu = \arccos \frac{a(e^2-1)}{r_0 e} - \frac{1}{e} \tag{3.35}$$

The hyperbolic eccentric anomaly is

$$F = \ln \frac{\sqrt{e+1} + \sqrt{e-1}\tan\frac{\nu}{2}}{\sqrt{e+1} - \sqrt{e-1}\tan\frac{\nu}{2}} \tag{3.36}$$

The hyperbolic mean anomaly is

$$M = e\sinh F - F \tag{3.37}$$

and the initial time until periapse is

$$t_0 = \frac{Mh^3}{\mu^2(e^2-1)^{\frac{3}{2}}} \tag{3.38}$$

In the perifocal frame, the initial position is

$$x = r_0\cos\nu, \quad y = r_0\sin\nu, \quad z = 0 \tag{3.39}$$

The initial velocity is

$$v = \sqrt{2\left(\frac{v_\infty^2}{2} + \frac{\mu}{r_0}\right)} \tag{3.40}$$

with tangential component

$$v_t = \frac{h}{r_0} \tag{3.41}$$

and radial component

$$v_r = \sqrt{v^2 - v_t^2} \tag{3.42}$$

The signed flight path angle is

$$\gamma = \arctan \frac{v_r}{v_t} \cdot \left(\frac{\nu}{|\nu|} \right) \tag{3.43}$$

The initial velocity in the perifocal frame is then

$$v_x = -v \sin(\nu - \gamma), \quad v_y = v \cos(\nu - \gamma), \quad v_z = 0 \tag{3.44}$$

To transform position and velocity from the perifocal frame to the ICRF, we first find the semi-minor axis of the approach hyperbola as

$$b = a\sqrt{e^2 - 1} \tag{3.45}$$

In the perifocal frame, the arrival asymptote is described by the vector

$$\mathbf{S} = [a \;\; b \;\; 0]^T \tag{3.46}$$

The arrival asymptote is normal to the B-plane, such that the normal vector of the B-plane is

$$\hat{\mathbf{S}} = \frac{\mathbf{S}}{|\mathbf{S}|} \tag{3.47}$$

In the perifocal frame, the axes of the perifocal frame are given by

$$\hat{\mathbf{P}} = [1 \;\; 0 \;\; 0]^T, \quad \hat{\mathbf{Q}} = [0 \;\; 1 \;\; 0]^T, \quad \hat{\mathbf{R}} = [0 \;\; 0 \;\; 1]^T \tag{3.48}$$

Two complementary angles are formed from $\hat{\mathbf{S}}$ as

$$\theta_S = \arctan\frac{S(2)}{S(1)}, \quad \theta_B = \theta_S - \frac{\pi}{2} \tag{3.49}$$

The B-vector that gives the B-plane its name is then

$$\mathbf{B} = b \cdot [\cos\theta_B \quad \sin\theta_B \quad 0]^T \tag{3.50}$$

The vectors $\hat{\mathbf{S}}$, $\hat{\mathbf{B}}$ now define the orientation of the perifocal plane in the ICRF. By applying suitable rotations to these vectors and $\mathbf{r}_0$, $\mathbf{v}_0$ as defined in the perifocal frame, the initial position and velocity of the probe can be expressed in the ICRF frame. Before doing so, we state Rodrigues' rotation formula as follows. A three-dimensional vector $\mathbf{v}$ rotated by an angle θ in a right-handed sense around a unit vector $\mathbf{k}$ becomes

$$\mathbf{v}' = \mathbf{v}\cos\theta + (\mathbf{k}\times\mathbf{v})\sin\theta + \mathbf{k}(\mathbf{k}\cdot\mathbf{v})(1-\cos\theta) \tag{3.51}$$

This is abbreviated as

$$\mathbf{v}' = \text{Rodrigues}(\mathbf{v}, \mathbf{k}, \theta) \tag{3.52}$$

First, we rotate $\mathbf{S}$, $\mathbf{B}$, $\mathbf{r}_0$, and $\mathbf{v}_0$ around $\mathbf{k} = \mathbf{R}/|\mathbf{R}|$ by an angle

$$\theta = \Omega - \arctan\frac{\mathbf{v}_0(2)}{\mathbf{v}_0(1)} \tag{3.53}$$

such that

$$\begin{aligned}
\mathbf{S}' &= \text{Rodrigues}(\mathbf{S}, \mathbf{k}, \theta) \\
\mathbf{B}' &= \text{Rodrigues}(\mathbf{B}, \mathbf{k}, \theta) \\
\mathbf{r}_0' &= \text{Rodrigues}(\mathbf{r}_0, \mathbf{k}, \theta) \\
\mathbf{v}_0' &= \text{Rodrigues}(\mathbf{v}_0, \mathbf{k}, \theta)
\end{aligned} \tag{3.54}$$

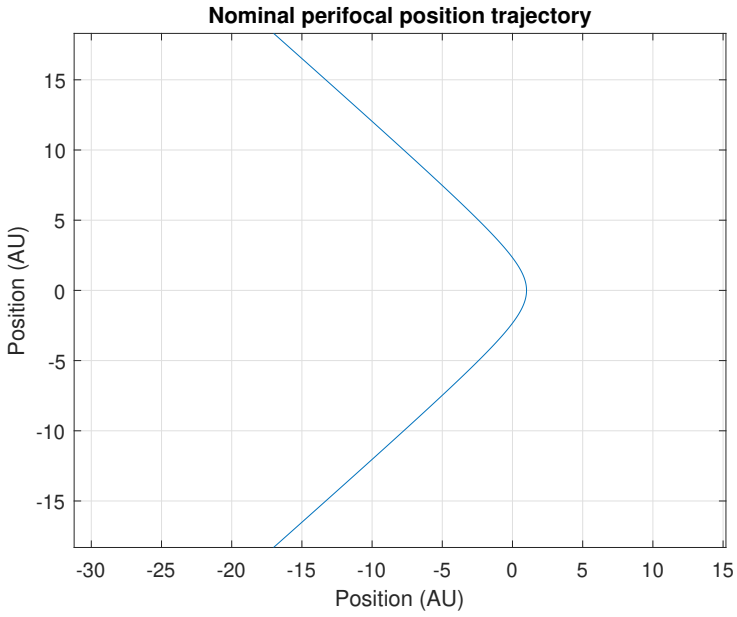

Fig. 3.1: Nominal position trajectory in perifocal plane

Next, we rotate $\mathbf{S}'$, $\mathbf{r}_0'$, and $\mathbf{v}_0'$ around $\mathbf{k} = \mathbf{B}'/|\mathbf{B}'|$ by an angle $\theta = \delta$ (the declination of the target star) such that

$$\begin{aligned} \mathbf{S}'' &= \text{Rodrigues}(\mathbf{S}', \mathbf{k}, \theta) \\ \mathbf{r}_0'' &= \text{Rodrigues}(\mathbf{r}_0', \mathbf{k}, \theta) \\ \mathbf{v}_0'' &= \text{Rodrigues}(\mathbf{v}_0', \mathbf{k}, \theta) \end{aligned} \tag{3.55}$$

Finally, we rotate $\mathbf{r}_0''$ and $\mathbf{v}_0''$ around $\mathbf{k} = \mathbf{S}''/|\mathbf{S}''|$ by an angle $\theta = -\phi$ (the orientation angle of the flyby hyperbola) such that

$$\begin{aligned} \mathbf{r}_0''' &= \text{Rodrigues}(\mathbf{r}_0'', \mathbf{k}, \theta) \\ \mathbf{v}_0''' &= \text{Rodrigues}(\mathbf{v}_0'', \mathbf{k}, \theta) \end{aligned} \tag{3.56}$$

This final result, $\mathbf{r}_0'''$ and $\mathbf{v}_0'''$, represents the initial position and velocity of the probe in the ICRF frame, and will for convenience simply be written as $\mathbf{r}_0$, $\mathbf{v}_0$.

The nominal trajectory is plotted in Figures 3.1 and 3.2 in the perifocal position and velocity planes, respectively. The ICRF position and velocity components and magnitudes are also plotted with respect to time in Figures 3.3-3.6.

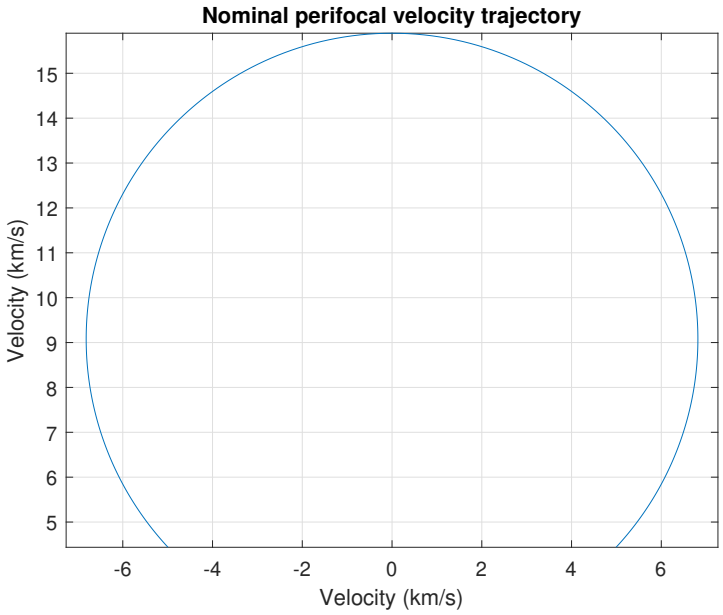

Fig. 3.2: Nominal velocity trajectory in perifocal plane

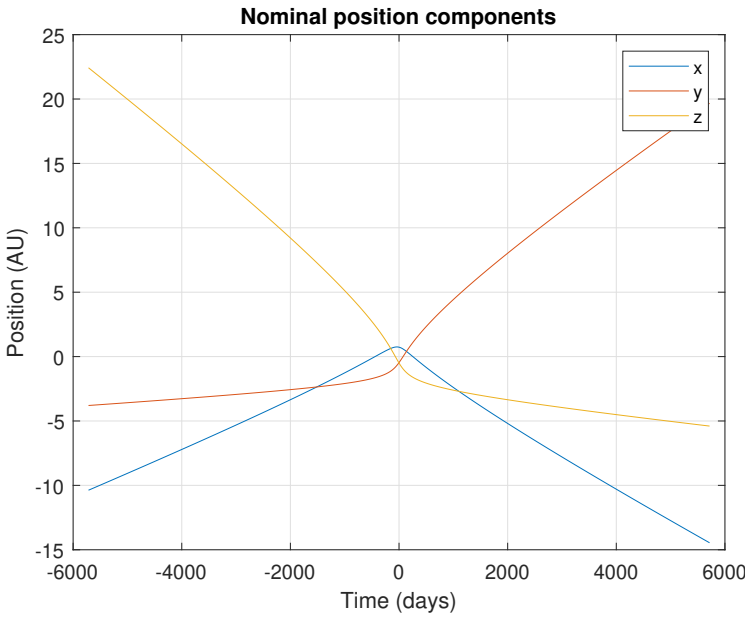

Fig. 3.3: Nominal position components in ICRF frame

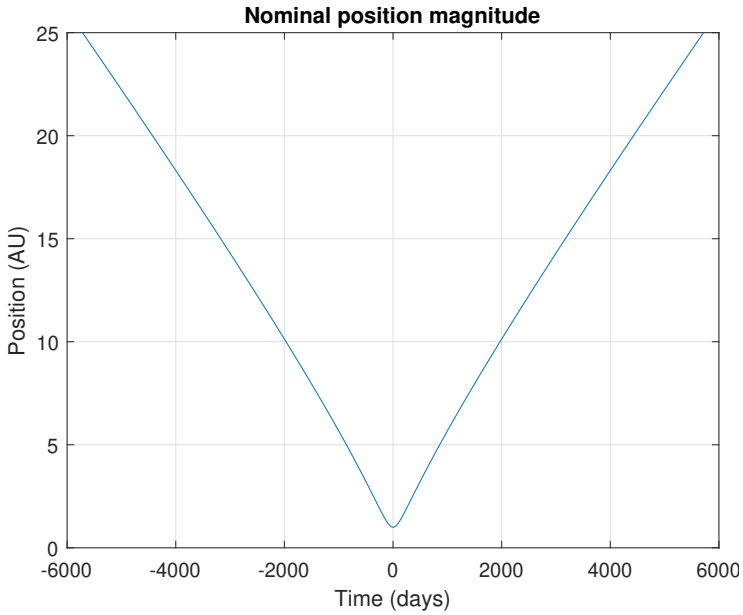

Fig. 3.4: Nominal position magnitude in ICRF frame

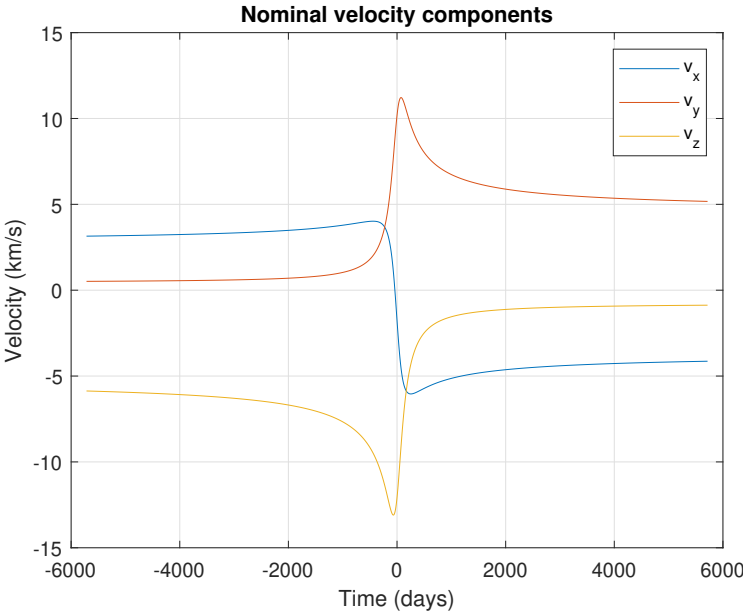

Fig. 3.5: Nominal velocity components in ICRF frame

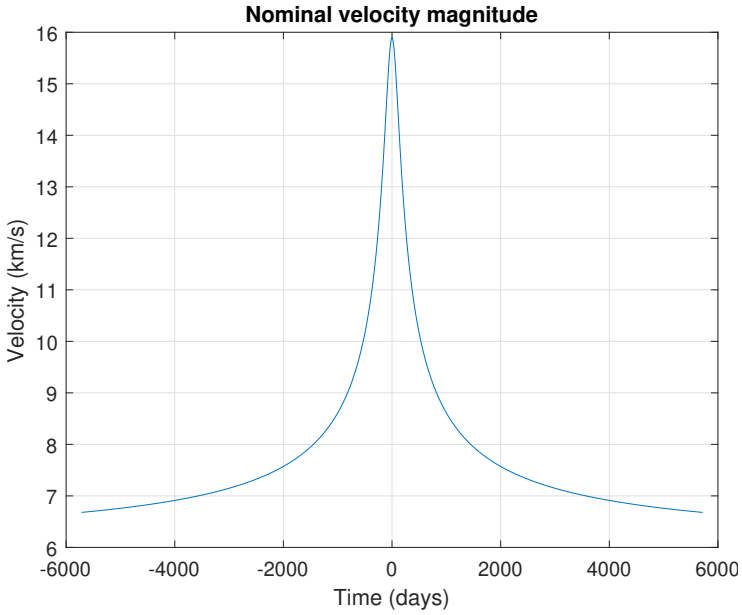

Fig. 3.6: Nominal velocity magnitude in ICRF frame

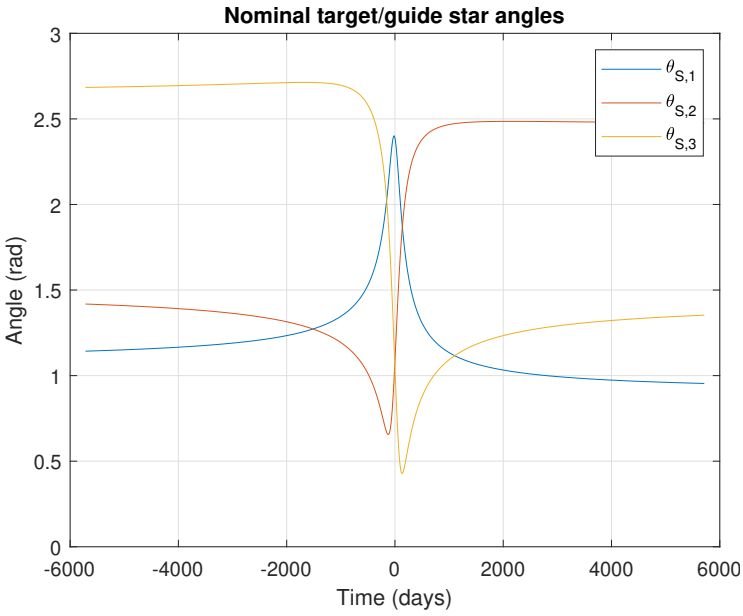

Fig. 3.7: Nominal target star/guide star angles

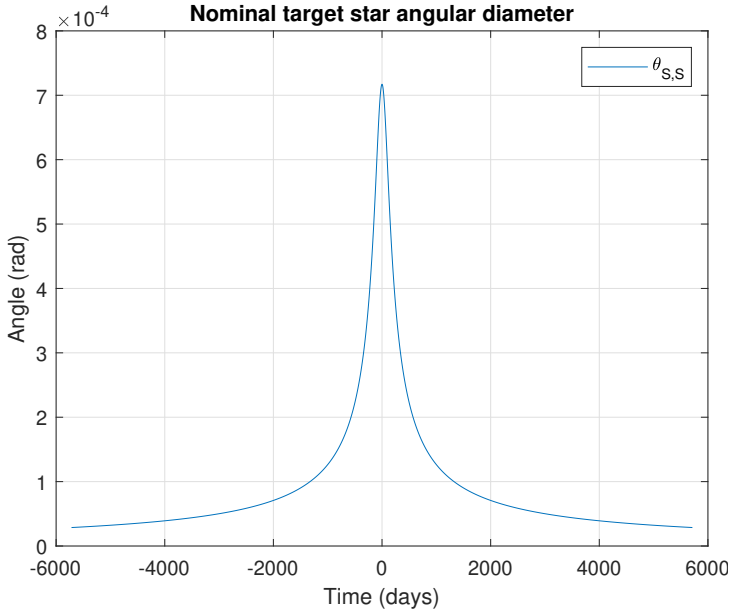

Fig. 3.8: Nominal target star angular diameters

3.11 Integration Step Size

As a general rule, the appropriate step size in time or space for any numerical simulation is that which balances algorithmic error with arithmetic error. Smaller step sizes typically result in smaller algorithmic error because the linearizations and other approximations used in each step are more accurate for smaller distances, but they result in larger arithmetic error because round-off errors and other errors from finite-precision arithmetic are incurred with each computation. For this study, the nominal position and velocity of the probe can always be computed with negligible error using Kepler's equations as implemented in a Matlab routine, so the final position and velocity $\mathbf{r}_f$, $\mathbf{v}_f$ are known exactly. The probe's position and velocity are propagated from $\mathbf{r}_0$, $\mathbf{v}_0$ over a time span from $-t_0$ to $+t_0$ using an eighth-order Runge-Kutta integrator, without process noise, using time step counts logarithmically spaced between 40 and 400,000. The time step count used in all subsequent computations is that which results in the smallest value of $||\mathbf{r}_f - \mathbf{r}_{f,\text{nom}}||$. This is

$$N_T = 4000 \tag{3.57}$$

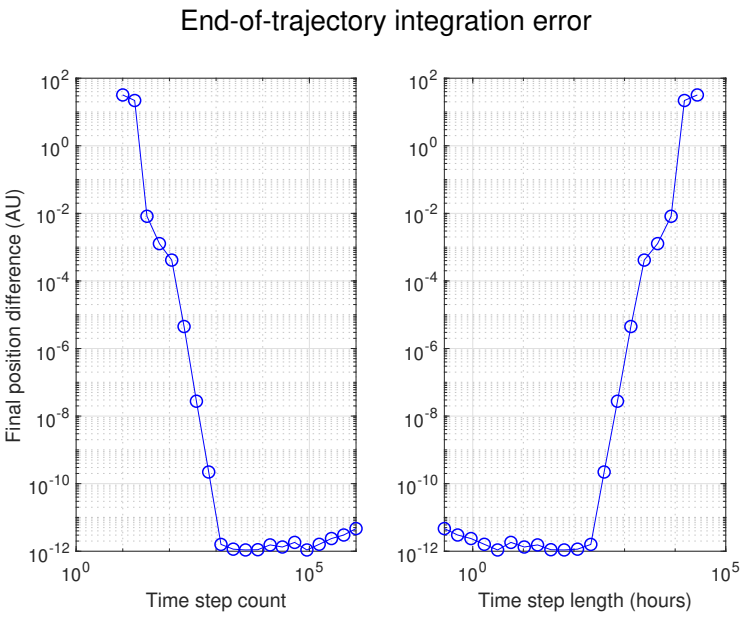

Fig. 3.9: Integration step size study

$$||\mathbf{r}_f - \mathbf{r}_{f,\text{nom}}|| = 1.09 \cdot 10^{-12} \text{ AU} \tag{3.58}$$

corresponding to a time step of

$$\Delta t = 2.8584 \text{ days} \tag{3.59}$$

The results of the integration step size study are shown in Figure 3.9.

3.12 Noise Strength

Process noise and measurement noise strengths must be defined for every Kalman filter. The measurement noise is set such that the 1σ error in discrete angle measurements is equal to

$$\sigma_\theta = 1 \cdot 10^{-3} \text{ rad} \tag{3.60}$$

with a scalar variance of

$$R = 1 \cdot 10^{-6} \text{ rad}^2 \tag{3.61}$$

This value preserves the order of magnitude of the nominal 1σ measurement noise of 0.00559 rad used in a 2006 study of angles-only navigation for a hyperbolic flyby of Jupiter [35] and drops the significant digits; this is taken as an adequate value for measurement noise for lack of strong reasons to use a more rigorously defined value.

The appropriate value for process noise is more difficult to choose, as standard astrodynamics and filtering texts [16, 23–27, 36–38] leave that question nearly entirely unanswered. Process noise is fundamentally intended as a way to compensate for perturbation accelerations that are too small or too poorly understood to compute in the truth model or navigation model, so one might establish a value for process noise by detailed perturbation analysis: developing a complex deterministic truth dynamics model that incorporates a large number of perturbations that depend on parameters that are not well known, running a large number of Monte Carlo simulations with truth trajectories governed by perturbation parameters that have been randomly selected from probability distributions describing the current best estimates of those parameters, and tuning the time-varying noise strength used within the filter covariance propagation equations such that the time-varying covariance of the filter, beginning at the nominal initial conditions and operating without measurement updates, matches the time-varying covariance of the truth trajectories. The time-varying noise strength values thus obtained could be fit to a curve or stored as an array for later use, and the filter development could proceed with a simplified truth model using the same noise strength as the filter, or it could continue with the more complex truth model.

While conceptually attractive, this procedure is computationally intensive. A simpler method makes no attempt to establish what values of perturbation accelerations might be physically expected, and is therefore unsuitable for use in detailed navigation studies. However, for a first study this method is acceptable. With the mass of the star at its nominal value, the probe is propagated from its nominal initial position and velocity for a length of time equal to its nominal initial time until periastron. The process noise in

the truth model is set to some arbitrary value, and the final position covariance of a Monte Carlo ensemble of trajectories is recorded. This process is repeated for a number of different values for process noise, and the process noise value that produces a desired final position covariance is chosen or interpolated from the results.

For this study, the desired ensemble position covariance at periastron is characterized by

$$\sigma_r = \sqrt{\sigma_x^2 + \sigma_y^2 + \sigma_z^2} = 0.01 \text{ AU} \tag{3.62}$$

This is achieved with a process noise strength of

$$Q_2 = 9.2584 \cdot 10^{-4} \text{ km}^2/\text{s}^3 \tag{3.63}$$

as interpolated from Figure 3.10. This value of Q is used for most scenarios, but for some alternate scenarios the Kalman filter is run with

$$Q_1 = 1.0139 \cdot 10^{-1} \text{ km}^2/\text{s}^3 \tag{3.64}$$

and

$$Q_3 = 1.0924 \cdot 10^{-5} \text{ km}^2/\text{s}^3 \tag{3.65}$$

corresponding to $\sigma_r = 0.1$ AU and $\sigma_r = 0.001$ AU.

3.13 Measurement Frequency

For simplicity, a full set of three or four measurements (depending upon the scenario) is taken and processed each integration step. The measurement frequency is not expected to dramatically affect the accuracy or consistency of the Kalman filter, but for some alternate scenarios the filter is run with one measurement set every ten integration steps and with one measurement set every one hundred integration steps, keeping the total number of integration steps and the process noise strength at their usual values.

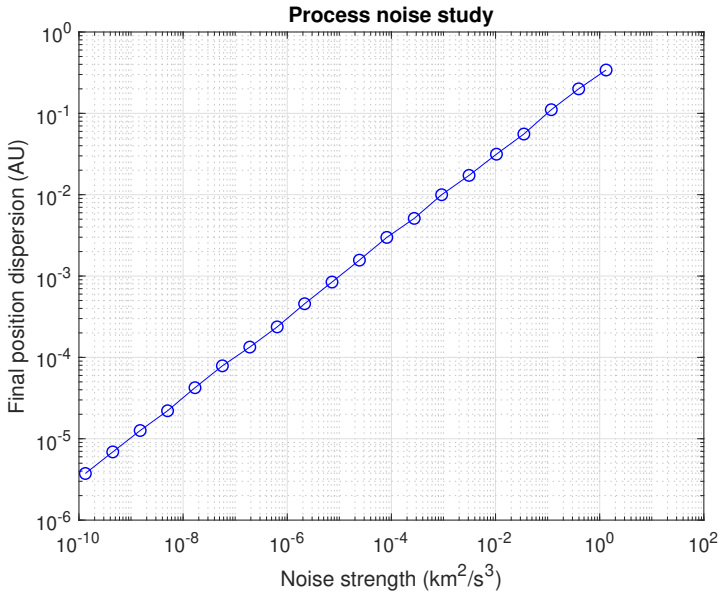

Fig. 3.10: Process noise study

3.14 Scenarios

Although gauging the utility of an extended Kalman filter for autonomous angles-only navigation in a realistic Starshot-inspired scenario is well beyond the scope of this project, it is possible to get some idea of the utility of such a filter simply by running the same simulation with a wide variety of input scenarios, in order to see which combinations of input parameters result in state estimation errors that are inconsistent with the estimated errors contained within the filter covariance matrix. Defining numerical thresholds for acceptable navigation accuracy is also beyond the scope of this work, as the acceptable navigation accuracy for any space mission depends strongly on the details of its concept of operations. Instead, the main objective of this study is to examine filter consistency in a variety of scenarios. Because there is no widely accepted method of numerically scoring the average consistency of a Kalman filter over time and Monte Carlo ensembles, each scenario is judged as "consistent" or "inconsistent" based on nothing more than visual inspection of Monte Carlo estimation error plots, based on an ensemble of $N_{MC} = 100$ runs.

Four combinations of filter states and measurements are considered:

Table 3.1: Parameter inputs for Scenario 1

Parameter	Value
k	1
R	$1 \cdot 10^{-6}$ rad^2
Q	$9.2584 \cdot 10^{-4}$ km^2/s^3
f_{pos}	$1 \cdot 10^{-3}$
f_{vel}	$1 \cdot 10^{-3}$

1. Filter state: $\mathbf{r}_P$, $\mathbf{v}_P$. Measurements: $\theta_{S,1}, \theta_{S,2}, \theta_{S,3}$. The true value of the star gravity μ is held constant, and the filter value is held equal to the true value.

2. Filter state: $\mathbf{r}_P$, $\mathbf{v}_P$, μ_S. Measurements: $\theta_{S,1}, \theta_{S,2}, \theta_{S,3}$. The true value of μ is held constant at a randomly chosen value, and μ is estimated in the filter state.

3. Filter state: $\mathbf{r}_P$, $\mathbf{v}_P$. Measurements: $\theta_{S,1}, \theta_{S,2}, \theta_{S,3}, \theta_{S,S}$. The true value of μ is held constant, and the filter value is held equal to the true value.

4. Filter state: $\mathbf{r}_P$, $\mathbf{v}_P$, μ_S. Measurements: $\theta_{S,1}, \theta_{S,2}, \theta_{S,3}, \theta_{S,S}$. The true value of μ is held constant at a randomly chosen value, and μ is estimated in the filter state.

For each filter formulation, rows and columns of the state dynamics matrix, measurement geometry matrix, and covariance matrix are deleted as necessary from those defined earlier in this chapter, which correspond to the fourth filter formulation in this list.

Fourteen scenarios are examined. In all cases, $N_T = 4000$ time steps are used with a star mass 1σ scaling factor of $f_\mu = 0.018$, reflecting the current observational uncertainty in the gravity of Proxima Centauri [15]. The scenarios are defined in Table 3.2 as variations on a nominal set of parameters in Table 3.1.

3.15 Performance Metrics

The performance of the EKF in this project is assessed using the following metrics:

1. *Condition number of the observability Gramian.* A perfectly observable system has a condition number of unity; the condition number of a highly unobservable system is

Table 3.2: Parameter variations for Scenarios 1-14

Scenario	Parameter Variation
1	Nominal scenario
2	$k = 10$
3	$k = 100$
4	$k = \infty$ (No measurements)
5	$R = 1 \cdot 10^{-8}$ rad^2
6	$R = 1 \cdot 10^{-10}$ rad^2
7	$Q = 1.1039 \cdot 10^{-1}$ km^2/s^3
8	$Q = 1.0924 \cdot 10^{-5}$ km^2/s^3
9	$f_{\text{pos}} = 1 \cdot 10^{-1}$
10	$f_{\text{pos}} = 1 \cdot 10^{-2}$
11	$f_{\text{pos}} = 1 \cdot 10^{-4}$
12	$f_{\text{vel}} = 1 \cdot 10^{-1}$
13	$f_{\text{vel}} = 1 \cdot 10^{-2}$
14	$f_{\text{vel}} = 1 \cdot 10^{-4}$

infinite. With finite precision arithmetic, a system is practically unobservable with a condition number of about 10^{15} or higher.

2. *State estimation errors.* The most important measure of a navigation algorithm's performance is the state estimation error achieved. These are considered as individual state components, and as 3σ root-sum-square (RSS) errors for each relevant group of components (probe position, probe velocity, star gravity). To demonstrate that the extended Kalman filter has been properly implemented and initialized (that is, to demonstrate filter consistency), the individual Monte Carlo errors are plotted over time, as also the filter covariance results from each Monte Carlo run. These are then compared for all scenarios and all filter types.

3.16 RSS Errors and Confidence Intervals

Because the individual x, y, and z components of the position and velocity errors are expected to behave similarly, it is desirable to combine all three components of the position and velocity errors to gain some sense of the total error. This applies both to the true errors, computed from the difference between the truth state and the filter state, and to the estimated errors, computed from the filter covariance matrix. Because the numerical

results of a Monte Carlo study will vary from ensemble to ensemble, it is also desirable to compute confidence intervals for these combined error measures.

At any instant t_k of the ith Monte Carlo run, the root-sum-square (RSS) true position error is

$$\sigma_{r_{k,i}} = \sqrt{(\hat{x}_{k,i} - x_{k,i})^2 + (\hat{y}_{k,i} - y_{k,i})^2 + (\hat{z}_{k,i} - z_{k,i})^2} \tag{3.66}$$

The RSS true velocity error is

$$\sigma_{v_{k,i}} = \sqrt{(\hat{v}_{x_{k,i}} - v_{x_{k,i}})^2 + (\hat{v}_{y_{k,i}} - v_{y_{k,i}})^2 + (\hat{v}_{z_{k,i}} - v_{z_{k,i}})^2} \tag{3.67}$$

The RSS true gravity error is

$$\sigma_{\mu_{k,i}} = \sqrt{(\hat{\mu}_{k,i} - \mu_{k,i})^2} \tag{3.68}$$

The RSS estimated position error comes from the filter covariance as

$$\hat{\sigma_{r}}_{k,i} = \sqrt{\hat{\sigma}^2_{x_{k,i}} + \hat{\sigma}^2_{y_{k,i}} + \hat{\sigma}^2_{z_{k,i}}} \tag{3.69}$$

where $\hat{\sigma}_{x_{k,i}}$, $\hat{\sigma}_{y_{k,i}}$, and $\hat{\sigma}_{z_{k,i}}$ are the square roots of the appropriate diagonal elements of the filter covariance matrix $\mathbf{P}_{k,i}$.

The RSS estimated velocity error comes from the filter covariance as

$$\hat{\sigma_{v}}_{k,i} = \sqrt{\hat{\sigma}^2_{v_{x_{k,i}}} + \hat{\sigma}^2_{v_{y_{k,i}}} + \hat{\sigma}^2_{v_{z_{k,i}}}} \tag{3.70}$$

where $\hat{\sigma}_{v_{x_{k,i}}}$, $\hat{\sigma}_{v_{y_{k,i}}}$, and $\hat{\sigma}_{v_{z_{k,i}}}$ are the square roots of the appropriate diagonal elements of the filter covariance matrix $\mathbf{P}_{k,i}$.

The RSS estimated gravity error comes from the filter covariance as

$$\hat{\sigma_{\mu}}_{k,i} = \sqrt{\hat{\sigma}^2_{\mu_{k,i}}} \tag{3.71}$$

where $\hat{\sigma}_{\mu_{k,i}}$ is the square root of the appropriate diagonal element of the filter covariance matrix $\mathbf{P}_{k,i}$.

At any instant t_k, the RSS true position error for an ensemble of N_{MC} Monte Carlo runs is found as

$$\sigma_{r_k} = \sqrt{\sigma_{x_k}^2 + \sigma_{y_k}^2 + \sigma_{z_k}^2} \tag{3.72}$$

where σ_{x_k}, σ_{y_k}, and σ_{z_k} are the standard deviations of the true position errors for each component, found as

$$\sigma_{x_k} = \sqrt{\frac{1}{N_{MC}} \sum_{i=1}^{N_{MC}} (\delta x_{k,i} - \overline{\delta x}_k)^2} \tag{3.73}$$

where

$$\delta x_{k,i} = \hat{x}_{k,i} - x_{k,i} \tag{3.74}$$

is the true x position error for the ith Monte Carlo run at time t_k and

$$\overline{\delta x}_k = \frac{1}{N_{MC}} \sum_{i=1}^{N_{MC}} \delta x_{k,i} \tag{3.75}$$

is the mean true x position error for the Monte Carlo ensemble.

The RSS true velocity error σ_{v_k} and RSS true gravity error σ_{μ_k} at t_k are computed similarly. Note that σ_{μ_k} is computed from a single component, so the RSS calculations are redundant and were kept simply to preserve commonality of Matlab code.

A confidence interval $[\sigma_{x_k}^-, \sigma_{x_k}^+]$ can be computed for the standard deviation σ_{x_k} of the true x position error $\delta x_{k,i}$ at time t_k for Monte Carlo run i, assuming that the errors $\delta x_{k,i}$ follow a zero-mean Gaussian distribution, as is already assumed for the extended Kalman filter. The endpoints of the confidence interval are found as

$$\sigma_{x_k}^- = \sigma_{x_k} \sqrt{\frac{N_{MC}}{\chi^2_{1-\frac{\alpha}{2},n}}}, \quad \sigma_{x_k}^+ = \sigma_{x_k} \sqrt{\frac{N_{MC}}{\chi^2_{\frac{\alpha}{2},n}}} \tag{3.76}$$

where $\chi^2_{f,n}$ is the argument of the χ^2 cumulative distribution function with n degrees of freedom that returns the value f, and $\alpha = 1 - \text{CL}$ is related to the confidence level CL for which one desires to construct the confidence interval. All confidence intervals in this study use a confidence level of 99.7%, which for a univariate Gaussian distribution corresponds to a confidence interval of the mean plus or minus $N_\sigma = 3$ standard deviations.

Similarly, confidence intervals may be constructed for the true y and z position errors, each component of the true velocity errors, and the true gravity error. An ad-hoc confidence interval $[\sigma^-_{r_k}, \sigma^+_{r_k}]$ may then be constructed for the complete RSS true position error as

$$\sigma^-_{r_k} = \sqrt{(\sigma^-_{x_k})^2 + (\sigma^-_{y_k})^2 + (\sigma^-_{z_k})^2}, \quad \sigma^+_{r_k} = \sqrt{(\sigma^+_{x_k})^2 + (\sigma^+_{y_k})^2 + (\sigma^+_{z_k})^2} \tag{3.77}$$

Ad-hoc confidence intervals $[\sigma^-_{v_k}, \sigma^+_{v_k}]$ and $[\sigma^-_{\mu_k}, \sigma^+_{\mu_k}]$ may be similarly constructed for the complete RSS true velocity error and RSS true gravity error. These intervals are "ad-hoc" because the author is not sufficiently skilled in probability and statistics to confidently state they capture the true variation in RSS position and velocity error, but they seem intuitively reasonable. The confidence interval for the gravity error is exact because the RSS gravity error is constructed from a single component.

CHAPTER 4

RESULTS

This study is intended to look at filter consistency and filter performance under various conditions. First, filter consistency will be examined for each scenario. Then, the effects of different input parameter values on filter performance will be examined. Finally, the observability of the nominal scenario for each filter formulation will be briefly discussed. In all plots wherein the filter formulation is unstated, the filter with three measurements and seven states is used.

4.1 Filter Consistency

The meaning of "consistency" for this study is as follows: when the true state errors from many Monte Carlo runs are plotted (in gray) and the 3σ filter covariance results from those runs are plotted (in red), the 3σ filter covariance curves bound the true state error curves, and the spread of the filter results is much smaller than the spread of the true errors. This also applies to the measurement innovations and their 3σ filter covariance results. It may therefore be said that for any individual Monte Carlo run, the state errors obtained from the square roots of the diagonal elements of the filter covariance are reasonable bounds of the true state errors.

4.1.1 A Consistent Filter

Scenario 1, as defined in Chapter 3, is designated as the "nominal" scenario to which others are compared because its process noise setting is relatively small and its initial position and velocity error fractions are also small, resulting in a well-behaved filter that is consistent for all instants simulated before periapse and all instants simulated after periapse. As shown in Figure 4.1, the x position errors are consistent with their filter estimates for each of the four filter formulations. Remember for this and future plots that N_x and N_z are,

respectively, the number of states and the number of measurements in the filter formulation. Also remember that $f_\mu = 0.018$ for all scenarios.

For convenience, individual position and velocity component error plots will no longer be shown in the remainder of this report. Instead, plots will generally display the 3σ RSS position, velocity, and gravity errors, along with 99.7% confidence intervals for those values. These are constructed as described in Section 3.16. When Monte Carlo results are shown for individual scenarios, the true RSS errors will continue to be shown in gray, and the 3σ RSS position, velocity, and gravity errors will still be shown in red. As shown in Figures 4.2, 4.3, and 4.4, the RSS position, velocity, and gravity errors are also consistent for this scenario.

As seen in Figure 4.5, the measurement innovations are consistent with their filter estimates. This plot shows the innovations for the angle between the target star and the first reference direction, which is the $[1, 0, 0]$ vector.

The measurement innovations for $\theta_{S,1}$, $\theta_{S,2}$, and $\theta_{S,3}$ behave identically, remaining nearly constant at values virtually equal to the 1σ measurement noise. As seen in Figure 4.6, the innovations for $\theta_{S,S}$ (the star angular diameter measurement) grow and shrink in time, but they remain bounded by their predicted covariance for all except the last portion of the trajectory when the state vector does not contain μ, and for the entire trajectory when it does. All scenarios except Scenarios 2, 3, 4, and 9 display similar patterns for the angular diameter measurement innovations. Scenarios 2 and 3 contain the measurement innovations within the covariance bound for the entire trajectory for both filters (see Figure 4.7), Scenario 4 does not take measurements, and Scenario 9 is entirely inconsistent.

4.1.2 An Inconsistent Filter

As an example of an inconsistent filter, consider Scenario 9, which differs from Scenario 1 only in the use of $f_{\text{pos}} = 0.1$ instead of $f_{\text{pos}} = 0.001$. Because the initial position error is about 100 times larger, the filter linearization is poor and the RSS error estimates encoded in the filter covariance matrix are no longer consistent with the true RSS errors, as seen in Figures 4.8, 4.9, and 4.10.

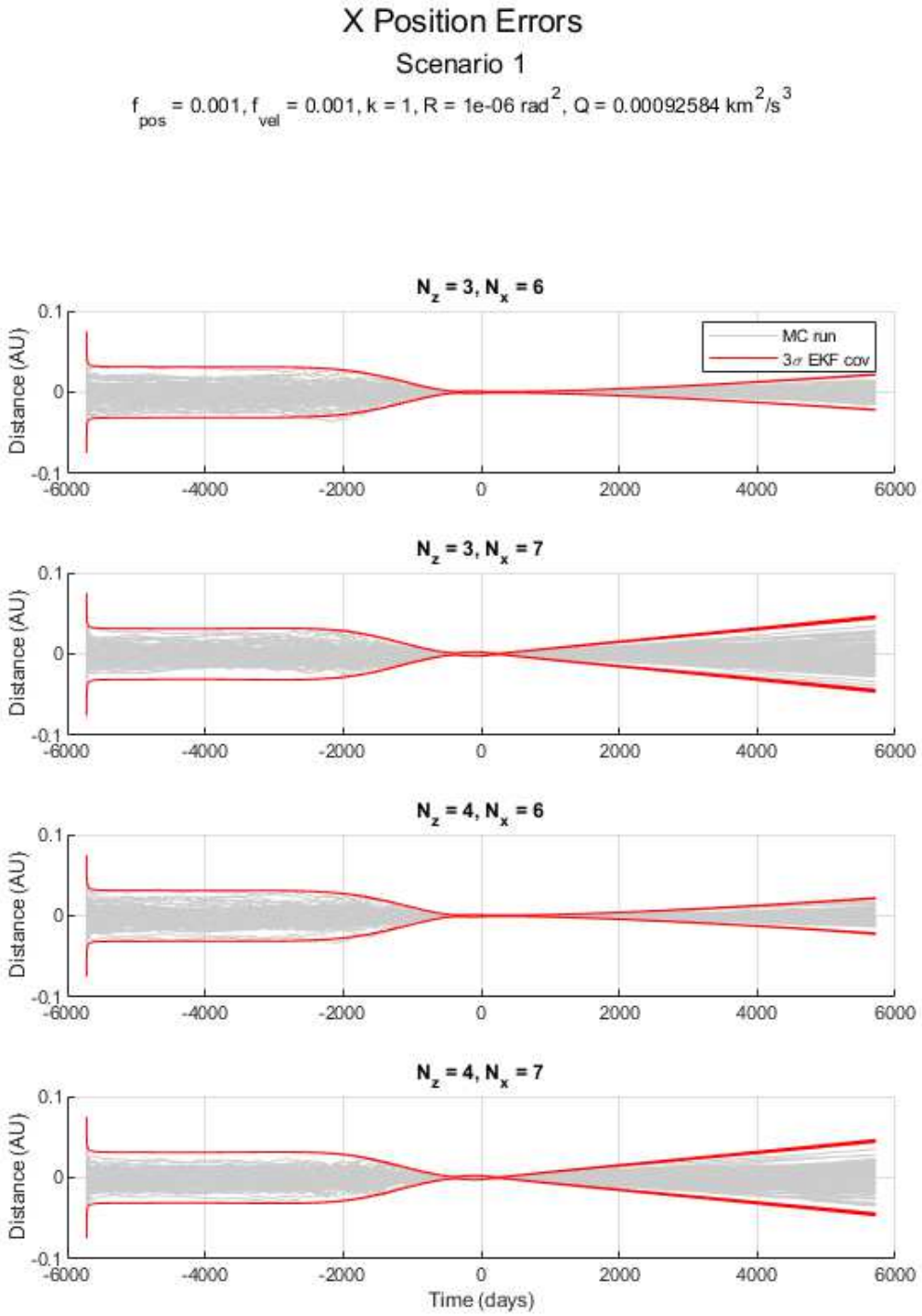

Fig. 4.1: Monte Carlo x position errors and 3σ filter covariance bounds for Scenario 1

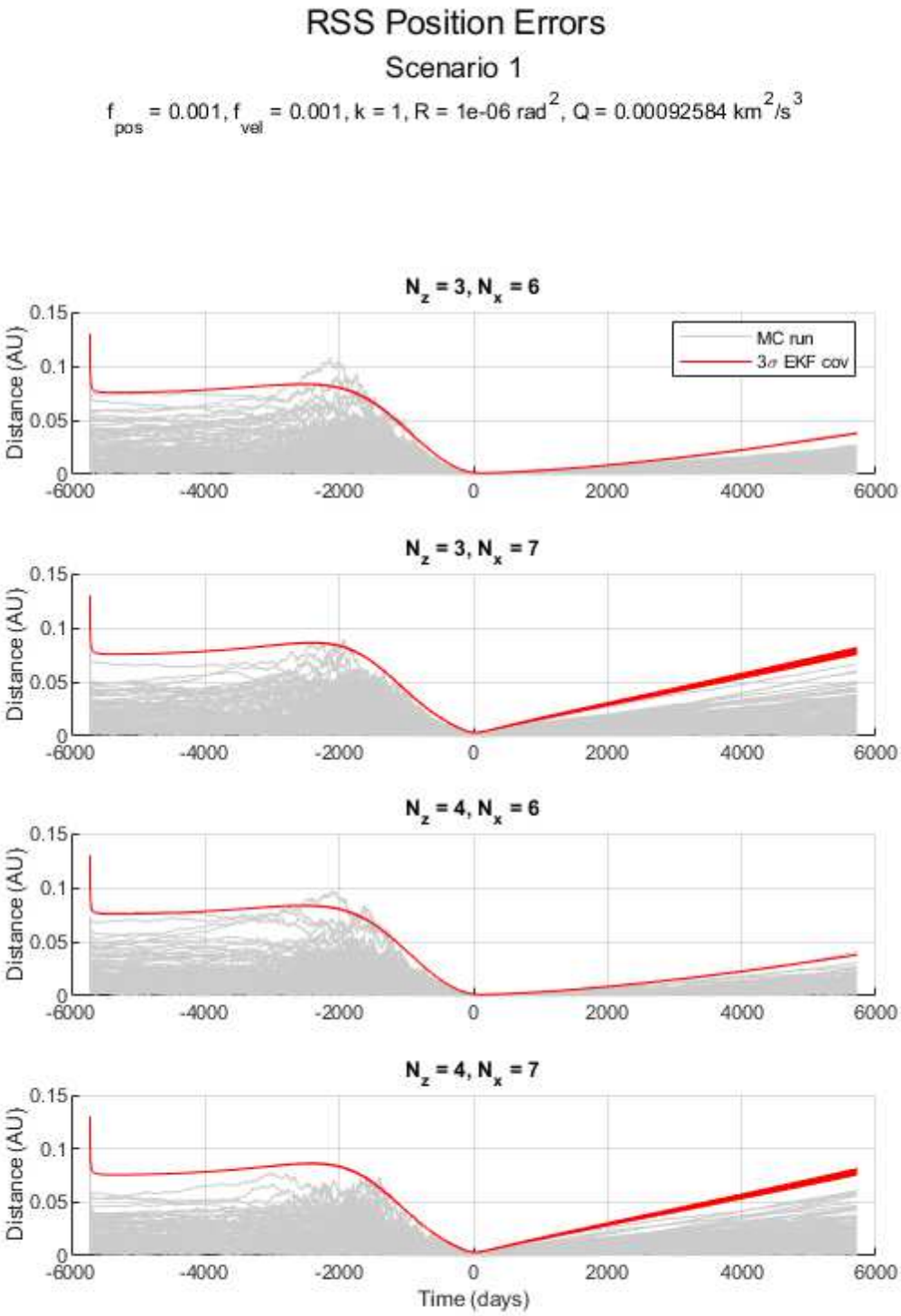

Fig. 4.2: Monte Carlo RSS position errors and 3σ filter covariance bounds for Scenario 1

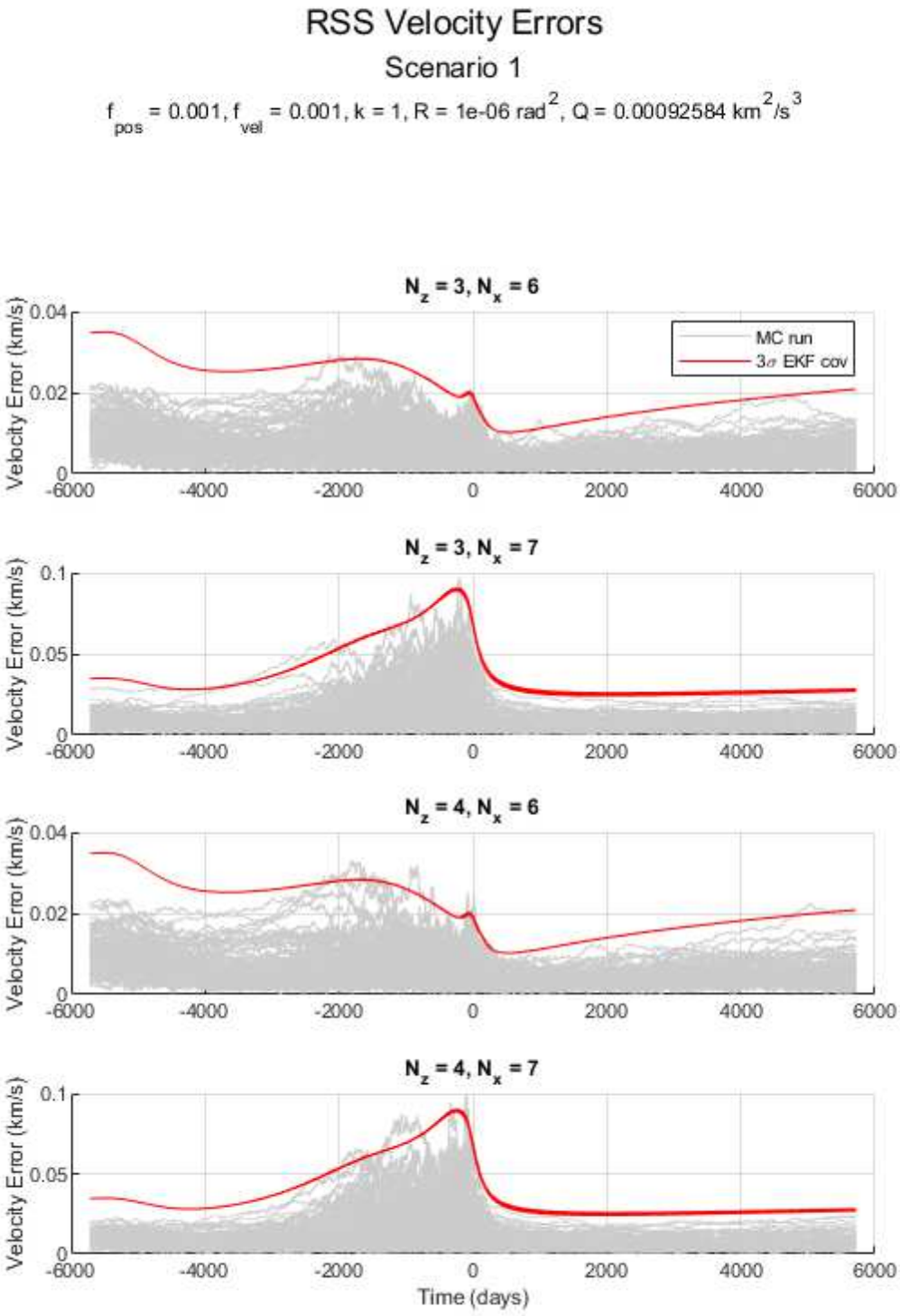

Fig. 4.3: Monte Carlo RSS velocity errors and 3σ filter covariance bounds for Scenario 1

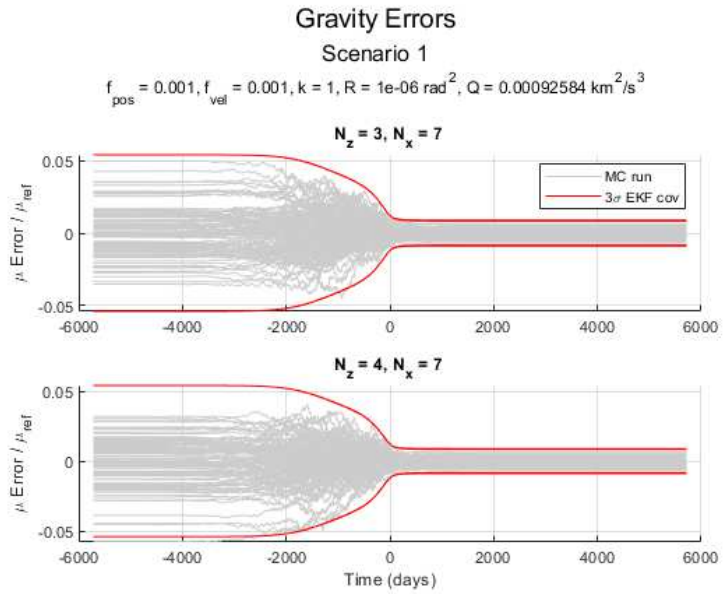

Fig. 4.4: Monte Carlo RSS gravity errors and 3σ filter covariance bounds for Scenario 1

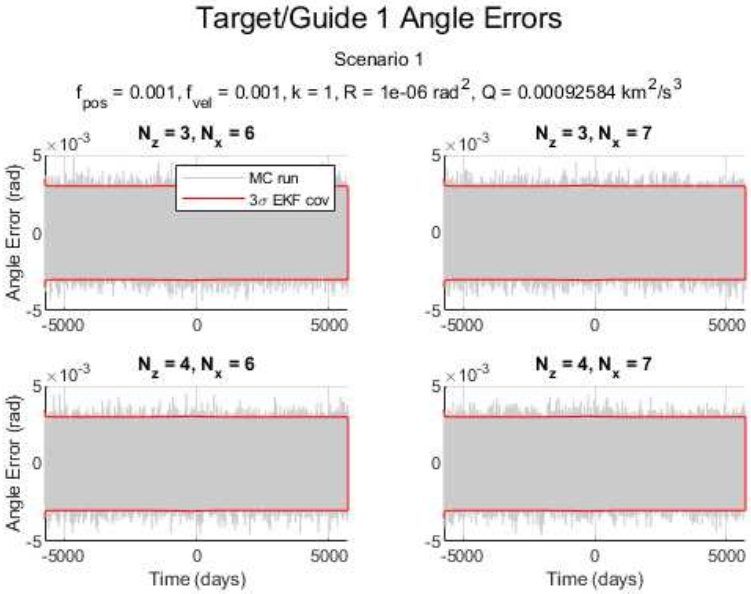

Fig. 4.5: Monte Carlo target/guide star 1 innovations and 3σ filter covariance bounds for Scenario 1

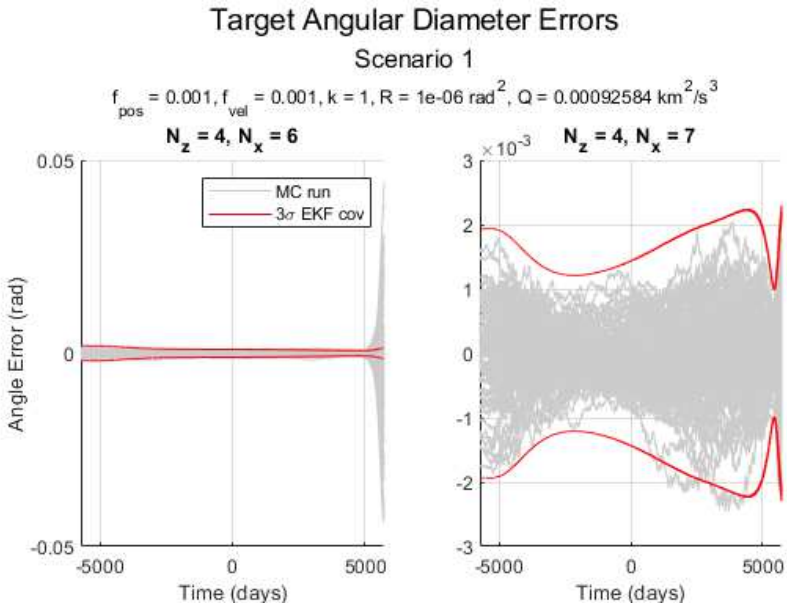

Fig. 4.6: Monte Carlo target star angular diameter innovations and 3σ filter covariance bounds for Scenario 1

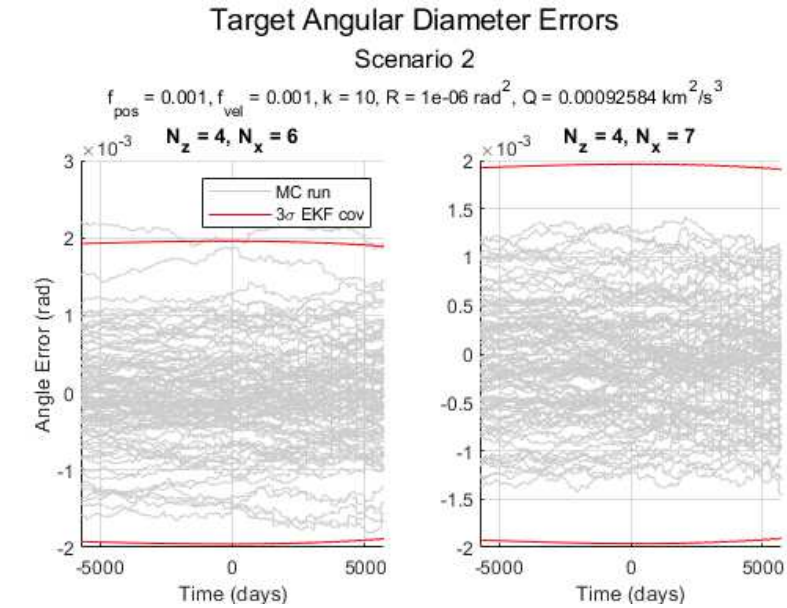

Fig. 4.7: Monte Carlo target star angular diameter innovations and 3σ filter covariance bounds for Scenario 2

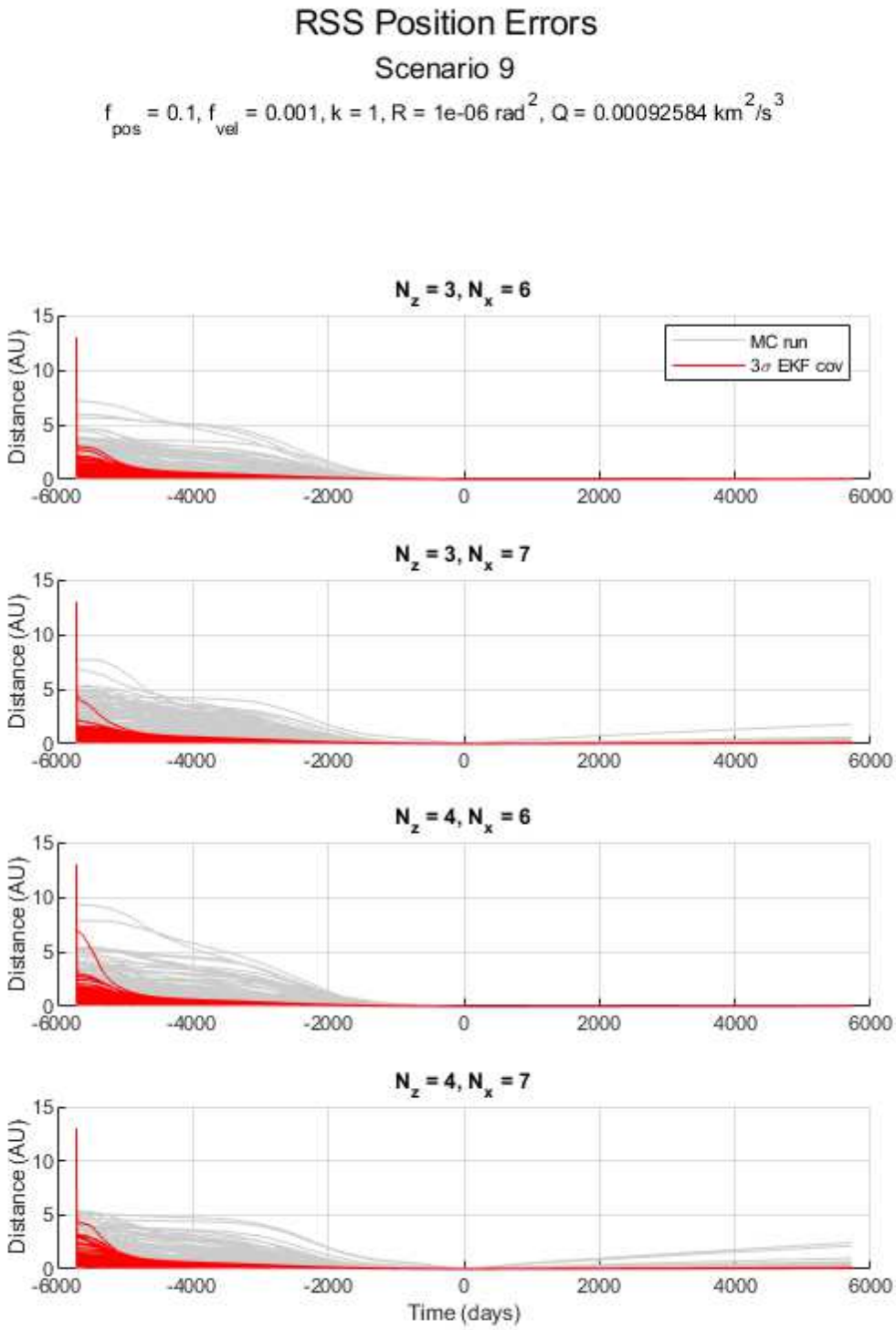

Fig. 4.8: Monte Carlo RSS position errors and 3σ filter covariance bounds for Scenario 9

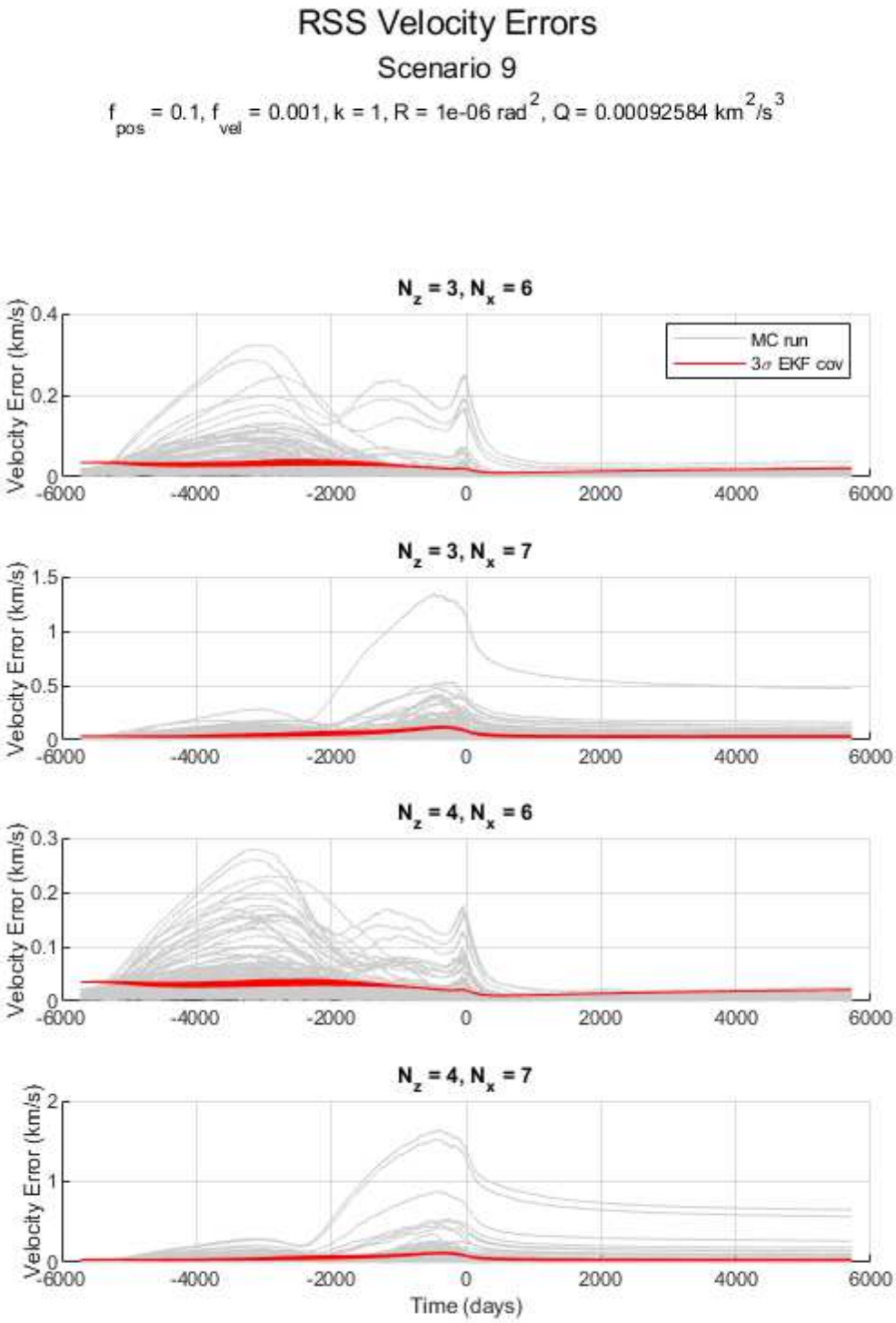

Fig. 4.9: Monte Carlo RSS velocity errors and 3σ filter covariance bounds for Scenario 9

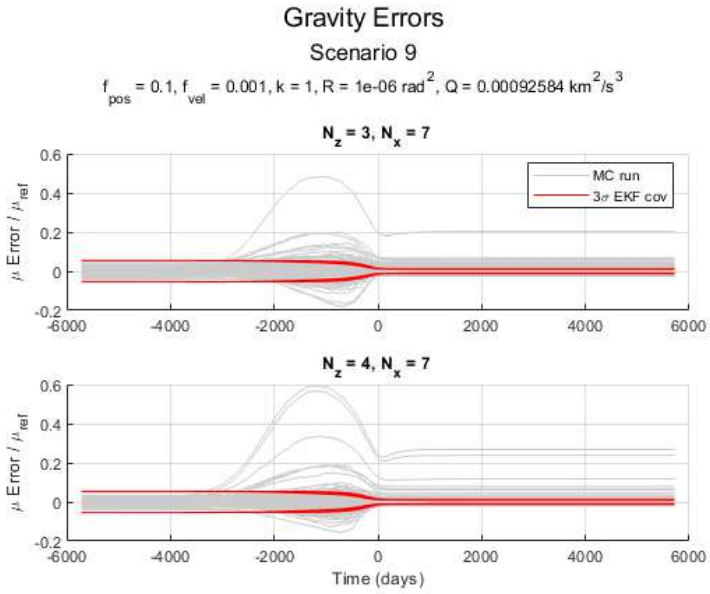

Fig. 4.10: Monte Carlo RSS gravity errors and 3σ filter covariance bounds for Scenario 9

4.1.3 Filter Consistency for All Scenarios

Having presented examples of a consistent filter and an inconsistent filter, the consistency of each state group, measurement, and filter type for each scenario is now presented in Table 4.1. For convenience, plots are omitted for most scenarios. Here "Y" means that the state group or measurement is consistent, "Y(T)" means that it generally seems to be consistent, but the spread of the filter covariance values from Monte Carlo run to Monte Carlo run is relatively large compared to the spread of the true state errors from run to run, "-" means that it is not considered, "N" means that it is inconsistent for the entire trajectory, "N(P)" means that it is inconsistent near periapse but consistent for the rest of the trajectory, and "N(E)" means that it is inconsistent near the end of the trajectory but consistent before then.

All scenarios apart from Scenario 9 are consistent in position, velocity, and gravity estimates for the entire trajectory; Scenario 9 is inconsistent in all states for the entire trajectory. Since the measurement equations and state dynamics as formulated in this study depend only on the position of the probe, it is not surprising that good filter operation depends principally on keeping the position error small - in this case, under 1-10% 1σ

upon filter initialization, or below 0.25-2.5 AU. Future studies might examine the launch and cruise phases of the probe in detail, to determine whether or not such a small initial position uncertainty is feasible after a cruise of several light years. Scenario 3, which differs from Scenario 1 by taking measurements 100 times less frequently, displays inconsistent innovations for $\theta_{S,1}$, $\theta_{S,2}$, and $\theta_{S,3}$ near periapse but, unlike the other scenarios, maintains consistency for $\theta_{S,S}$ for the entire trajectory. Meanwhile, the innovations for $\theta_{S,1}$, $\theta_{S,2}$, and $\theta_{S,3}$ are consistent for the entire trajectory in Scenario 9. It has been suggested [23] that innovation or residual monitoring is a vital tool for detecting incipient inconsistency in real-world filter applications, but judging from the results of Scenarios 3 and 9 one should not simply conflate consistent measurement innovations with consistent state estimates.

4.2 Filter Performance

For this study, "filter performance" refers to the state estimation accuracy achieved by a filter, not to the consistency of said filter's results with its covariance estimates.

First, the effects on performance and observability of including or excluding the star angular diameter and the star mass state from the filter will be discussed. Afterwards, the effects of different parameters on filter performance will be discussed with sole reference to the three-measurement, seven-state filter ($N_z = 3, N_x = 7$), because this filter is of greater scientific interest than either six-state filter and the fourth measurement will be shown to be of little value. Interested readers will find plotted results for all other filters in the appendix. Finally, the RSS position, velocity and gravity errors will be displayed for all scenarios, followed by sequential discussion of the effects of changing measurement interval, measurement noise, process noise, initial position error fraction, and initial velocity error fraction on the RSS position errors, position error fractions, velocity errors, velocity error fractions, and gravity errors.

From this point on, all descriptions of filter performance will refer to the true RSS position, velocity, and gravity errors for each scenario and their respective confidence intervals, computed as described in Section 3.16. The use of true RSS errors in the remainder of this study, rather than estimated RSS errors derived from the Monte Carlo ensemble of

Table 4.1: Consistency of Scenarios 1-14

1	N_x	N_z	**r**	**v**	$\theta_{S,1/2/3}$	$\theta_{S,S}$	μ	8	N_x	N_z	**r**	**v**	$\theta_{S,1/2/3}$	$\theta_{S,S}$	μ
	3	6	Y	Y	Y	-	-		3	6	Y	Y	Y	-	-
	3	7	Y	Y	Y	-	Y		3	7	Y	Y	Y	-	Y
	4	6	Y	Y	Y	N(E)	-		4	6	Y	Y	Y	N(E)	-
	4	7	Y	Y	Y	Y	Y		4	7	Y	Y	Y	Y	Y
2	N_x	N_z	**r**	**v**	$\theta_{S,1/2/3}$	$\theta_{S,S}$	μ	9	N_x	N_z	**r**	**v**	$\theta_{S,1/2/3}$	$\theta_{S,S}$	μ
	3	6	Y	Y	Y	-	-		3	6	N	N	Y	-	-
	3	7	Y	Y	Y	-	Y		3	7	N	N	Y	-	N
	4	6	Y	Y	Y	Y	-		4	6	N	N	Y	N	-
	4	7	Y	Y	Y	Y	Y		4	7	N	N	Y	N	N
3	N_x	N_z	**r**	**v**	$\theta_{S,1/2/3}$	$\theta_{S,S}$	μ	10	N_x	N_z	**r**	**v**	$\theta_{S,1/2/3}$	$\theta_{S,S}$	μ
	3	6	Y	Y	N(P)	-	-		3	6	Y	Y	Y	-	-
	3	7	Y	Y	N(P)	-	Y		3	7	Y	Y	Y	-	Y
	4	6	Y	Y	N(P)	Y	-		4	6	Y	Y	Y	N(E)	-
	4	7	Y	Y	N(P)	Y	Y		4	7	Y	Y	Y	Y	Y
4	N_x	N_z	**r**	**v**	$\theta_{S,1/2/3}$	$\theta_{S,S}$	μ	11	N_x	N_z	**r**	**v**	$\theta_{S,1/2/3}$	$\theta_{S,S}$	μ
	3	6	Y	Y	-	-	-		3	6	Y	Y	Y	-	-
	3	7	Y	Y	-	-	Y		3	7	Y	Y	Y	-	Y
	4	6	Y	Y	-	-	-		4	6	Y	Y	Y	N(E)	-
	4	7	Y	Y	-	-	Y		4	7	Y	Y	Y	Y	Y
5	N_x	N_z	**r**	**v**	$\theta_{S,1/2/3}$	$\theta_{S,S}$	μ	12	N_x	N_z	**r**	**v**	$\theta_{S,1/2/3}$	$\theta_{S,S}$	μ
	3	6	Y	Y	Y	-	-		3	6	Y	Y	Y	-	-
	3	7	Y	Y	Y	-	Y		3	7	Y	Y	Y	-	Y
	4	6	Y	Y	Y	N(E)	-		4	6	Y	Y	Y	N(E)	-
	4	7	Y	Y	Y	Y	Y		4	7	Y	Y	Y	Y	Y
6	N_x	N_z	**r**	**v**	$\theta_{S,1/2/3}$	$\theta_{S,S}$	μ	13	N_x	N_z	**r**	**v**	$\theta_{S,1/2/3}$	$\theta_{S,S}$	μ
	3	6	Y	Y	Y	-	-		3	6	Y	Y	Y	-	-
	3	6	Y	Y	Y	-	Y		3	7	Y	Y	Y	-	Y
	4	6	Y	Y	Y	N(E)	-		4	6	Y	Y	Y	N(E)	-
	4	7	Y	Y	Y	Y	Y		4	7	Y	Y	Y	Y	Y
7	N_x	N_z	**r**	**v**	$\theta_{S,1/2/3}$	$\theta_{S,S}$	μ	14	N_x	N_z	**r**	**v**	$\theta_{S,1/2/3}$	$\theta_{S,S}$	μ
	3	6	Y(T)	Y(T)	Y	-	-		3	6	Y	Y	Y	-	-
	3	7	Y(T)	Y(T)	Y	-	Y		3	7	Y	Y	Y	-	Y
	4	6	Y(T)	Y(T)	Y	N(E)	-		4	6	Y	Y	Y	N(E)	-
	4	7	Y(T)	Y(T)	Y	Y	Y		4	7	Y	Y	Y	Y	Y

filter covariances, allows the results from Scenario 9 to be compared with the results from all other scenarios, despite the inconsistency of the filter for that scenario.

4.2.1 Relative Performance of Different Filter Types

As described in 3.14, four separate filter types are considered, distinguished by the presence or absence of the star angular diameter measurement and the gravity of the star. Theoretically, the angular diameter measurement is necessary to achieve a complete position solution with a single measurement set, so it should improve observability and reduce state errors. The star gravity is included for scientific interest only, since the filter is otherwise assumed to use a precisely correct value for that parameter.

Observability of Nominal Scenario

Although the angles-only measurement set only directly observes the probe's position, the probe's velocity is also observable through the coupling of position and velocity in the probe dynamics. It is therefore hoped that the star gravity μ is also observable through dynamic coupling, even though it appears nowhere in the measurement equations. As shown in Figure 4.11, the condition number of the observability Gramian for filters with seven states is above the finite-precision threshold of 10^{16} for the entire trajectory, and the condition number for filters with six states quickly falls below that threshold and ends at about 10^6. Since μ is the seventh state, this suggests that it cannot be estimated from angles-only measurements. By and large, this is true: the gravity errors are nearly constant for most of the time before periapse, and nearly constant for most of the time after periapse. (See Section 4.2.7.) However, for each scenario examined except Scenario 9, the gravity error drops sharply in the thousand days on either side of periapse, when the curvature of the trajectory is largest. This illustrates the limitations of the linear observability Gramian as a measure of observability for nonlinear systems - it correctly predicts the filter's failure to change the gravity estimate for most of the trajectory, but fails to predict the sharp drop in gravity estimation errors near periapse. Note that both six-state filters have nearly precisely the same observability, as do both seven-state filters. It will be seen in Section

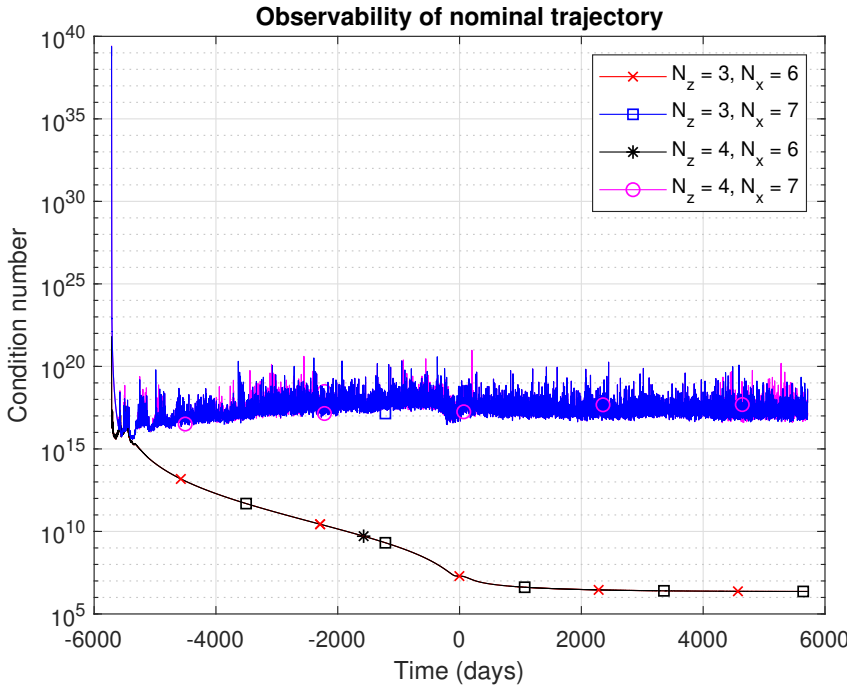

Fig. 4.11: Condition number of observability Gramian for different filter formulations

4.2.1 that the six-state filters also perform nearly precisely the same as each other, as do the seven-state filters.

Relative Performance for Nominal Scenario

The relative performance of the different filters is consistent in all scenarios, so it may be illustrated in Figure 4.12 by the results from the nominal scenario without reference to other scenarios. All four filters are initialized with the same error settings, but the seven-state filters soon develop larger errors than the six-state filters. Within each pair of filters (six state or seven state), the filter with the star angular diameter measurement is sometimes more accurate than the filter without and sometimes less accurate, but the four-measurement error is always within the confidence interval of the three-measurement error and vice versa; that is, within the uncertainty of the limited Monte Carlo ensemble, the three-measurement error and four-measurement error are practically identical.

These results are easily explained. The six-state filters are more accurate than the seven-state filters simply because the seven-state filters do not enjoy a precise match between

the star gravity in the truth model and the star gravity in the filter model. The four-measurement filters are no more accurate than the three-measurement filters because the 1σ measurement error (usually $1 \cdot 10^{-3}$ rad, but $1 \cdot 10^{-4}$ rad in Scenario 5 and $1 \cdot 10^{-5}$ rad in Scenario 6) is much larger than the true star angular diameter, which begins and ends at $2.9 \cdot 10^{-5}$ rad and peaks at $7.2 \cdot 10^{-4}$ rad. With such small angles to measure, a noisy instrument can provide little useful information. By contrast, the angles between the target star and the reference directions ("guide stars") vary between 0.43 and 2.7 rad, compared to which the measurement error is small. Note that this simple explanation predicts that the four-measurement filters would perform better than the three-measurement filters for Scenarios 5 and 6, as at periapse the true star angular diameter is seventy times the 1σ measurement error for Scenario 6, but these scenarios also display practically identical performance for three and four measurements. This may point to a flaw in the author's implementation or understanding of the fourth measurement, or it may simply show that the measurement requires yet smaller noise to become useful. However, this study was not pursued with even smaller measurement noise because a 1σ angular measurement error of $1 \cdot 10^{-5}$ rad is already extremely small [35], especially for small and simple "starchip" equipment, and use of overly precise nonlinear measurements (such as angles-only observations) can cause naive EKFs to diverge because the higher-order terms of the measurement's derivative with respect to the state become large relative to the first-order measurement geometry matrix [39].

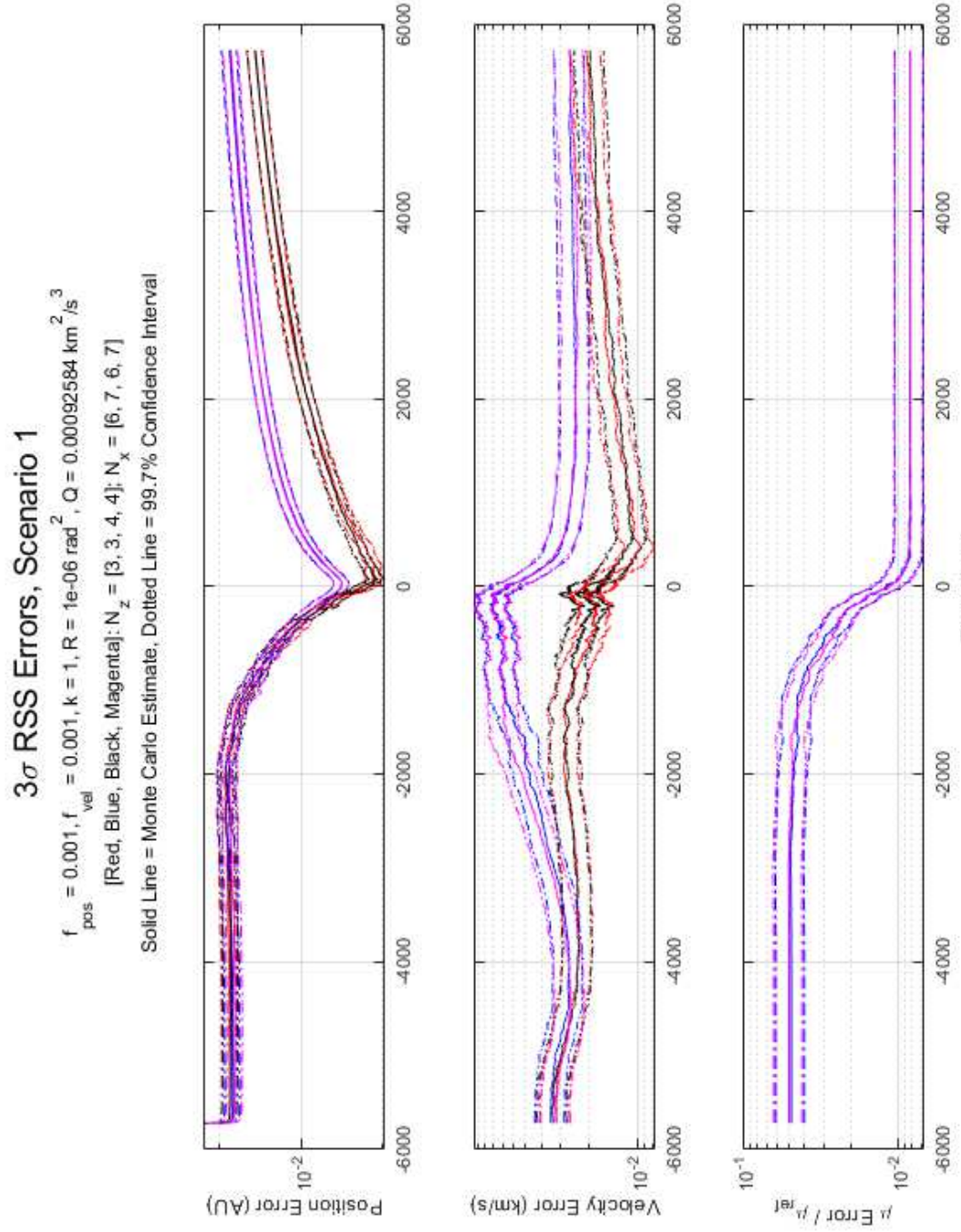

Fig. 4.12: Monte Carlo 3σ RSS errors and 99.7% confidence intervals over time for Scenario 1

4.2.2 Filter Performance for All Scenarios

Figure 4.13 displays the RSS position, velocity, and gravity errors for each scenario, computed using all Monte Carlo runs. Since the plots are too crowded to distinguish some curves individually, only a few features will be described at this time.

First, note that despite the large differences in initial position error between the various scenarios, all except Scenario 4 (with $k = \infty$) and Scenario 9 (with $f_{pos} = 0.1$) converge to similarly small estimation errors at periapse, and after periapse the RSS errors grow nearly linearly (though this is not immediately apparent from a logarithmic plot). This is to be expected, as the magnitude of the position states decreases until periapse and increases nearly linearly thereafter (see Figure 3.4). The largest position errors belong to the scenarios with the largest initial position error, process noise, and measurement interval, and vice versa. Notably, the parameter that produces the largest and smallest position errors (apart from Scenario 4) is none other than initial position error fraction.

Just as the range of the probe and the RSS position errors both reach their minimum values at periapse, so do the velocity of the probe and the RSS velocity errors both reach their maximum values at periapse. Apart from Scenario 4, the scenarios with greatest and smallest velocity errors at periapse and the end of the flyby are those with the greatest and smallest values of process noise, followed by that with the largest initial position error fraction. Surprisingly, the initial velocity error fraction seems not to dramatically affect the subsequent velocity errors, at least not in ways that can be distinguished on this plot. This may be because process noise directly and incessantly acts upon the velocity derivatives, as does position error, while initial velocity error only acts upon the position derivatives. Therefore, the filter can quickly correct the velocity estimate as long as the position estimate is reasonably accurate.

Like the position errors and velocity errors, the gravity errors reflect the trends in the true gravity of the star: it stays constant, and they stay nearly constant, only changing near periapse when the curvature of the trajectory is greatest. Notably, they do decrease by about an order of magnitude despite the linear observability Gramian's insistence that

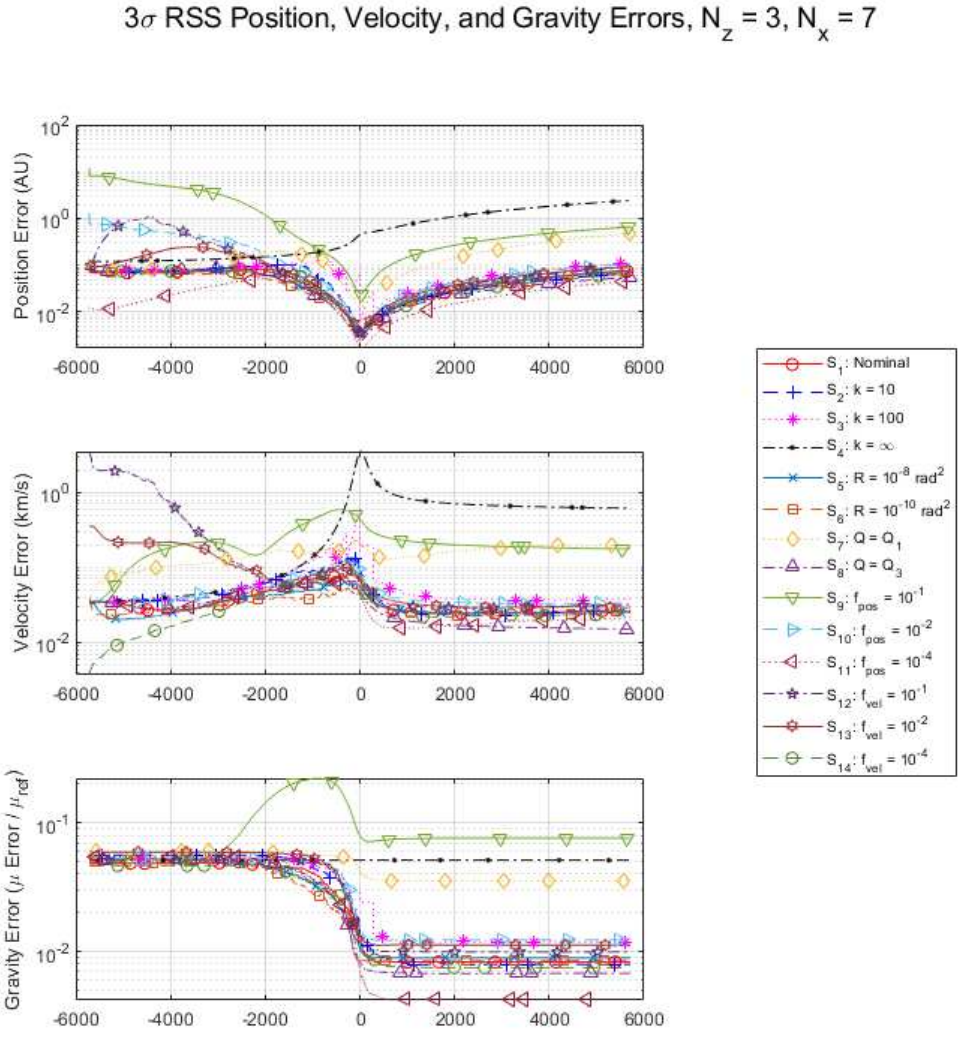

Fig. 4.13: Monte Carlo 3σ RSS errors for all states and all scenarios

they remain unobservable. Since Scenario 4 takes no measurements and treats the star mass as constant in the filter state, its gravity errors do not change, and there is very little change in the gravity errors for the scenarios with large process noise and large initial position error either. In these cases, the filter attributes most of the unexpected trajectory changes near periapse to random disturbance accelerations or to incorrect position estimates rather than to incorrect gravity estimates. Conversely, when process noise and initial position error are small, these trajectory changes are attributed to gravity errors and the gravity estimate is adjusted accordingly.

4.2.3 Filter Performance: RSS Position Errors

The most important aspect of filter performance is the magnitude of the RSS position errors achieved.

Changing Measurement Interval, Measurement Noise, and Process Noise

One may suppose that, everything else being equal, a filter that processes measurements more frequently will be more accurate than one that processes measurements less frequently. The top subplot in Figure 4.14 compares RSS position errors for Scenarios 1, 2, 3, and 4, respectively with a measurement set taken every 1, 10, and 100 time steps, and with no measurements taken at all. Naturally, the Scenario 4 errors are greatest, and it is clearly necessary to take some measurements in order to reduce estimation errors. The Scenario 3 errors are clearly larger than the Scenario 1 and 2 errors, but the Scenario 1 and 2 errors are identical to the precision of the Monte Carlo ensemble. For this flyby, there seems to be little point in taking measurement sets at intervals less than 28.5 days.

Likewise, one may suppose that, everything else being equal, reduced measurement noise improves the accuracy of filter estimates. However, the RSS positions displayed in the middle subplot by Scenarios 1, 5, and 6 are identical to within the precision of the ensemble. This may ease the work of the imagined “starchip” engineer, as the other sources of uncertainty in the problem are large enough that an EKF can achieve the same performance with a cheap camera system as with an expensive camera system.

In the bottom subplot, the three process noise values represented by Scenarios 1, 7, and 8 produce distinctly different position errors, with the greatest noise producing the greatest error and the least noise producing the least error. Since the process noise settings differ by an order of magnitude each in the position dispersion they produce at periapse (respectively 0.01, 0.1, and 0.001 AU), navigation engineers for similar flyby missions should make sure to use realistic values for process noise in their calculations rather than arbitrarily assuming a particular dispersion and choosing process noise to suit.

Changing Initial Position and Velocity Error Fractions

Since the initial position error fraction acts directly upon the RSS position error and the initial velocity error fraction acts upon it at the remove of a single integration time step, it is not surprising to see in Figure 4.15 large differences in filter performance during the early inbound leg of the flyby for Scenarios 1 and 9-14. The RSS position errors for these scenarios converge to similar values before periapse, but not to identical errors within the precision of the ensemble. By the end of the outbound leg, the position errors for the different initial position error settings remain distinct and ordered as one would expect, with the largest errors corresponding to the largest settings and vice versa. Initial settings of $f_{vel} = 0.1$ and $f_{vel} = 0.01$ produce end errors that are identical to the precision of their confidence intervals, as do initial settings of $f_{vel} = 0.001$ and $f_{vel} = 0.0001$. As previously discussed, the filter is relatively insensitive to initial velocity errors because they can be easily corrected by improved position estimates, but larger initial velocity errors generally correspond to larger position errors.

4.2.4 Filter Performance: RSS Position Error Fraction

Although the size of the RSS position error is the most important aspect of filter performance operationally, its tendency to follow the upward or downward trends in the distance between the probe and the star makes it useful to examine the RSS position error as a fraction of the true distance, in order to separate the effects of the filter from the effects of the trajectory.

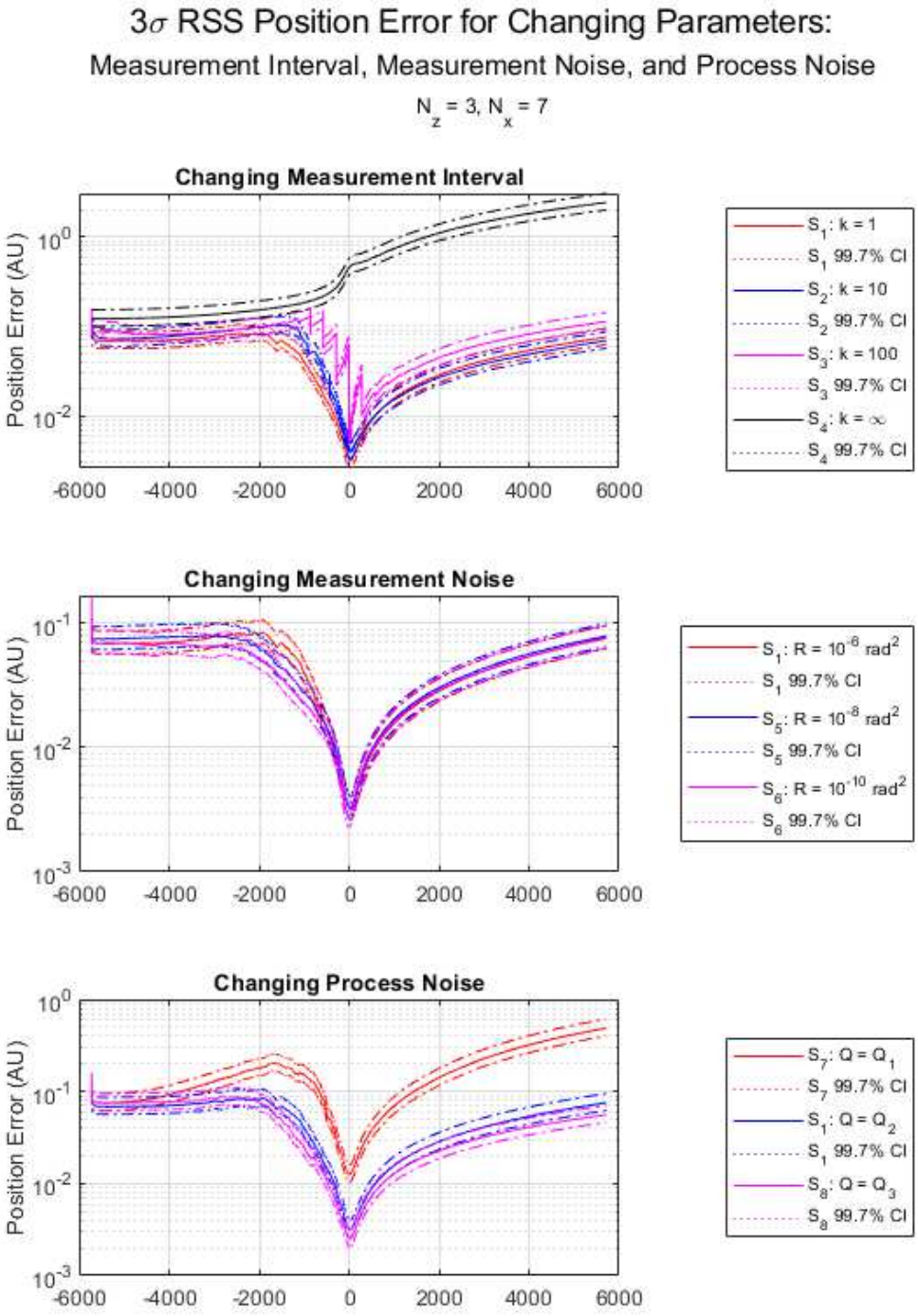

Fig. 4.14: Monte Carlo 3σ RSS position errors and 99.7% confidence intervals for scenarios with varying measurement interval, measurement noise, and process noise

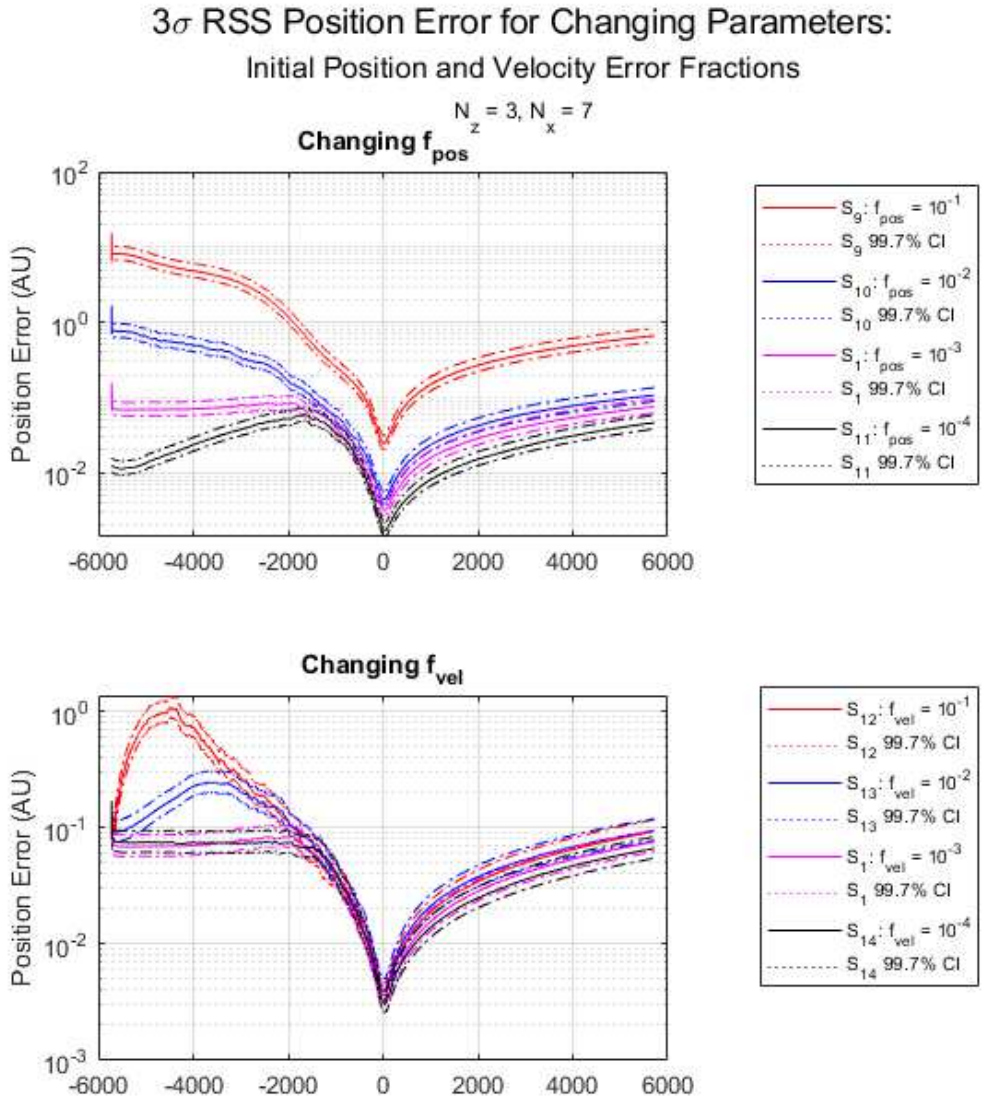

Fig. 4.15: Monte Carlo 3σ RSS position errors and 99.7% confidence intervals for scenarios with varying initial position and velocity error fractions

Changing Measurement Interval, Measurement Noise, and Process Noise

The top subplot in Figure 4.16 compares position error fraction for Scenarios 1, 2, 3, and 4, with varying measurement interval. The middle subplot compares position error fraction for Scenarios 1, 5, and 6, with varying measurement noise. The bottom subplot makes the comparison for Scenarios 1, 7, and 8, with differing process noise. The relative behaviors of the scenarios in each set is the same for the RSS position error fractions as for the RSS position error magnitudes, and will not be discussed separately. For each scenario, the RSS position error fraction drops sharply after the first measurement set is processed, rises until the greater trajectory curvature near periapse starts to make the measurements useful (compare the behavior of Scenario 4 to Scenarios 1, 2, and 3), reaches a minimum at periapse that is nearly identical to the former minimum after the first measurement set, and increases slowly thereafter.

Changing Initial Position and Velocity Error Fractions

It is more useful to consider the effects of different initial position and velocity error fractions on later position error fractions, as they are more closely related. Figure 4.17 shows much of the behavior in Figure 4.16 to be an artifact of the constant value of f_{pos} in each scenario therein, namely $f_{pos} = 0.001$. Scenarios 1, 9, 10, and 11 begin with different settings for f_{pos} and end with position error fractions that are distinctly different from the initial settings (except Scenario 1) and from each other, with final values in the order one would expect: greater initial position error fractions correspond to greater final position error fractions. There appears to be little need for the mission designer or filter designer to achieve a better position error fraction upon filter initialization than about $f_{pos} = 0.001$, since reducing that by a factor of 10 at the beginning of the flyby only reduces the position error fraction at the end of the flyby by about a factor of 2. Meanwhile, the final velocity error fractions for initial settings of $f_{vel} = 0.1$ and $f_{vel} = 0.01$ are the same to the precision of the Monte Carlo ensemble, as are the final velocity error fractions for initial settings of r$f_{vel} = 0.001$ and $f_{vel} = 0.0001$. At periapse, these are about 50% smaller than their initial values.

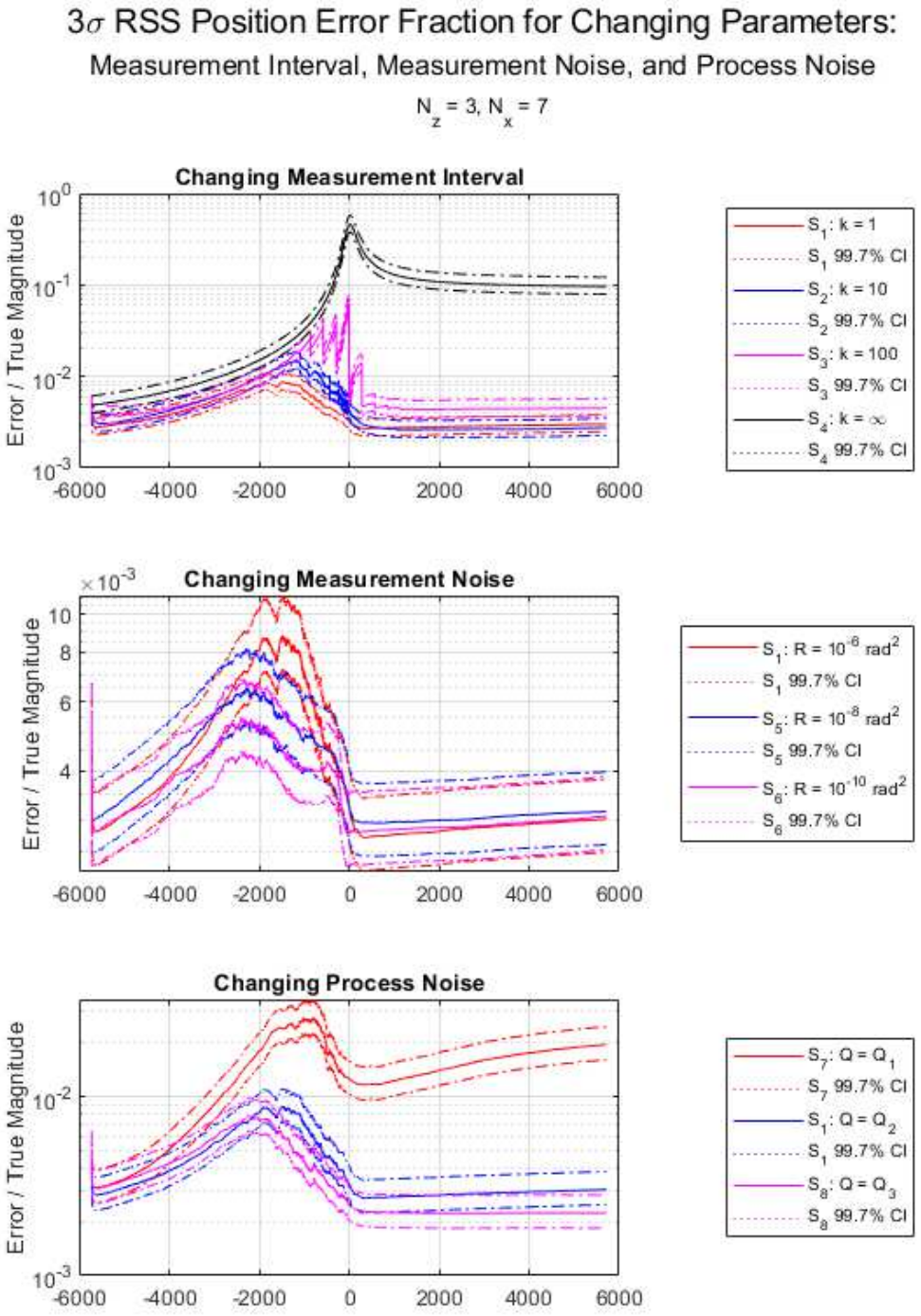

Fig. 4.16: Monte Carlo 3σ RSS position error fractions and 99.7% confidence intervals for scenarios with varying measurement interval, measurement noise, and process noise

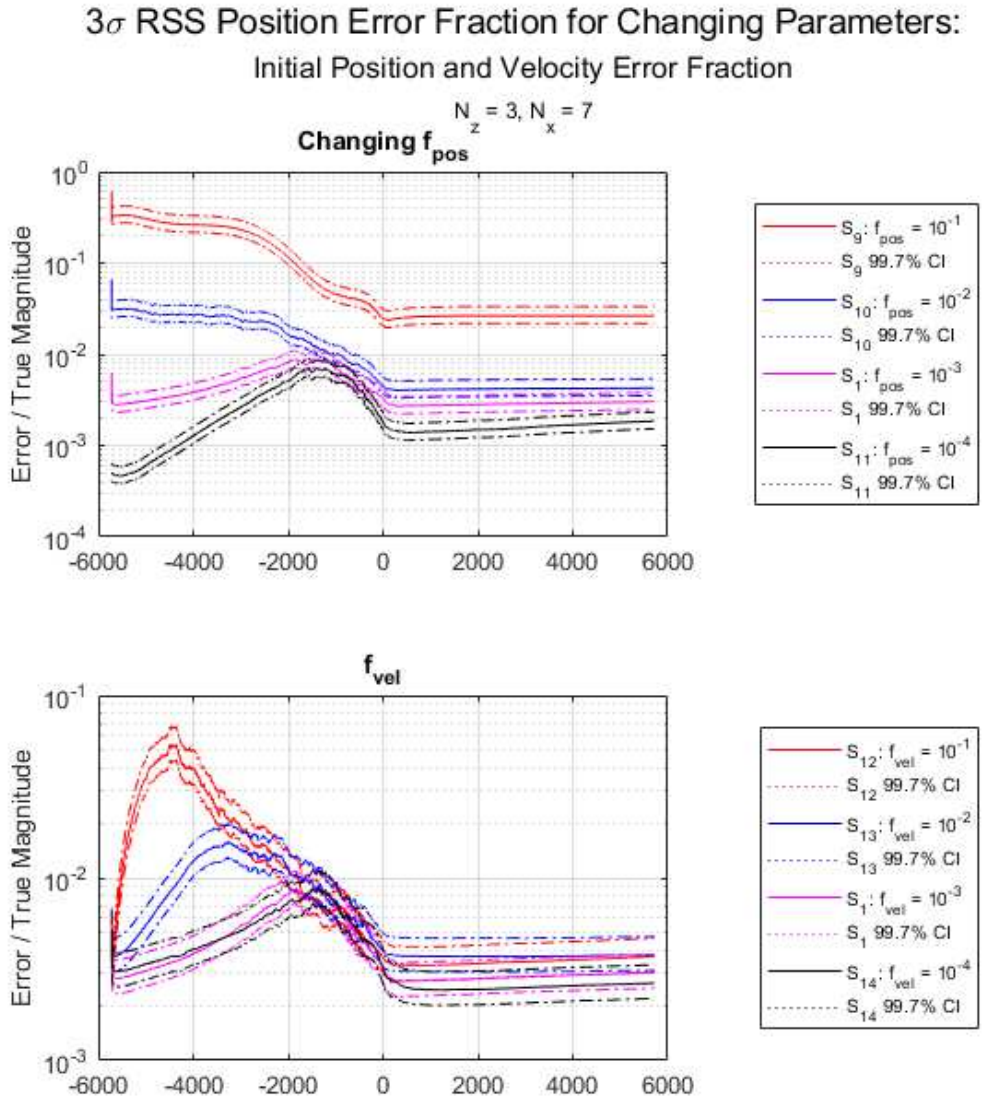

Fig. 4.17: Monte Carlo 3σ RSS position error fractions and 99.7% confidence intervals for scenarios with varying initial position and velocity error fractions

4.2.5 Filter Performance: RSS Velocity Errors

The magnitude of the RSS velocity error is, of course, a highly important measure of filter performance.

Changing Measurement Interval, Measurement Noise, and Process Noise

The top subplot in Figure 4.18 compares RSS velocity errors for Scenarios 1, 2, 3, and 4, with varying measurement interval. The middle subplot compares velocity errors for Scenarios 1, 5, and 6, with varying measurement noise. The bottom subplot makes the comparison for Scenarios 1, 7, and 8, with differing process noise. Once again, there is little difference between the results for measurement intervals of 2.85 days ($k = 1$, Scenario 1) and 28.5 days ($k = 10$, Scenario 2), while the errors for larger intervals are distinctly higher. Changing the measurement noise produces no significant difference in the filter results, and greater process noise produces greater velocity errors. For Scenario 1 and all other scenarios with the same process noise ($Q = Q_2$), the velocity errors at the end of the flyby are substantially the same as those at the start of the flyby, but Scenario 7's larger process noise causes its velocity error to increase by nearly an order of magnitude over the duration of the flyby, and Scenario 8's smaller process noise causes its error to decrease by nearly an order of magnitude.

Changing Initial Position and Velocity Error Fractions

As shown in Figure 4.19, the final velocity error is nearly insensitive to the initial velocity error fraction: the results for Scenarios 12, 1, and 13 (with $f_{vel} = 0.1$, 0.01, and 0.001, respectively) are identical to the precision of the Monte Carlo ensemble, and the velocity error fraction for Scenario 14 (with $f_{vel} = 0.0001$) is only slightly smaller. The RSS velocity errors behave as expected with respect to the initial position error fraction: larger values of f_{pos} lead to distinctly larger final velocity errors.

4.2.6 Filter Performance: RSS Velocity Error Fraction

Just as the position error magnitudes may be compared to the magnitude of the true

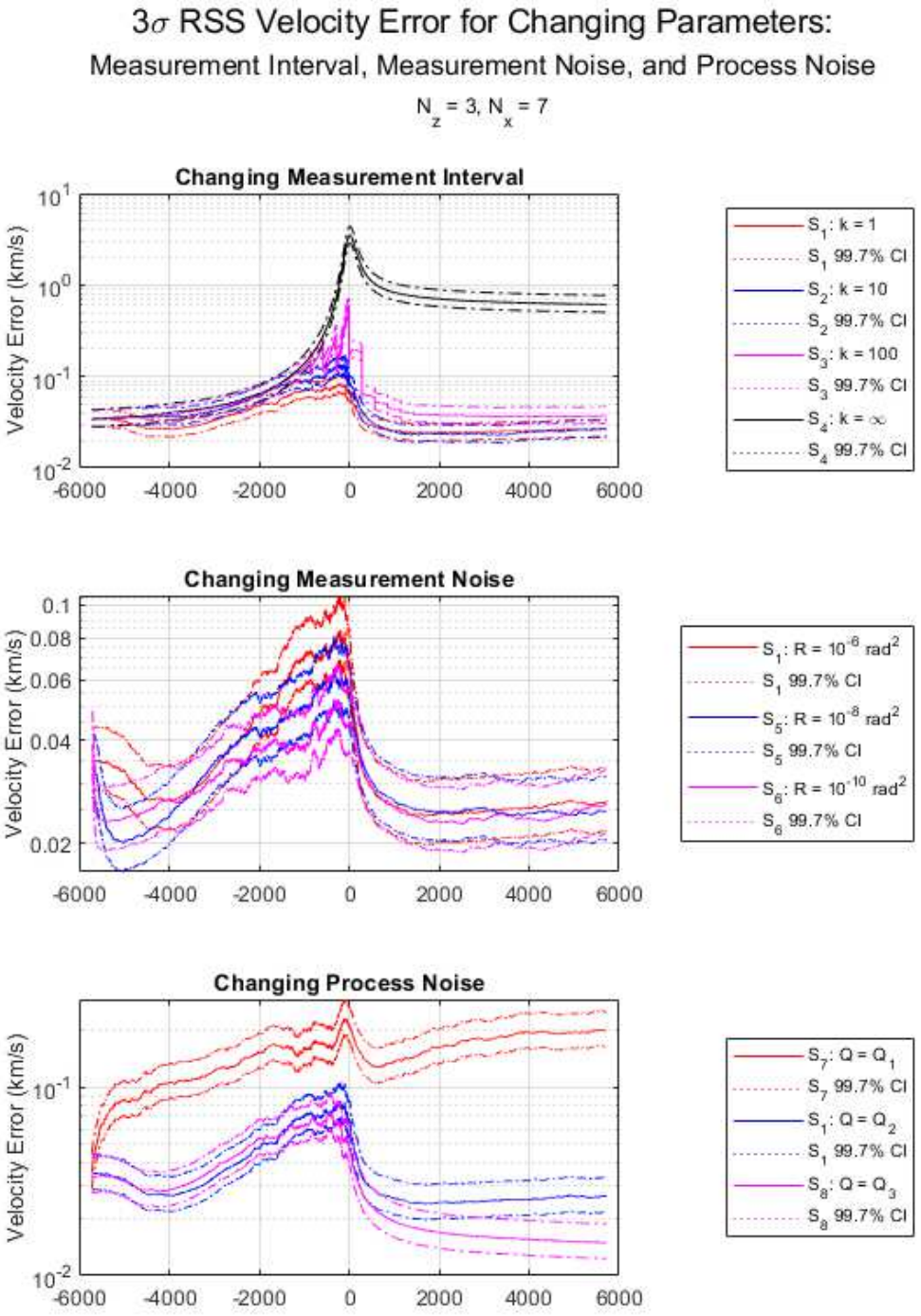

Fig. 4.18: Monte Carlo 3σ velocity errors and 99.7% confidence intervals for scenarios with varying measurement interval, measurement noise, and process noise

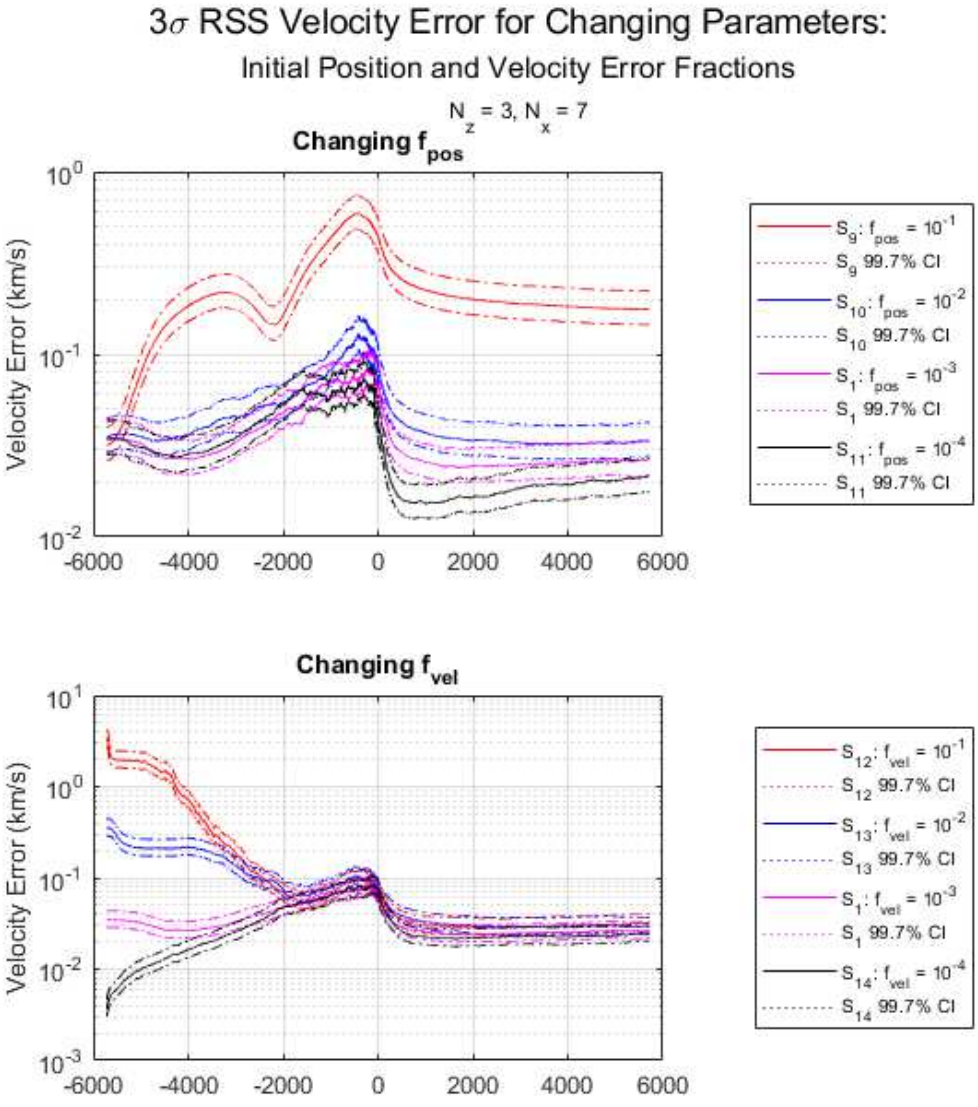

Fig. 4.19: Monte Carlo 3σ RSS velocity errors and 99.7% confidence intervals for scenarios with varying initial position and velocity error fractions

position, so may the velocity error magnitudes be compared to the magnitude of the true velocity at each instant.

Changing Measurement Interval, Measurement Noise, and Process Noise

As before, the top subplot in Figure 4.20 compares RSS velocity error fractions for Scenarios 1, 2, 3, and 4, with varying measurement interval. The middle subplot compares velocity error fractions for Scenarios 1, 5, and 6, with varying measurement noise. The bottom subplot makes the comparison for Scenarios 1, 7, and 8, with differing process noise. The relative behaviors of the scenarios in each set is the same for the velocity error fractions as for the velocity error magnitudes, and will not be discussed separately.

Changing Initial Position and Velocity Error Fractions

The relative behaviors of RSS velocity error fractions for scenarios differing in f_{pos} and f_{vel} is identical to the relative behaviors of RSS velocity error magnitudes, and will not be discussed separately, though it is displayed in Figure 4.21.

4.2.7 Filter Performance: Gravity Errors

As the "minimal scientific return" for the starchip flyby, the gravity errors are of essential interest. Because the variables in the problem have been scaled such that the nominal star gravity has a value of unity, the gravity error magnitudes are effectively also the gravity error fractions, and therefore the gravity errors as proportions of the true value of μ will not be discussed separately.

Changing Measurement Interval, Measurement Noise, and Process Noise

As before, the top subplot in Figure 4.22 compares gravity error magnitudes for Scenarios 1, 2, 3, and 4, with varying measurement interval. The middle subplot compares gravity error magnitudes for Scenarios 1, 5, and 6, with varying measurement noise. The bottom subplot makes the comparison for Scenarios 1, 7, and 8, with differing process noise. Thanks to the brief, nearly impulsive interaction of the probe with the star on its hyperbolic flyby

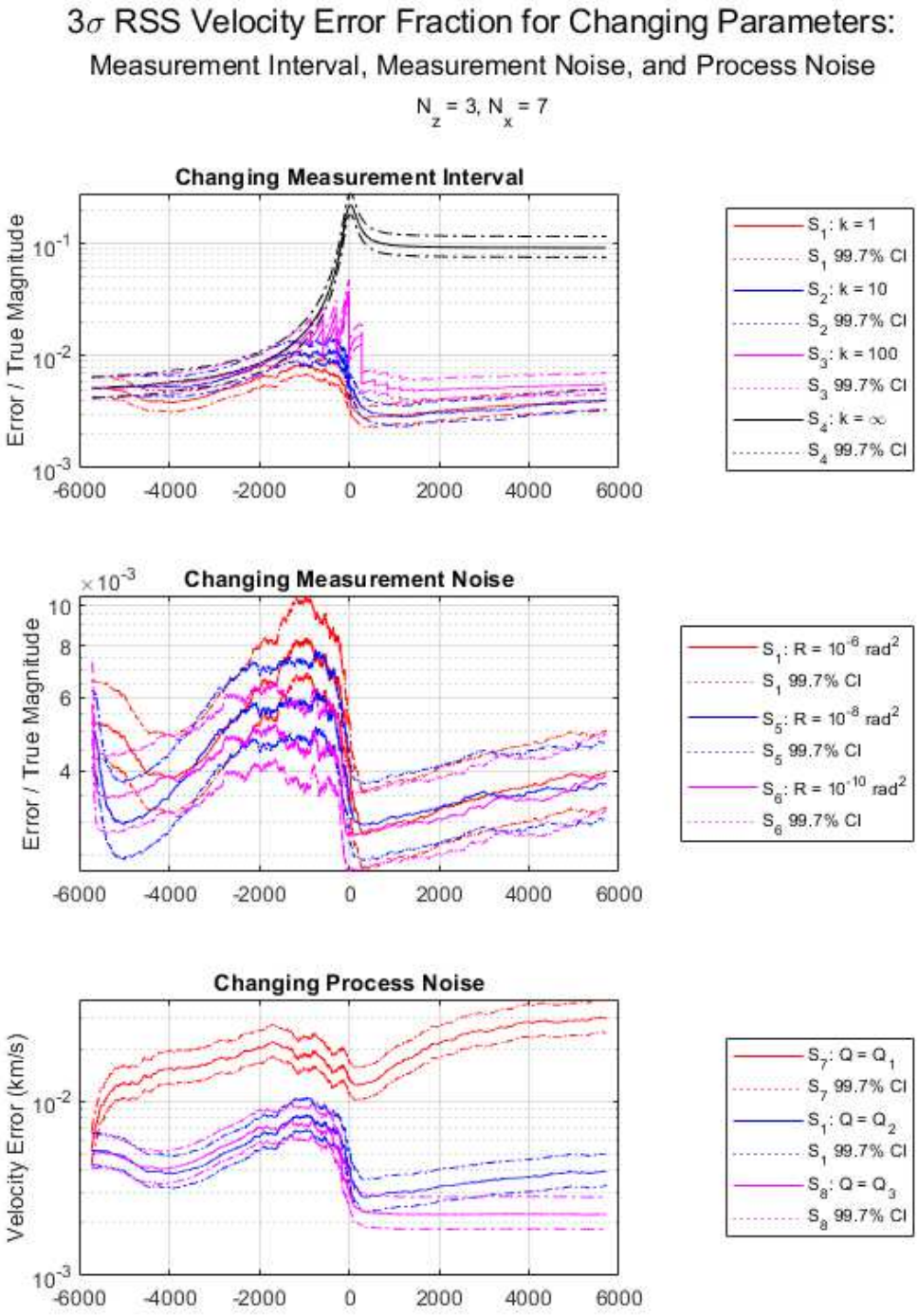

Fig. 4.20: Monte Carlo 3σ RSS velocity error fractions and 99.7% confidence intervals for scenarios with varying measurement interval, measurement noise, and process noise

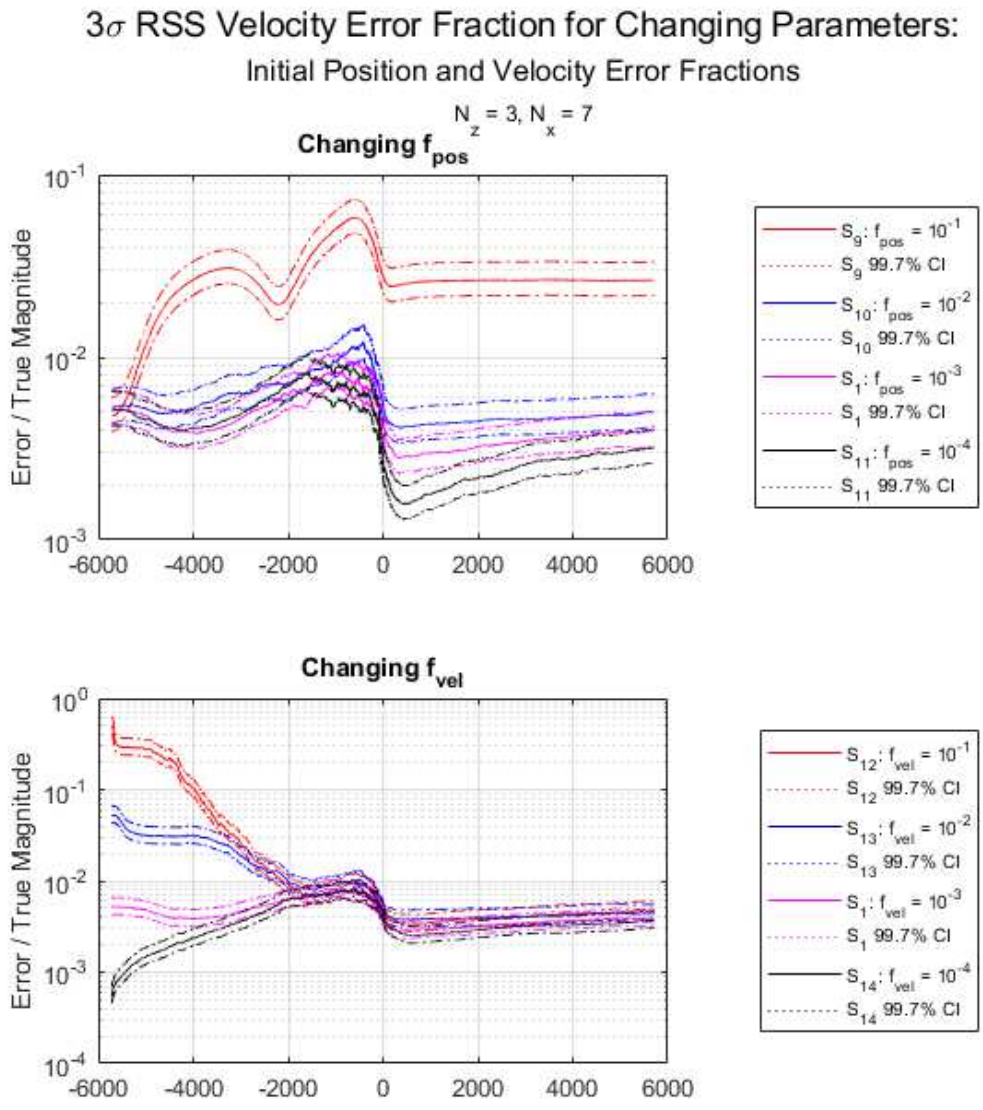

Fig. 4.21: Monte Carlo 3σ RSS velocity error fractions and 99.7% confidence intervals for scenarios with varying initial position and velocity error fractions

and the representation of the star gravity as constant both in the truth model and in the filter model, the gravity errors undergo what nearly amounts to a step change between the inbound and outbound legs of the flight, with nearly constant values before and after and a sharp decrease in the period of greatest curvature near periapse, when the measurements are most effective. (Again, compare the behavior of Scenario 4, with no measurements, to the behaviors of Scenarios 1-3, to see at what time the measurements become useful.) Scenarios 1 and 2 end with nearly identical gravity errors; those of Scenario 3 are somewhat larger; and those of Scenario 4 are unchanged from initial conditions. Changing the measurement noise has no effect on the gravity errors, and greater process noise produces distinctly greater gravity errors.

Changing Initial Position and Velocity Error Fractions

At first glance, the gravity error results in Figure 4.23 for differing initial velocity error fractions appear counterintuitive: the gravity errors for $fvel = 0.01$ appear distinctly larger than those for $f_{vel} = 0.1$. Upon closer inspection, the confidence intervals are seen to overlap such that the $f_{vel} = 0.1$ errors are within the confidence interval for $f_{vel} = 0.01$ and vice versa, so the errors for those two scenarios may be described as equal within the precision of the Monte Carlo ensemble. Likewise, the errors for $f_{vel} = 0.001$ and $f_{vel} = 0.0001$ are not significantly different from each other, though they are distinctly smaller than the errors for $f_{vel} = 0.1$ and $f_{vel} = 0.01$. Meanwhile, different settings for f_{pos} produce distinctly different gravity errors. This relative insensitivity of filter results to initial position error fraction was also seen in the position and velocity results.

4.3 Numerical Results For All Scenarios

Because this study has been conducted at a very high level, this chapter has focused on qualitative discussion of the results obtained rather than direct exposition of their numerical values, and a number of plots have been omitted for brevity. The interested reader will find tables of numerical results and confidence intervals for the average position error magnitudes, velocity error magnitudes, and gravity error magnitudes at periapse and the

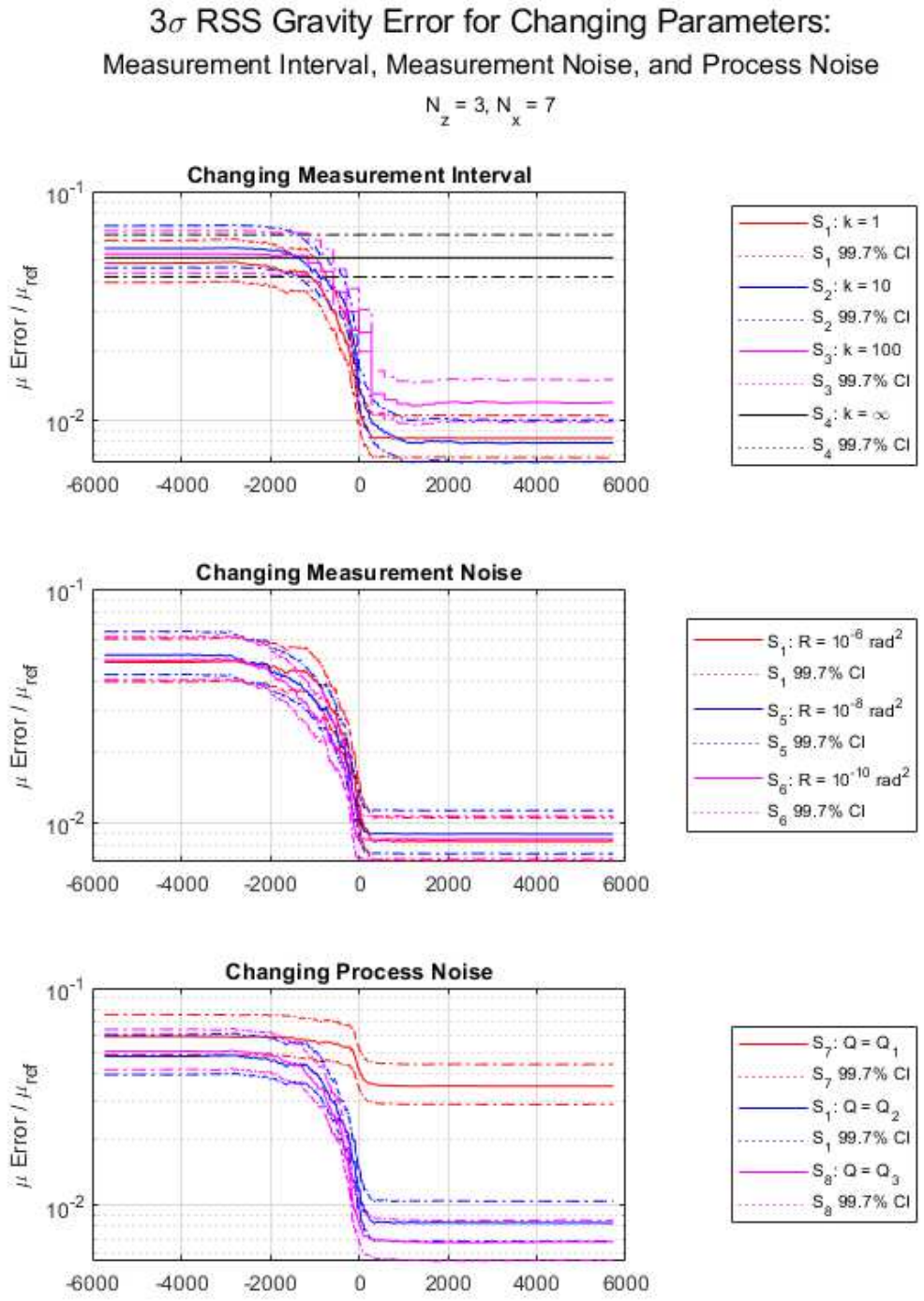

Fig. 4.22: Monte Carlo 3σ gravity errors and 99.7% confidence intervals for scenarios with varying measurement interval, measurement noise, and process noise

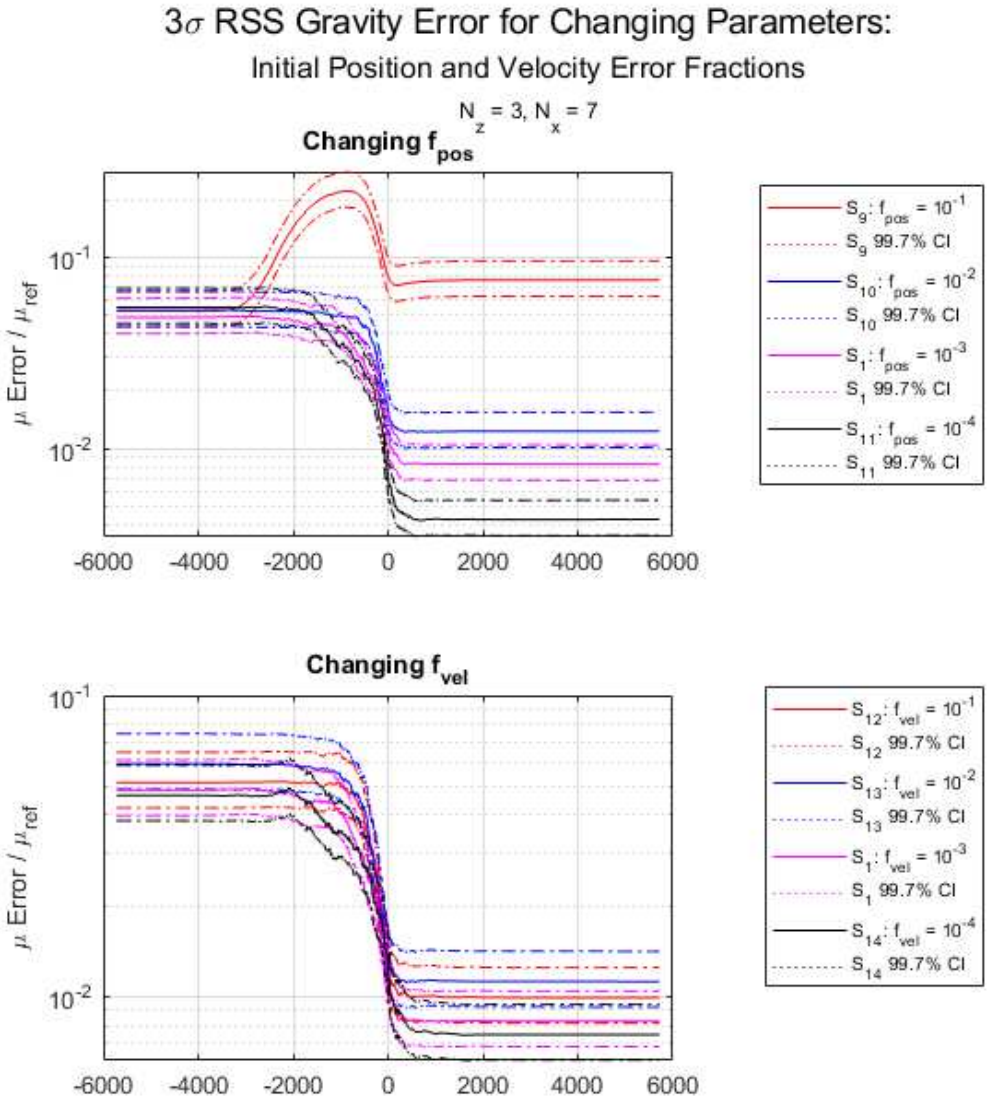

Fig. 4.23: Monte Carlo 3σ gravity errors and 99.7% confidence intervals for scenarios with varying initial position and velocity error fractions

end of the flyby for all scenarios and filters in Appendix A. The same data is then plotted in Figures A.1-A.5 for an alternative presentation of the overlapping confidence intervals. Plots that have been omitted from this chapter for brevity are found in Appendix B should any reader wish to examine them and draw alternative conclusions.

CHAPTER 5
CONCLUSIONS

Inspired by the Breakthrough Starshot concept for a miniature interstellar probe, this study has examined the use of angles-only measurements in an extended Kalman filter aboard such a probe for autonomous estimation of position, velocity, and the standard gravitational parameter of the target star. As far as the author knows, this is the first study to directly simulate navigation performance for the interstellar approach problem.

5.1 Filter Performance

A nominal trajectory was defined for a hyperbolic approach to Proxima Centauri with an excess velocity similar to that of the Voyager spacecraft, and a nominal set of input parameters was identified for which the state estimation error covariance predicted by the Kalman filter was consistent with the state estimation error covariance demonstrated through Monte Carlo simulation. This set of input parameters was known as the "nominal scenario," and the filter performance was repeatedly examined for scenarios that individually varied the measurement frequency, measurement error variance, process noise, initial position error, and initial velocity error. Measurement frequency varied between 2.85 and 285 days, measurement error variance between 10^{-6} and 10^{-10} rad^2, process noise between $1.0139 \cdot 10^{-1}$ km^2/s^3 and $1.0924 \cdot 10^{-5}$ km^2/s^3, initial 1σ position error between 10% and 0.01% referred to an initial range of 25 AU, and initial 1σ velocity error between 10% and 0.01% referred to an initial speed at 25 AU corresponding to a hyperbolic excess velocity of $2 \cdot 10^{-5} c$. The only setting found to cause the filter to fail (provide inconsistent estimates of position, velocity, and star mass) was that of 10% initial position uncertainty.

Among the scenarios which exhibited consistent filter performance, those with larger measurement intervals, measurement noise, process noise, initial position error, and initial velocity error generally displayed larger state estimation errors than those with smaller

settings for those values, as was expected. In all cases, the star gravity estimation error assumed a nearly constant value for almost all of the inbound leg of the flight, decreased rapidly shortly before and after periapse, and maintained a nearly constant value for the remainder of the outbound leg. The inclusion or exclusion of the star angular diameter from the measurement set made virtually no difference to the performance of the filter in any case, because the angular diameter of the star was small in comparison to the measurement noise. The inclusion of the star gravity in the filter state always increased the position and velocity estimation errors by a small amount relative to filters using mass values exactly equal to those used in the truth dynamics. Regardless of the initial position and velocity error settings, all filters eventually converged to very similar RSS position, velocity, and gravity errors shortly before periapse. Errors after periapse were more varied. Measurement interval, measurement noise, and process noise all significantly affected filter performance; the RSS position, velocity, and gravity errors were not seen to converge before periapse for different values of these settings, unlike for different values of initial position and velocity error.

Altogether, these results demonstrate that onboard position and velocity estimation is possible with angles-only measurements for a slow interstellar probe on hyperbolic approach to its target star, but more detailed or more accurate results may require other measurement types or other methods of estimation, some of which will be suggested in the following section.

5.2 Future Work

As this has been the simplest possible study of interstellar approach navigation, there are any number of ways to improve and extend the work. Some possible future directions are briefly listed as follows:

- Dynamics models

  The position and velocity of the probe in the truth model and filter model could be made more realistic by including the effects of stellar radiation pressure, gravita-

tional perturbations from multiple bodies (possibly including a variety of probabilistic models for the planetary population of the target system), drag and torques from interstellar dust and the interstellar magnetic field, and special and general relativity. More detailed models of the probe would require attitude knowledge, and therefore attitude dynamics. Translational and rotational controls, such as thrusters or momentum wheels, could also be considered.

- Measurement models

  Improvements to the measurement set could include line-of-sight measurements to the target star or nearby planets, stellar irradiance sensors, a variety of planet observations, and pulsar observations. The angles-only measurement model could be made more detailed by considering limiting magnitudes of visible objects, exclusion cones near bright objects, field of view limitations, a limiting camera slew rate, or image processing algorithms. Observability might also be improved by a study of optimal measurement choice and scheduling, in order to pick the stars, planets, or pulsars that would provide the most information as targets of observation. Finally, stellar aberration and relativistic measurement effects should be accounted for in studies of high-speed interstellar navigation.

- Initial conditions

  This study considered the interstellar approach problem at ranges and speeds commensurate with present-day technology, but future studies should obviously begin the approach navigation at larger ranges from the target star and at higher speeds. Also, it would be desirable to derive an initial covariance for the probe from engineering principles and mission design, rather than leaving it as an arbitrary input parameter.

- Filter formulations

Because the parameter values used in a navigation filter will never exactly match the actual values of the quantities they represent in nature, all filters applied to real-world problems suffer from some amount of mismatch with the "truth." It would be useful to investigate the sensitivity of an EKF to various degrees of filter mismatch. It would also be useful to repeat this study with a number of more sophisticated filter formulations, including consider filters, factorized filters, Gaussian mixture filters, and information filters. Finally, it would be worthwhile to investigate methods of starting the filter at various points on the trajectory with no initial estimate.

- Observability

  Since the linear observability Gramian is the simplest extension of linear observability theory to nonlinear systems, it might be worthwhile to repeat the observability study with more sophisticated measures of observability for nonlinear systems.

- State vectors

  More complex filter and measurement models require more parameters, which are then candidates for inclusion in the filter state. These include biases, misalignments, correlation times, and scale factors for measurement models, as well as parameters used in measurements such as the star diameter, star luminosity, and so forth. The positions, velocities, masses, and diameters of any planets orbiting the target star are also attractive candidates for estimation. In a mission with multiple spacecraft, the position and velocity of each must be estimated.

- Spacecraft and mission definitions

  Finally, the general field of navigation performance studies for interstellar missions could be expanded by applying estimation theory to missions with varying destinations, speeds, objectives, sizes, trajectories, means of propulsion, and so forth.

The interested researcher will find any one of the directions listed above a fruitful avenue for years of contributions to interstellar studies and the wider field of space navigation theory.

Bibliography

[1] Jackson, A., "Dispersion analysis of small-scale-spacecraft interstellar trajectories," 2017.

[2] Gilster, P., *Centauri dreams: imagining and planning interstellar exploration*, Springer Science & Business Media, 2004.

[3] Richards, G., "Planetary detection from an interstellar probe." *Journal of the British Interplanetary Society*, Vol. 28, 1975, pp. 579–585.

[4] Richards, G., "Project Daedalus-The navigation problem," *Journal of the British Interplanetary Society*, Vol. 28, 1975, pp. 150–160.

[5] Wang, B., "Ghost ship nuclear fusion spaceship concept design," April 2014.

[6] Freeland, R. and Lamontagne, M., "Firefly Icarus: an unmanned interstellar probe using z-pinch fusion propulsion," *JBIS*, Vol. 68, 2015, pp. 68–80.

[7] Smith, R., Sheikh, S., and Swinney, R., "Navigation to the Alpha Centauri star system," *JBIS*, Vol. 69, 2016, pp. 379–389.

[8] Smith, R. and Swinney, R., "Granularity and ambiguity in navigating the void," *JBIS*, Vol. 69, 2016, pp. 390–401.

[9] Lubin, P., "A roadmap to interstellar flight," *arXiv preprint arXiv:1604.01356*, 2016.

[10] Daukantas, P., "Breakthrough Starshot," *Optics and Photonics News*, Vol. 28, No. 5, 2017, pp. 26–33.

[11] Brashears, T., Lubin, P., Hughes, G. B., McDonough, K., Arias, S., Lang, A., Motta, C., Meinhold, P., Batliner, P., Griswold, J., et al., "Directed energy interstellar propulsion of wafersats," *Nanophotonics and Macrophotonics for Space Environments IX*, Vol. 9616, International Society for Optics and Photonics, 2015, p. 961609.

[12] Häfner, T., Kushwaha, M., Celik, O., and Bellizzi, F., "Project Dragonfly: Sail to the stars," *Acta Astronautica*, 2018.

[13] Hein, A. M., Long, K. F., Fries, D., Perakis, N., Genovese, A., Zeidler, S., Langer, M., Osborne, R., Swinney, R., Davies, J., et al., "The Andromeda Study: A Femto-Spacecraft Mission to Alpha Centauri," *arXiv preprint arXiv:1708.03556*, 2017.

[14] Parkin, K. L., "The Breakthrough Starshot System Model," *arXiv preprint arXiv:1805.01306*, 2018.

[15] Anglada-Escudé, G., Amado, P. J., Barnes, J., Berdinas, Z. M., Butler, R. P., Coleman, G. A., de La Cueva, I., Dreizler, S., Endl, M., Giesers, B., et al., "A terrestrial planet candidate in a temperate orbit around Proxima Centauri," *Nature*, Vol. 536, No. 7617, 2016, pp. 437–440.

[16] Tapley, B. D., Schutz, B. E., and Born, G. H., *Statistical Orbit Determination*, Elsevier, 2004.

[17] Yan, H.-t., Dai, Z., Hu, Y.-p., and Chen, L., "Optical measurement aided autonomous navigation for pinpoint Mars landing," *Optik-International Journal for Light and Electron Optics*, Vol. 157, 2018, pp. 976–987.

[18] Enright, J., Jovanovic, I., Kazemi, L., Zhang, H., and Dzamba, T., "Autonomous optical navigation using nanosatellite-class instruments: a Mars approach case study," *Celestial Mechanics and Dynamical Astronomy*, Vol. 130, No. 2, 2018, pp. 13.

[19] Owen Jr, W. M., Dumont, P. J., and Jackman, C. D., "Optical navigation preparations for New Horizons Pluto flyby," 2012.

[20] Miller, J. K., Carranza, E., Stanbridge, D., and Williams, B. G., "New Horizons Navigation to Pluto," *AAS Guidance and Control Conference*, 2008.

[21] Kubitschek, D. G., Mastrodemos, N., Werner, R. A., Kennedy, B. M., Synnott, S. P., Null, G. W., Bhaskaran, S., Riedel, J. E., and Vaughan, A. T., "Deep Impact Autonomous Navigation: the trials of targeting the unknown," 2006.

[22] Bhaskaran, S., Nandi, S., Broschart, S., Wallace, M., Cangahuala, L. A., and Olson, C., "Small body landings using autonomous onboard optical navigation," *The Journal of the Astronautical Sciences*, Vol. 58, No. 3, 2011, pp. 409–427.

[23] Maybeck, P. S., *Stochastic models, estimation, and control*, Vol. 1, Academic press, 1979.

[24] Crassidis, J. L. and Junkins, J. L., *Optimal estimation of dynamic systems*, Chapman and Hall/CRC, 2004.

[25] Bar-Shalom, Y., Li, X. R., and Kirubarajan, T., *Estimation with applications to tracking and navigation: theory algorithms and software*, John Wiley & Sons, 2004.

[26] Battin, R. H., *An Introduction to the Mathematics and Methods of Astrodynamics, revised edition*, American Institute of Aeronautics and Astronautics, 1999.

[27] Vallado, D. A., *Fundamentals of Astrodynamics and Applications*, Microcosm Press, 4th ed., 2013.

[28] Psiaki, M. L., "Absolute orbit and gravity determination using relative position measurements between two satellites," *Journal of Guidance, Control, and Dynamics*, Vol. 34, No. 5, 2011, pp. 1285–1297.

[29] Fujimoto, K., Stacey, N., and Turner, J. M., "Stereoscopic Image Velocimetry as a Measurement Type For Autonomous Asteroid Gravimetry," *AIAA/AAS Astrodynamics Specialist Conference*, 2016, p. 5566.

[30] Smith, D. E., Zuber, M. T., Mazarico, E., Genova, A., Neumann, G. A., Sun, X., Torrence, M. H., and Mao, D.-d., "Trilogy, a planetary geodesy mission concept for measuring the expansion of the solar system," *Planetary and space science*, Vol. 153, 2018, pp. 127–133.

[31] Grosch, C. B. and Paetznick, H. R., "Method of deriving orbital perturbing parameters from onboard optical measurements of an ejected probe or a natural satellite," *NASA Contractor Report*, Aug. 1969.

[32] Christian, P. and Loeb, A., "Interferometric Measurement of Acceleration at Relativistic Speeds," *The Astrophysical Journal Letters*, Vol. 834, No. 2, 2017, pp. L20.

[33] Moon, T. K. and Stirling, W. C., *Mathematical methods and algorithms for signal processing*, Vol. 1, Prentice hall Upper Saddle River, NJ, 2000.

[34] Quarta, A. A. and Mengali, G., "Electric sail mission analysis for outer solar system exploration," *Journal of guidance, control, and dynamics*, Vol. 33, No. 3, 2010, pp. 740–755.

[35] Stastny, N. B., *Autonomous optical navigation at Jupiter: a linear covariance analysis*, Master's thesis, Utah State University, 2006.

[36] Curtis, H. D., *Orbital Mechanics for Engineering Students*, Butterworth-Heinemann, 3rd ed., 2014.

[37] Montenbruck, O. and Gill, E., *Satellite Orbits: Models, Methods, and Applications*, Springer, 2005.

[38] Zarchan, P. and Musoff, H., *Fundamentals of Kalman Filtering: A Practical Approach*, American Institute of Aeronautics and Astronautics, 2nd ed., 2005.

[39] Zanetti, R., DeMars, K. J., and Bishop, R. H., "Underweighting nonlinear measurements," *Journal of guidance, control, and dynamics*, Vol. 33, No. 5, 2010, pp. 1670–1675.

APPENDICES

APPENDIX A

NUMERICAL RESULTS

Because this study is conducted at a very high level and with a very simplified setup, the numerical values of the results are of little use in an absolute sense, but they do provide valuable insight into the problem and allow important trends to be uncovered. In case the reader wishes to examine the results beyond the discussions in Chapter 4 and Chapter 5, the numerical results of all scenarios are provided in this appendix in Tables A.1-A.9. The RSS position, velocity, and gravity errors at periapse and the end of the flyby are presented here for all scenarios and all filters for the interested reader. The same data is then plotted in Figures A.1-A.5 as an alternative presentation.

Table A.1: Monte Carlo 3σ RSS position errors and 99.7% confidence intervals at periapse and end of flyby, Scenarios 1-5

Scenario 1		$3\sigma_r$, AU, periapse			$3\sigma_r$, AU, end		
N_z	N_x	CI-	3σ	CI+	CI-	3σ	CI+
3	6	0.00123	0.001494	0.001882	0.03056	0.03711	0.04674
3	7	0.002671	0.003243	0.004086	0.06222	0.07556	0.09519
4	6	0.001463	0.001777	0.002238	0.03012	0.03658	0.04608
4	7	0.002633	0.003198	0.004028	0.06005	0.07292	0.09186
Scenario 2		$3\sigma_r$, AU, periapse			$3\sigma_r$, AU, end		
N_z	N_x	CI-	3σ	CI+	CI-	3σ	CI+
3	6	0.003312	0.004022	0.005066	0.03194	0.03879	0.04886
3	7	0.003821	0.00464	0.005846	0.05683	0.06901	0.08693
4	6	0.003252	0.003949	0.004974	0.03374	0.04097	0.05161
4	7	0.004298	0.005269	0.006574	0.06328	0.07684	0.0968
Scenario 3		$3\sigma_r$, AU, periapse			$3\sigma_r$, AU, end		
N_z	N_x	CI-	3σ	CI+	CI-	3σ	CI+
3	6	0.03593	0.04363	0.05496	0.04426	0.05374	0.0677
3	7	0.0524	0.06363	0.08016	0.09324	0.1132	0.1426
4	6	0.03663	0.04448	0.05604	0.04355	0.05288	0.06662
4	7	0.04359	0.05293	0.6668	0.0805	0.9775	0.1231
Scenario 4		$3\sigma_r$, AU, periapse			$3\sigma_r$, AU, end		
N_z	N_x	CI-	3σ	CI+	CI-	3σ	CI+
3	6	0.2346	0.2849	0.3588	1.463	1.777	2.239
3	7	0.3709	0.4504	0.5674	1.989	2.416	3.043
4	6	0.2092	0.254	0.32	1.445	1.755	2.211
4	7	0.3667	0.4453	0.561	1.918	2.33	2.935
Scenario 5		$3\sigma_r$, AU, periapse			$3\sigma_r$, AU, end		
N_z	N_x	CI-	3σ	CI+	CI-	3σ	CI+
3	6	0.0004119	0.0005002	0.0006302	0.03075	0.03734	0.04704
3	7	0.002714	0.003296	0.004152	0.06501	0.07895	0.09946
4	6	0.0003597	0.0004368	0.0005502	0.03005	0.03649	0.04597
4	7	0.002476	0.003007	0.003788	0.06658	0.08086	0.1019

Table A.2: Monte Carlo 3σ RSS position errors and 99.7% confidence intervals at periapse and end of flyby, Scenarios 6-10

Scenario 6		$3\sigma_r$, AU, periapse			$3\sigma_r$, AU, end		
N_z	N_x	CI-	3σ	CI+	CI-	3σ	CI+
3	6	0.0001978	0.0002402	0.0003026	0.02813	0.03417	0.04304
3	7	0.002298	0.002791	0.003516	0.06329	0.07685	0.09681
4	6	0.000182	0.000221	0.0002784	0.02907	0.0353	0.04447
4	7	0.002335	0.002835	0.003572	0.069	0.0838	0.1056
Scenario 7		$3\sigma_r$, AU, periapse			$3\sigma_r$, AU, end		
N_z	N_x	CI-	3σ	CI+	CI-	3σ	CI+
3	6	0.003193	0.003878	0.004885	0.3162	0.384	0.4837
3	7	0.01033	0.01255	0.01581	0.4006	0.4865	0.6128
4	6	0.003292	0.003998	0.005036	0.3031	0.3681	0.4637
4	7	0.007626	0.009261	0.01167	0.3291	0.3997	0.5035
Scenario 8		$3\sigma_r$, AU, periapse			$3\sigma_r$, AU, end		
N_z	N_x	CI-	3σ	CI+	CI-	3σ	CI+
3	6	0.001038	0.00126	0.001587	0.004897	0.005947	0.007492
3	7	0.002062	0.002504	0.003154	0.04605	0.05593	0.07045
4	6	0.0009844	0.001195	0.001506	0.004571	0.005551	0.006993
4	7	0.001724	0.002094	0.002638	0.03767	0.04575	0.05763
Scenario 9		$3\sigma_r$, AU, periapse			$3\sigma_r$, AU, end		
N_z	N_x	CI-	3σ	CI+	CI-	3σ	CI+
3	6	0.007239	0.00879	0.01107	0.04913	0.05967	0.07516
3	7	0.02043	0.02481	0.03126	0.544	0.6606	0.8322
4	6	0.006187	0.007513	0.009464	0.04	0.04857	0.06119
4	7	0.02973	0.03611	0.04549	0.8707	1.057	1.332
Scenario 10		$3\sigma_r$, AU, periapse			$3\sigma_r$, AU, end		
N_z	N_x	CI-	3σ	CI+	CI-	3σ	CI+
3	6	0.00186	0.00144	0.001814	0.03094	0.03757	0.04733
3	7	0.003702	0.004496	0.005663	0.08825	0.1072	0.135
4	6	0.001385	0.001682	0.002119	0.02823	0.03428	0.04319
4	7	0.003386	0.004111	0.005179	0.07906	0.096	0.1209

Table A.3: Monte Carlo 3σ RSS position errors and 99.7% confidence intervals at periapse and end of flyby, Scenarios 11-14

Scenario 11		$3\sigma_r$, AU, periapse			$3\sigma_r$, AU, end		
N_z	N_x	CI-	3σ	CI+	CI-	3σ	CI+
3	6	0.001191	0.001447	0.001822	0.03328	0.04042	0.05091
3	7	0.001508	0.001831	0.002307	0.03817	0.04635	0.05839
4	6	0.001126	0.001367	0.001722	0.02987	0.03627	0.0457
4	7	0.001732	0.002103	0.00265	0.03674	0.04462	0.0562
Scenario 12		$3\sigma_r$, AU, periapse			$3\sigma_r$, AU, end		
N_z	N_x	CI-	3σ	CI+	CI-	3σ	CI+
3	6	0.001456	0.001769	0.002228	0.03044	0.03697	0.04657
3	7	0.003005	0.00365	0.004597	0.0765	0.0929	0.117
4	6	0.00153	0.001858	0.002341	0.02723	0.03306	0.04165
4	7	0.003076	0.003736	0.004706	0.06825	0.08288	0.1044
Scenario 13		$3\sigma_r$, AU, periapse			$3\sigma_r$, AU, end		
N_z	N_x	CI-	3σ	CI+	CI-	3σ	CI+
3	6	0.001644	0.001997	0.002515	0.02984	0.03624	0.04565
3	7	0.003273	0.003975	0.005007	0.07783	0.09452	0.1191
4	6	0.00139	0.001688	0.002126	0.03027	0.03676	0.04631
4	7	0.003193	0.003878	0.004885	0.08407	0.1021	0.1286
Scenario 14		$3\sigma_r$, AU, periapse			$3\sigma_r$, AU, end		
N_z	N_x	CI-	3σ	CI+	CI-	3σ	CI+
3	6	0.001219	0.00148	0.001865	0.02953	0.003585	0.04517
3	7	0.002625	0.003188	0.004016	0.05462	0.06633	0.08355
4	6	0.001376	0.001671	0.002105	0.03319	0.0403	0.05077
4	7	0.002306	0.0028	0.003527	0.05265	0.06394	0.08054

Table A.4: Monte Carlo 3σ velocity errors and 99.7% confidence intervals at periapse and end of flyby, Scenarios 1-5

Scenario 1		$3\sigma_v$, km/s, periapse			$3\sigma_v$, km/s, end		
N_z	N_x	CI-	3σ	CI+	CI-	3σ	CI+
3	6	0.01423	0.01728	0.02176	0.01715	0.02083	0.02624
3	7	0.05532	0.06717	0.08462	0.02182	0.0265	0.03339
4	6	0.01735	0.02107	0.02654	0.0162	0.01967	0.02478
4	7	0.05333	0.06476	0.08157	0.02188	0.02657	0.03347
Scenario 2		$3\sigma_v$, km/s, periapse			$3\sigma_v$, km/s, end		
N_z	N_x	CI-	3σ	CI+	CI-	3σ	CI+
3	6	0.03357	0.04076	0.05135	0.01762	0.0214	0.02696
3	7	0.08473	0.1029	0.1296	0.02231	0.02709	0.03412
4	6	0.0334	0.04056	0.05109	0.01834	0.02227	0.02806
4	7	0.1053	0.1279	0.1611	0.0236	0.02865	0.0361
Scenario 3		$3\sigma_v$, km/s, periapse			$3\sigma_v$, km/s, end		
N_z	N_x	CI-	3σ	CI+	CI-	3σ	CI+
3	6	0.288	0.3498	0.4406	0.0207	0.02514	0.03167
3	7	0.4997	0.6068	0.7643	0.03084	0.03745	0.04718
4	6	0.289	0.3509	0.4421	0.02068	0.02512	0.03164
4	7	0.4478	0.5438	0.685	0.0278	0.03375	0.04252
Scenario 4		$3\sigma_v$, km/s, periapse			$3\sigma_v$, km/s, end		
N_z	N_x	CI-	3σ	CI+	CI-	3σ	CI+
3	6	1.755	2.131	2.685	0.3707	0.4502	0.5671
3	7	2.811	3.414	4.301	0.5049	0.6132	0.7724
4	6	1.555	1.888	2.378	0.3659	0.4443	0.5597
4	7	2.741	3.328	4.192	0.4896	0.5946	0.749
Scenario 5		$3\sigma_v$, km/s, periapse			$3\sigma_v$, km/s, end		
N_z	N_x	CI-	3σ	CI+	CI-	3σ	CI+
3	6	0.006394	0.007765	0.009781	0.01532	0.01861	0.02344
3	7	0.04613	0.05602	0.07056	0.02048	0.02487	0.03132
4	6	0.005632	0.006839	0.008615	0.01562	0.01896	0.02389
4	7	0.0402	0.04882	0.06149	0.02105	0.02556	0.0322

Table A.5: Monte Carlo 3σ velocity errors and 99.7% confidence intervals at periapse and end of flyby, Scenarios 6-10

Scenario 6		$3\sigma_v$, km/s, periapse			$3\sigma_v$, km/s, end		
N_z	N_x	CI-	3σ	CI+	CI-	3σ	CI+
3	6	0.003774	0.004583	0.005773	0.01575	0.01913	0.0241
3	7	0.03679	0.04468	0.05628	0.02144	0.02603	0.03279
4	6	0.003668	0.004455	0.005612	0.01374	0.01669	0.02102
4	7	0.03715	0.04512	0.05683	0.0233	0.02829	0.03564
Scenario 7		$3\sigma_v$, km/s, periapse			$3\sigma_v$, km/s, end		
N_z	N_x	CI-	3σ	CI+	CI-	3σ	CI+
3	6	0.04979	0.06046	0.07617	0.1546	0.1878	0.2366
3	7	0.1762	0.214	0.2696	0.1636	0.1987	0.2503
4	6	0.05254	0.06381	0.08038	0.1616	0.1963	0.2472
4	7	0.1361	0.1652	0.2081	0.159	0.193	0.2432
Scenario 8		$3\sigma_v$, km/s, periapse			$3\sigma_v$, km/s, end		
N_z	N_x	CI-	3σ	CI+	CI-	3σ	CI+
3	6	0.01089	0.01322	0.01665	0.002345	0.002848	0.003588
3	7	0.04057	0.04927	0.06206	0.01233	0.01498	0.01887
4	6	0.01056	0.01282	0.01615	0.002385	0.002896	0.003648
4	7	0.03372	0.04095	0.05159	0.01015	0.01233	0.01553
Scenario 9		$3\sigma_v$, km/s, periapse			$3\sigma_v$, km/s, end		
N_z	N_x	CI-	3σ	CI+	CI-	3σ	CI+
3	6	0.08787	0.1067	0.1344	0.02252	0.02735	0.03445
3	7	0.3651	0.4433	0.5584	0.1453	0.1764	0.2222
4	6	0.07582	0.09207	0.116	0.02056	0.02497	0.03146
4	7	0.5341	0.6485	0.817	0.2322	0.282	0.3553
Scenario 10		$3\sigma_v$, km/s, periapse			$3\sigma_v$, km/s, end		
N_z	N_x	CI-	3σ	CI+	CI-	3σ	CI+
3	6	0.01378	0.01674	0.02108	0.01702	0.02067	0.02603
3	7	0.04382	0.08965	0.1129	0.02756	0.03346	0.04215
4	6	0.0167	0.02029	0.02555	0.01553	0.01886	0.02375
4	7	0.06371	0.07736	0.09746	0.02593	0.03149	0.03967

Table A.6: Monte Carlo 3σ velocity errors and 99.7% confidence intervals at periapse and end of flyby, Scenarios 11-14

Scenario 11		$3\sigma_v$, km/s, periapse			$3\sigma_v$, km/s, end		
N_z	N_x	CI-	3σ	CI+	CI-	3σ	CI+
3	6	0.01394	0.01693	0.02133	0.01788	0.02171	0.02734
3	7	0.03483	0.0423	0.05328	0.01756	0.02133	0.02686
4	6	0.01309	0.01589	0.02002	0.01631	0.01981	0.02495
4	7	0.04466	0.05424	0.06832	0.0163	0.0198	0.02494
Scenario 12		$3\sigma_v$, km/s, periapse			$3\sigma_v$, km/s, end		
N_z	N_x	CI-	3σ	CI+	CI-	3σ	CI+
3	6	0.01728	0.02099	0.02644	0.01662	0.02019	0.02543
3	7	0.06053	0.0735	0.09259	0.02632	0.03197	0.04027
4	6	0.01827	0.02218	0.02794	0.01517	0.01842	0.0232
4	7	0.0606	0.07359	0.09271	0.02263	0.02748	0.03462
Scenario 13		$3\sigma_v$, km/s, periapse			$3\sigma_v$, km/s, end		
N_z	N_x	CI-	3σ	CI+	CI-	3σ	CI+
3	6	0.01955	0.02374	0.02991	0.01066	0.02016	0.0254
3	7	0.064	0.07772	0.0979	0.02421	0.0294	0.03704
4	6	0.01658	0.02014	0.02537	0.01639	0.01991	0.02508
4	7	0.05995	0.0728	0.09171	0.02674	0.03247	0.0409
Scenario 14		$3\sigma_v$, km/s, periapse			$3\sigma_v$, km/s, end		
N_z	N_x	CI-	3σ	CI+	CI-	3σ	CI+
3	6	0.01398	0.01698	0.02138	0.01596	0.01939	0.02442
3	7	0.05931	0.07203	0.09073	0.02027	0.02462	0.03102
4	6	0.01608	0.01953	0.0246	0.0184	0.02235	0.02815
4	7	0.0507	0.06157	0.07756	0.01986	0.02411	0.03038

Table A.7: Monte Carlo 3σ gravity errors and 99.7% confidence intervals at periapse and end of flyby, Scenarios 1-5

Scenario 1		$3\sigma_\mu/\mu$, periapse			$3\sigma_\mu/\mu$, end		
N_z	N_x	CI-	3σ	CI+	CI-	3σ	CI+
3	7	0.009762	0.01185	0.01493	0.00681	0.00827	0.01042
4	7	0.009389	0.0114	0.01436	0.006796	0.008253	0.0104
Scenario 2		$3\sigma_\mu/\mu$, periapse			$3\sigma_\mu/\mu$, end		
N_z	N_x	CI-	3σ	CI+	CI-	3σ	CI+
3	7	0.01254	0.01522	0.01918	0.006509	0.007904	0.009957
4	7	0.01596	0.01938	0.02441	0.007058	0.008571	0.0108
Scenario 3		$3\sigma_\mu/\mu$, periapse			$3\sigma_\mu/\mu$, end		
N_z	N_x	CI-	3σ	CI+	CI-	3σ	CI+
3	7	0.02457	0.02984	0.03759	0.009783	0.01188	0.01496
4	7	0.02574	0.03126	0.03938	0.007877	0.009565	0.01205
Scenario 4		$3\sigma_\mu/\mu$, periapse			$3\sigma_\mu/\mu$, end		
N_z	N_x	CI-	3σ	CI+	CI-	3σ	CI+
3	7	0.0422	0.05124	0.06455	0.0422	0.05124	0.06455
4	7	0.04264	0.05178	0.06523	0.0422	0.05178	0.06523
Scenario 5		$3\sigma_\mu/\mu$, periapse			$3\sigma_\mu/\mu$, end		
N_z	N_x	CI-	3σ	CI+	CI-	3σ	CI+
3	7	0.008658	0.01076	0.01355	0.007331	0.008902	0.01121
4	7	0.007634	0.00927	0.01168	0.007557	0.009177	0.01156

Table A.8: Monte Carlo 3σ gravity errors and 99.7% confidence intervals at periapse and end of flyby, Scenarios 6-10

Scenario 6		$3\sigma_\mu/\mu$, periapse			$3\sigma_\mu/\mu$, end		
N_z	N_x	CI-	3σ	CI+	CI-	3σ	CI+
3	7	0.007007	0.008509	0.01072	0.006963	0.008455	0.01065
4	7	0.007086	0.008605	0.01084	0.006948	0.008438	0.01063
Scenario 7		$3\sigma_\mu/\mu$, periapse			$3\sigma_\mu/\mu$, end		
N_z	N_x	CI-	3σ	CI+	CI-	3σ	CI+
3	7	0.03487	0.04235	0.05335	0.02911	0.03536	0.04454
4	7	0.02574	0.03125	0.03937	0.02183	0.02651	0.0334
Scenario 8		$3\sigma_\mu/\mu$, periapse			$3\sigma_\mu/\mu$, end		
N_z	N_x	CI-	3σ	CI+	CI-	3σ	CI+
3	7	0.006903	0.008383	0.01056	0.005573	0.006768	0.008526
4	7	0.005513	0.006695	0.008433	0.004578	0.00556	0.007004
Scenario 9		$3\sigma_\mu/\mu$, periapse			$3\sigma_\mu/\mu$, end		
N_z	N_x	CI-	3σ	CI+	CI-	3σ	CI+
3	7	0.06575	0.07984	0.1006	0.06252	0.07593	0.09565
4	7	0.09445	0.1147	0.1445	0.0976	0.1185	0.1493
Scenario 10		$3\sigma_\mu/\mu$, periapse			$3\sigma_\mu/\mu$, end		
N_z	N_x	CI-	3σ	CI+	CI-	3σ	CI+
3	7	0.01324	0.01607	0.02025	0.01011	0.01227	0.01546
4	7	0.01155	0.01402	0.01766	0.009428	0.01145	0.01442

Table A.9: Monte Carlo 3σ gravity errors and 99.7% confidence intervals at periapse and end of flyby, Scenarios 11-14

Scenario 11		$3\sigma_\mu/\mu$, periapse			$3\sigma_\mu/\mu$, end		
N_z	N_x	CI-	3σ	CI+	CI-	3σ	CI+
3	7	0.005752	0.006985	0.008799	0.003501	0.004251	0.005355
4	7	0.007467	0.009068	0.01142	0.003557	0.004319	0.005441
Scenario 12		$3\sigma_\mu/\mu$, periapse			$3\sigma_\mu/\mu$, end		
N_z	N_x	CI-	3σ	CI+	CI-	3σ	CI+
3	7	0.01056	0.01282	0.01615	0.008156	0.009905	0.01248
4	7	0.01093	0.01328	0.01672	0.008169	0.009921	0.0125
Scenario 13		$3\sigma_\mu/\mu$, periapse			$3\sigma_\mu/\mu$, end		
N_z	N_x	CI-	3σ	CI+	CI-	3σ	CI+
3	7	0.01132	0.01375	0.01732	0.009233	0.01121	0.01412
4	7	0.01055	0.01281	0.01614	0.009263	0.01125	0.01417
Scenario 14		$3\sigma_\mu/\mu$, periapse			$3\sigma_\mu/\mu$, end		
N_z	N_x	CI-	3σ	CI+	CI-	3σ	CI+
3	7	0.01032	0.01253	0.01579	0.006153	0.007472	0.009413
4	7	0.00876	0.01064	0.0134	0.00583	0.00708	0.008918

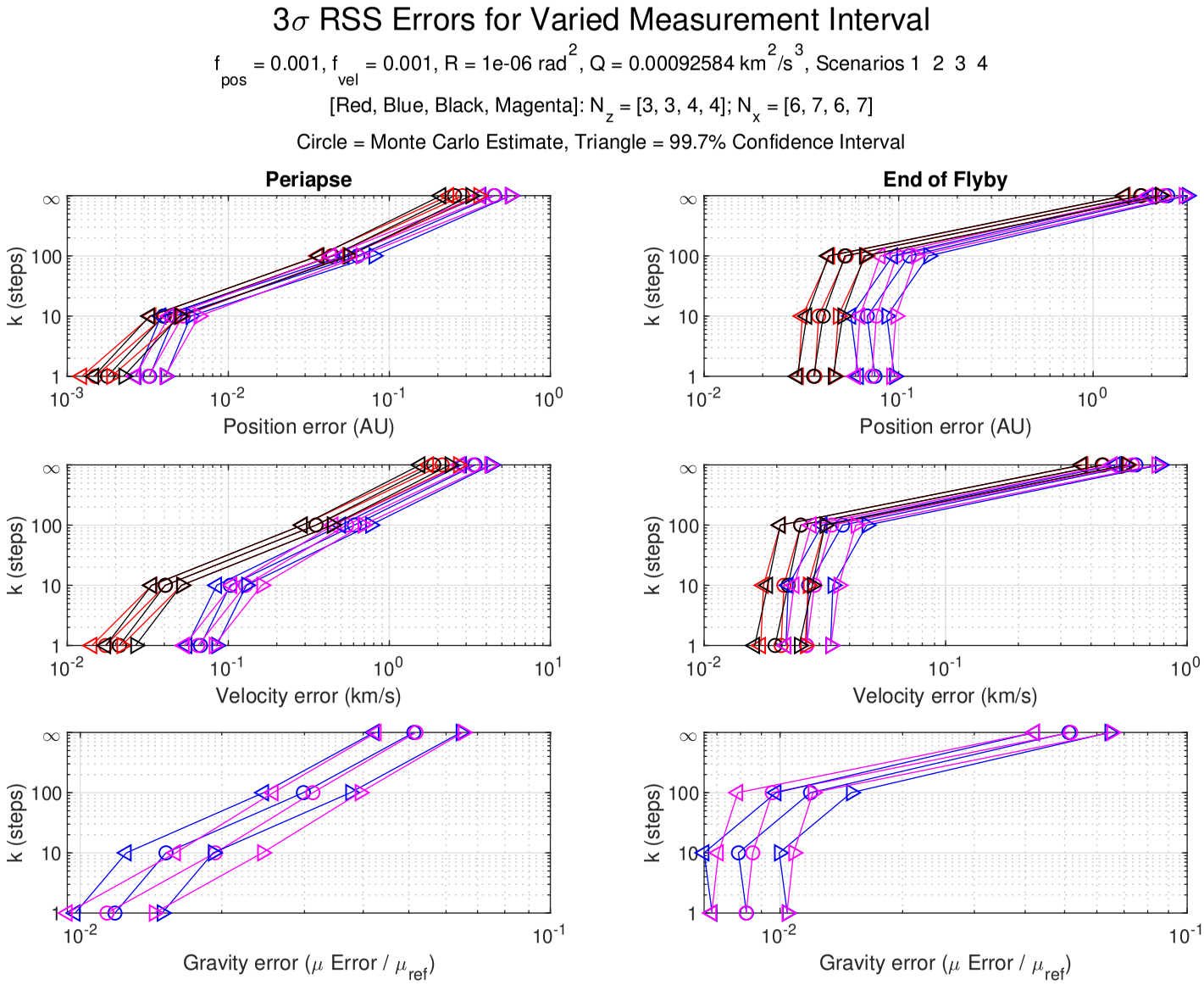

Fig. A.1: Monte Carlo 3σ RSS errors and 99.7% confidence intervals at periapse and end of flyby for varying measurement interval (Scenarios 1, 2, and 3)

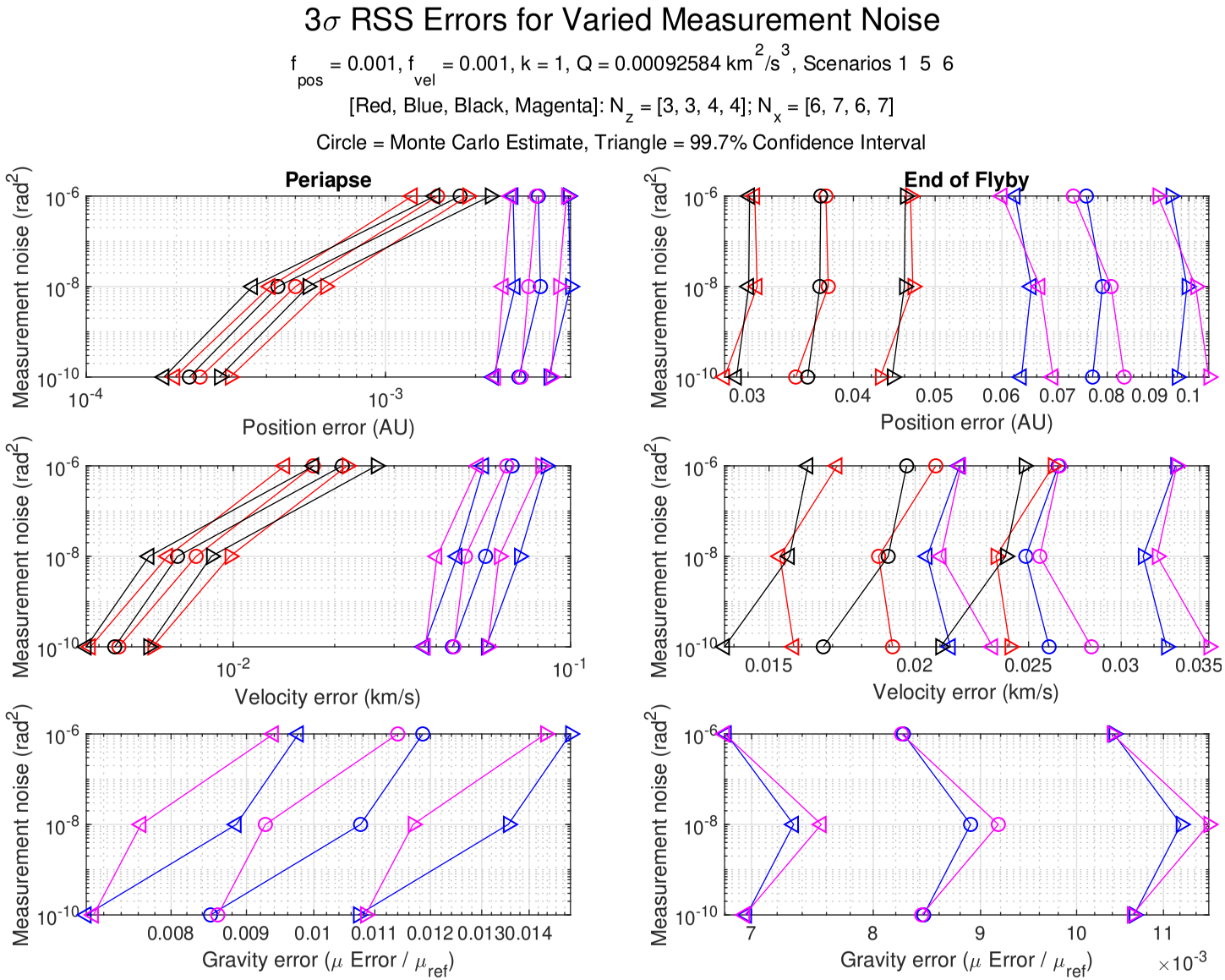

Fig. A.2: Monte Carlo 3σ RSS errors and 99.7% confidence intervals at periapse and end of flyby for varying measurement noise (Scenarios 1, 4, and 5)

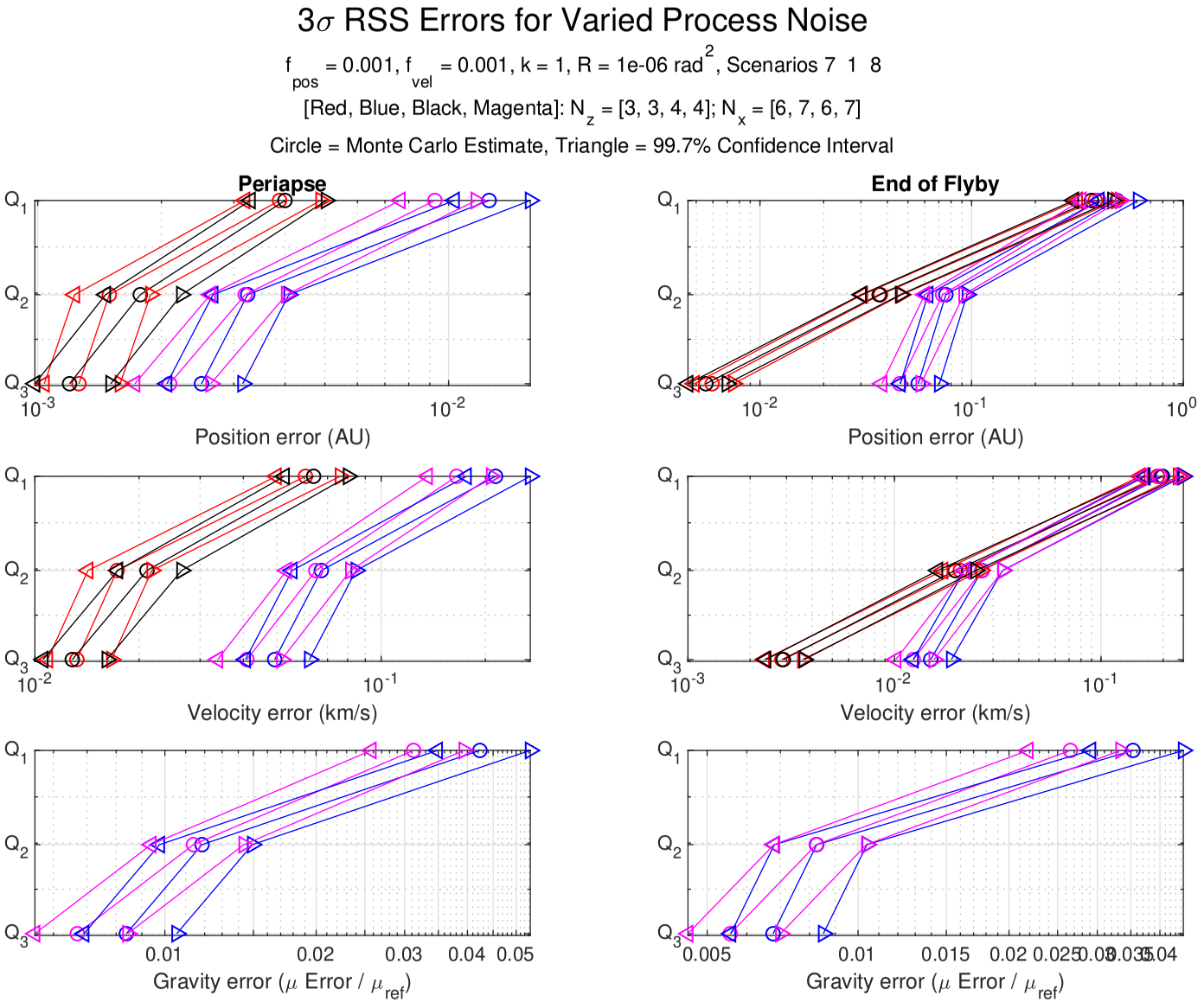

Fig. A.3: Monte Carlo 3σ RSS errors and 99.7% confidence intervals at periapse and end of flyby for varying process noise (Scenarios 6, 1, and 7)

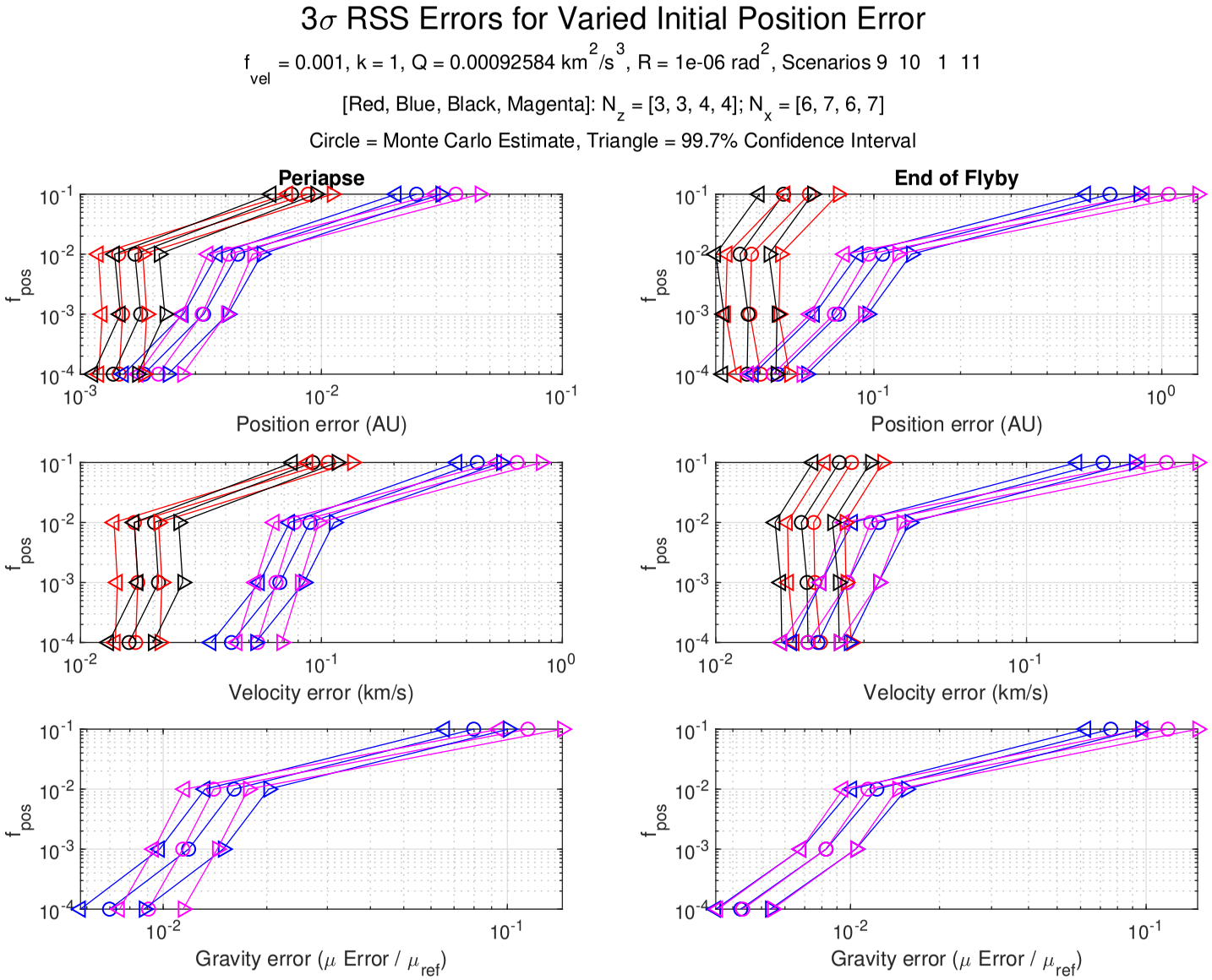

Fig. A.4: Monte Carlo 3σ RSS errors and 99.7% confidence intervals at periapse and end of flyby for varying initial position error fraction (Scenarios 8, 9, 1, and 10)

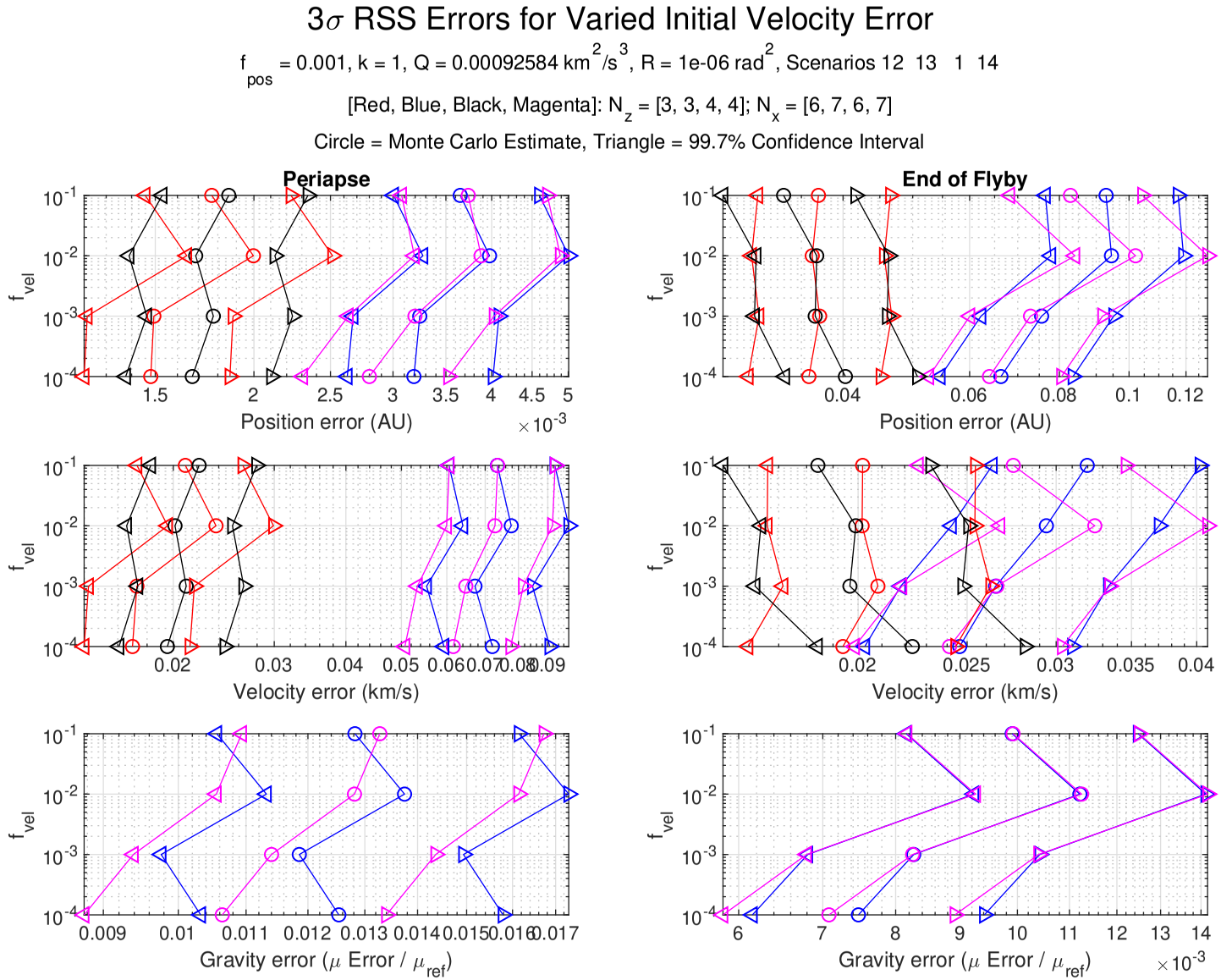

Fig. A.5: Monte Carlo 3σ RSS errors and 99.7% confidence intervals at periapse and end of flyby for varying initial velocity error fraction (Scenarios 11, 12, 1, and 13)

APPENDIX B

EXTRA PLOTS

The plots in this appendix were excluded from Chapter 4 because they do not change the results and conclusions presented therein, but the reader may yet find them interesting.

B.1 Relative Performance of Filter Types for All Scenarios

Although the six-state filter pairs have consistently lower errors than the seven-state filter pairs for all scenarios (and the six-state and seven-state filters are paired for all scenarios), the time evolution of the differences between the six-state filter errors and the seven-state filter errors differs from scenario to scenario. Therefore, Figure 4.12 for Scenario 1 is repeated in Figure B.1, and the same results are presented for Scenarios 2-14 in Figures B.2-B.14.

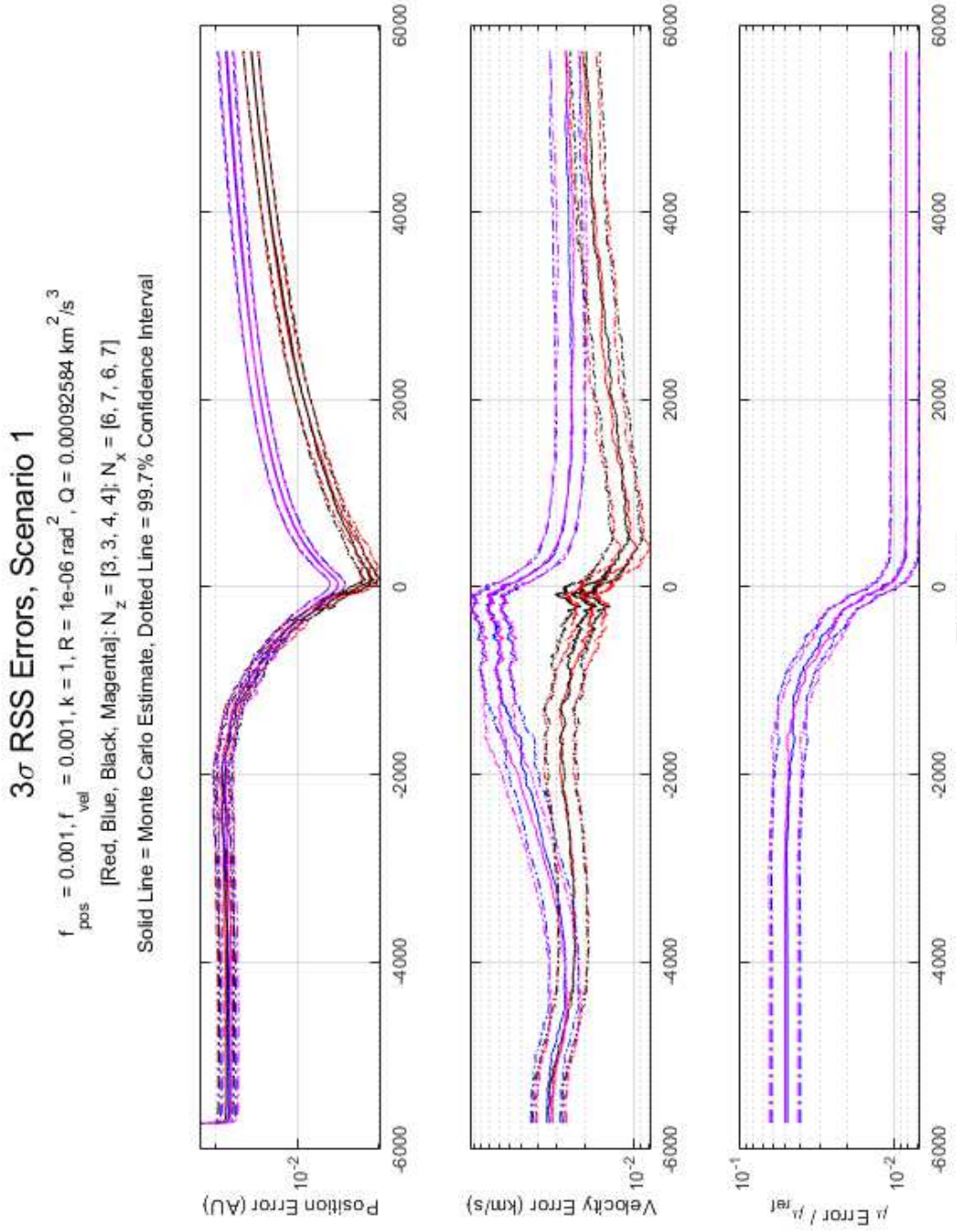

Fig. B.1: Monte Carlo 3σ RSS errors and 99.7% confidence intervals over time for Scenario 1

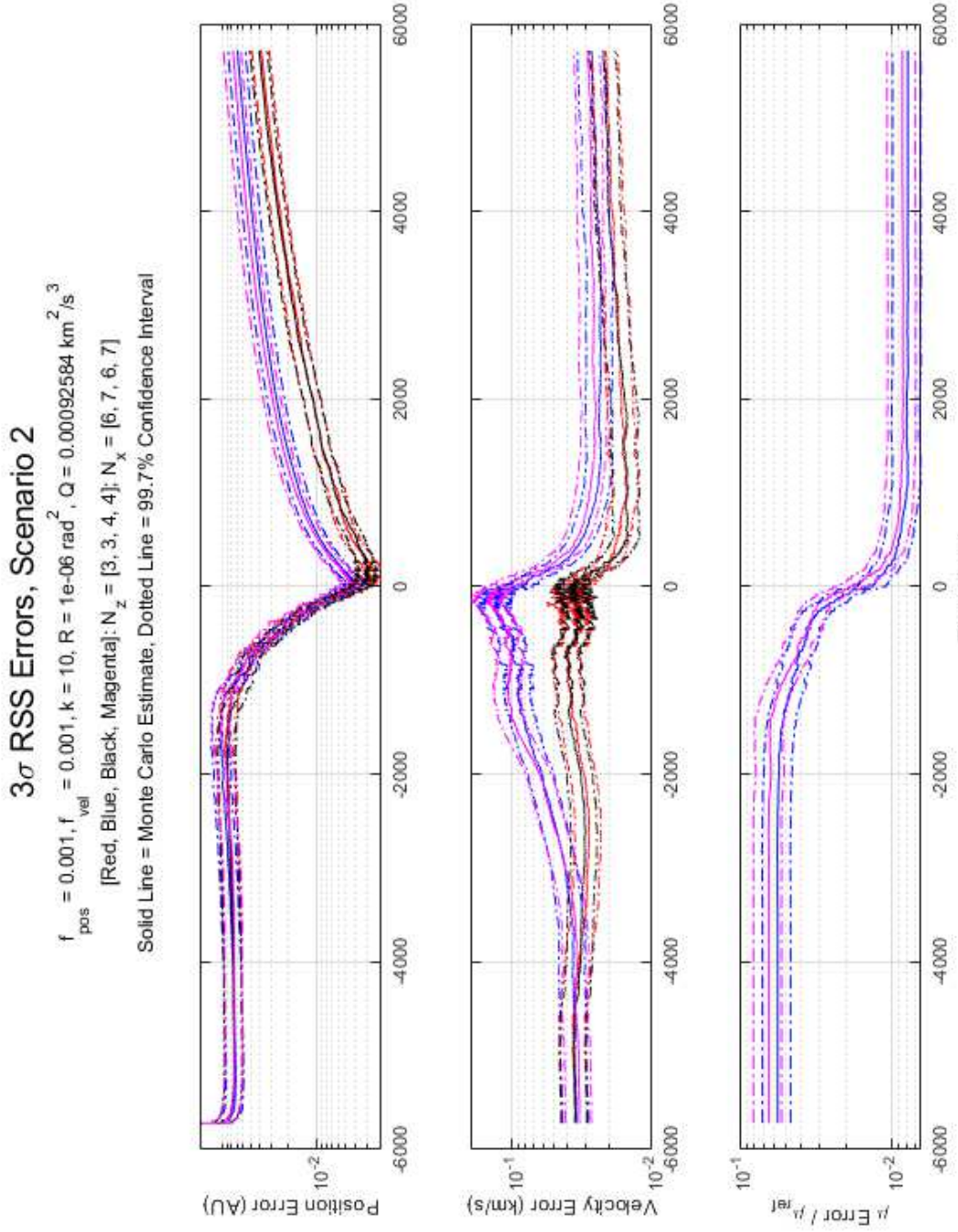

Fig. B.2: Monte Carlo 3σ RSS errors and 99.7% confidence intervals over time for Scenario 2

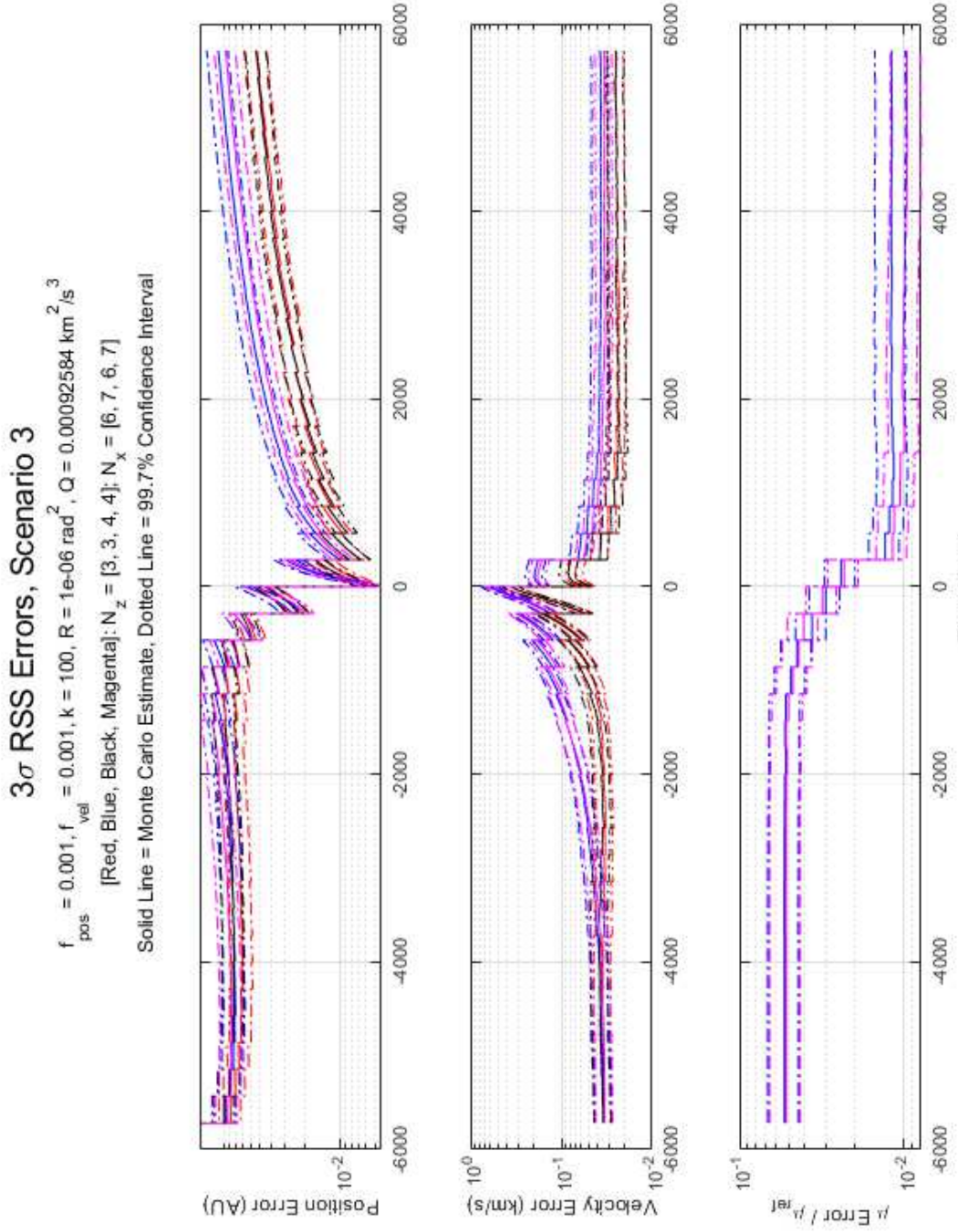

Fig. B.3: Monte Carlo 3σ RSS errors and 99.7% confidence intervals over time for Scenario 3

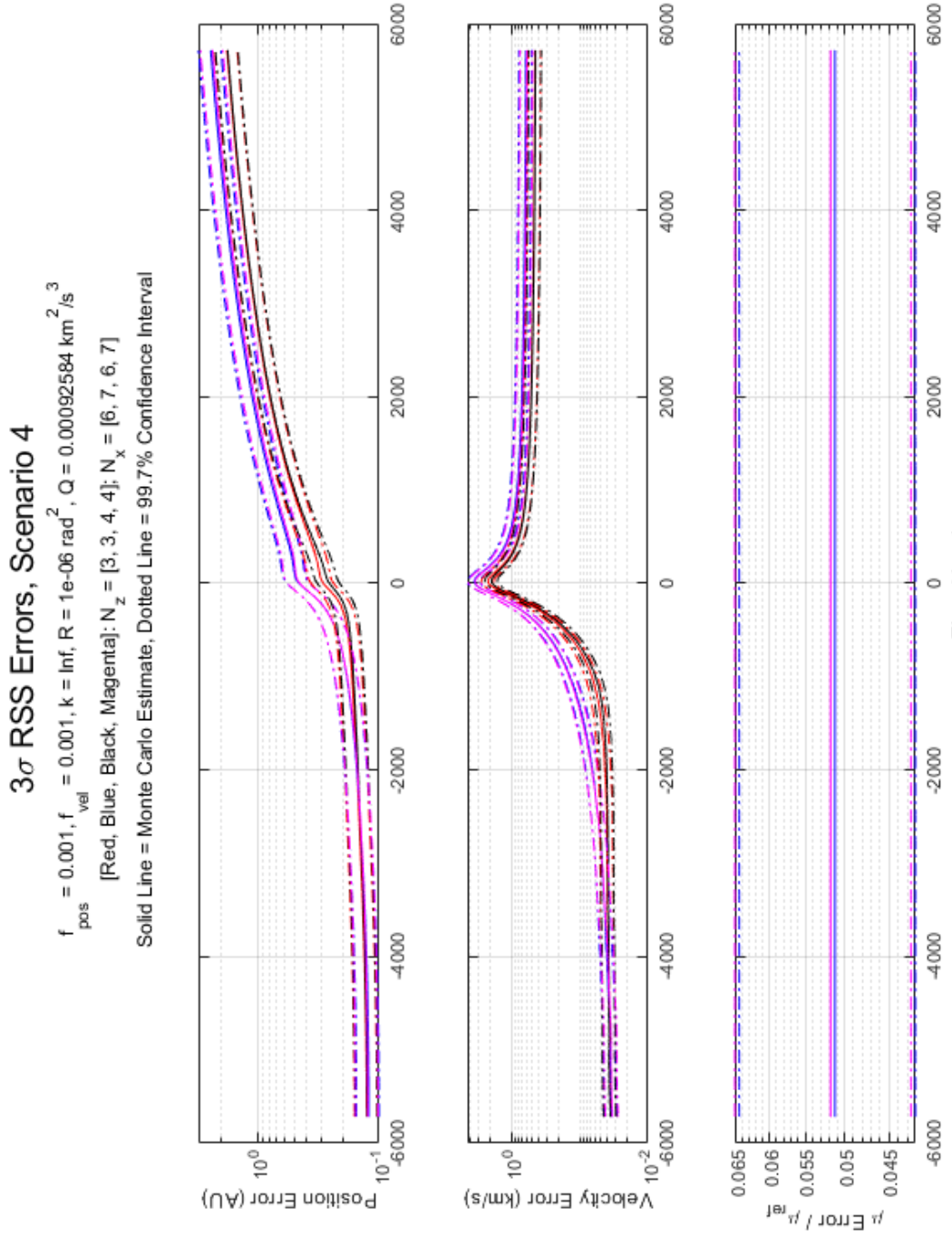

Fig. B.4: Monte Carlo 3σ RSS errors and 99.7% confidence intervals over time for Scenario 4

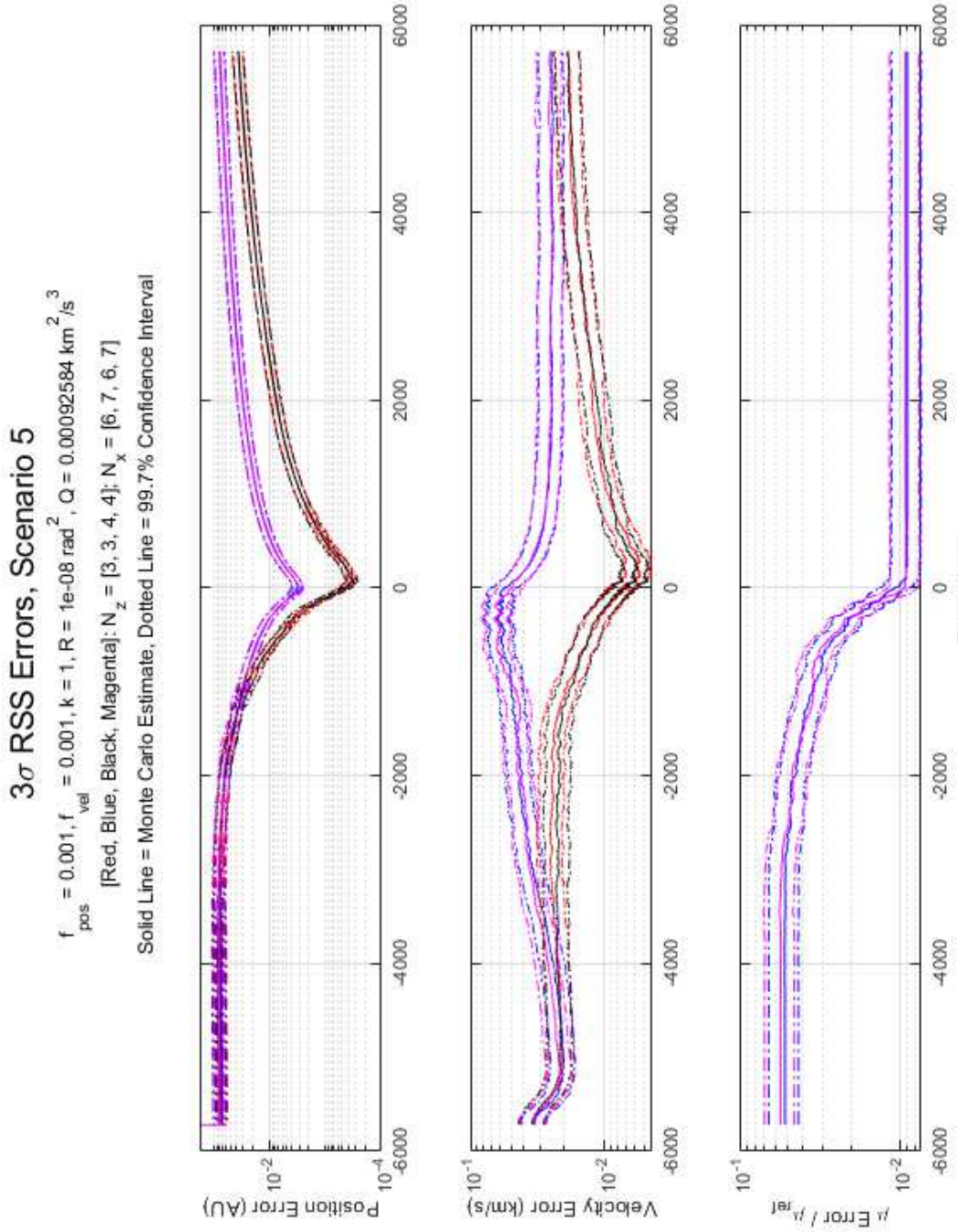

Fig. B.5: Monte Carlo 3σ RSS errors and 99.7% confidence intervals over time for Scenario 5

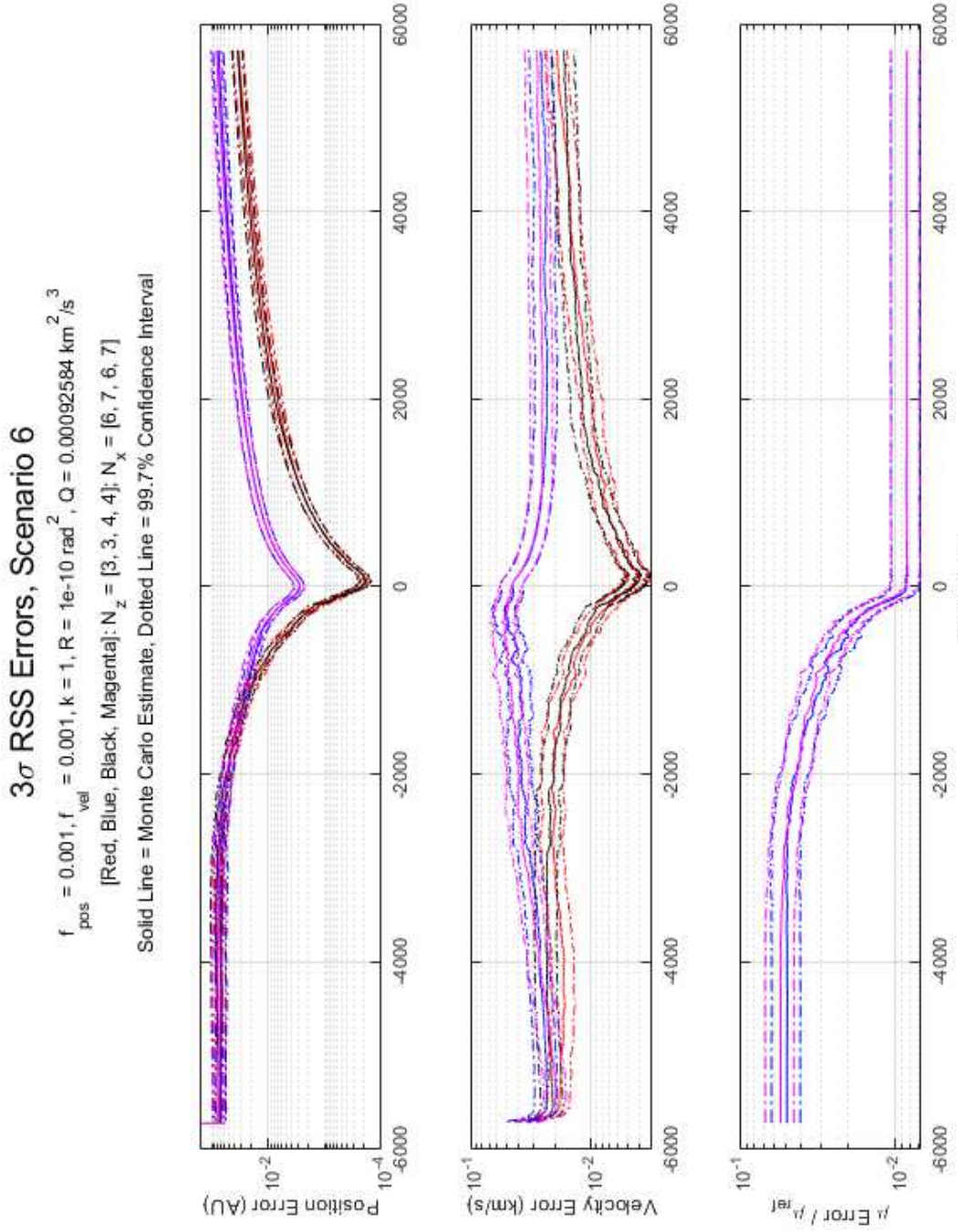

Fig. B.6: Monte Carlo 3σ RSS errors and 99.7% confidence intervals over time for Scenario 6

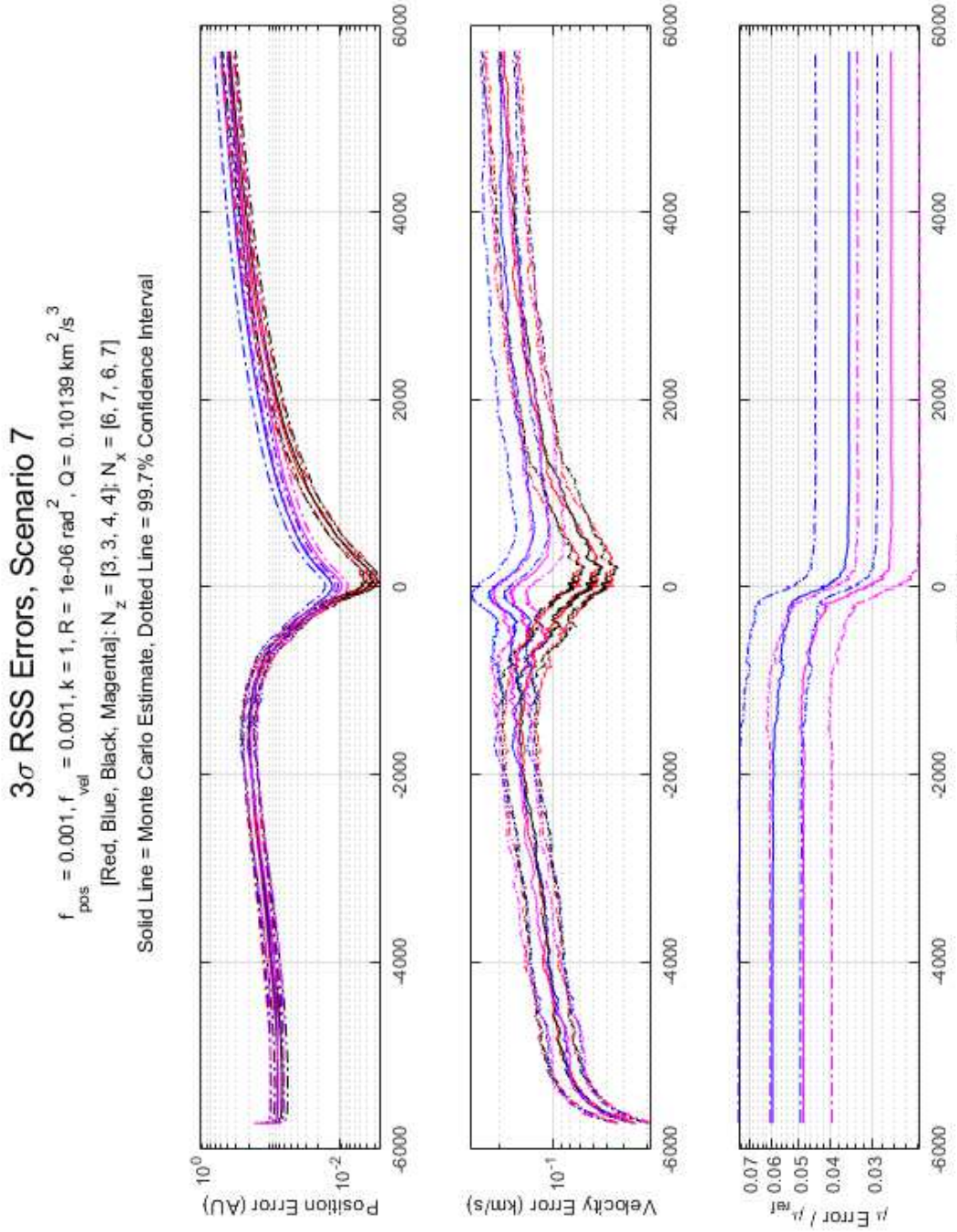

Fig. B.7: Monte Carlo 3σ RSS errors and 99.7% confidence intervals over time for Scenario 7

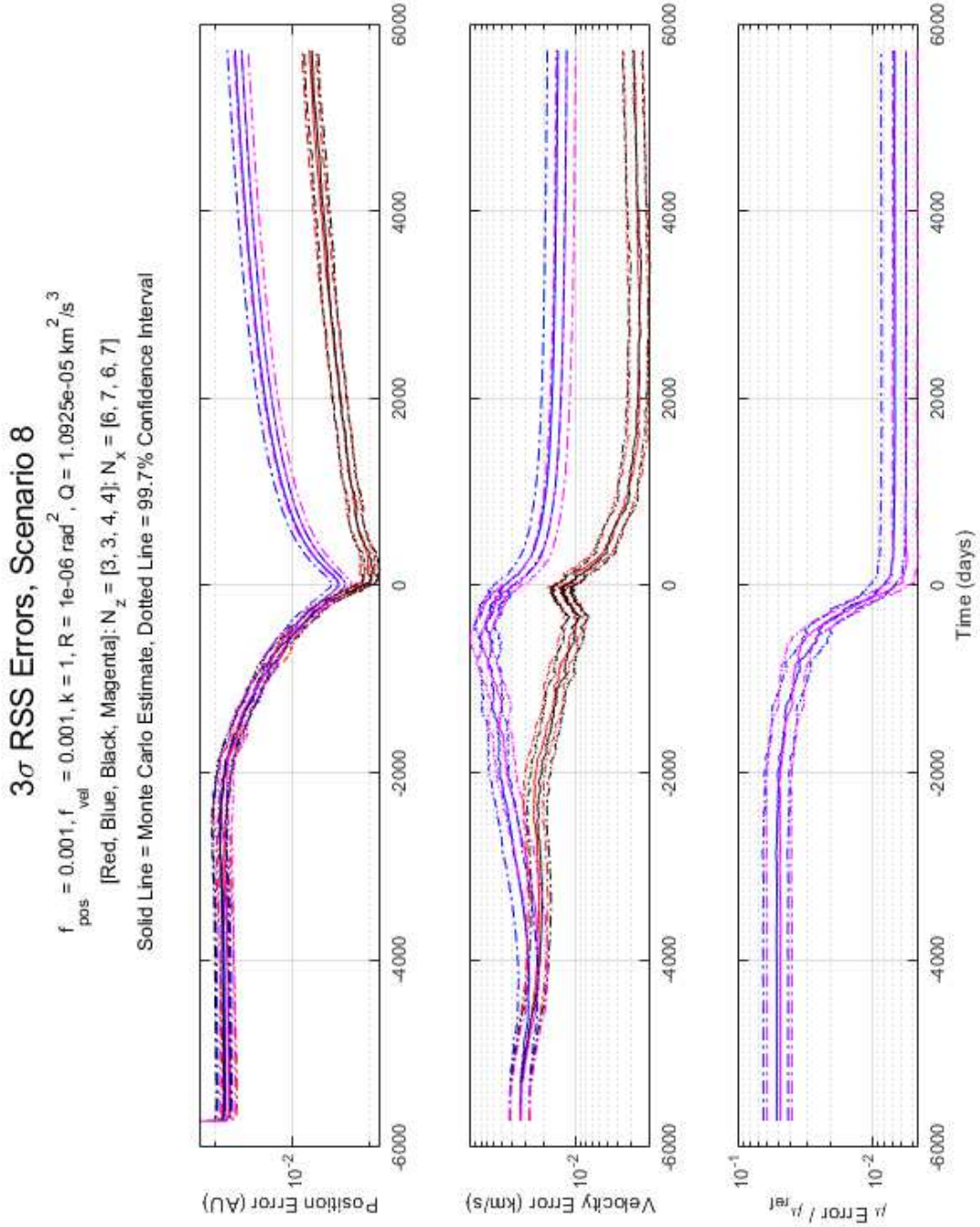

Fig. B.8: Monte Carlo 3σ RSS errors and 99.7% confidence intervals over time for Scenario 8

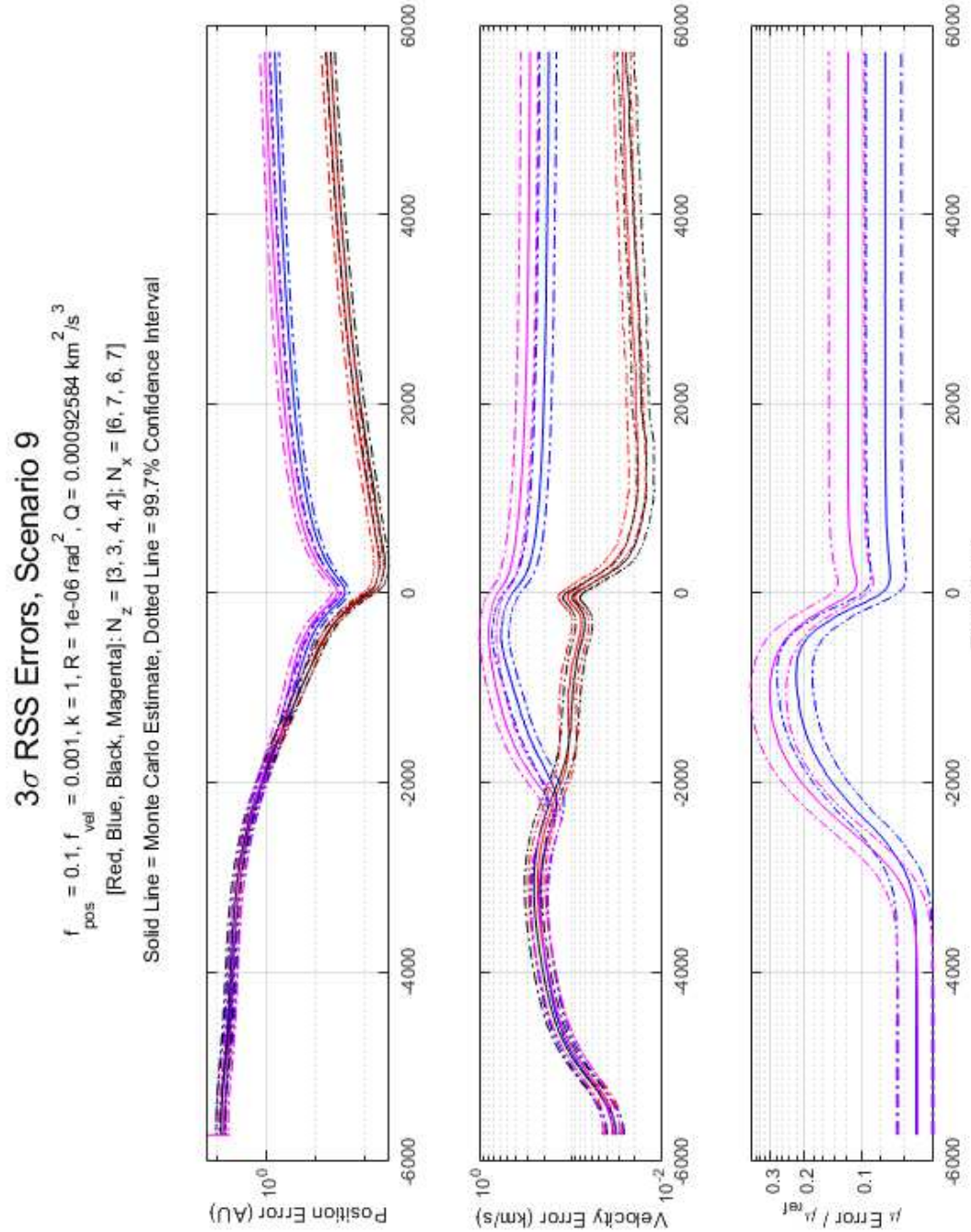

Fig. B.9: Monte Carlo 3σ RSS errors and 99.7% confidence intervals over time for Scenario 9

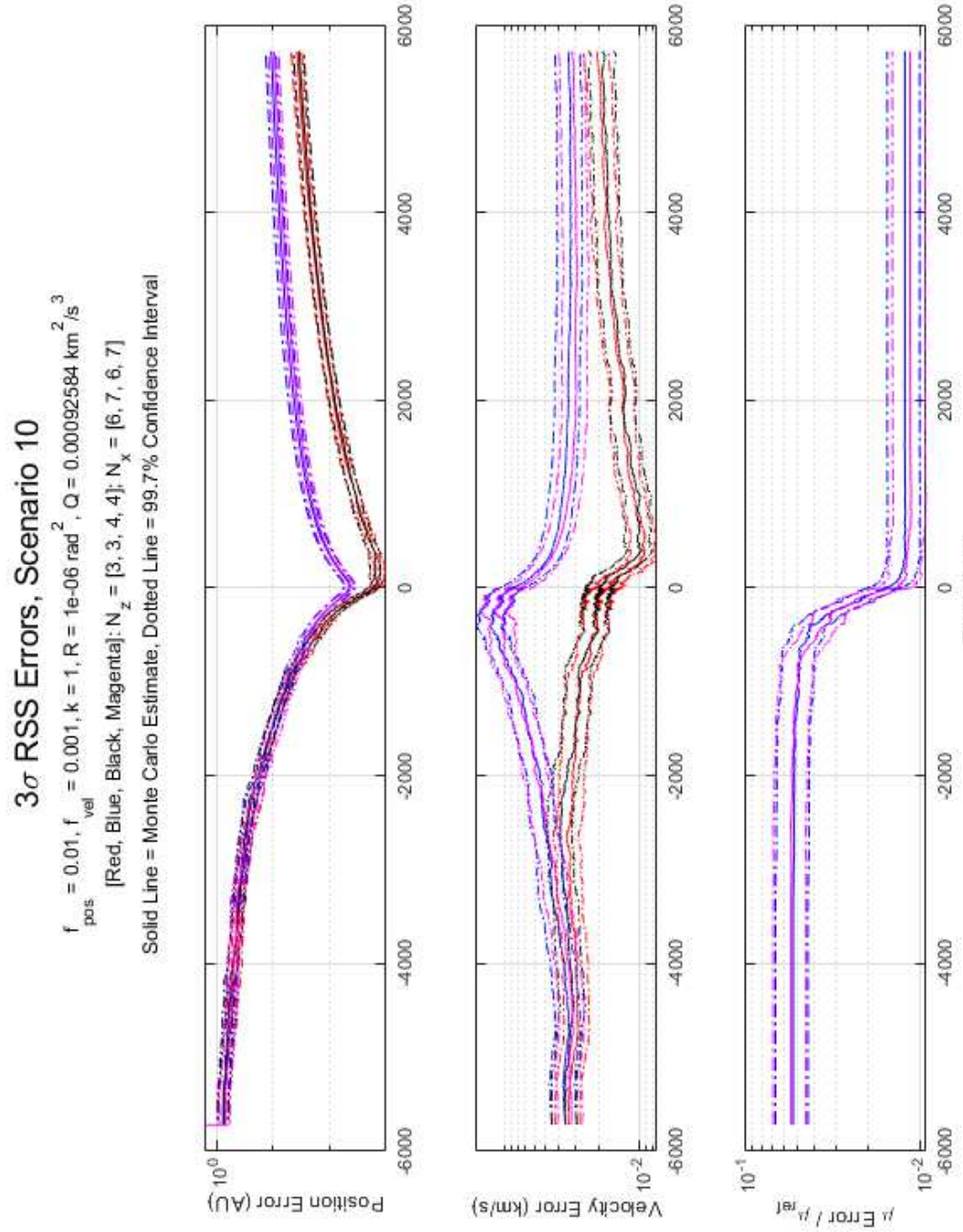

Fig. B.10: Monte Carlo 3σ RSS errors and 99.7% confidence intervals over time for Scenario 10

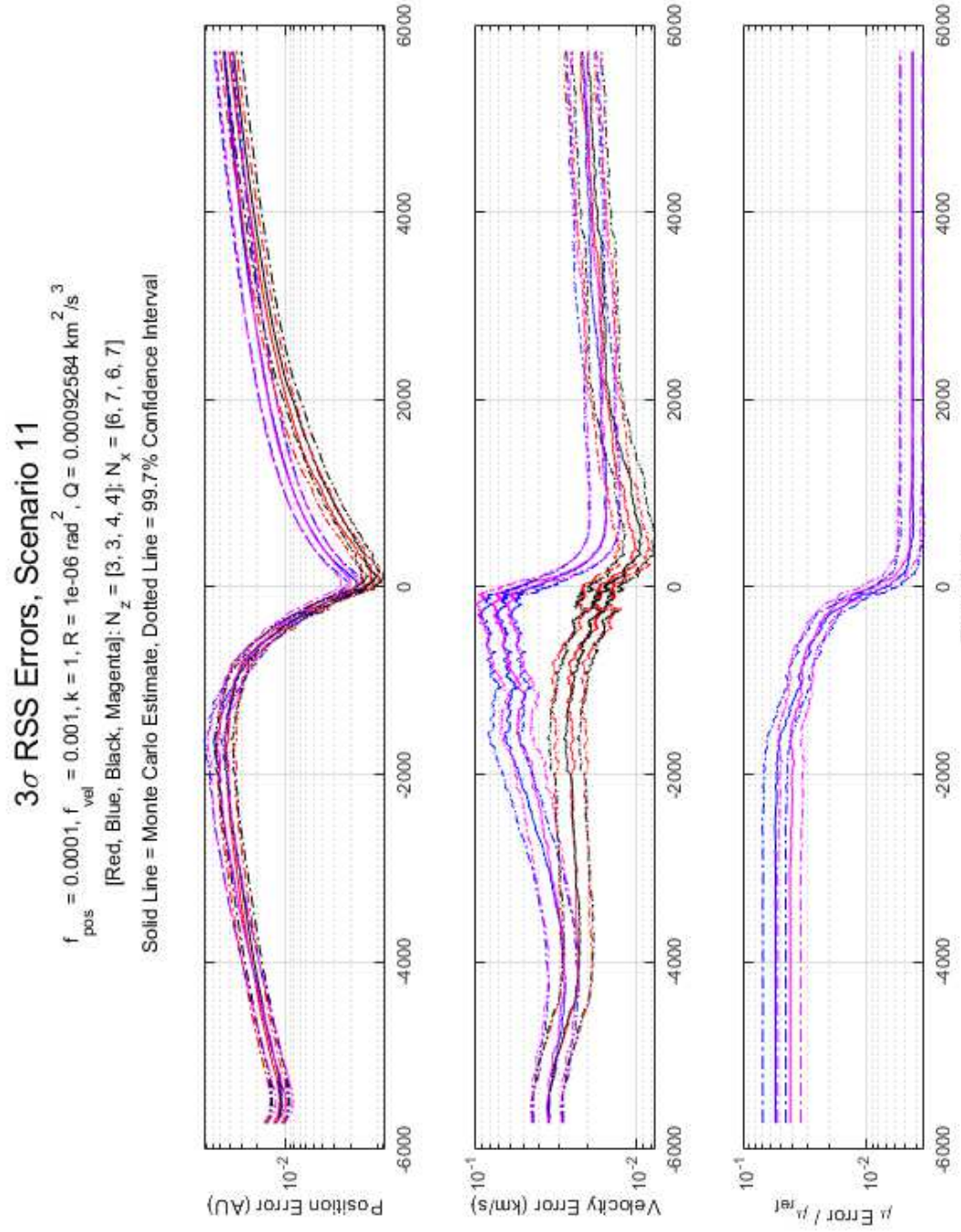

Fig. B.11: Monte Carlo 3σ RSS errors and 99.7% confidence intervals over time for Scenario 11

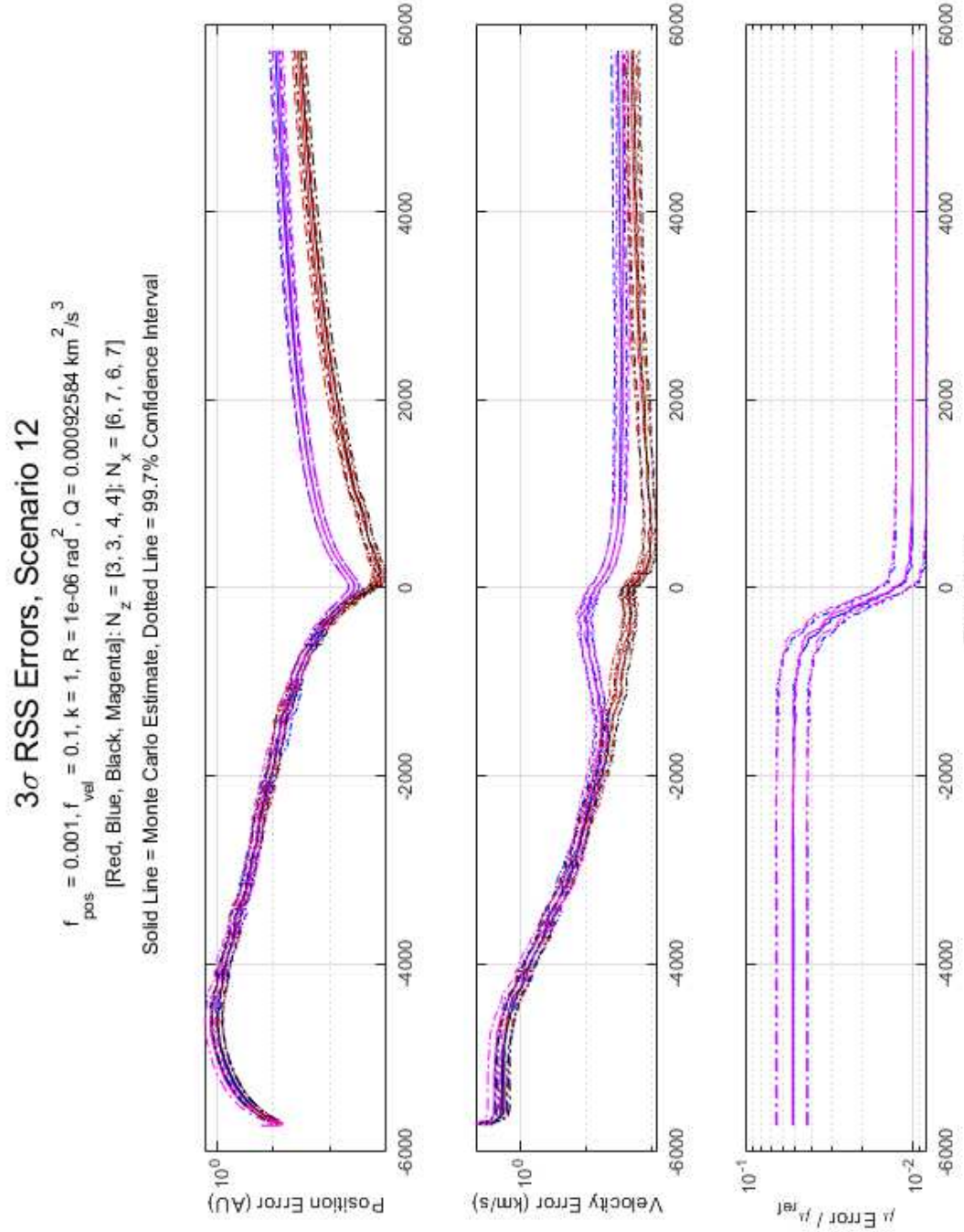

Fig. B.12: Monte Carlo 3σ RSS errors and 99.7% confidence intervals over time for Scenario 12

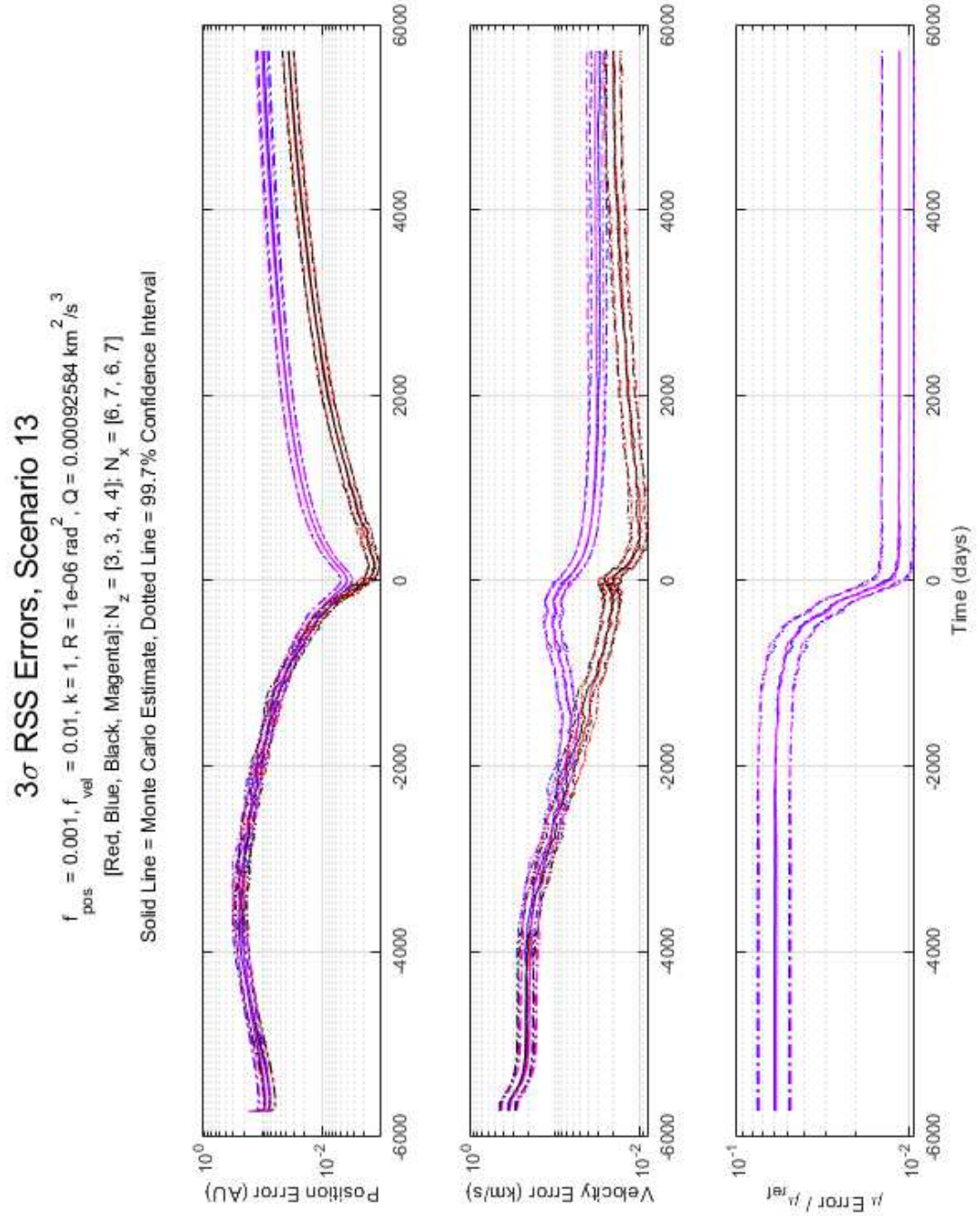

Fig. B.13: Monte Carlo 3σ RSS errors and 99.7% confidence intervals over time for Scenario 13

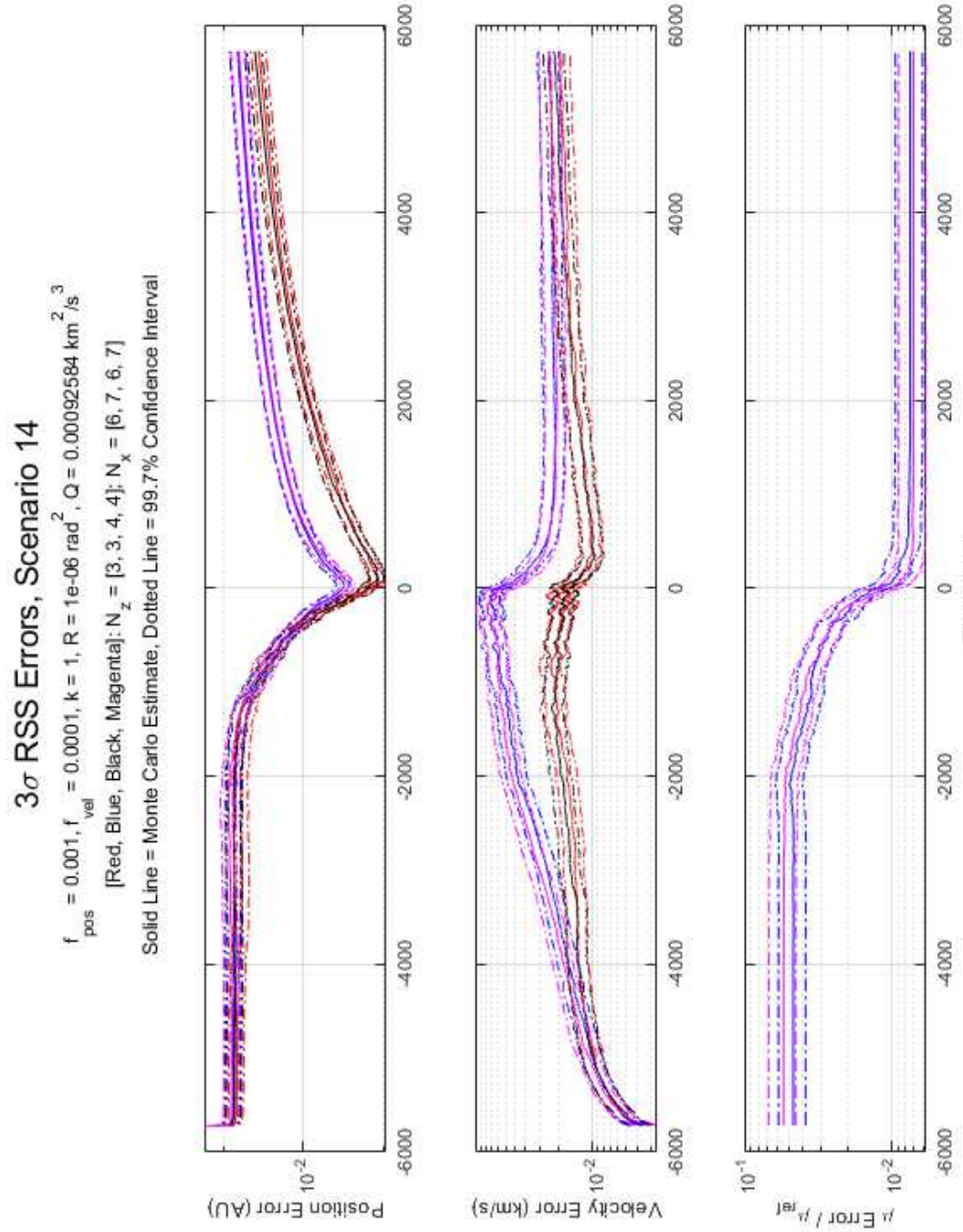

Fig. B.14: Monte Carlo 3σ RSS errors and 99.7% confidence intervals over time for Scenario 14

B.2 Filter Performance for All Scenarios

Figure 4.13 displays the RSS position, velocity, and gravity errors for all scenarios, averaged over all Monte Carlo runs, for $N_z = 3, N_x = 7$. Figures B.15-B.18 display this information for all four filter formulations.

B.3 Filter Performance: RSS Position Errors

Figures B.19-B.22 and Figures B.23-B.26 display the RSS position errors achieved by each filter formulation for different measurement intervals, measurement noise values, process noise strengths, initial position error fractions, and initial velocity error fractions.

B.4 Filter Performance: RSS Position Error Fraction

Figures B.27-B.30 and Figures B.31-B.34 display the RSS position error fractions achieved by each filter formulation for different measurement intervals, measurement noise values, process noise strengths, initial position error fractions, and initial velocity error fractions.

B.5 Filter Performance: RSS Velocity Errors

Figures B.35-B.38 and Figures B.39-B.42 display the RSS velocity errors achieved by each filter formulation for different measurement intervals, measurement noise values, process noise strengths, initial position error fractions, and initial velocity error fractions.

B.6 Filter Performance: RSS Velocity Error Fraction

Figures B.43-B.46 and Figures B.47-B.50 display the velocity error fractions achieved by each filter formulation for different measurement intervals, measurement noise values, process noise strengths, initial position error fractions, and initial velocity error fractions.

B.7 Filter Performance: Gravity Errors

Figures B.51-B.52 and Figures B.53-B.54 display the gravity errors achieved by each filter formulation for different measurement intervals, measurement noise values, process

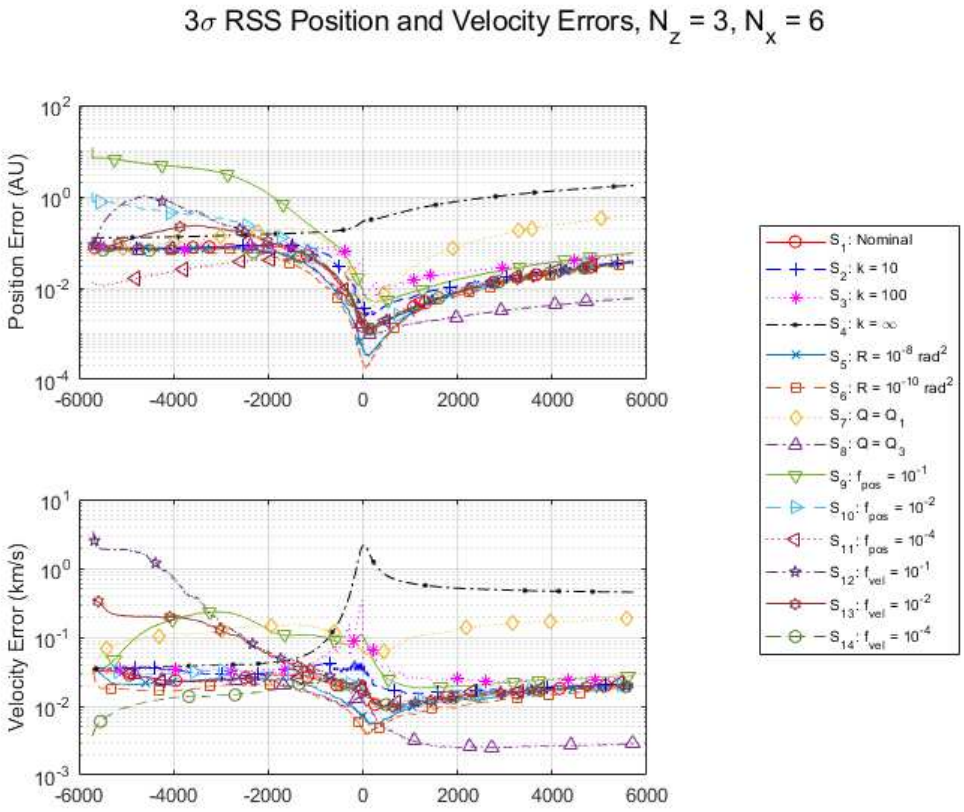

Fig. B.15: Monte Carlo 3σ RSS position, velocity, and gravity errors for all scenarios, $N_z = 3, N_x = 6$

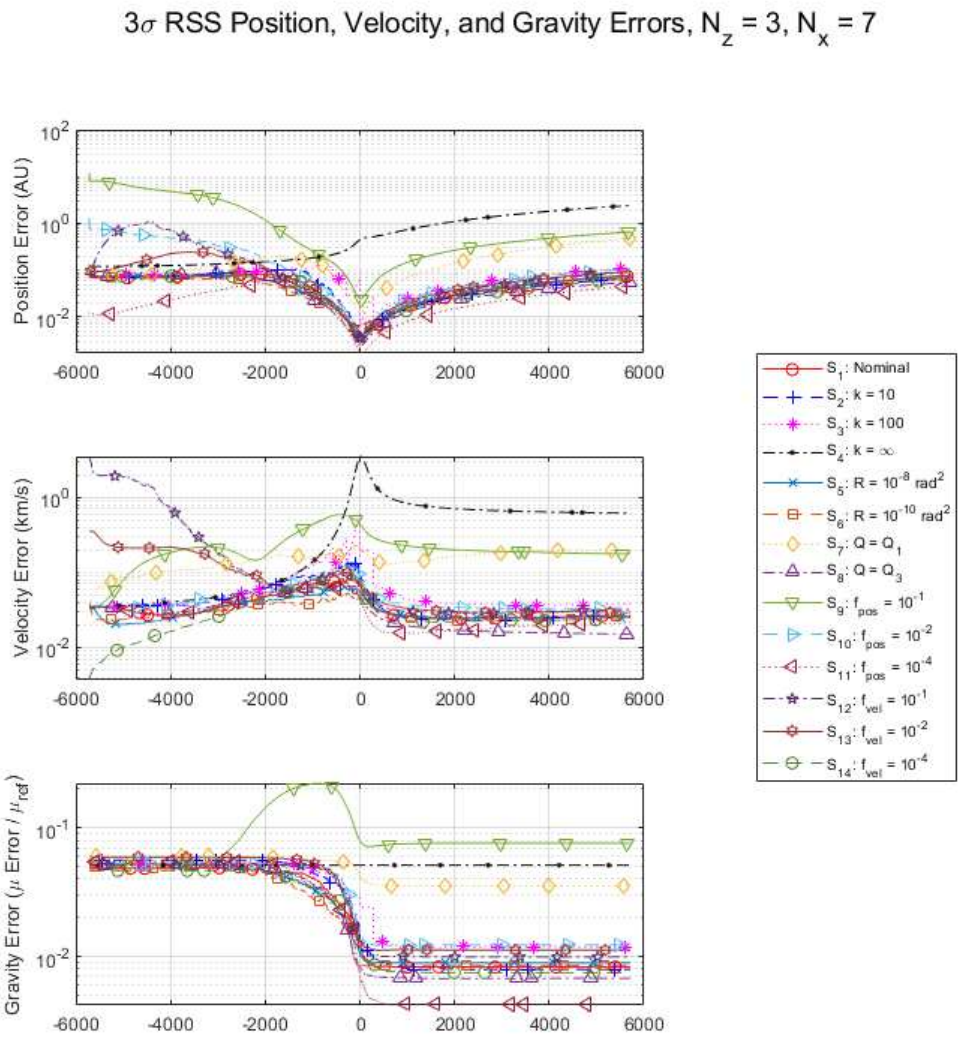

Fig. B.16: Monte Carlo 3σ RSS position, velocity, and gravity errors for all scenarios, $N_z = 3, N_x = 7$

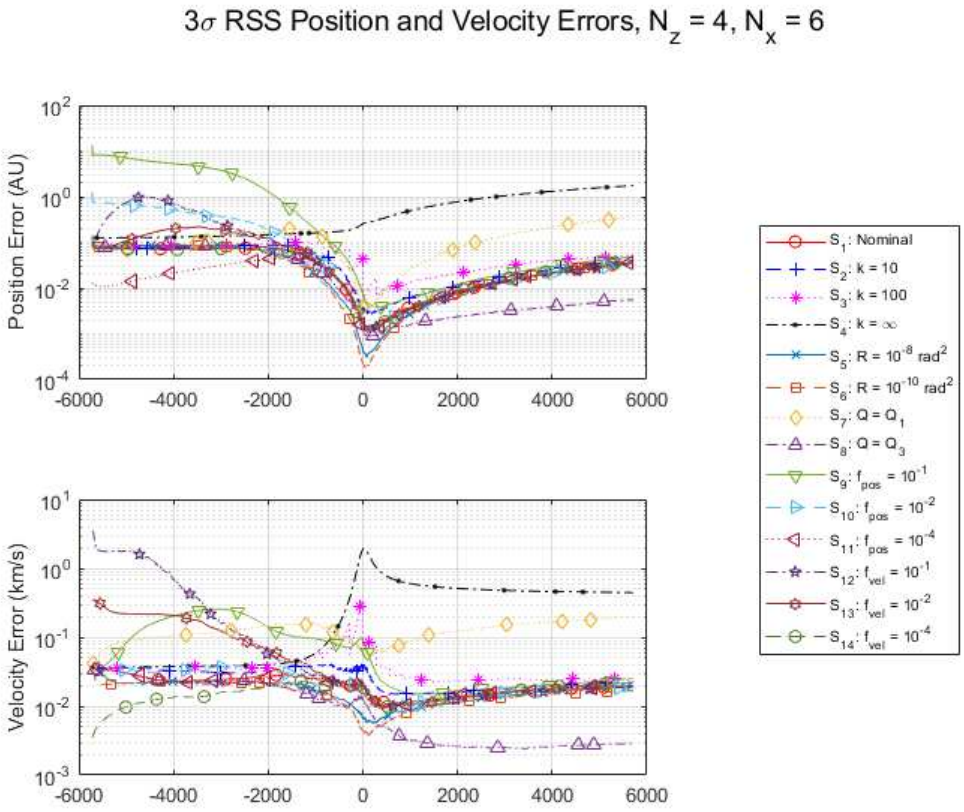

Fig. B.17: Monte Carlo 3σ RSS position, velocity, and gravity errors for all scenarios, $N_z = 4, N_x = 6$

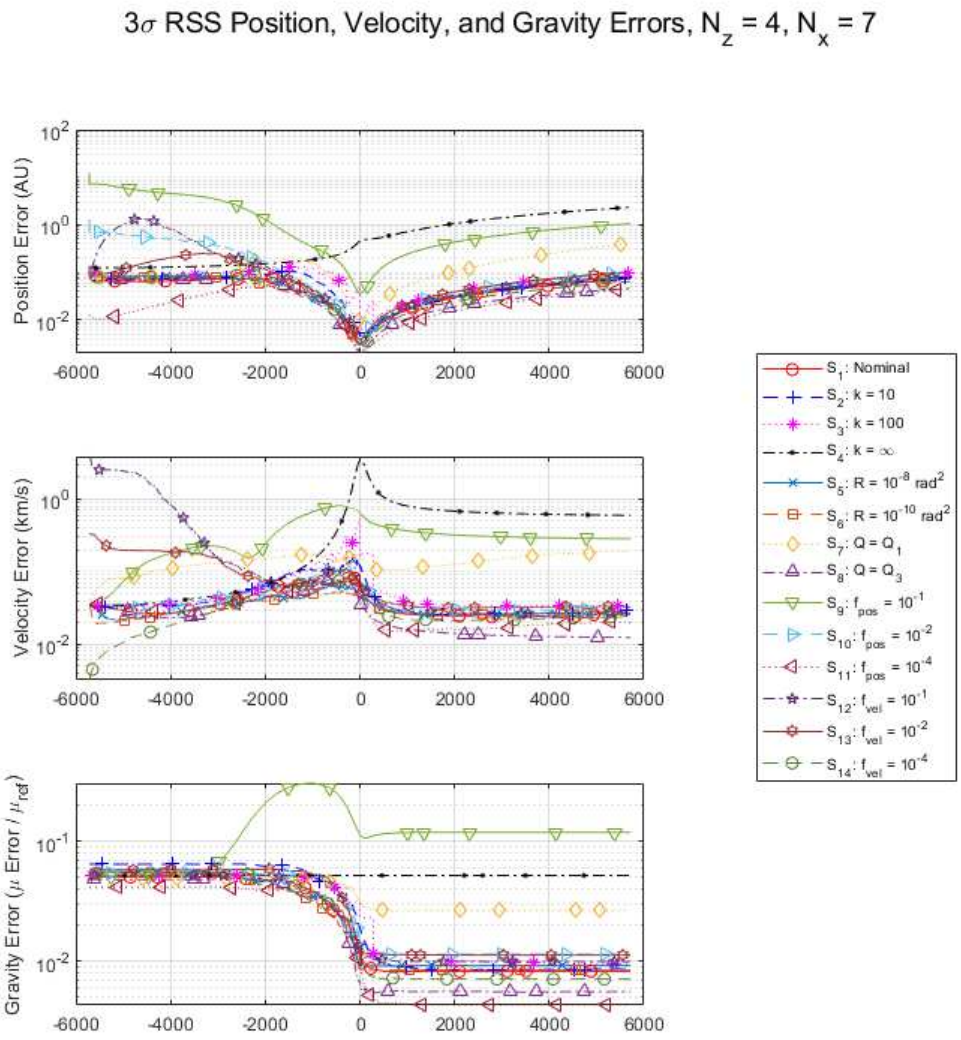

Fig. B.18: Monte Carlo 3σ RSS position, velocity, and gravity errors for all scenarios, $N_z = 4, N_x = 7$

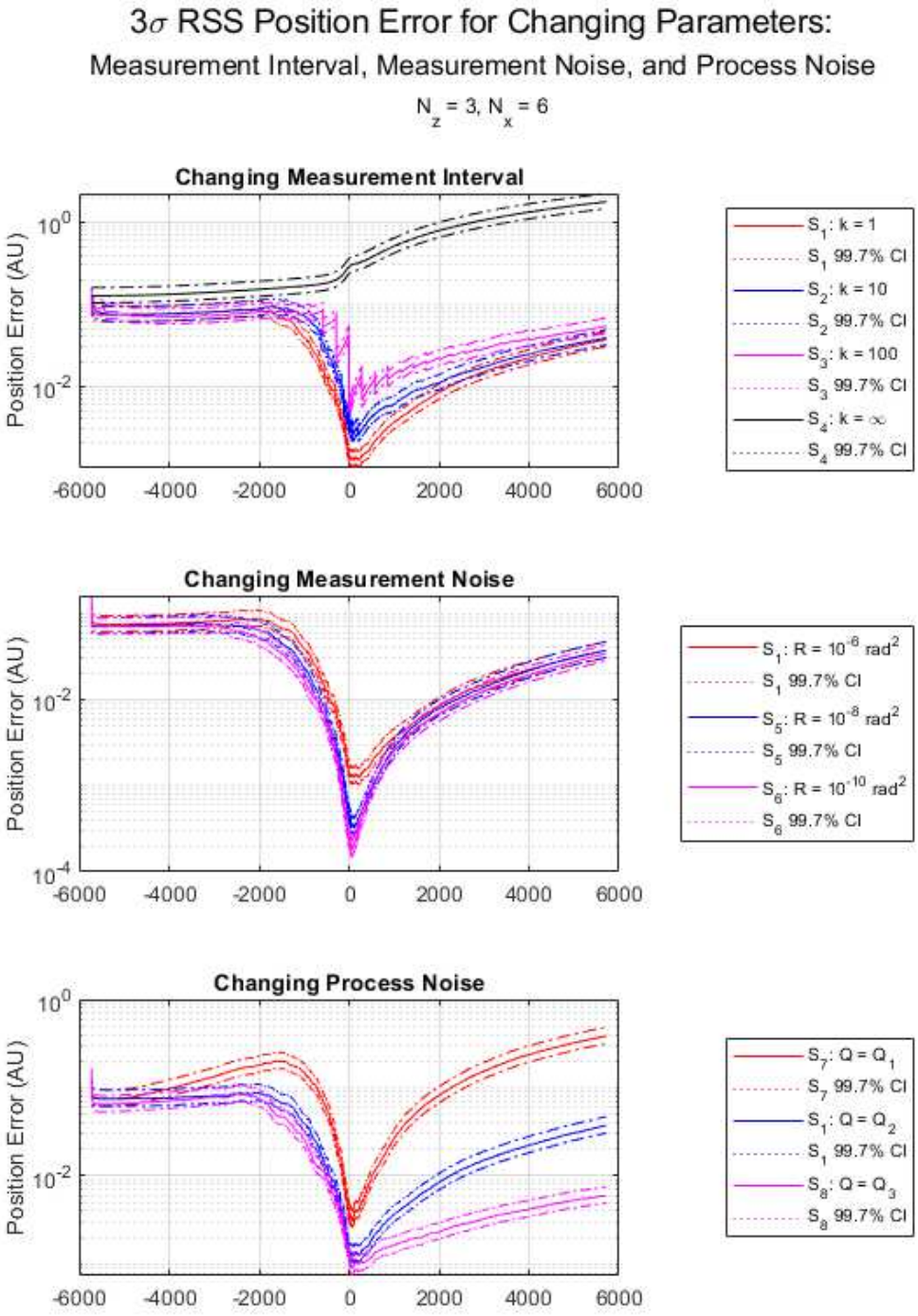

Fig. B.19: Monte Carlo 3σ RSS position errors and 99.7% confidence intervals for scenarios with varying measurement interval, measurement noise, and process noise, $N_z = 3, N_x = 6$

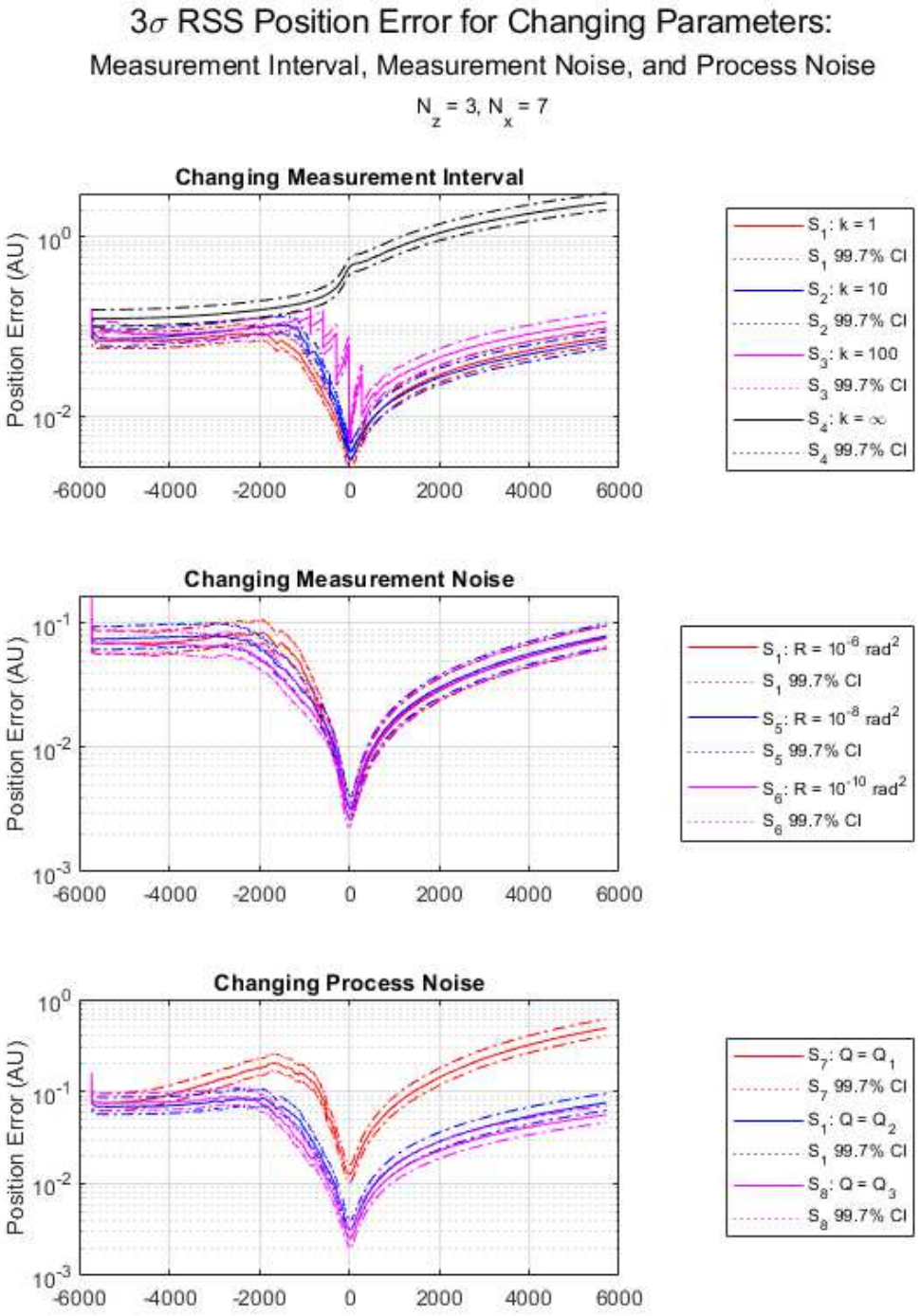

Fig. B.20: Monte Carlo 3σ RSS position errors and 99.7% confidence intervals for scenarios with varying measurement interval, measurement noise, and process noise, $N_z = 3, N_x = 7$

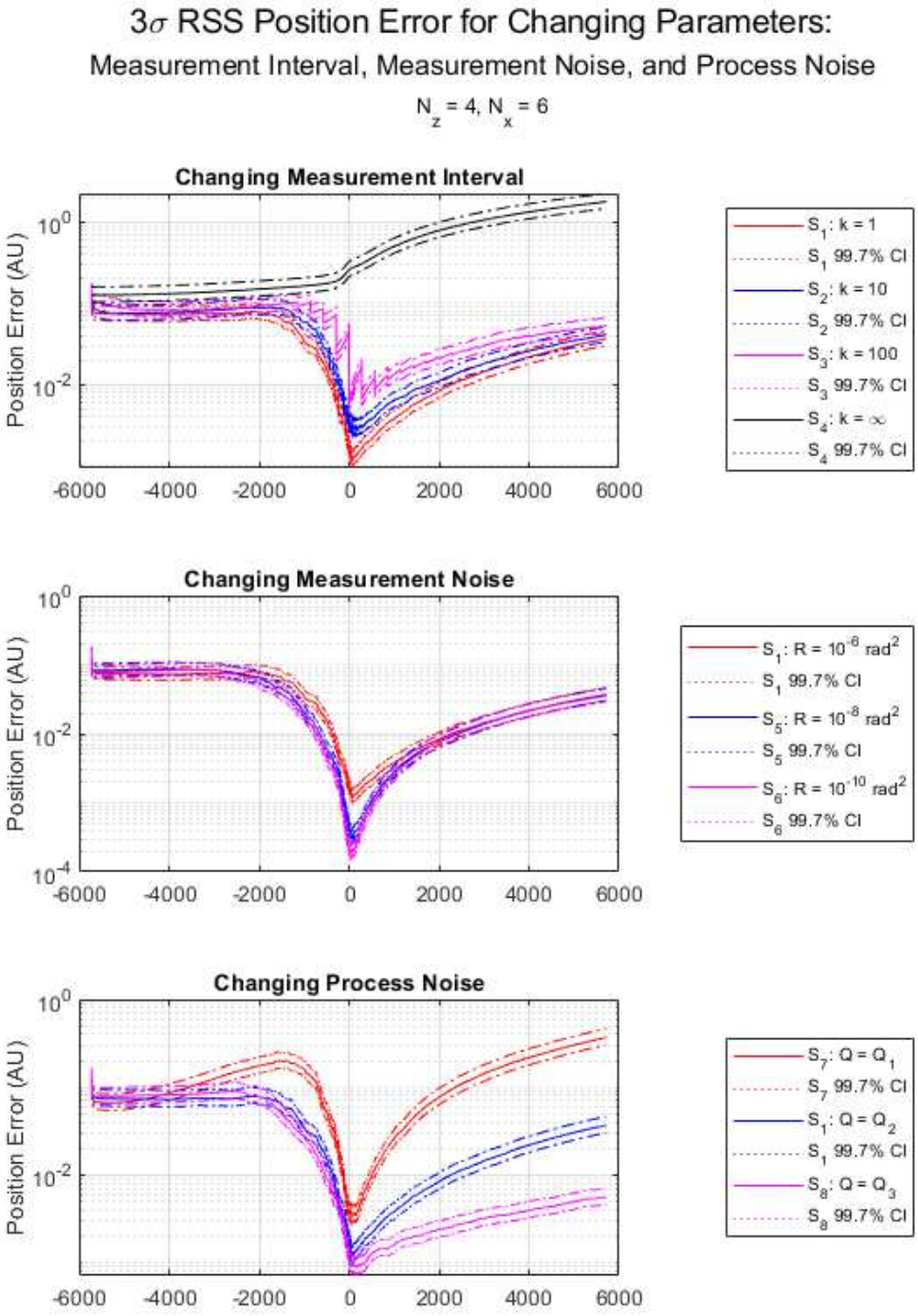

Fig. B.21: Monte Carlo 3σ RSS position errors and 99.7% confidence intervals for scenarios with varying measurement interval, measurement noise, and process noise, $N_z = 4, N_x = 6$

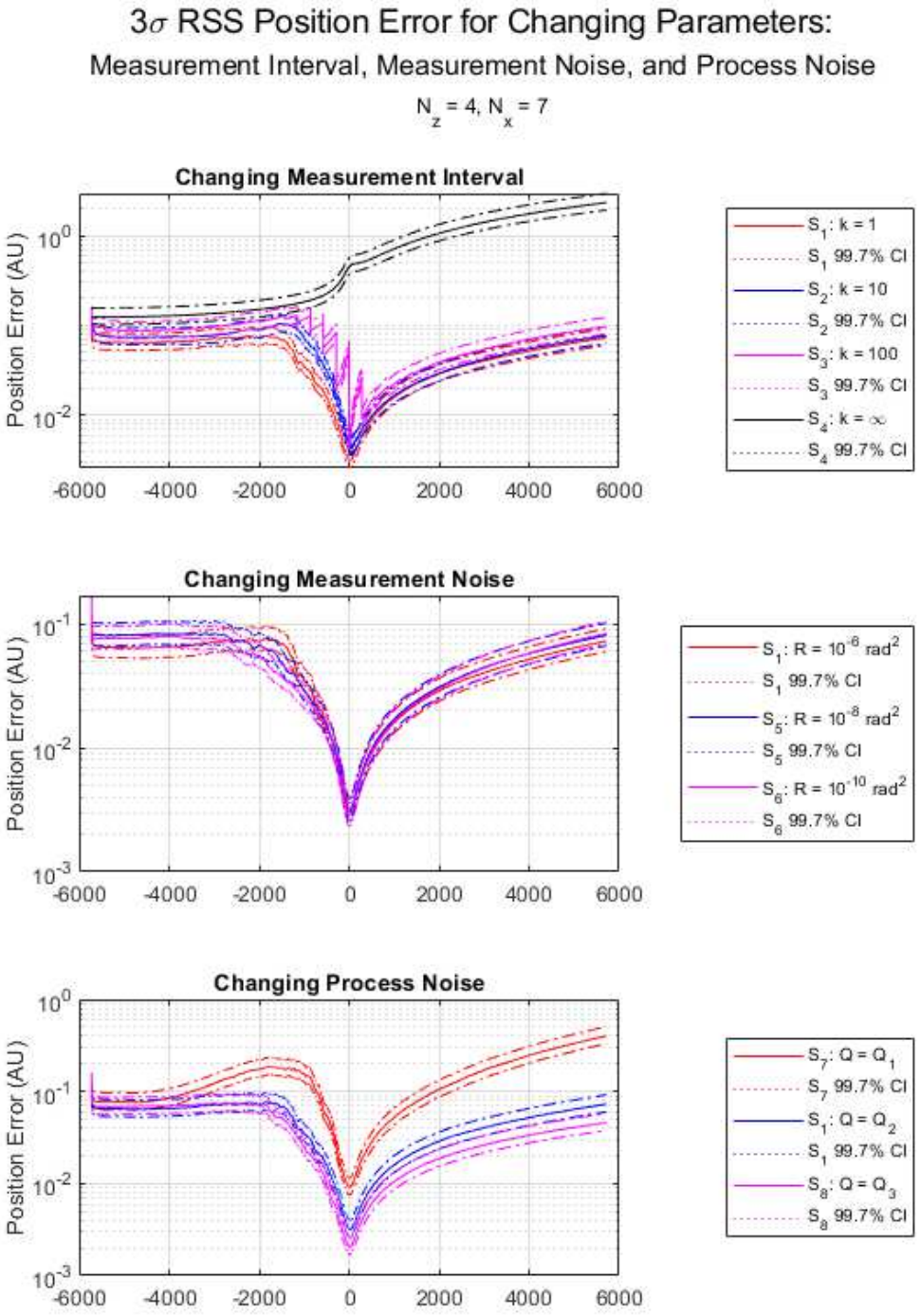

Fig. B.22: Monte Carlo 3σ RSS position errors and 99.7% confidence intervals for scenarios with varying measurement interval, measurement noise, and process noise, $N_z = 4, N_x = 7$

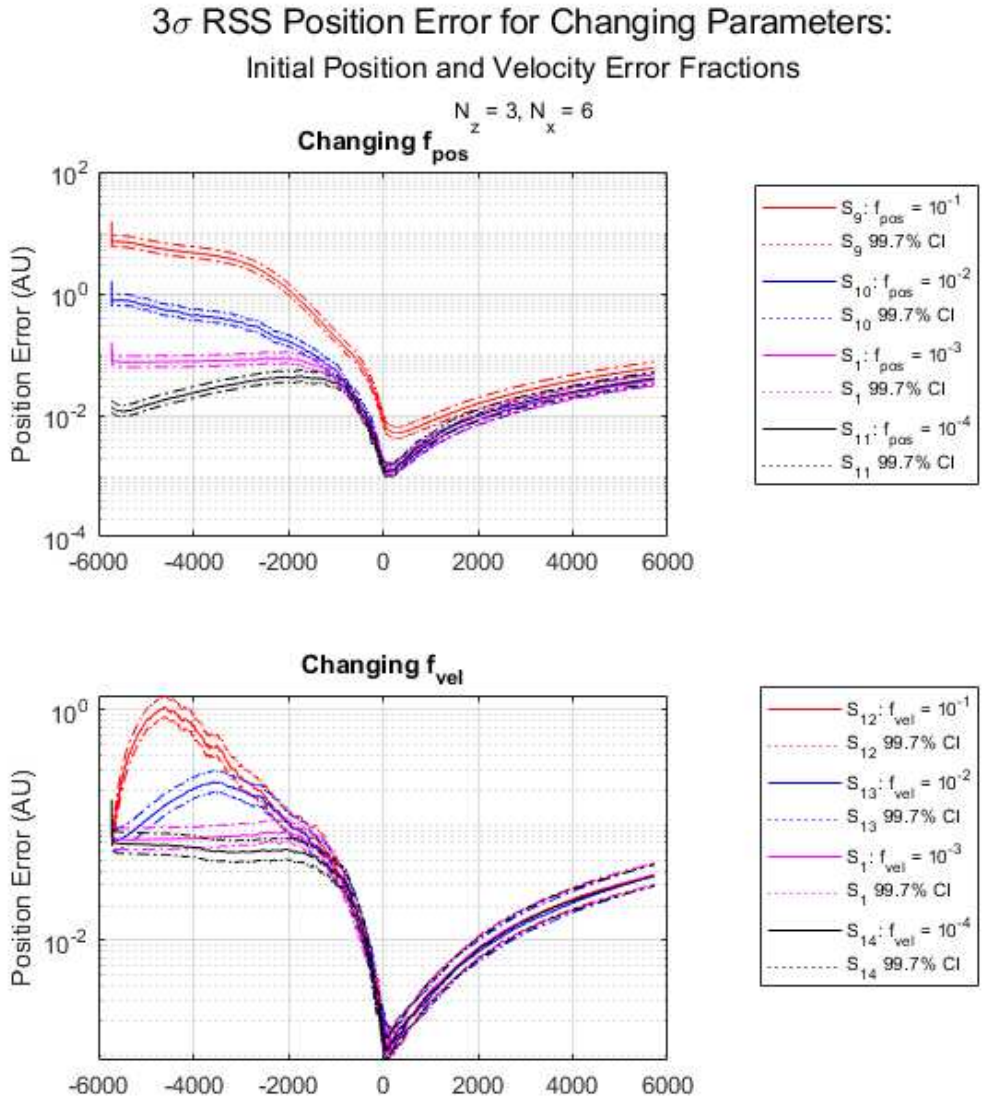

Fig. B.23: Monte Carlo 3σ RSS position errors and 99.7% confidence intervals for scenarios with varying initial position and velocity error fractions, $N_z = 3, N_x = 6$

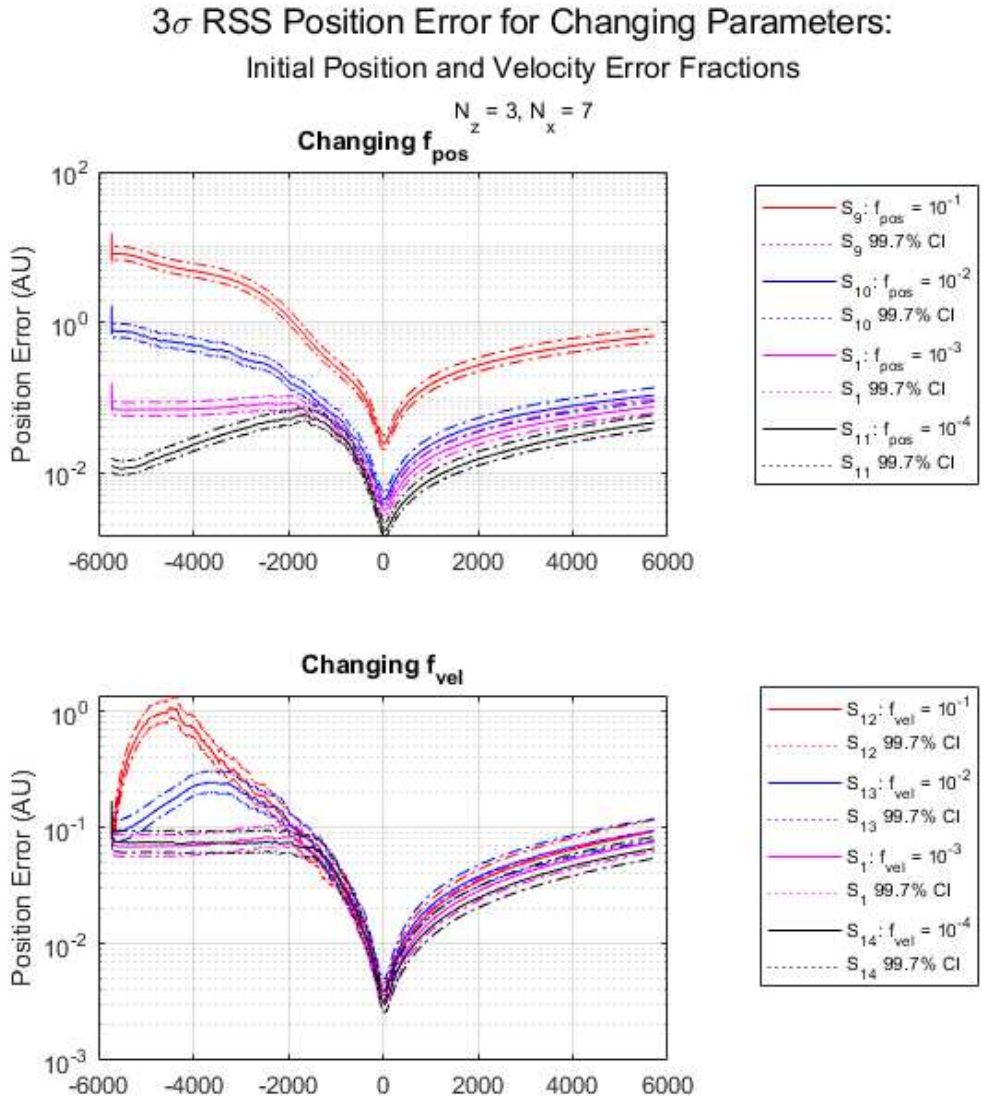

Fig. B.24: Monte Carlo 3σ RSS position errors and 99.7% confidence intervals for scenarios with varying initial position and velocity error fractions, $N_z = 3, N_x = 7$

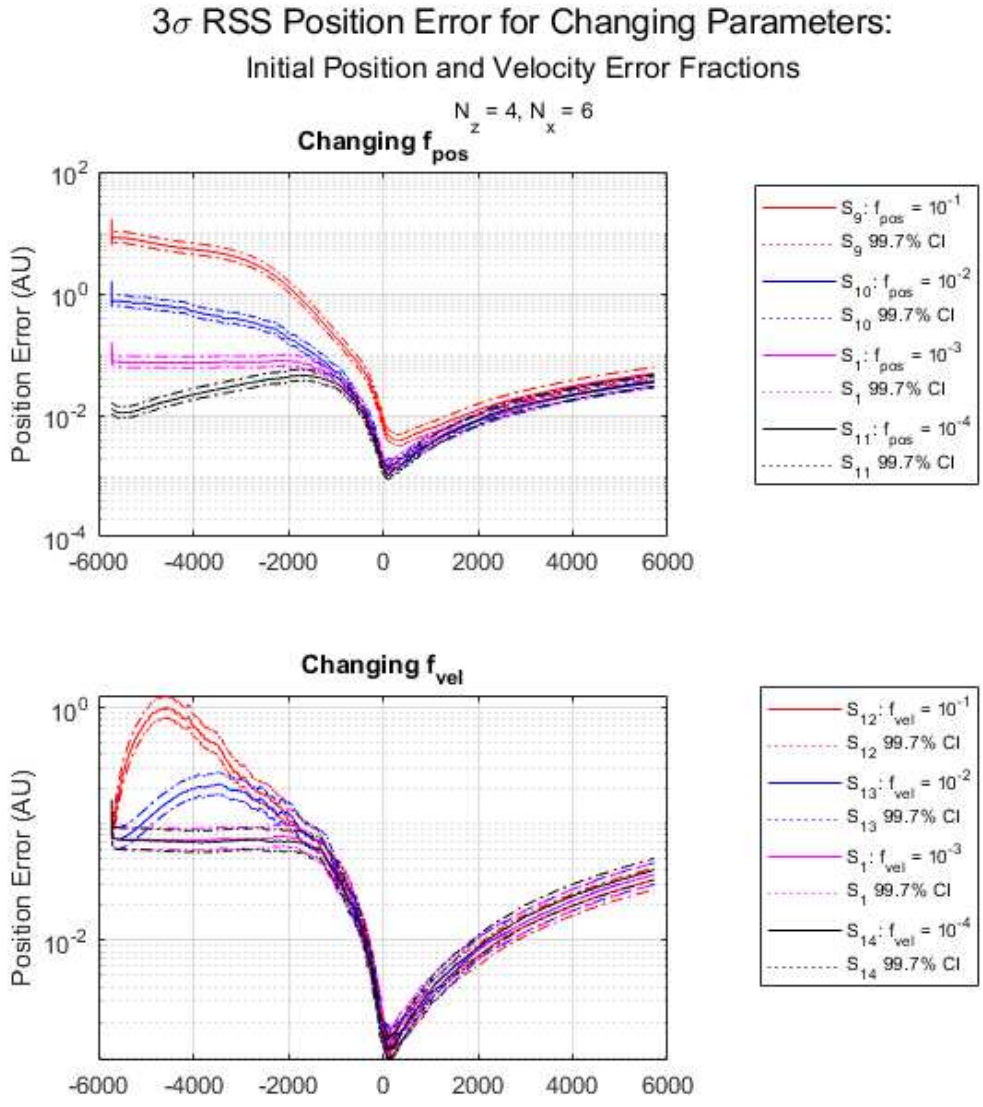

Fig. B.25: Monte Carlo 3σ RSS position errors and 99.7% confidence intervals for scenarios with varying initial position and velocity error fractions, $N_z = 4, N_x = 6$

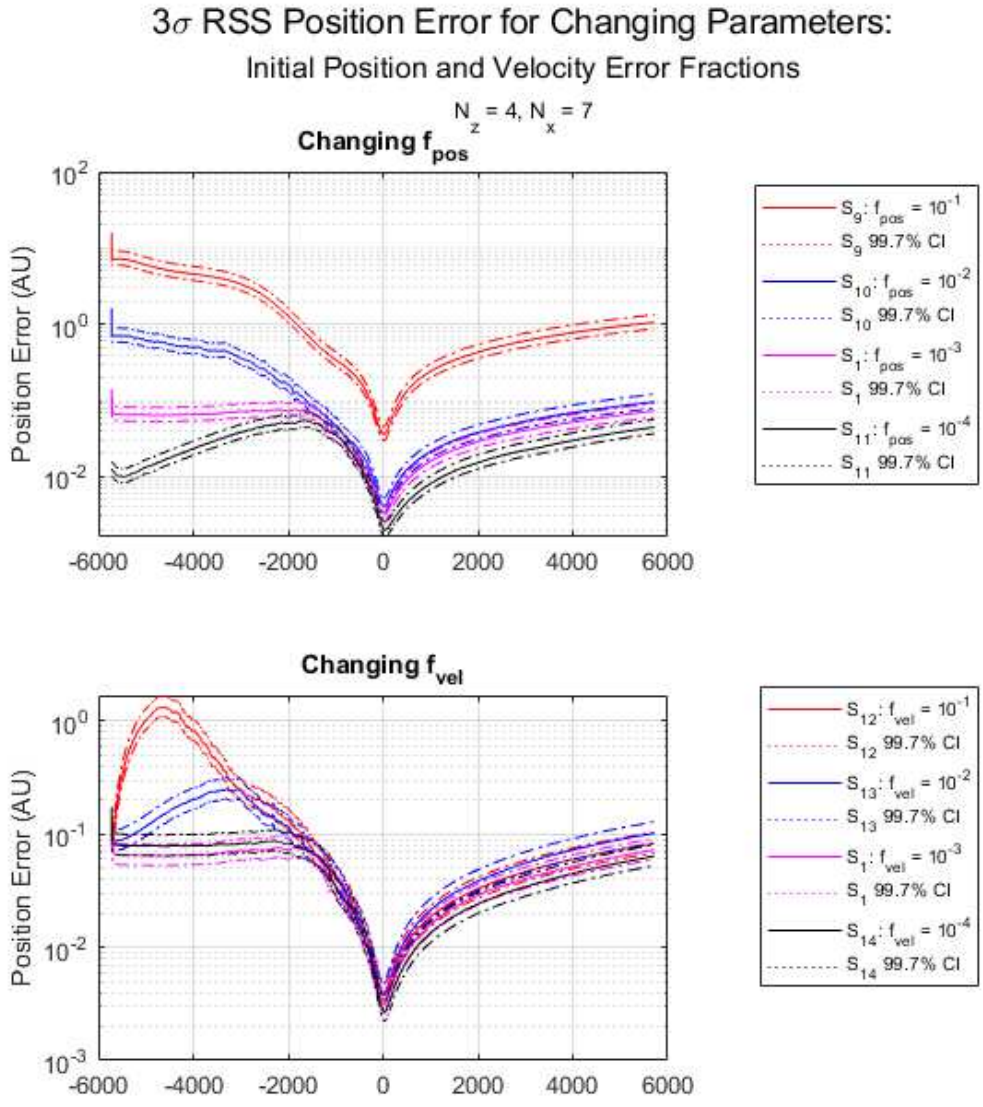

Fig. B.26: Monte Carlo 3σ RSS position errors and 99.7% confidence intervals for scenarios with varying initial position and velocity error fractions, $N_z = 4, N_x = 7$

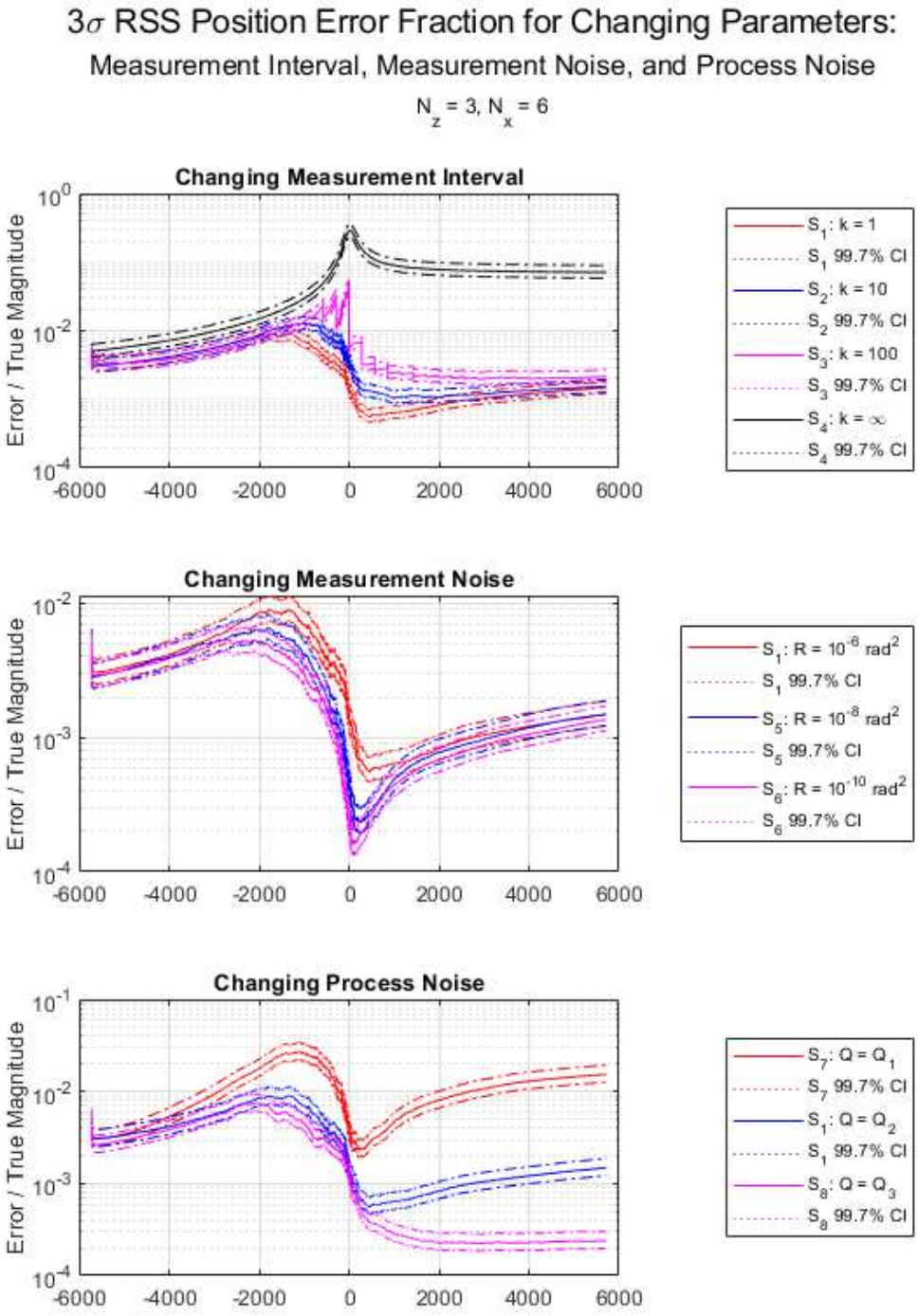

Fig. B.27: Monte Carlo 3σ RSS position error fractions and 99.7% confidence intervals for scenarios with varying measurement interval, measurement noise, and process noise, $N_z = 3, N_x = 6$

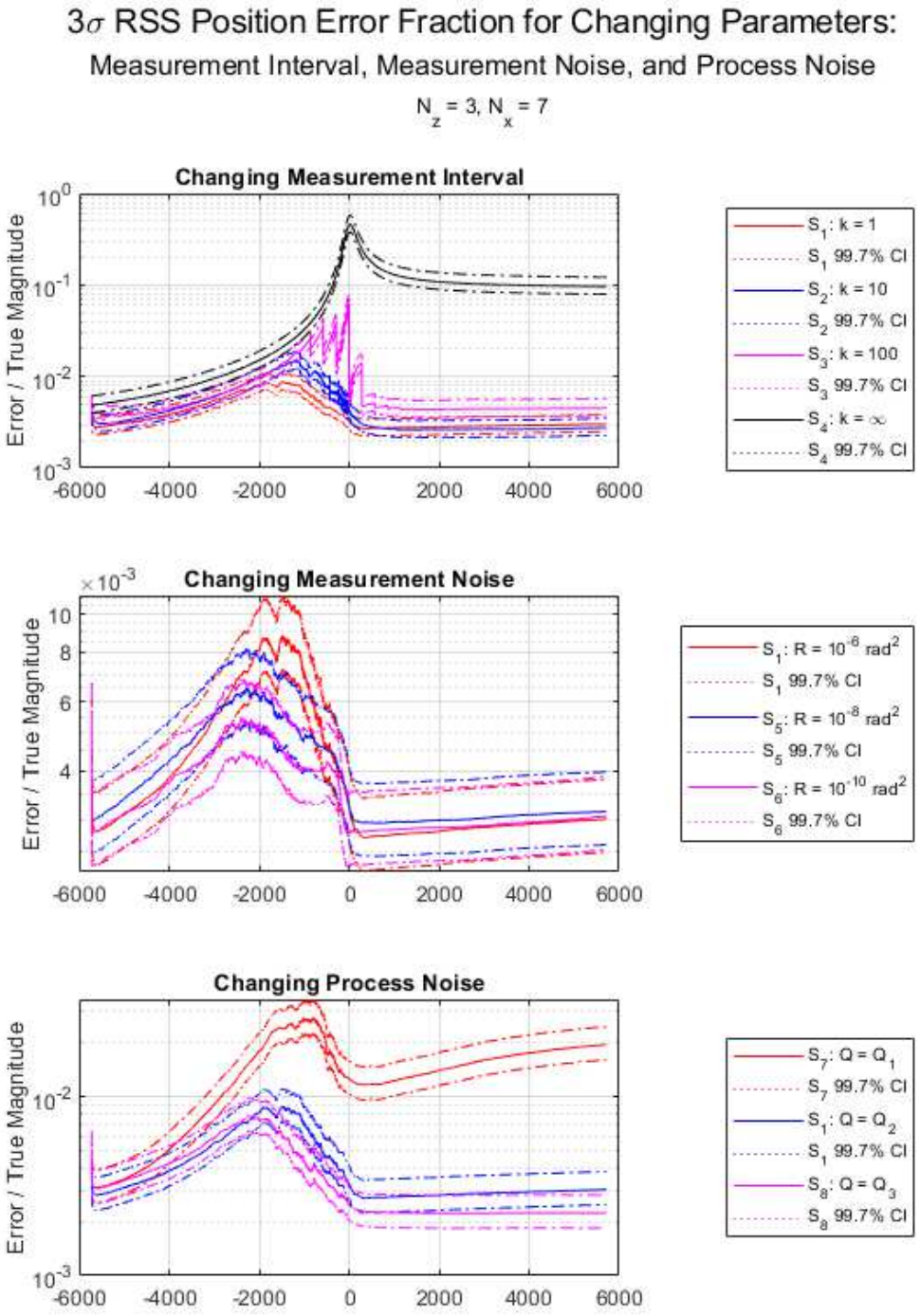

Fig. B.28: Monte Carlo 3σ RSS position error fractions and 99.7% confidence intervals for scenarios with varying measurement interval, measurement noise, and process noise, $N_z = 3, N_x = 7$

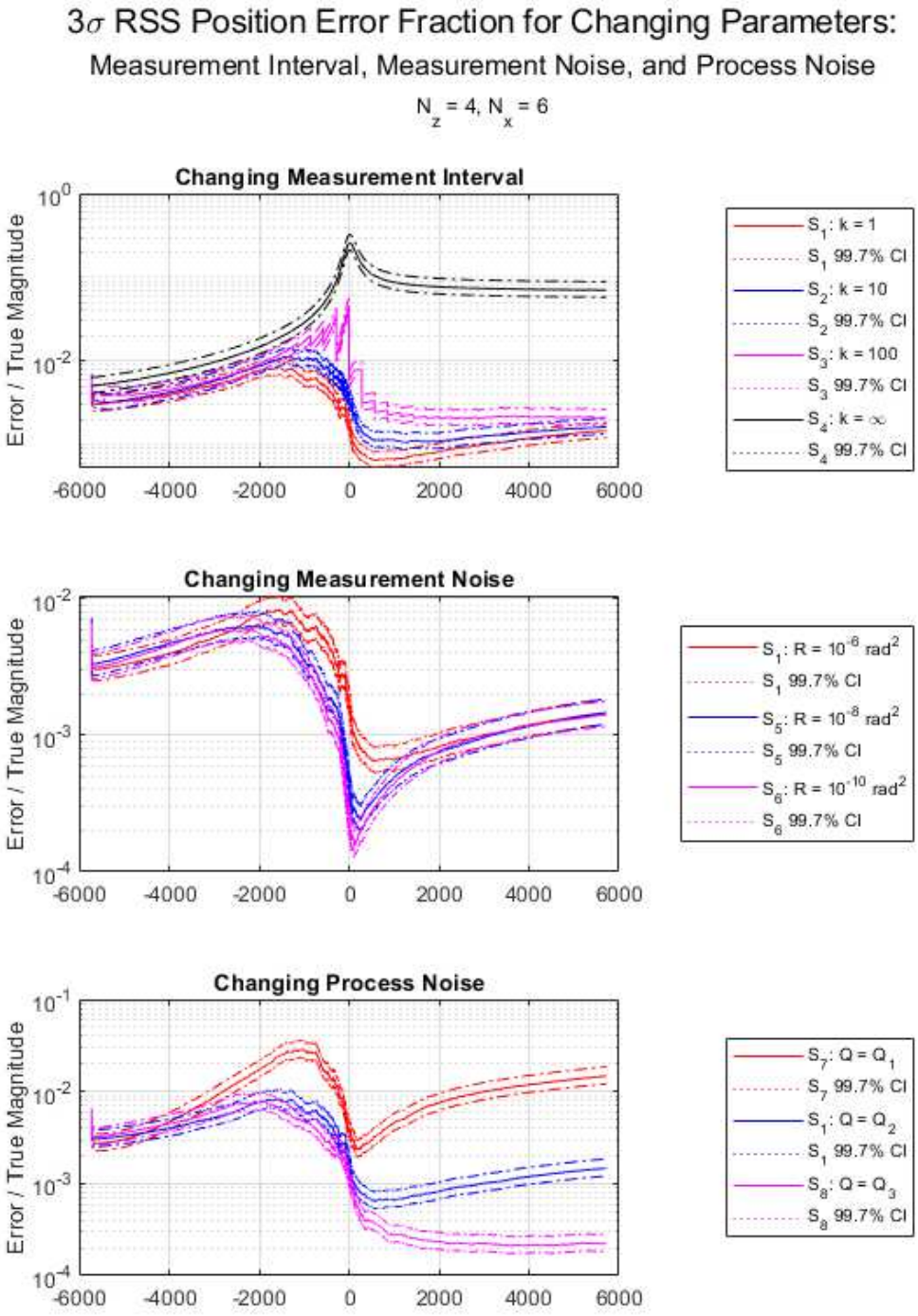

Fig. B.29: Monte Carlo 3σ RSS position error fractions and 99.7% confidence intervals for scenarios with varying measurement interval, measurement noise, and process noise, $N_z = 4, N_x = 6$

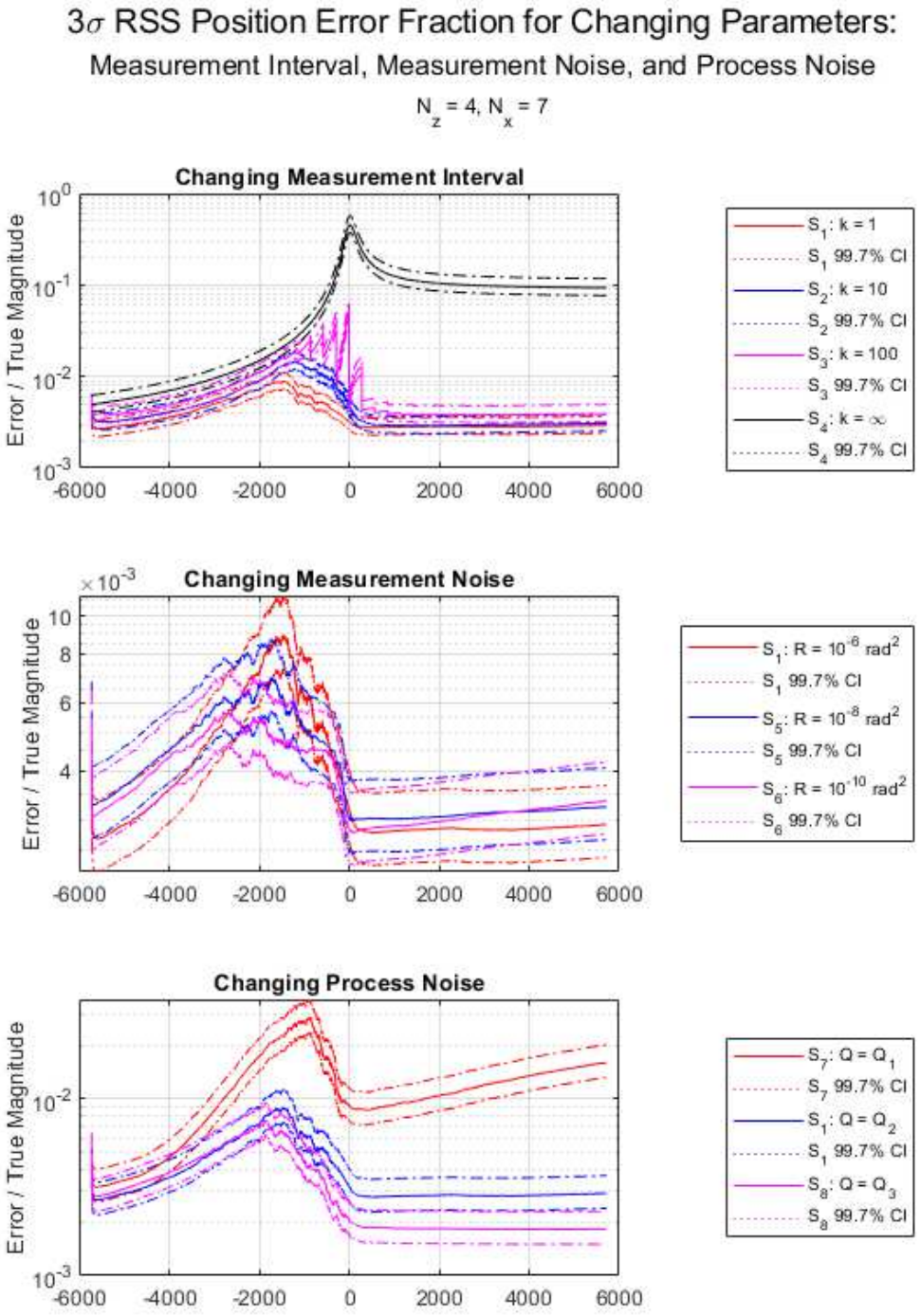

Fig. B.30: Monte Carlo 3σ RSS position error fractions and 99.7% confidence intervals for scenarios with varying measurement interval, measurement noise, and process noise, $N_z = 4, N_x = 7$

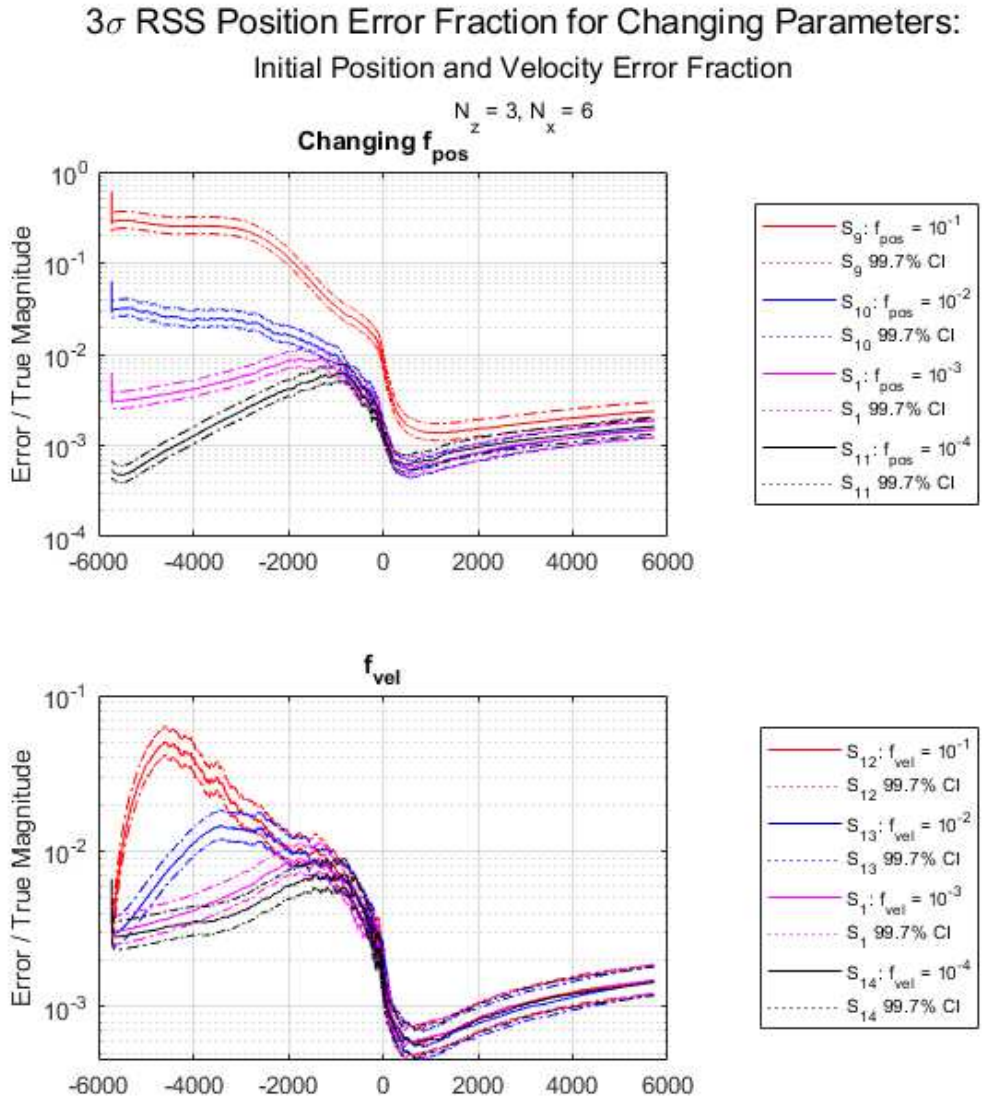

Fig. B.31: Monte Carlo 3σ RSS position error fractions and 99.7% confidence intervals for scenarios with varying initial position and velocity error fractions, $N_z = 3, N_x = 6$

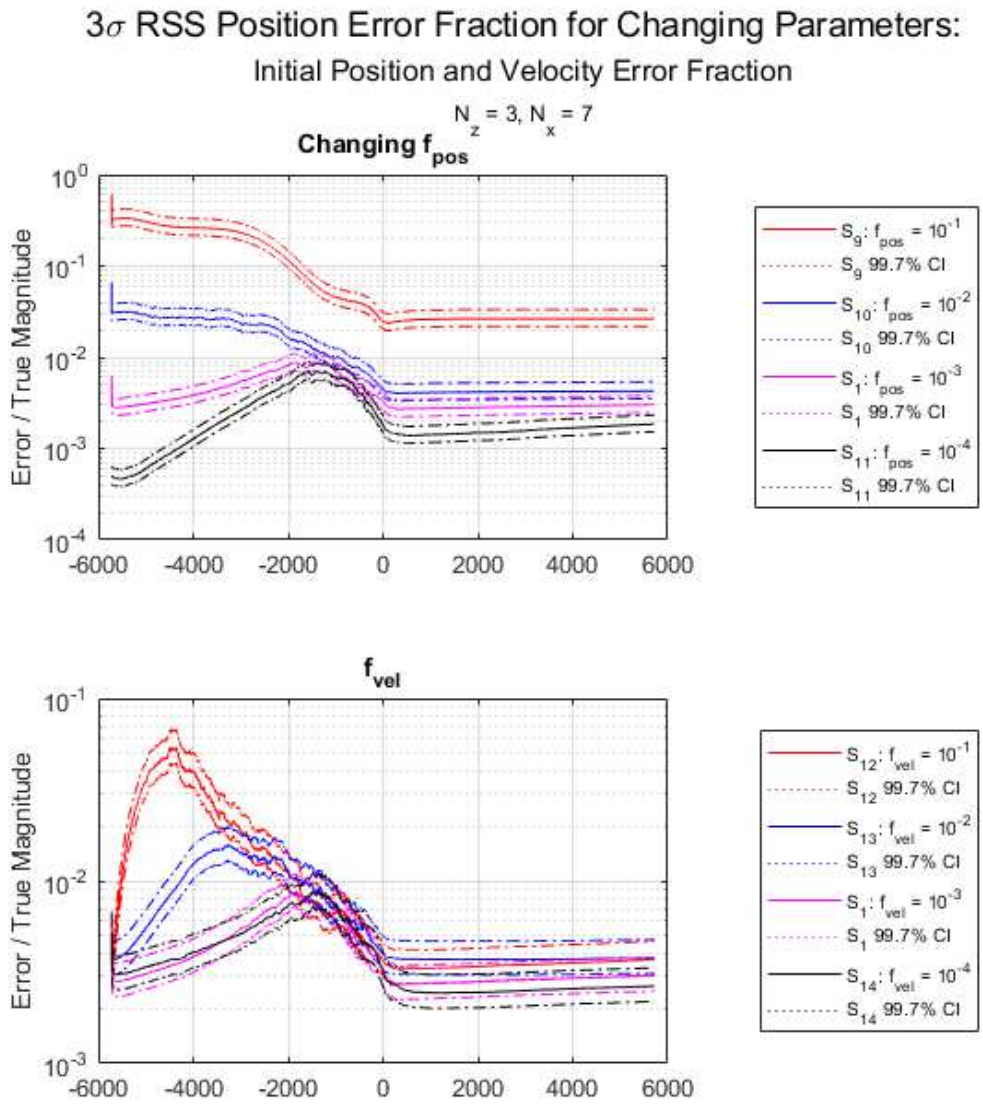

Fig. B.32: Monte Carlo 3σ RSS position error fractions and 99.7% confidence intervals for scenarios with varying initial position and velocity error fractions, $N_z = 3, N_x = 7$

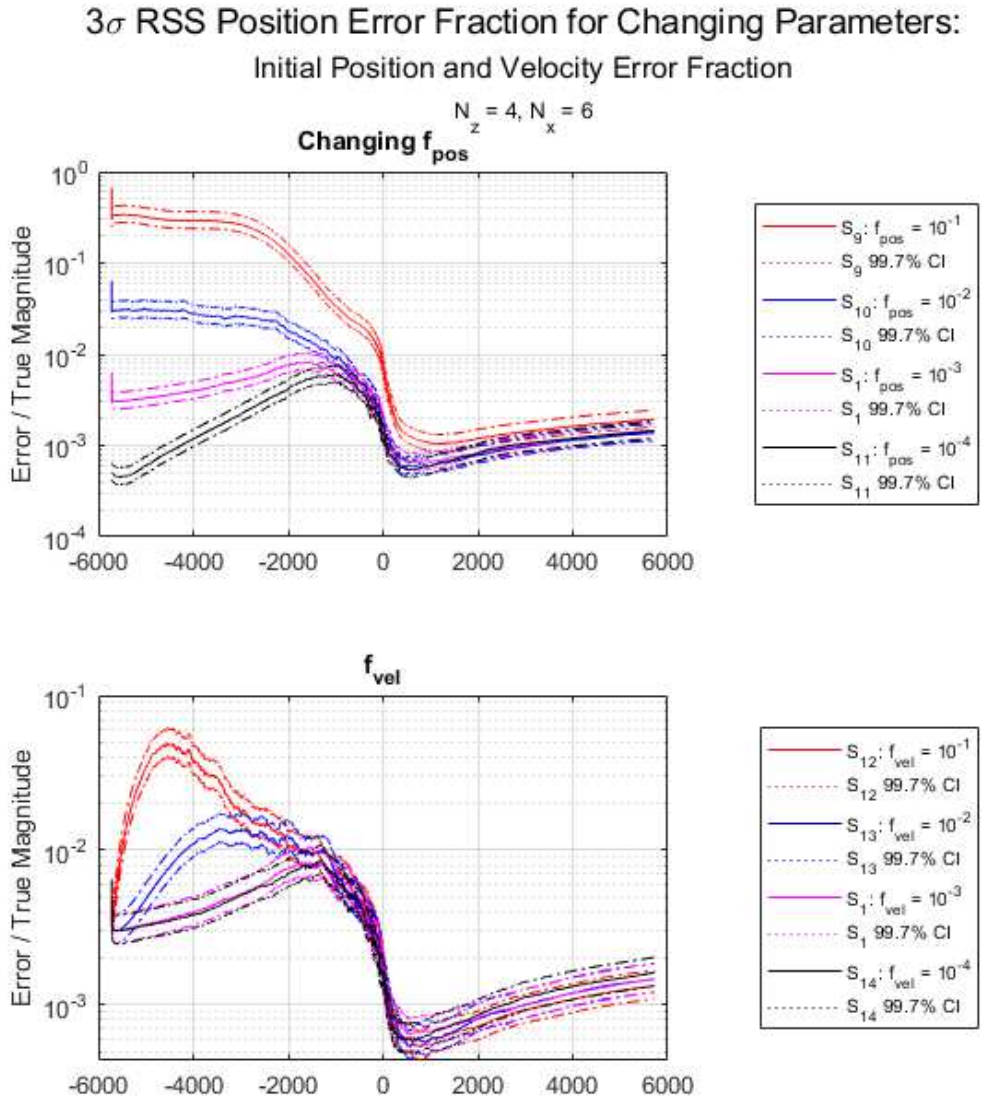

Fig. B.33: Monte Carlo 3σ RSS position error fractions and 99.7% confidence intervals for scenarios with varying initial position and velocity error fractions, $N_z = 4, N_x = 6$

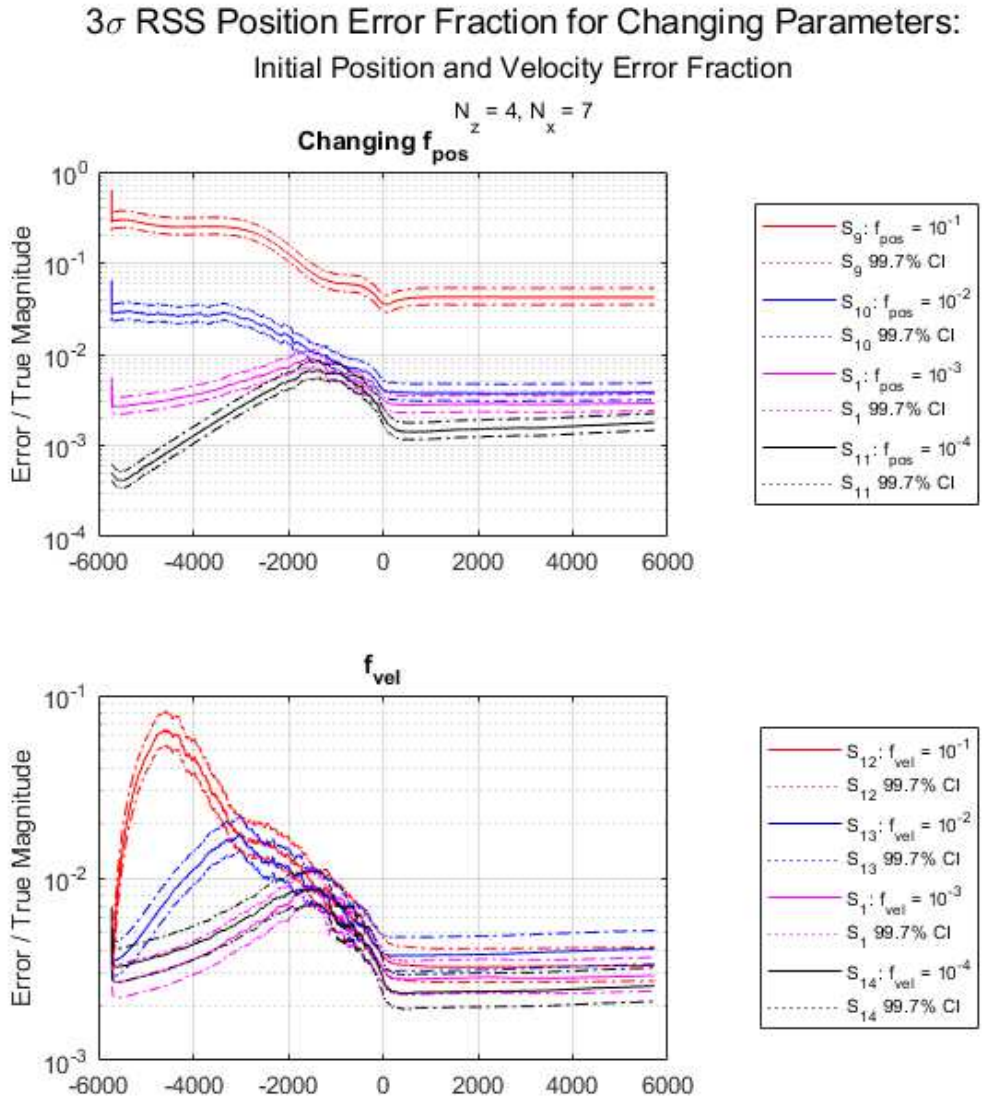

Fig. B.34: Monte Carlo 3σ RSS position error fractions and 99.7% confidence intervals for scenarios with varying initial position and velocity error fractions, $N_z = 4, N_x = 7$

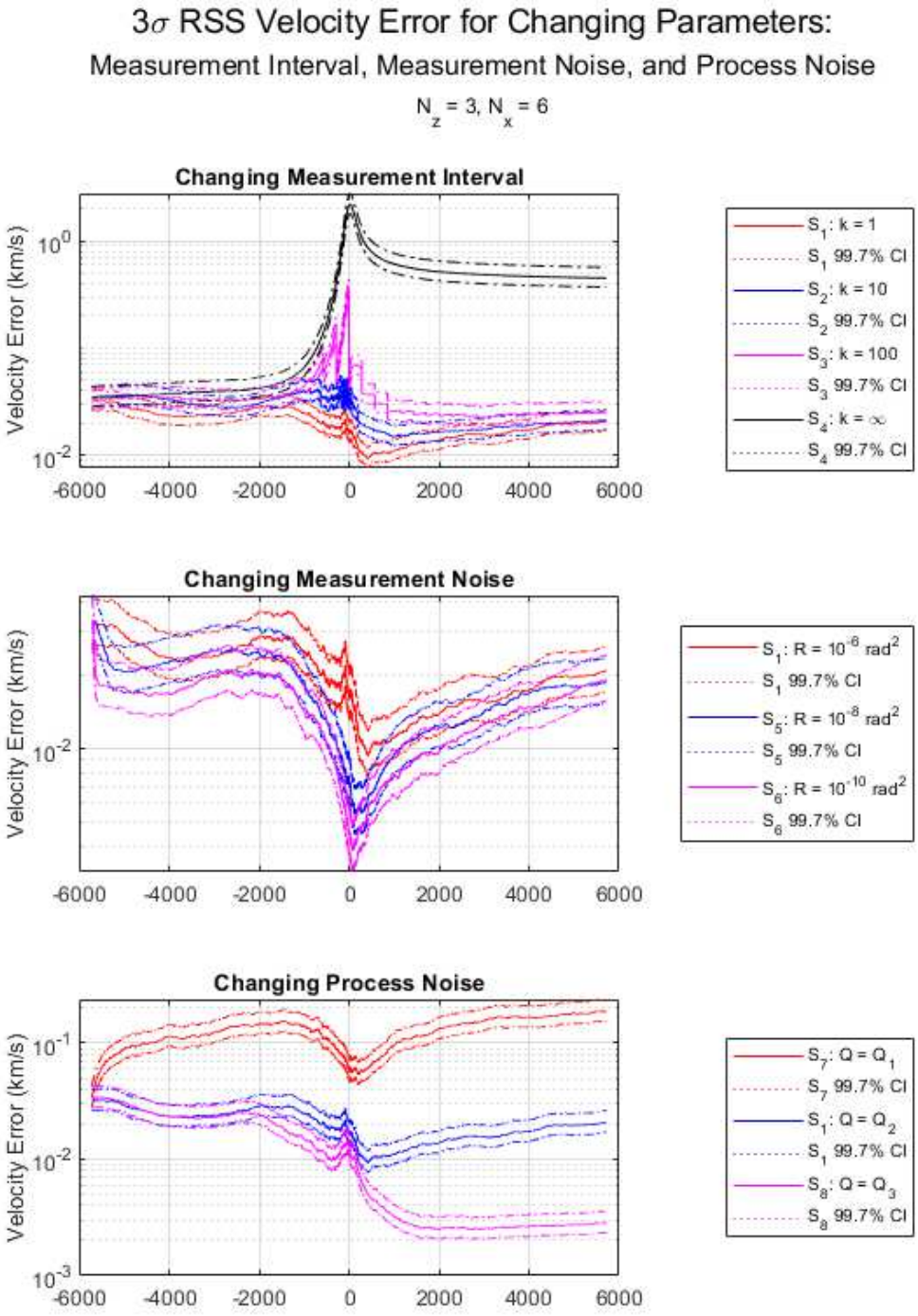

Fig. B.35: Monte Carlo 3σ RSS velocity errors and 99.7% confidence intervals for scenarios with varying measurement interval, measurement noise, and process noise, $N_z = 3, N_x = 6$

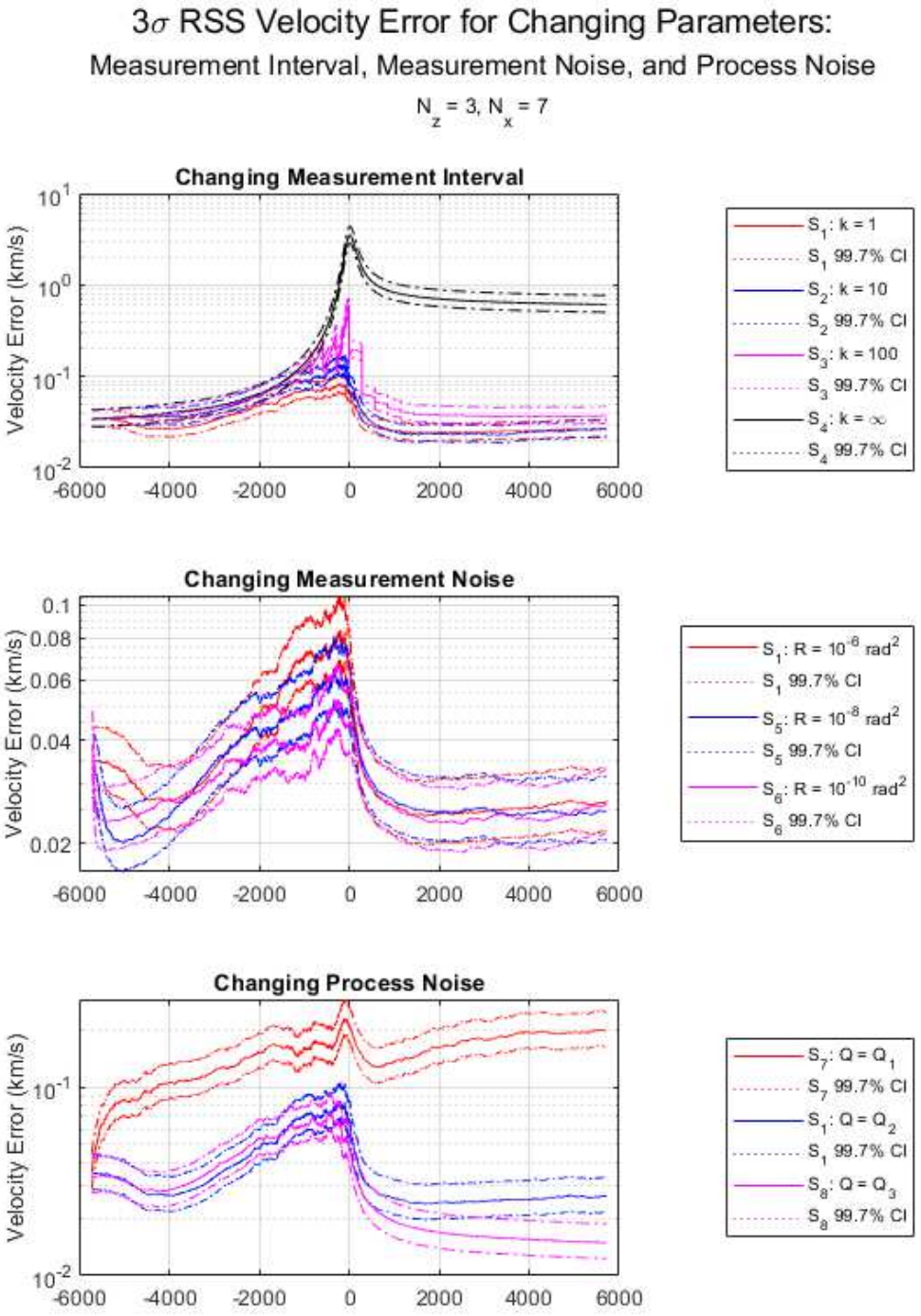

Fig. B.36: Monte Carlo 3σ RSS velocity errors and 99.7% confidence intervals for scenarios with varying measurement interval, measurement noise, and process noise, $N_z = 3, N_x = 7$

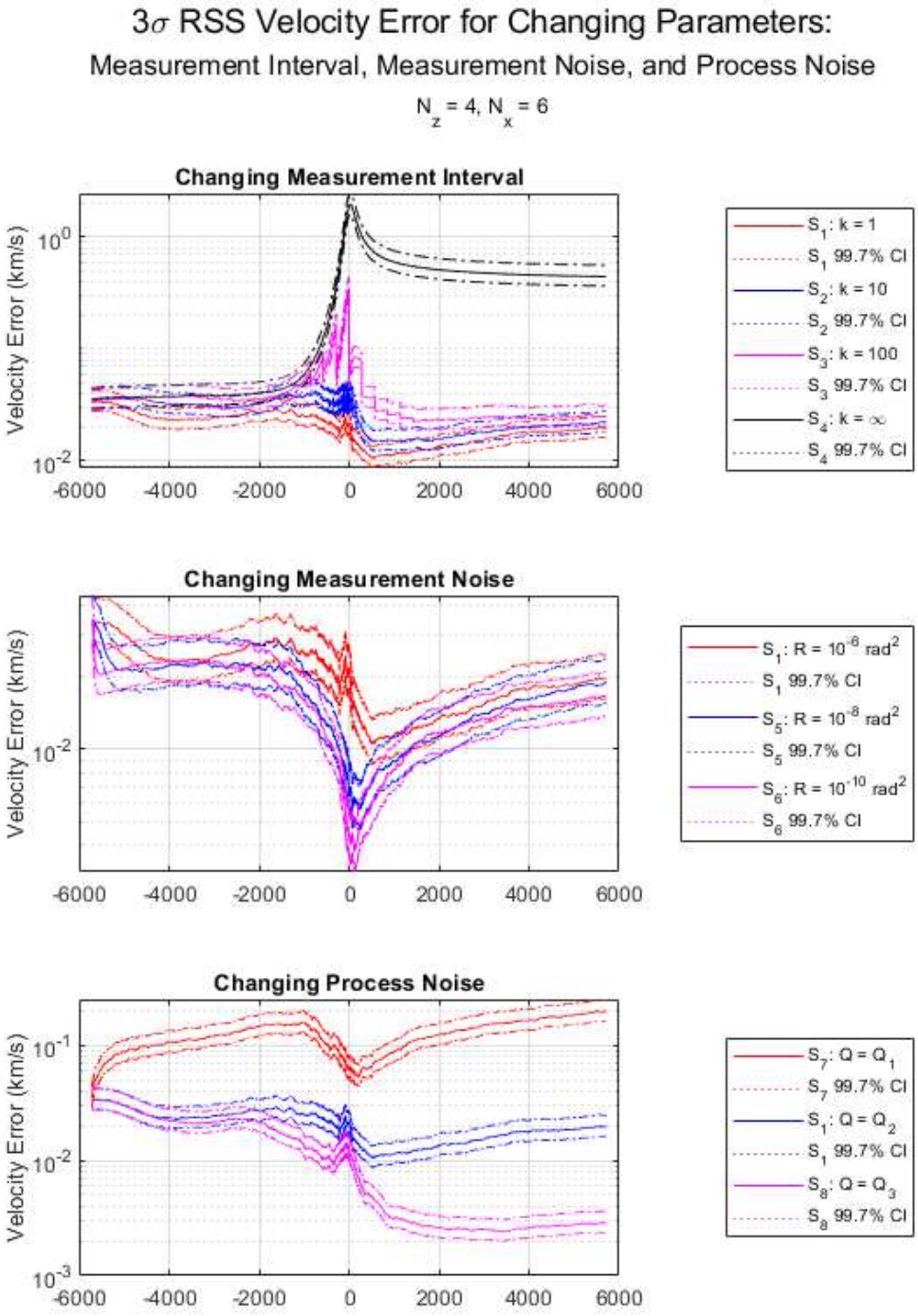

Fig. B.37: Monte Carlo 3σ RSS velocity errors and 99.7% confidence intervals for scenarios with varying measurement interval, measurement noise, and process noise, $N_z = 4, N_x = 6$

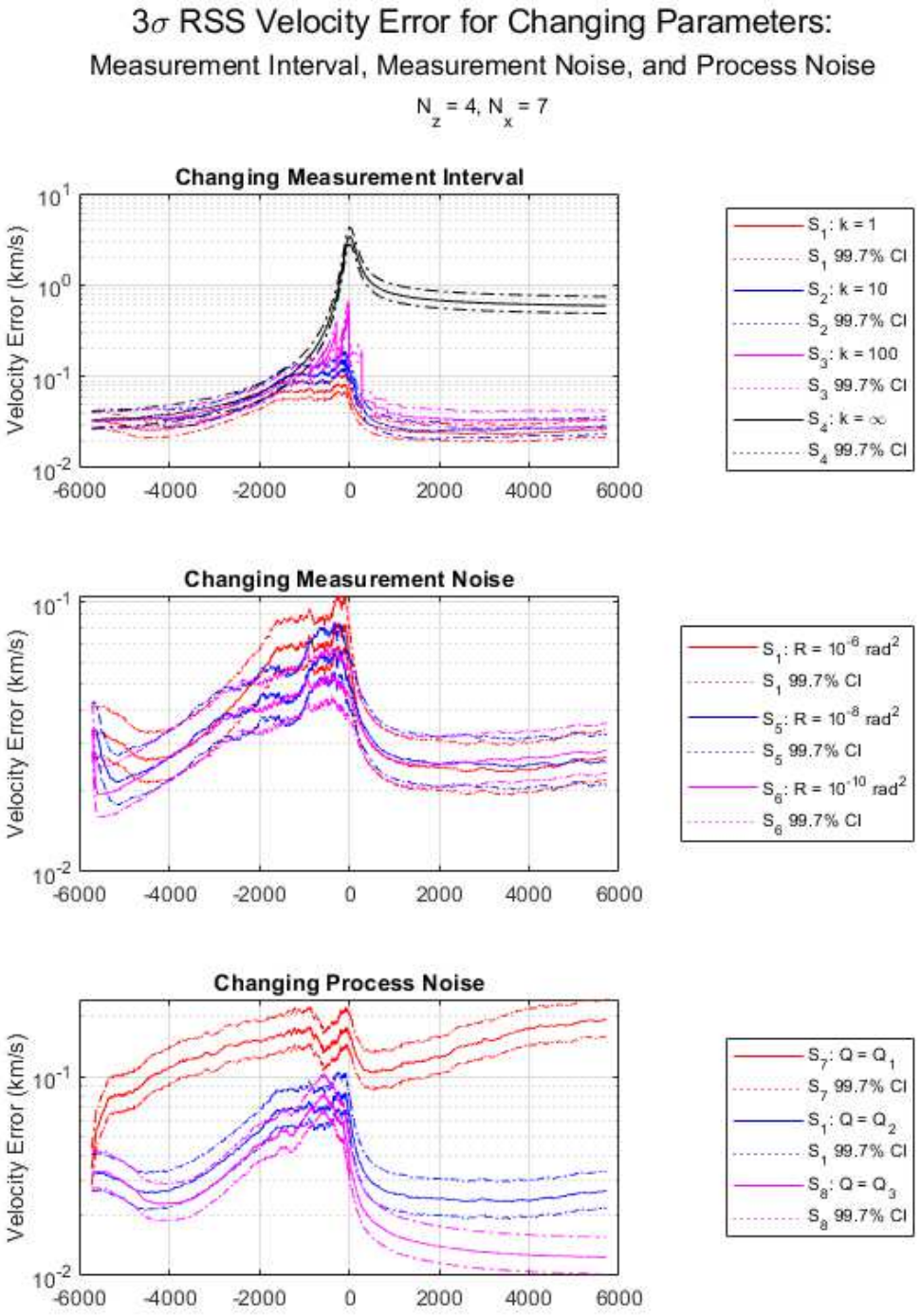

Fig. B.38: Monte Carlo 3σ RSS velocity errors and 99.7% confidence intervals for scenarios with varying measurement interval, measurement noise, and process noise, $N_z = 4, N_x = 7$

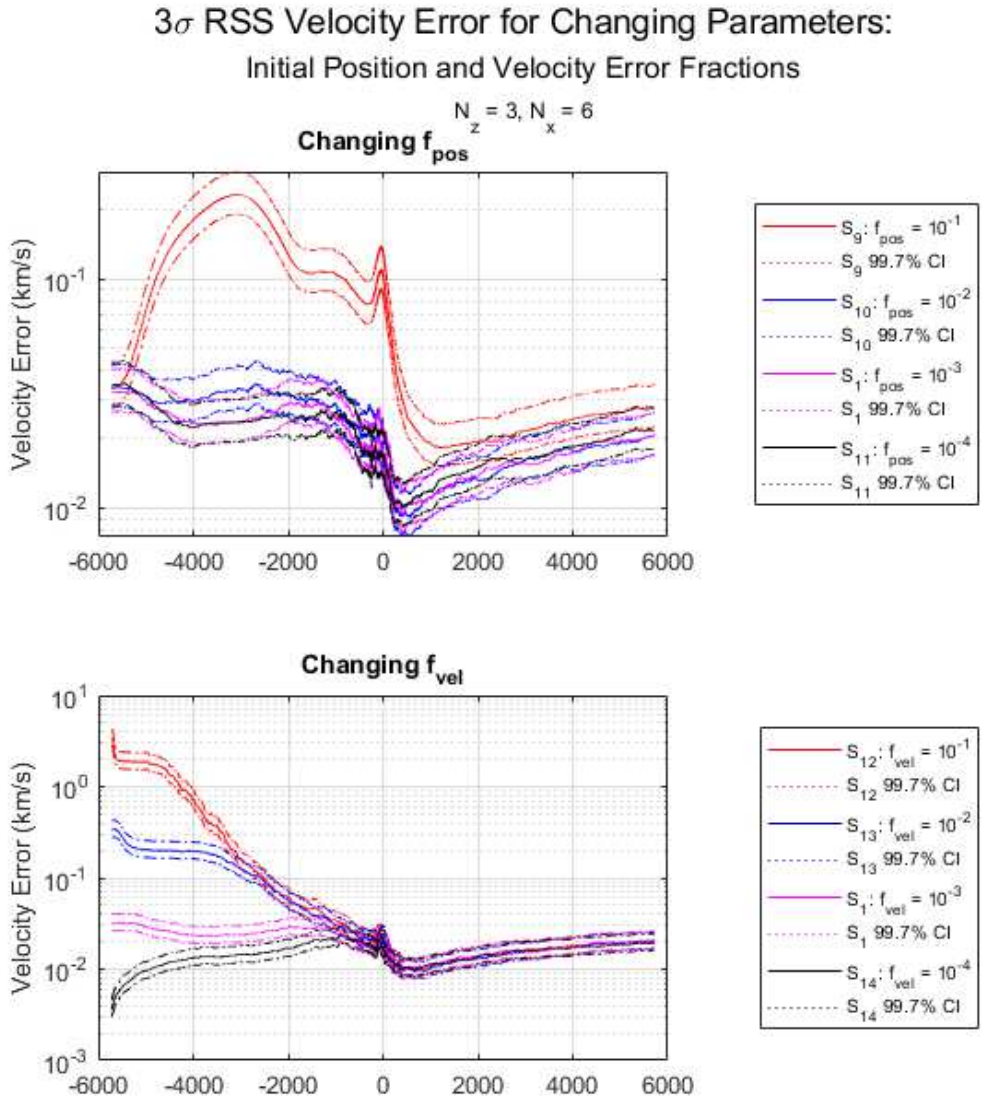

Fig. B.39: Monte Carlo 3σ RSS velocity errors and 99.7% confidence intervals for scenarios with varying initial position and velocity error fractions, $N_z = 3, N_x = 6$

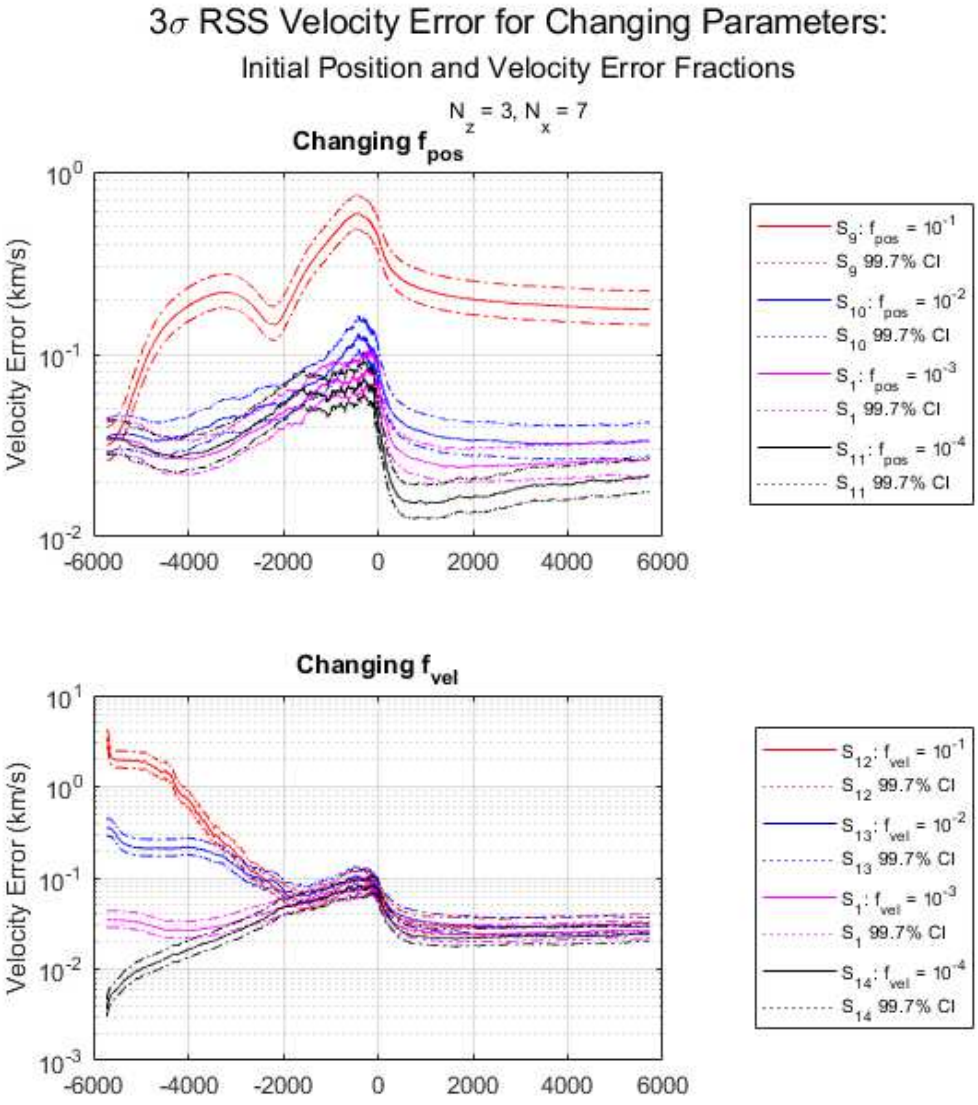

Fig. B.40: Monte Carlo 3σ RSS velocity errors and 99.7% confidence intervals for scenarios with varying initial position and velocity error fractions, $N_z = 3, N_x = 7$

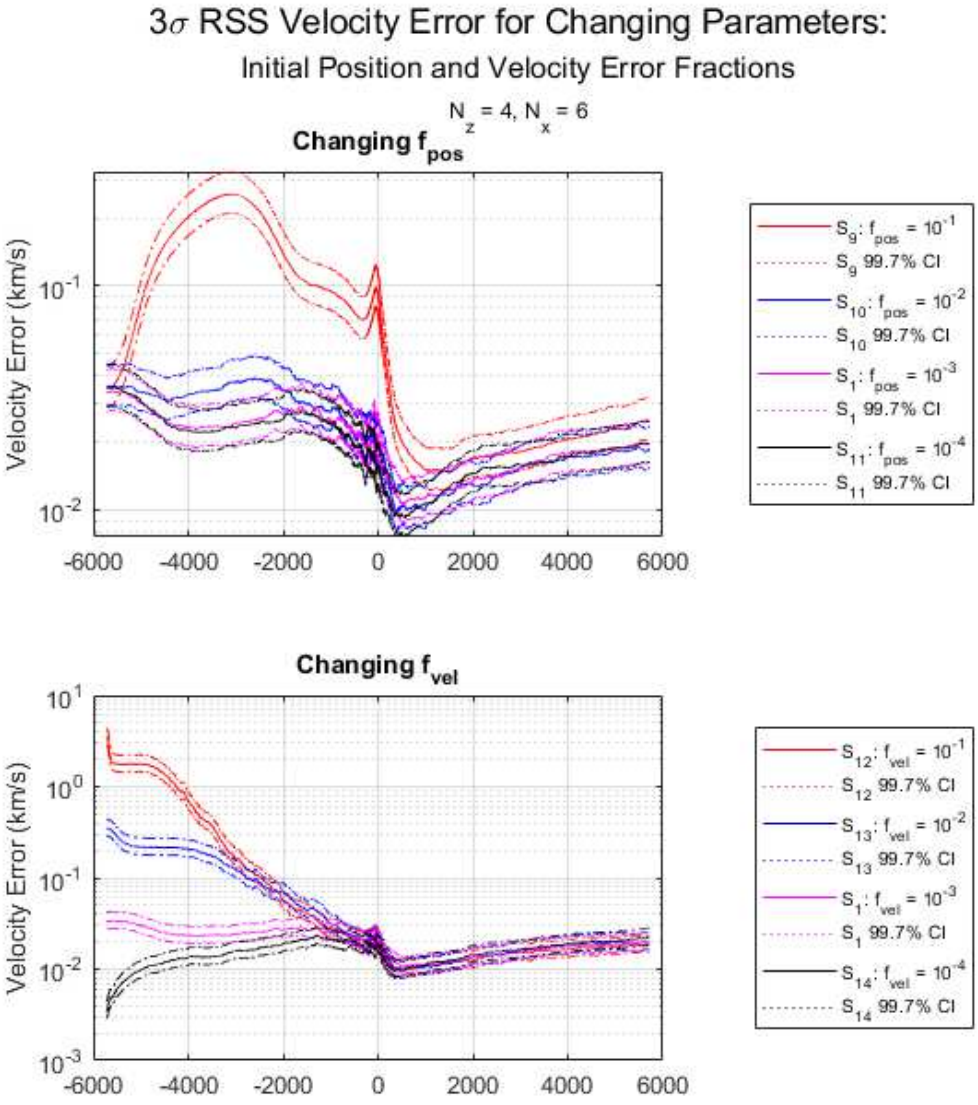

Fig. B.41: Monte Carlo 3σ RSS velocity errors and 99.7% confidence intervals for scenarios with varying initial position and velocity error fractions, $N_z = 4, N_x = 6$

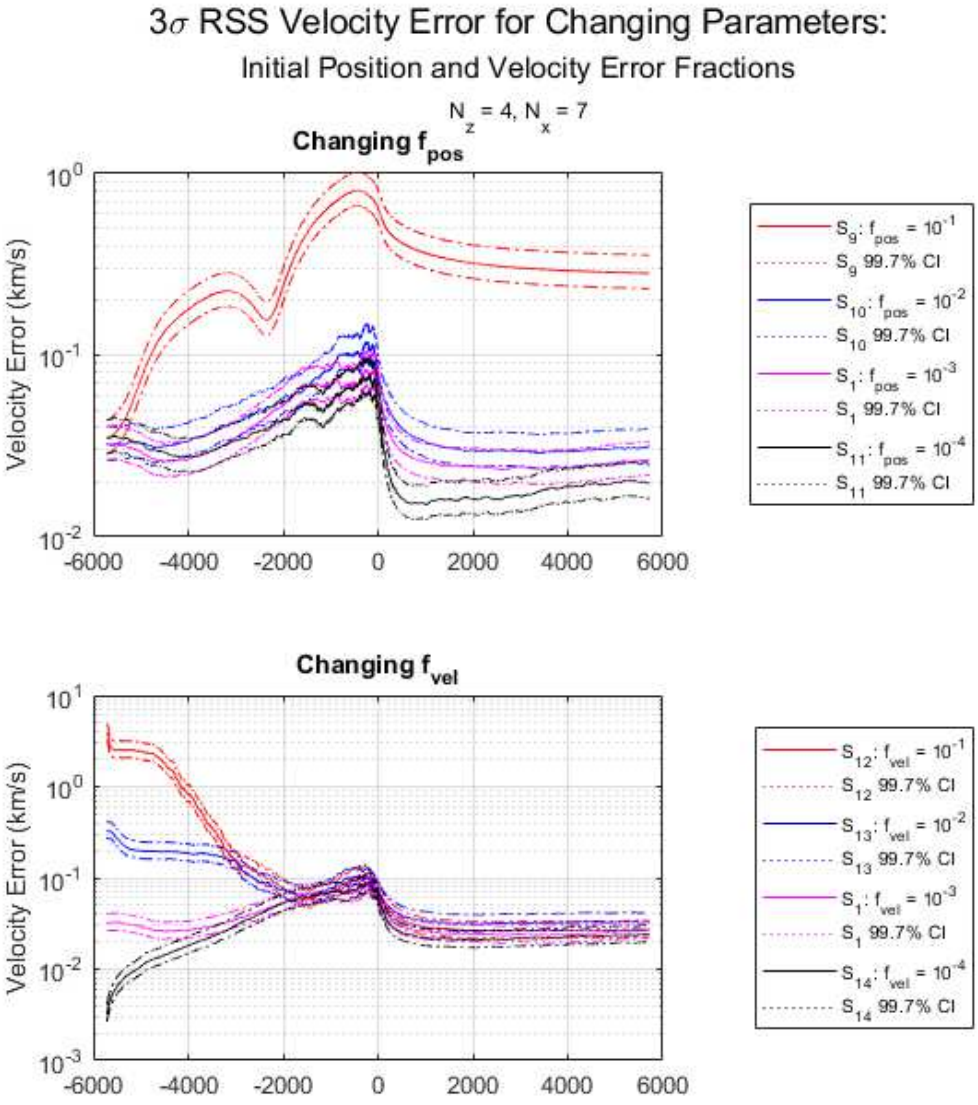

Fig. B.42: Monte Carlo 3σ RSS velocity errors and 99.7% confidence intervals for scenarios with varying initial position and velocity error fractions, $N_z = 4, N_x = 7$

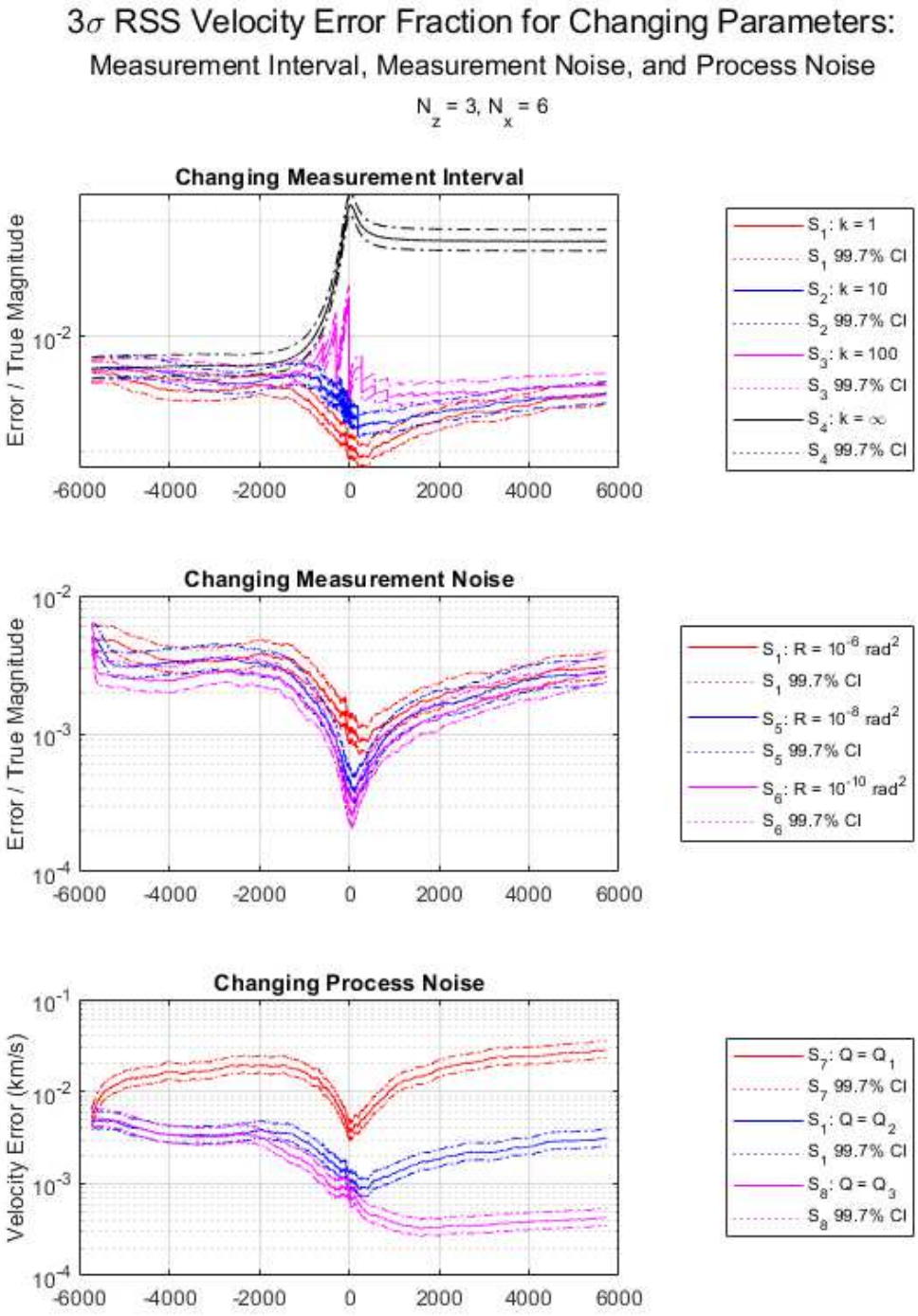

Fig. B.43: Monte Carlo 3σ RSS velocity error fractions and 99.7% confidence intervals for scenarios with varying measurement interval, measurement noise, and process noise, $N_z = 3, N_x = 6$

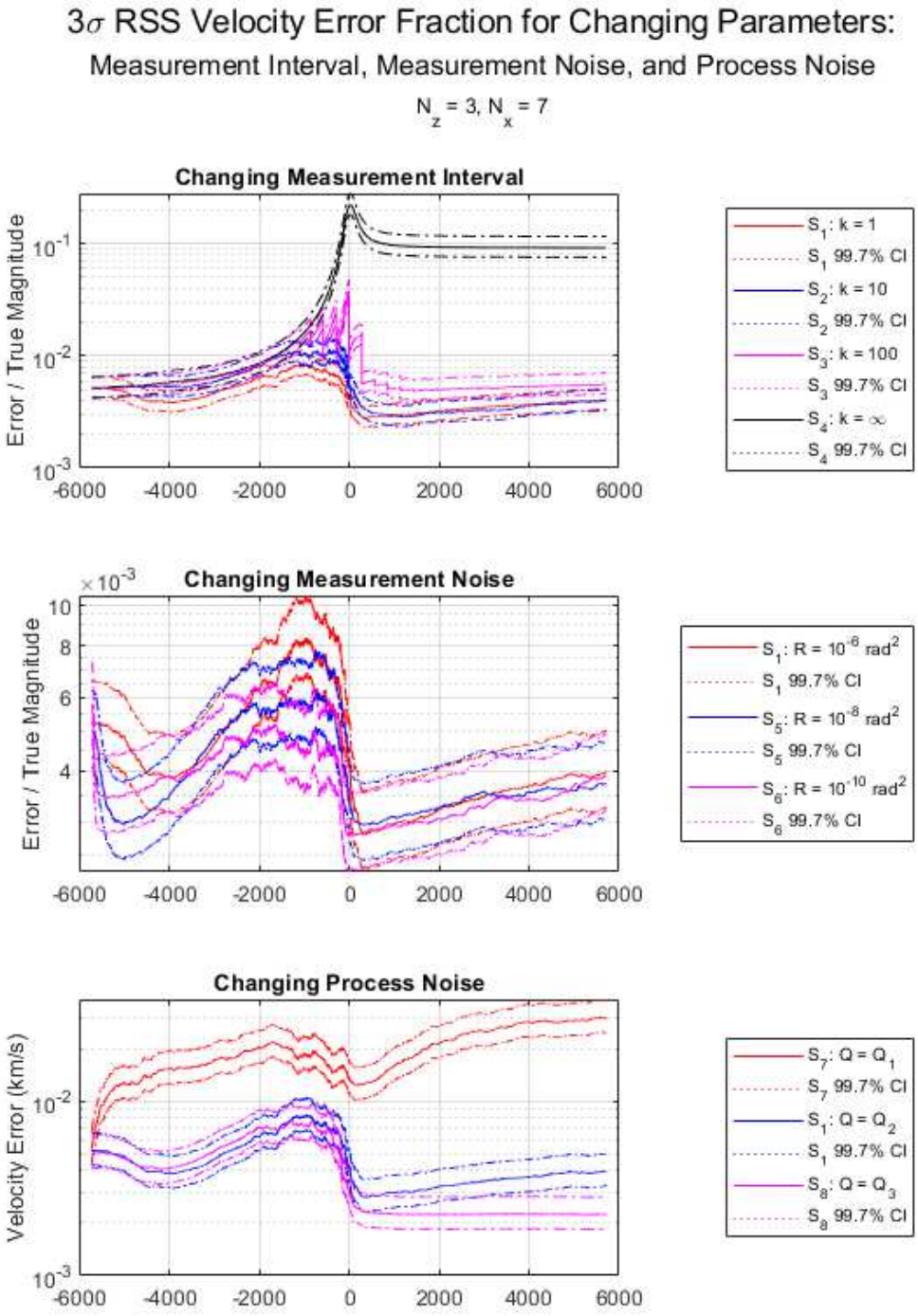

Fig. B.44: Monte Carlo 3σ RSS velocity error fractions and 99.7% confidence intervals for scenarios with varying measurement interval, measurement noise, and process noise, $N_z = 3, N_x = 7$

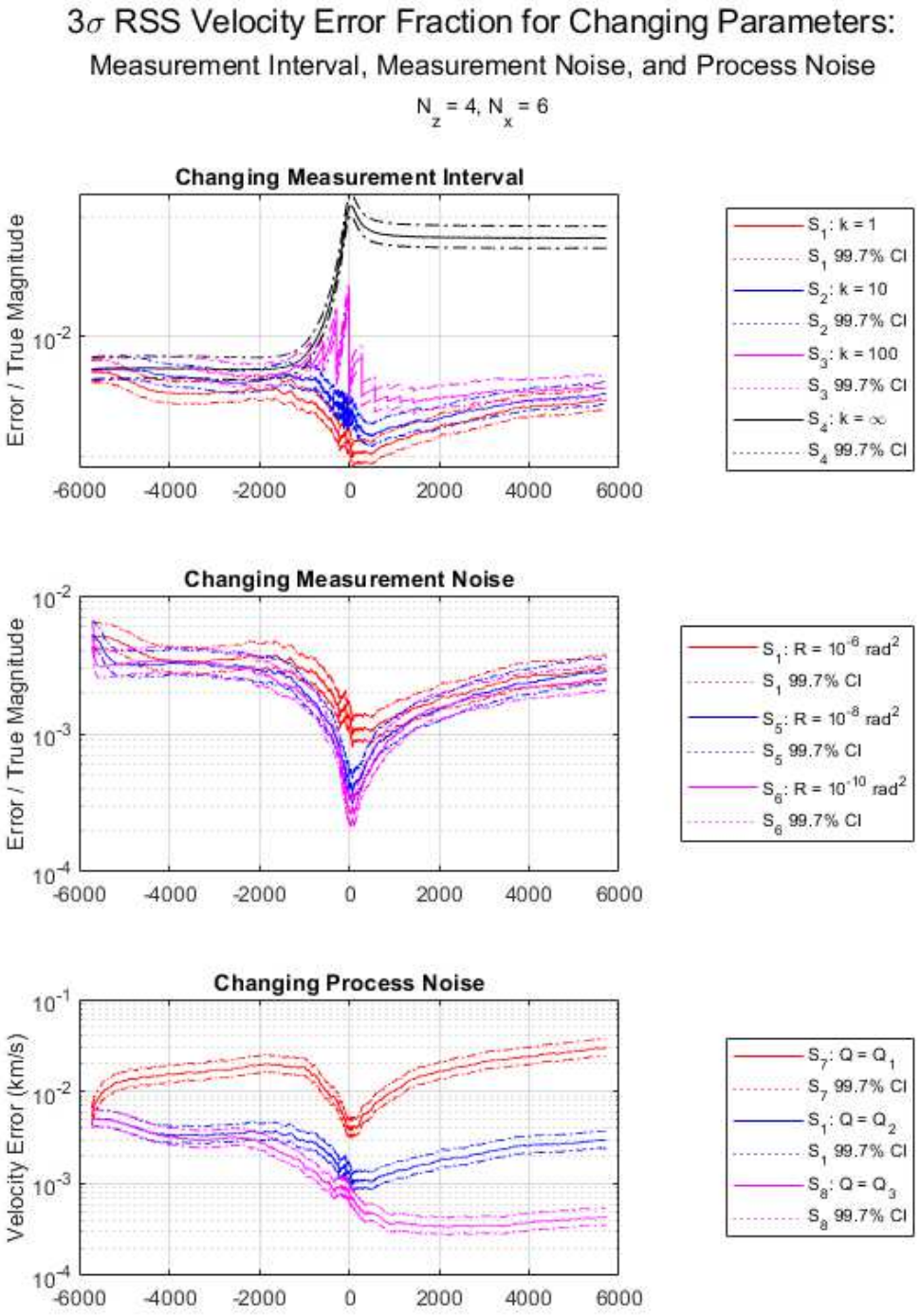

Fig. B.45: Monte Carlo 3σ RSS velocity error fractions and 99.7% confidence intervals for scenarios with varying measurement interval, measurement noise, and process noise, $N_z = 4, N_x = 6$

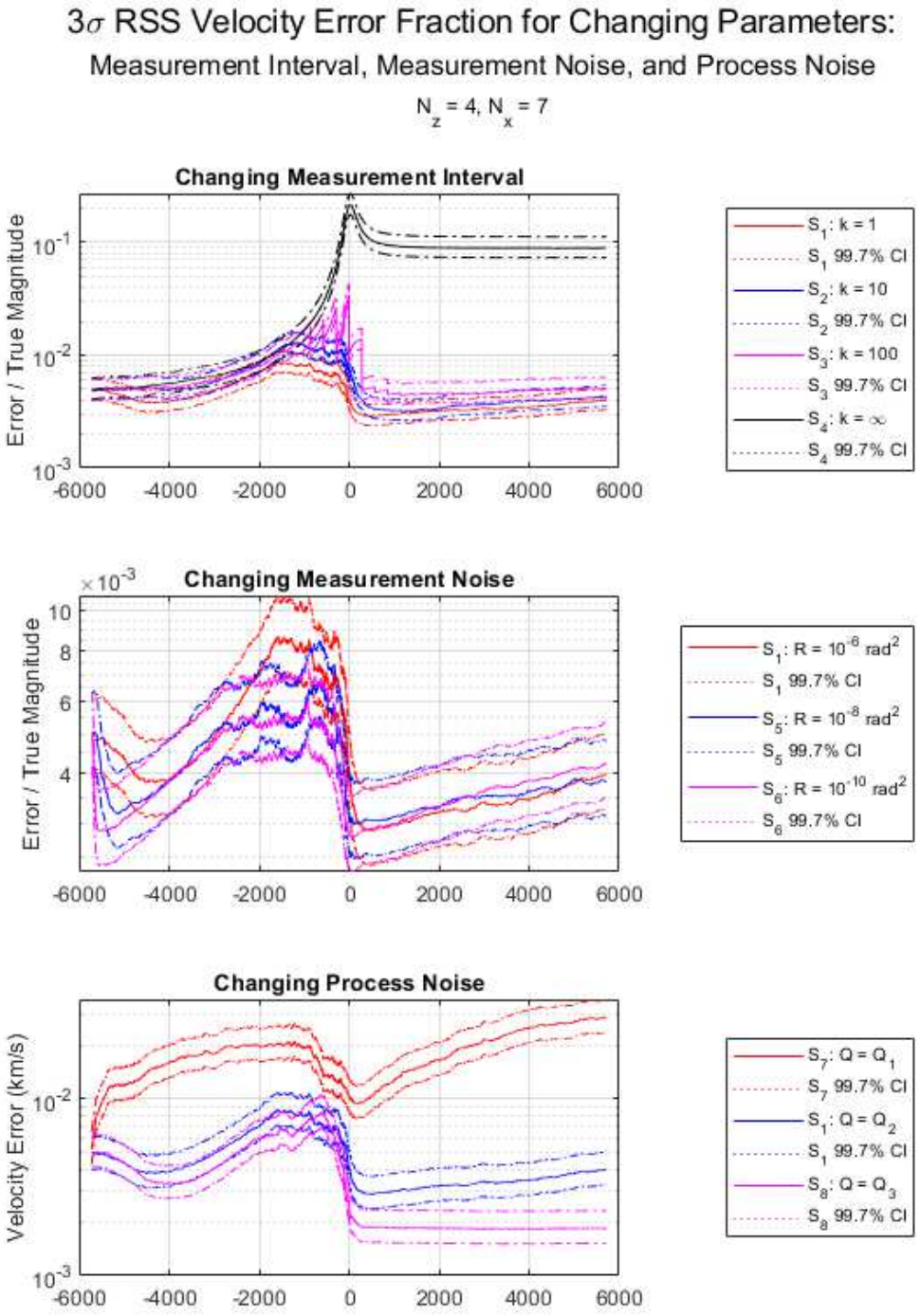

Fig. B.46: Monte Carlo 3σ RSS velocity error fractions and 99.7% confidence intervals for scenarios with varying measurement interval, measurement noise, and process noise, $N_z = 4, N_x = 7$

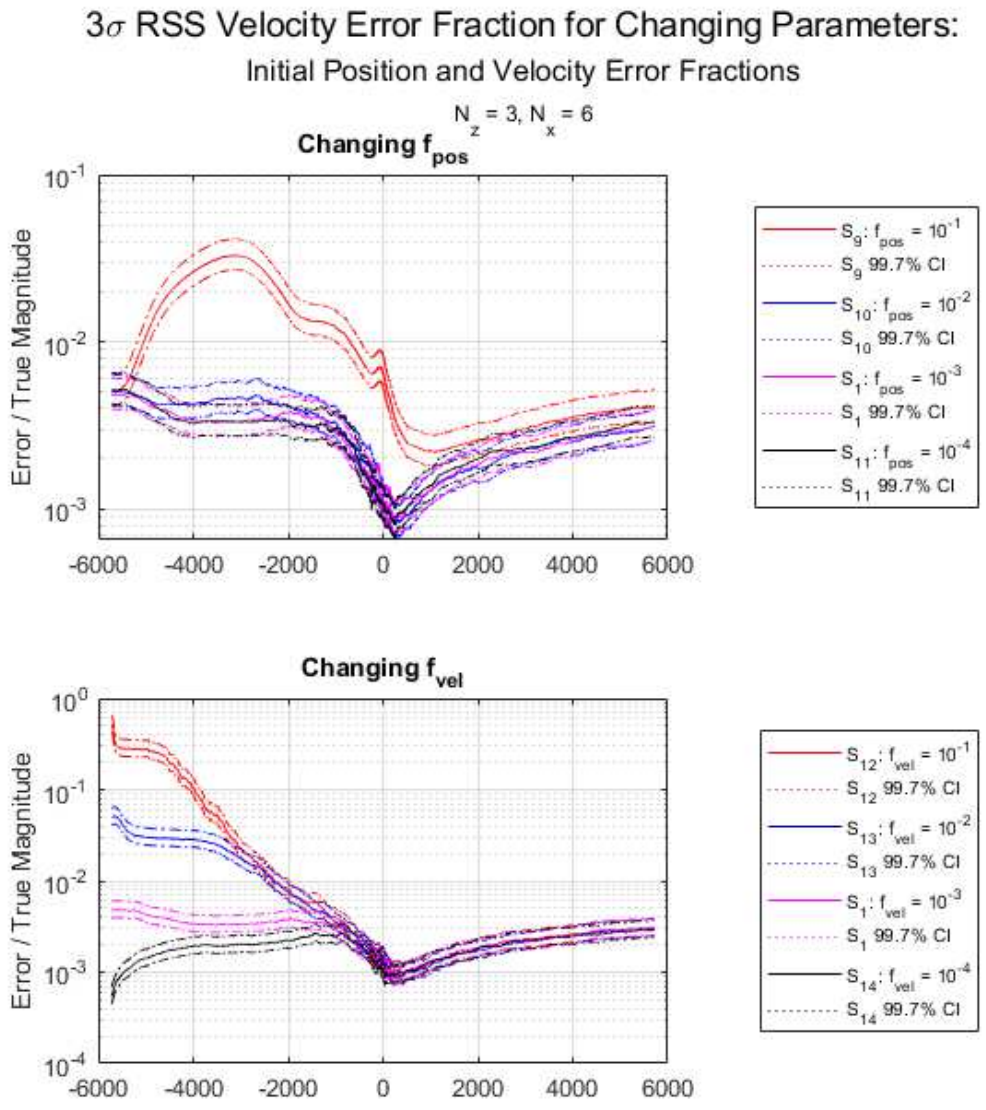

Fig. B.47: Monte Carlo 3σ RSS velocity error fractions and 99.7% confidence intervals for scenarios with varying initial position and velocity error fractions, $N_z = 3, N_x = 6$

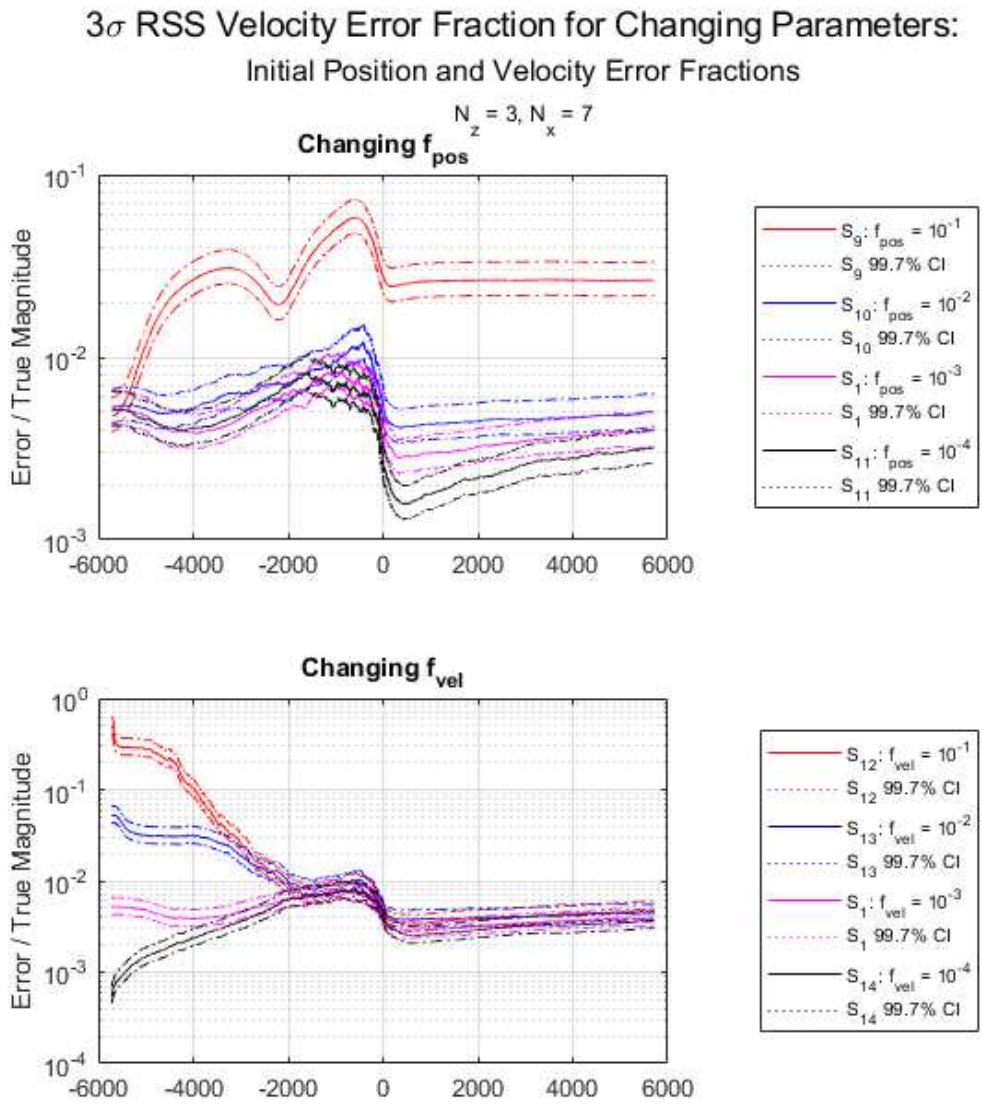

Fig. B.48: Monte Carlo 3σ RSS velocity error fractions and 99.7% confidence intervals for scenarios with varying initial position and velocity error fractions, $N_z = 3, N_x = 7$

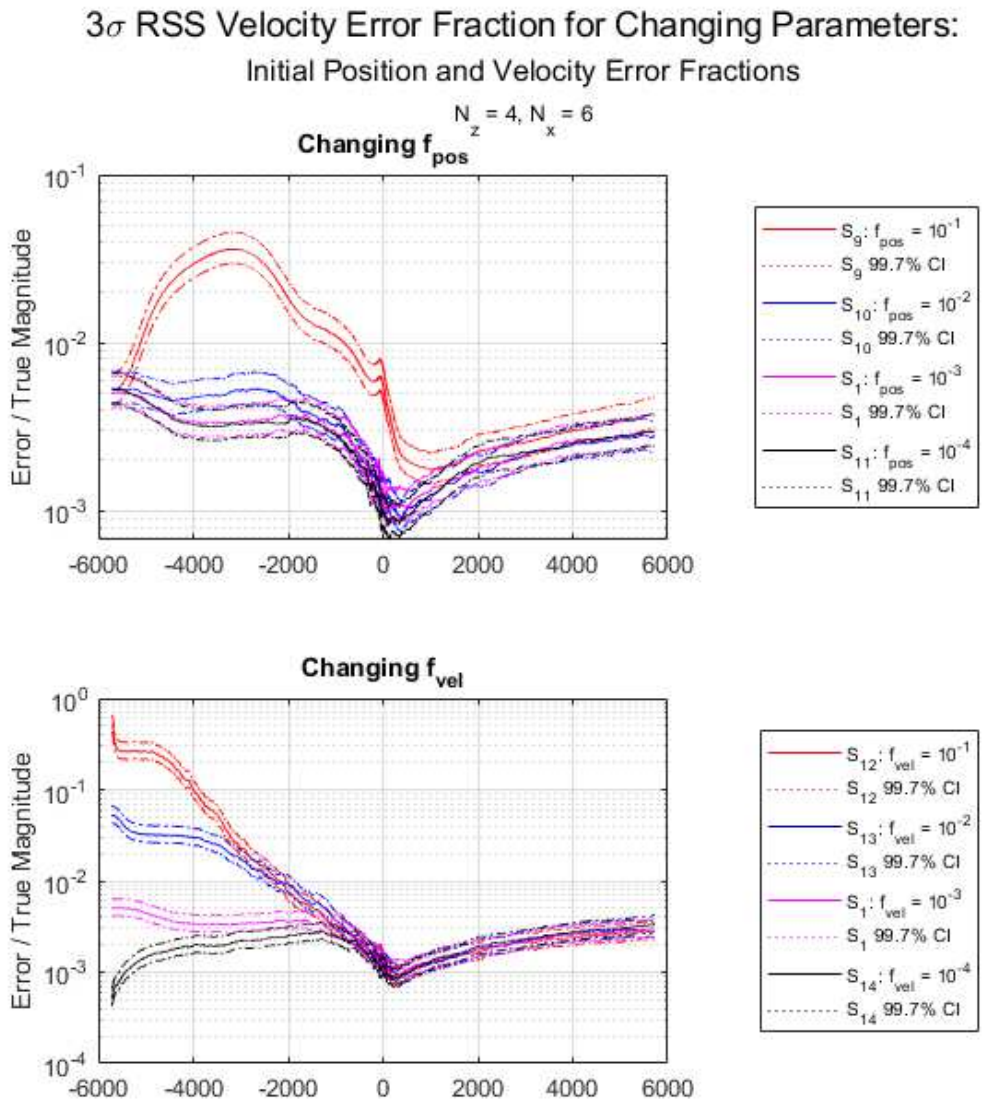

Fig. B.49: Monte Carlo 3σ RSS velocity error fractions and 99.7% confidence intervals for scenarios with varying initial position and velocity error fractions, $N_z = 4, N_x = 6$

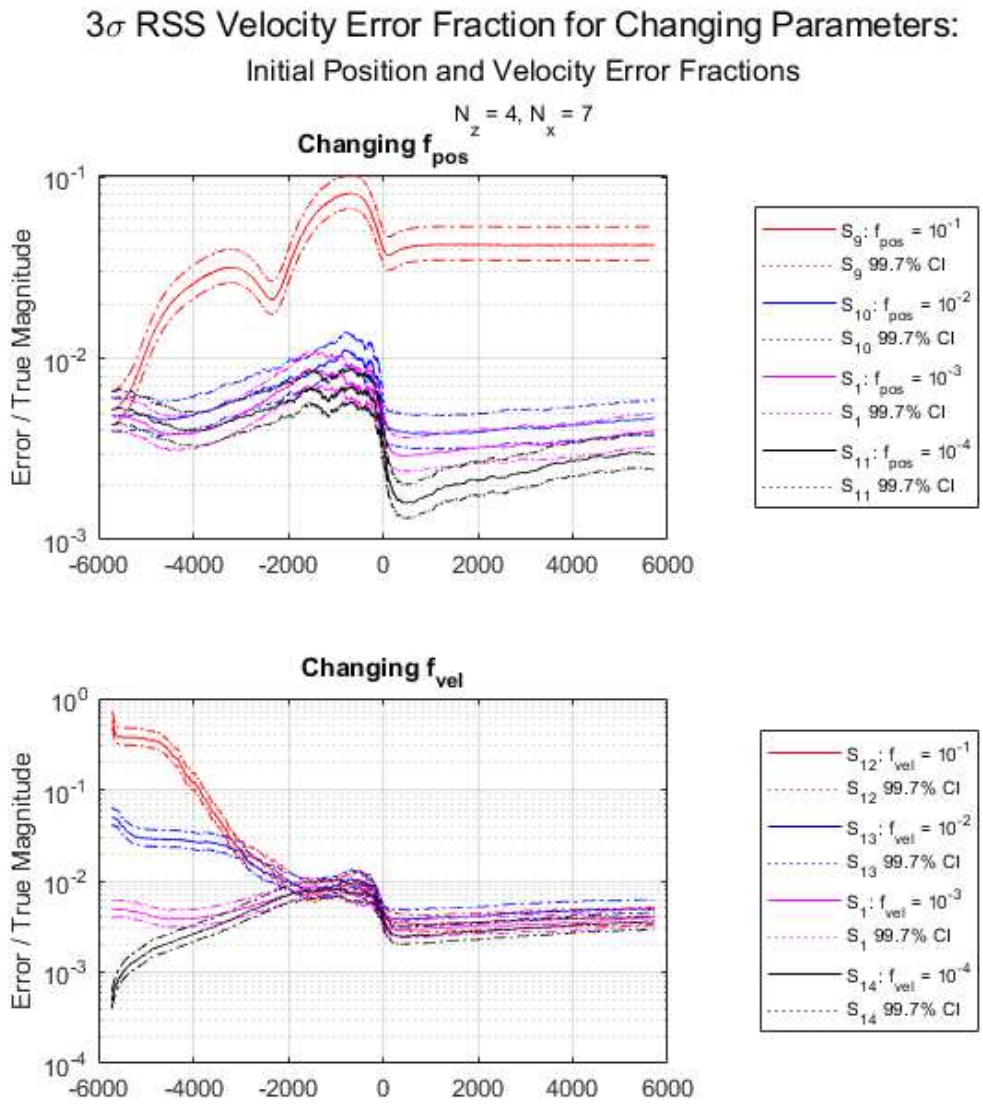

Fig. B.50: Monte Carlo 3σ RSS velocity error fractions and 99.7% confidence intervals for scenarios with varying initial position and velocity error fractions, $N_z = 4, N_x = 7$

noise strengths, initial position error fractions, and initial velocity error fractions.

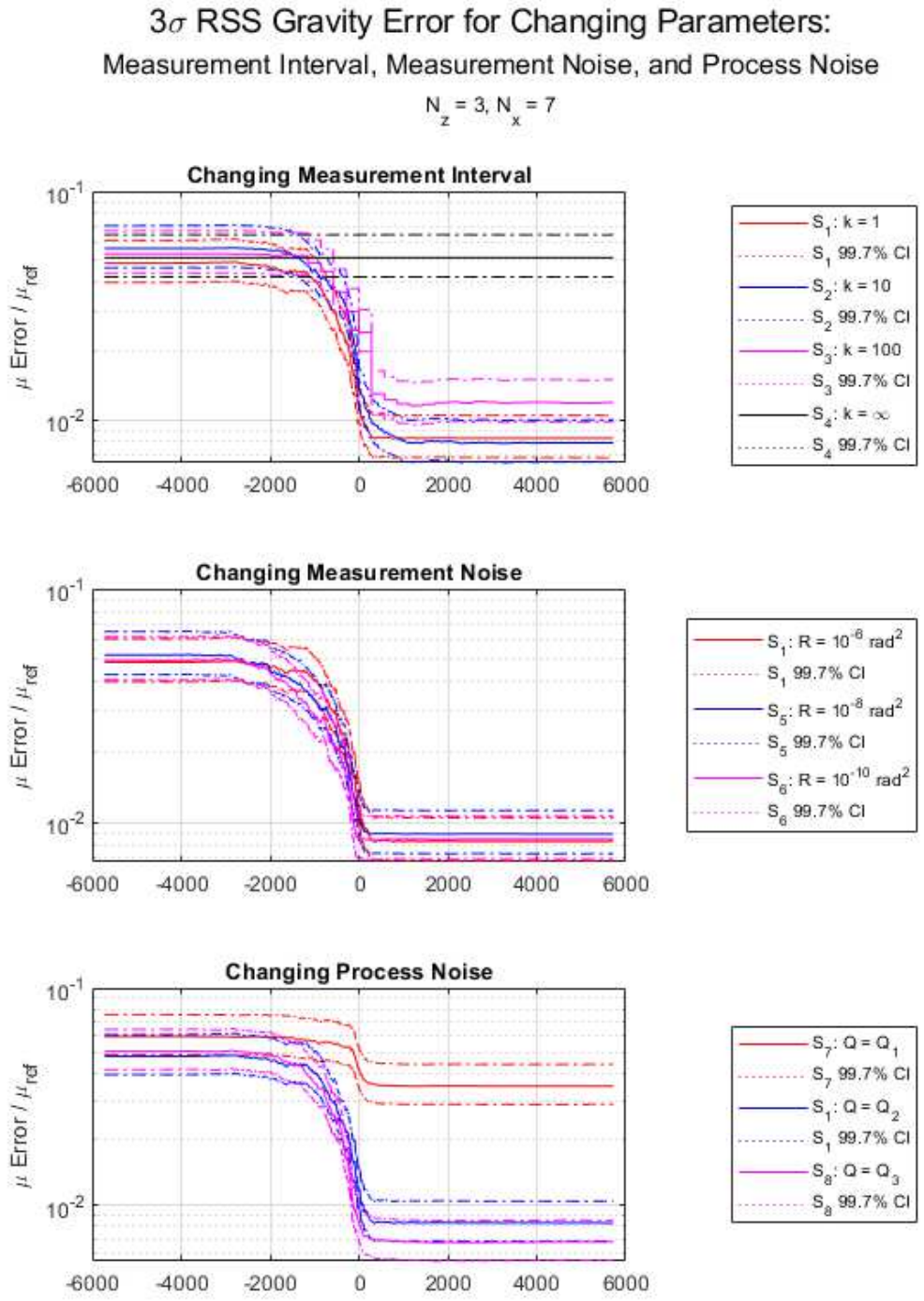

Fig. B.51: Monte Carlo 3σ gravity errors and 99.7% confidence intervals for scenarios with varying measurement interval, measurement noise, and process noise, $N_z = 3, N_x = 7$

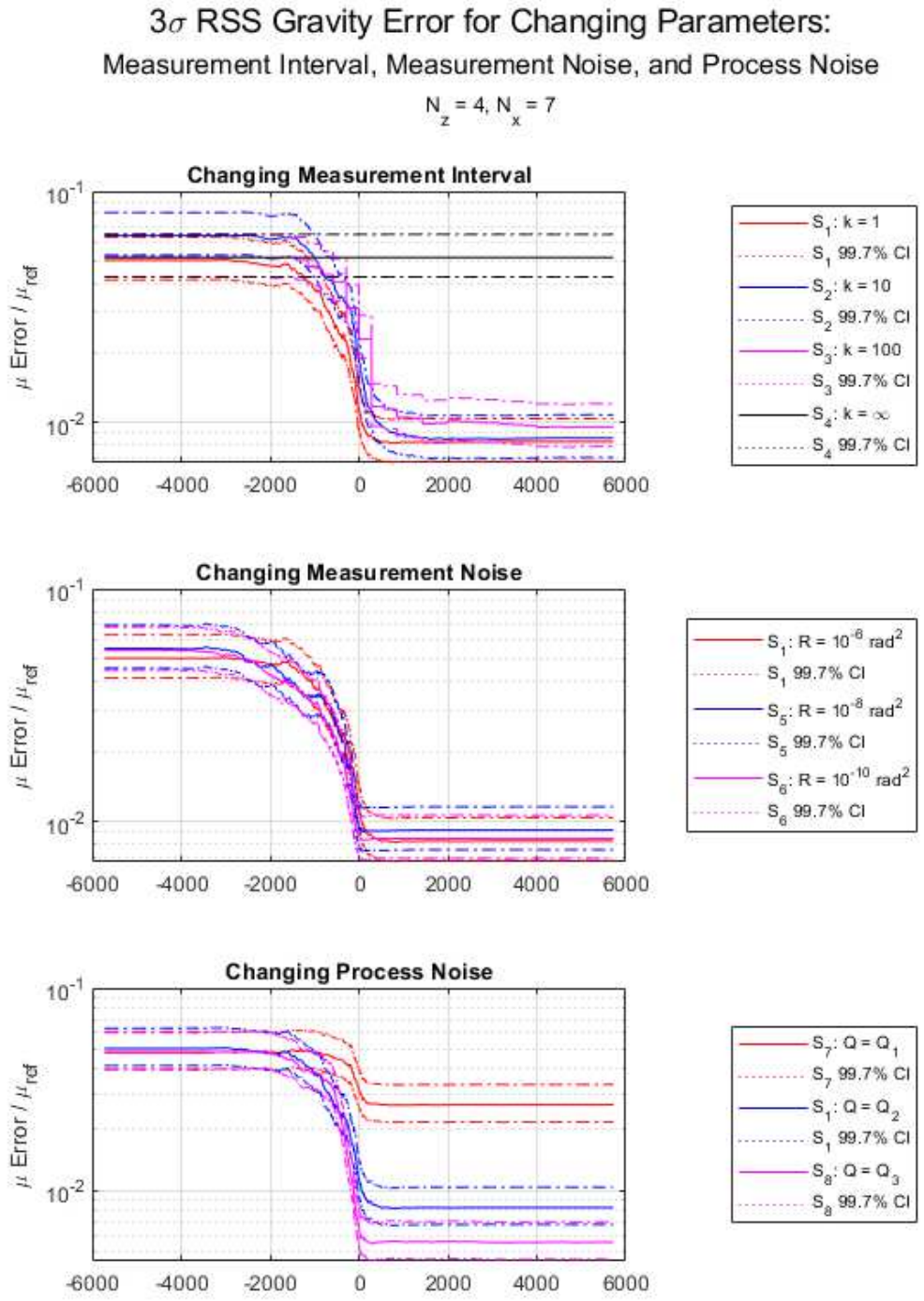

Fig. B.52: Monte Carlo 3σ gravity errors and 99.7% confidence intervals for scenarios with varying measurement interval, measurement noise, and process noise, $N_z = 4, N_x = 7$

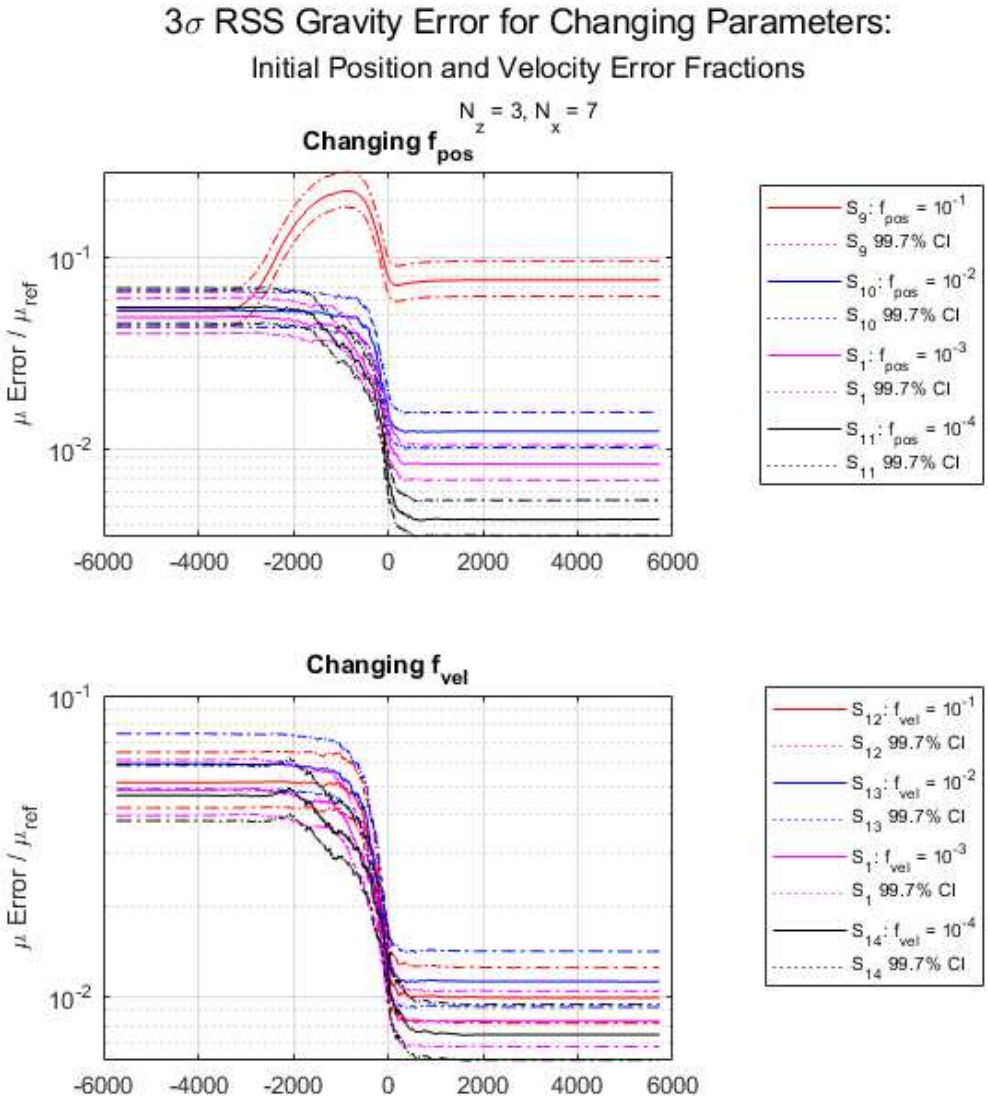

Fig. B.53: Monte Carlo 3σ gravity errors and 99.7% confidence intervals for scenarios with varying initial position and velocity error fractions, $N_z = 3, N_x = 7$

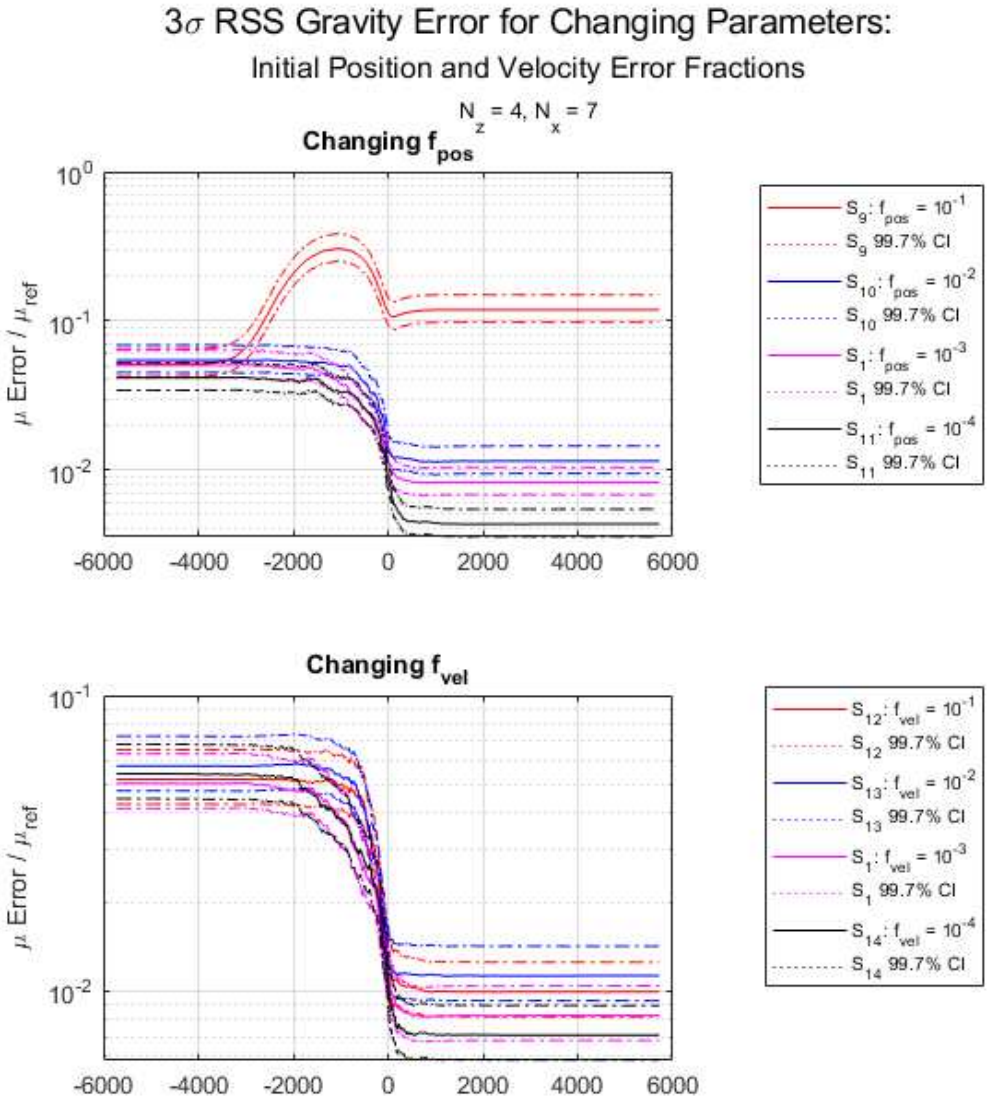

Fig. B.54: Monte Carlo 3σ gravity errors and 99.7% confidence intervals for scenarios with varying initial position and velocity error fractions, $N_z = 4, N_x = 7$